University of Southampton

Faculty of Environmental and Life Sciences

School of Ocean and Earth Science

A Laboratory Acoustic Study of Fluid and Ice Saturation Effects in Sands

by

Hanif Santyabudhi Sutiyoso

ORCID ID https://orcid.org/0000-0002-3111-2414

Thesis for the degree of Doctor of Philosophy

June 2025

University of Southampton

Abstract

Faculty of Environmental and Life Sciences

School of Ocean and Earth Science

Doctor of Philosophy

A Laboratory Acoustic Study of Fluid and Ice Saturation Effects in Sands

by

Hanif Santyabudhi Sutiyoso

Compressional wave velocity and attenuation are fundamental geophysical properties commonly used to characterise subsurface conditions, offering insights into sediment composition, fluid content, and mechanical behaviour. Understanding these properties in water-saturated and ice-bearing sediments is particularly important for accurately assessing partial saturation in applications such as hydrocarbon exploration, carbon dioxide storage, and permafrost monitoring. Additionally, it is crucial for evaluating risks related to gas hydrate dissociation, given permafrost's capacity to store massive gas hydrate deposits. As climate change accelerates permafrost thaw and alters subsurface ice distribution, there is an urgent need to improve our understanding of how acoustic responses relate to changes in ice and water saturation. This relationship is complex, leaving gaps in how these acoustic properties behave under realistic pressure conditions and across relevant frequency ranges. This study addresses these gaps by experimentally investigating compressional wave velocity and attenuation in water-saturated and ice-bearing sands under controlled pressures within the sonic frequency range, providing valuable insights for subsurface monitoring and environmental risk assessment with frequencies relevant to field measurements.

This research presents novel experimental measurements of acoustic velocity and attenuation in unconsolidated sand with varying water and ice saturations within the sonic frequency range of 1–20 kHz, relevant to well-logging and high-resolution seismic applications. Measurements were conducted on jacketed sand packs (0.5 m in length, 0.069 m in diameter) using a custom-designed, water-filled acoustic pulse tube under hydrostatic confining pressures up to 10 megapascals. For water-saturated conditions, velocity decreases with increasing saturation up to ~75%, then rises towards full saturation, while attenuation increases at low saturation before slightly decreasing. These trends align with predictions from effective medium rock physics models using uniform and patchy saturation approaches. Velocity increases with frequency across all samples, contrasting with the more complex frequency-dependent pattern observed in attenuation.

In ice-bearing sediments, results show that as ice melts, compressional wave velocity consistently decreases while attenuation increases across all tested pressures. This behaviour is most pronounced at the lowest pressure (2.5 MPa), where weaker grain-to-grain contacts allow ice to play a greater role in supporting the sediment structure. While the sensitivity of velocity to ice saturation remains relatively consistent across pressures, attenuation shows stronger pressure dependence, with more significant increases at lower pressures, particularly at higher ice saturations. These findings suggest that effective pressure and ice morphology (pore-filling vs. load-bearing vs. cementing) significantly influence the acoustic response of ice-bearing sands within the tested pressure range. Comparisons with three-phase Biot-type rock physics models indicate that velocity is primarily governed by ice distribution within the pore space, whereas attenuation is further influenced by ice morphology and sediment permeability. The observed frequency-dependent trends in both velocity and attenuation highlight the complex interactions between ice, water, and sediment grains under varying conditions.

These findings highlight the complex relationship between pore fluids and ice content and how acoustic properties respond to these changes. They offer valuable applications for improving the interpretation of geophysical surveys in permafrost regions, enabling more accurate estimates of ice content and sediment stability. Future studies could build on these results by integrating field-scale data and refining rock physics models to better capture complex pore fluid interactions, further advancing our understanding of ice-bearing sediments for effective permafrost monitoring.

Table of Contents

Table of Tables

Table of Figures

Research Thesis: Declaration of Authorship

Print name: Hanif Santyabudhi Sutiyoso

Title of thesis: A Laboratory Acoustic Study of Fluid and Ice Saturation Effects in Sands

I declare that this thesis and the work presented in it are my own and has been generated by me as the result of my own original research.

I confirm that:

1. This work was done wholly or mainly while in candidature for a research degree at this University;
2. Where any part of this thesis has previously been submitted for a degree or any other qualification at this University or any other institution, this has been clearly stated;
3. Where I have consulted the published work of others, this is always clearly attributed;
4. Where I have quoted from the work of others, the source is always given. With the exception of such quotations, this thesis is entirely my own work;
5. I have acknowledged all main sources of help;
6. Where the thesis is based on work done by myself jointly with others, I have made clear exactly what was done by others and what I have contributed myself;
7. Parts of this work have been published as:

Journal Publications:

Sutiyoso, H.S., Sahoo, S.K., North, L.J., Minshull, T.A., Falcon-Suarez, I.H. & Best, A.I. (2024). Laboratory measurements of water saturation effects on the acoustic velocity and attenuation of sand packs in the 1–20 kHz frequency range. Geophysical Prospecting, 1–22. https://doi.org/10.1111/1365-2478.13607

Sutiyoso, H. S., Sahoo, S. K., North, L. J., Falcon-Suarez, I. H., Minshull, T. A., & Best, A. I. (2025). Laboratory measurement of sonic (1–20 kHz) P-wave velocity and attenuation during melting of ice-bearing sand. *Journal of Geophysical Research: Solid Earth*, 130, e2024JB030465. https://doi.org/10.1029/2024JB030465

Conference Proceedings:

Sutiyoso, H.S., Sahoo, S.K., Minshull, T.A., North, L.J., Falcon-Suarez, I.H., Best, A.I. (2022). Laboratory measurement of acoustic velocity and attenuation in partially saturated sand. 6th International Workshop on Rock Physics, A Coruña, Spain.

Sutiyoso, H.S., Sahoo, S.K., Best, A.I., Minshull, T.A., North, L.J. (2023). Laboratory study of velocity and attenuation of water saturated sand using acoustic pulse tube in 1-20 kHz frequency. 10th International Conference on Gas Hydrates (ICGH10), Singapore.

Sutiyoso, H.S., Sahoo, S.K., North, L.J., Minshull, T.A., Falcon-Suarez, I.H., Best, A.I. (2024). P-wave velocity and attenuation in melting ice at 1-20 kHz frequency. 7th International Workshop on Rock Physics, Pau, France.

Journal publications during PhD candidature but not included in this thesis:

Khan, S.H., Sahoo, S.K., Falcon-Suarez, I.H., Marin-Moreno, H., Sutiyoso, H.S., Madhusudhan, B.N., Majumder, C.B., Arora, A., Best A.I. (2024). Investigation of methane gas bubble dynamics and hydrate film growth during hydrate formation using 4-D time-lapse synchrotron X-ray computed tomography. Front. Earth Sci. 12:1438185. doi: 10.3389/feart.2024.1438185

Signature: ....Date: 3 June 2025

Acknowledgements

I would wholeheartedly like to thank my supervisory team: Prof. Angus Best, Prof. Tim Minshull, and Dr. Sourav Sahoo, for their guidance, advice, and discussions, as well as their encouragement throughout this thesis writing and doctoral journey. They taught me to always be curious and to ask the right questions, and they pushed me to become a better researcher. Special thanks to Angus for asking me questions during discussions, even simple ones like, “Why do we care?” which helped me think through what I had been doing and indirectly improved my scientific decision-making. Special thanks to Tim for his excellent support throughout this study from the very start, as he quickly assisted with my PhD application process; this study might have started late (or even not been possible!) if it had not been for his help. Special thanks to Sourav, who supported me 100% during this study, both in terms of the research and the daily life around it. Sometimes I see him as a big brother who helped me to succeed, and this made the process much more enjoyable.

I would like to thank Dr. Laurence North for all of his help in the laboratory and with data processing, as well as our discussions about anything from bicycles to running. These conversations made working in the lab less of a hassle and more enjoyable. I would also like to thank Dr. Ismael Himar Falcon-Suarez for all his advice, as well as tips and tricks for working in the laboratory, and more recently, for the part-time job and all our discussions about carbon storage, which always piqued my interest.

I am most grateful to my wife, *Intan*, who said yes when I caught her off-guard at that street food kiosk with the idea of living abroad for my PhD. Since then, she has always been supportive and critical of both my academic and life decisions, which has helped me become a better person. I can never thank you enough. And to our son, *Jayala*: I thought I had already learned a lot during this PhD, but oh boy, you taught me even more. Those big eyes always staring at me when I was writing this thesis encouraged me to push through it.

My parents, brother, and sister have always been very supportive, especially my mother, who was always eager to hear the details of my experiments, even though they are far from her field of work.

I would also like to thank the super-supportive group of friends, Hepilemon (slightly re-arranged from Happy Lemon, the boba place we called our HQ). To Mba Rikha, Mas Bam, Mba Arum, and Mas Fuad, thank you for being like family to me, my wife, and my son here.

Last but not least, I would like to acknowledge the funding provided by the Indonesian Endowment Fund for Education (Lembaga Pengelola Dana Pendidikan, LPDP). I also want to acknowledge the funding from UK NERC and NOC RISC for indirectly supporting my study through the acoustic pulse tube project.

As this PhD comes to an end, I am ready to move forward with all the experience I have gained from this journey!

Chapter 1 Introduction

1.1 Identifying and Addressing Gaps in Current Studies

Studies into the elastic wave properties of sediments have advanced significantly, yet several gaps limit a comprehensive understanding and the practical application of these findings. One major limitation is the lack of laboratory frequency-dependent measurements that align with field seismic or sonic logging frequencies. Laboratory studies are valuable as they allow controlled investigation of the physical parameters affecting elastic wave propagation in rocks and sediments. This enables the development and testing of theoretical models for interpreting field data, which is difficult in the field due to limited access to large rock volumes. In the field, assumptions about rock properties must often be made based on costly and limited core samples. Understanding the mechanisms, including frequency dependence, of wave propagation is key to accurately interpreting seismic and sonic log measurements for practical applications.

Most laboratory experiments focus on ultrasonic frequency ranges (150 kHz to 1 MHz) dictated by practical considerations such as obtainable geological core sample sizes (e.g., Amalokwu et al., 2014; Carcione and Seriani, 1998; Li et al., 2024; Nakano and Arnold, 1973; Prasad, 2002; Winkler, 1985), which differ significantly from the field measurement frequencies (~Hz to kHz) (e.g., Barriere et al., 2012; Murphy, 1984; Sutiyoso et al., 2024a). While high-frequency measurements provide valuable insights into basic rock properties like compressional and shear velocities (Batzle et al., 2006), applying experimental results to field-scale applications remains difficult, due to scaling effects (Barriere et al., 2012; Li et al., 2020) and inconsistent power law behaviour in attenuation data (Chotiros and Isakson, 2004). Scaling effects arise from the physical and interpretational discrepancies encountered when scaling up laboratory-scale measurements to field-scale seismic observations. These discrepancies are primarily driven by differences in frequency, wavelength, sample size, and heterogeneity of the medium. Expanding experimental studies to include field-relevant frequencies could improve the accuracy of field data interpretation and aid the validation of theoretical models (Chotiros and Isakson, 2004).

Another gap in the literature, to the best of my knowledge, involves limited focus on elastic properties of ice-bearing sediments. Many studies have concentrated on consolidated sediments (e.g., Pandit and King, 1979; Sondergeld and Rai, 2007; Timur, 1968), even though most near-surface permafrost consists of unconsolidated sediments (French, 2007). Unconsolidated material refers to loosely packed or uncemented sediment or soil, either at the surface or below, lacking layering or firm binding between particles (Jackson and Bates, 1997). Dou et al. (2016)

also highlight the importance of measuring elastic properties across a wide range of ice content to validate theoretical models. Additionally, while past studies have examined the effects of consolidation on wave velocities in frozen media, there is a noticeable lack of studies addressing wave attenuation under similar conditions (Li and Matsushima, 2024). This is significant because combining velocity and attenuation measurements can help quantify ice content in the field (Bustamante et al., 2023; Dou et al., 2016).

Addressing these gaps is necessary for advancing the understanding of elastic wave propagation under the mentioned conditions. Improving frequency-dependent measurements in controlled environments, such as using sediments with uniform properties, could enhance the interpretation of seismic and logging profiles and contribute to more robust theoretical models, particularly concerning frequency-related scaling effects. While quantitative scaling to field conditions must be approached with caution, laboratory experiments can be positioned to inform qualitative understanding of underlying physical mechanisms. Furthermore, developing comprehensive datasets and models for ice-bearing sediments is increasingly important for improving predictions of permafrost dynamics, especially in the context of accelerating climate change.

1.2 Research Aims

The general aim of this study is to investigate the effects of pore fluid on acoustic wave propagation in unconsolidated sand at sonic frequencies (1-20 kHz). This range is relevant for interpreting high-resolution seismic and well-logs data commonly used in geophysical surveys. The research focuses on two types of pore fluids: water-saturated and ice-bearing conditions.

The main aim of the study of water-saturated sand packs is to understand how water saturation influences P-wave velocity and attenuation of sand packs under varying conditions. The specific aims are as follows:

- Quantifying velocity and attenuation trends across varying water saturation levels, including dry, partially saturated, and fully saturated conditions, under elevating effective pressures.
- Investigating how water distribution, such as uniform or patchy saturation, affects elastic wave properties by comparing experimental results to theoretical rock physics models.
- Exploring other factors that might influence elastic wave properties, including permeability and the characteristics of gas bubbles.

The primary aim for the study of ice-bearing sand is to investigate the effects of ice saturation on P-wave velocity and attenuation during the melting process. This process is particularly relevant for understanding thawing permafrost. Further specific aims include:

- Measuring changes in velocity and attenuation as ice melts in unconsolidated sand under varying effective pressures.
- Analysing the frequency-dependent behaviour of acoustic parameters during ice melting.
- Investigating the effects of ice distribution and morphology on elastic wave properties by comparing experimental results to rock physics models that use three-phase approaches.
- Utilising rock physics models to estimate ice content during melting and interpret observed acoustic responses, while also identifying the mechanisms underlying elastic wave propagation.

This study aims to provide a more comprehensive understanding of how elastic waves behave in water-saturated and ice-bearing conditions. The findings could bridge the gap between laboratory results and field-scale geophysical observations by integrating experimental results at sonic frequencies with rock physics models. The results will be particularly useful for applications such as hydrocarbon exploration, carbon storage monitoring, and permafrost monitoring.

1.2.1 Scope of the thesis

The scope of the study is outlined as follows:

- Materials: The experiments use unconsolidated sediment, focusing on sand with a uniform grain diameter to minimise the influence of varying grain size on wave propagation. As a result, this study does not consider sediments with varying types or grain sizes.
- Frequency range: Measurements are limited to the sonic frequency range (1–20 kHz), with a cut-off frequency of approximately 3 kHz. This cut-off is determined by the sample length, which is set to half the propagating wavelength to ensure accurate representation of the sample's characteristics during wave propagation.
- Environmental conditions: The study controls effective pressure and temperature to simulate subsurface conditions relevant to field conditions. However, it does not examine how temperature changes affect elastic wave properties. Instead, the focus is on the effects of ice saturation.
- Rock physics models: This study applies two models, the Hydrate-Bearing Effective Sediment (HBES) model by Marín-Moreno et al. (2017) and the model by Leclaire et al.

(1994) representing the three-phase approach. The water-saturated study mainly uses the Biot-Stoll model (Stoll and Bryan, 1970), incorporated within the HBES model. Meanwhile, the ice-bearing study uses both the three-phase models.

1.3 Elastic wave properties of water-saturated and ice-bearing sediment

1.3.1 Definition of elastic waves and their properties

Elastic waves, such as compressional (P-waves) and shear (S-waves), are mechanical waves that propagate through particulate materials and are fundamental to geophysical studies (Fanchi, 2010). Elastic waves derive their names from their ability to propagate by temporarily deforming a medium—storing and releasing energy without permanently altering the medium's structure. This temporary deformation occurs due to elasticity, a material property that allows the medium to return to its original shape after the stress is removed. In elastic waves, particles oscillate around their equilibrium positions, transferring energy from one point to another without permanent displacement (Aki and Richards, 1980).

P-waves (primary or compressional waves), the fastest type of elastic wave, travel through solids, liquid, and gases and propagate by compressing and expanding the medium in the direction of travel, similar to sound waves in air, making them highly sensitive to changes in density and elasticity (Sheriff and Geldart, 1995). This sensitivity allows P-waves to serve as an important instrument in subsurface characterisation, helping geophysicists detect changes in rock type, pressure condition, and fluid content, which are crucial in applications ranging from resource exploration to environmental studies (e.g., Prasad, 2002; Schumann et al., 2014; Wagner et al., 2019). In contrast, S-waves (secondary or shear waves) travel slower than P-waves and can only propagate through solids, as they require a medium with shear strength (Aki and Richards, 1980). S-waves move by displacing particles perpendicular to the wave's direction, generating a shearing motion, which is useful for identifying rigid layers, such as bedrock, as well as detecting interfaces between solid and fluid-filled formations (Telford et al., 1990). Their inability to travel through fluids can help to differentiate lithological boundaries and fluid reservoirs. However, due to this characteristic, most studies focus on P-wave properties when investigating water/gas saturation effects (e.g., Barriere et al., 2012; Dutta et al., 1979; Dvorkin and Nur, 1998).

Velocity and attenuation are two fundamental properties of elastic waves that provide valuable insights into subsurface materials. Velocity is a key parameter in understanding the propagation of elastic waves. It reflects how quickly elastic waves travel through a material, which is governed by the material's density and elasticity (Mavko et al., 2009). Higher velocities are typically associated with materials that are denser and exhibit greater rigidity, such as crystalline rocks, whereas lower velocities are common in unconsolidated sediments or fluid-rich environments (e.g., Matsushima et al., 2016; Zimmer, 2003). For example, saturated sediments exhibit distinct velocity profiles compared to dry or partially saturated ones due to differences in fluid compressibility and density (e.g., Barriere et al., 2012; Chapman et al., 2021; Gei and Carcione, 2003). Additionally, velocity contrasts between layers can be used to delineate geological formation. For instance, Schumann et al. (2014) used compressional and shear wave velocities to characterise formations in the Nankai accretionary complex, one of the most intensively studied subduction zones on Earth (Figure 1.1). Accretionary prisms form at convergent plate boundaries by scraping and stacking sediments and rocks from the lower plate, resulting in thick vertical layers and horizontal shortening. They observed that sediments at the accretionary prism toe exhibited higher velocities (~1650–2200 m/s) due to tectonic compaction, which reduced porosity. In contrast, sediments from the incoming plate showed lower velocities (~1450–1650 m/s) from lesser consolidation. These insights highlight the importance of velocity as a key parameter for imaging and characterising the subsurface.

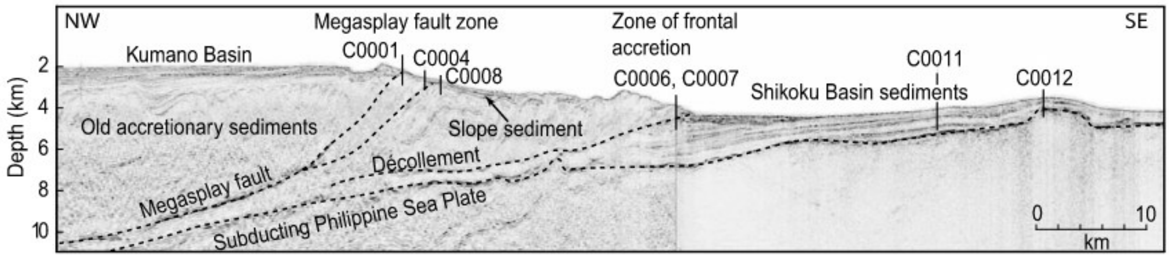

Figure 1.1 An example of a seismic profile across the Nankai accretionary complex, adapted from Schumann et al. (2014).

Attenuation refers to the loss of wave energy as it travels due to scattering, absorption, and intrinsic material properties (Aki and Richards, 1980). Attenuation is inversely related to the quality factor (Q), with a lower Q indicating higher attenuation. The quality factor is a dimensionless parameter that quantifies energy efficiency in a wave system, representing the ratio of energy stored in the system to the energy lost per wave cycle at resonance (Carcione et al., 2024). In geophysical studies, attenuation is a key indicator of the internal losses and heterogeneity within the material (e.g., Ayres and Theilen, 2001; Li et al., 2024; Winkler and Nur, 1982). For example, fluid-filled sediments generally exhibit higher attenuation compared to solid sediments due to energy loss at fluid-solid interfaces (Winkler and Nur, 1982). This energy dissipation also varies between P- and S-waves, as S-waves typically experience higher attenuation in unconsolidated or fluid-rich environments where the lack of rigidity dampens the wave's shear motion (Toksöz et al., 1979). Attenuation can be classified into apparent and intrinsic attenuation. Apparent attenuation arises from elastic scattering due to velocity and density heterogeneities, while intrinsic attenuation is a fundamental property of rocks linked to elastic wave energy conversion to heat (Buckingham, 2005; Matsushima et al., 2008). The latter controls the decay in amplitude and frequency changes in seismic waves, unaffected by external factors like scattering.

1.3.2 Water saturation effects on elastic properties behaviour

Compressional wave velocity and attenuation are both sensitive to pore fluid content (e.g., Barriere et al., 2012; Berryman, 1981; Knight and Nolen-Hoeksema, 1990; Rubino and Holliger, 2012). Research on the effects of pore fluid on elastic wave properties has been done through theoretical frameworks, field and laboratory experiments, and numerical approaches. A foundational contribution to this field is the theory of elastic wave propagation in fluid-saturated media developed by Biot (1956a, 1956b).

Biot's (1956a, 1956b) theory of poroelasticity provides a fundamental framework for describing wave propagation in fluid-saturated porous media. It models the porous medium as a two-phase system consisting of a solid matrix and a saturating fluid, accounting for the relative motion between them. A phase is a uniform and distinct portion of a chemical system that can, at least in theory, be separated. It has consistent and continuously changing chemical and physical properties (Jackson and Bates, 1997). The theory accounts for both the elastic deformation of the solid frame and the viscous flow of the pore fluid, which together control wave propagation behaviour.

A key aspect of Biot's theory is the division of wave propagation into low- and high-frequency regimes, separated by the characteristic or Biot frequency. This frequency depends on the porosity and permeability of the porous medium, as well as the viscosity and density of the pore fluid) (Mavko et al., 2009). In the low-frequency regime, the pore fluid and solid grains move in a coupled manner, and viscous effects are dominant (approximately equal the inertial forces acting on it). In contrast, in the high-frequency regime, the fluid cannot respond quickly enough to keep up with the solid matrix motion, leading to decoupled motion and increased energy dissipation due to both inertial and viscous effects. In this case, the medium behaves more like a solid with added damping effects.

The original theory assumes infinitesimal deformation with small displacements and strains. Macroscopic properties such as porosity, stress, and permeability are treated as volume averages of the underlying microscopic behaviour, assuming that the wavelength is much larger than the grain or pore scale. The fluid phase is assumed to be continuous, while the solid matrix may include isolated pores that do not contribute to the porosity. The solid frame is typically considered isotropic, with any anisotropy attributed to preferred orientations of pores or cracks—an assumption that limits the model's applicability in highly anisotropic formations.

Biot's theory primarily describes intrinsic attenuation, caused by viscous dissipation due to relative motion between the fluid and solid frame, and heat loss, rather than scattering. This attenuation is associated with wavelength-scale fluid pressure equilibration between compressional wave peaks and troughs. Because wavelengths are assumed to be much larger than the pore scale, scattering effects are considered negligible. Later extensions of Biot’s model, such as the Biot-Stoll model (Stoll and Kan, 1981) and other developments (e.g., Berryman, 1980; Lee et al., 2024; Williams et al., 2002), introduce additional attenuation mechanisms such as squirt flow and local flow between pores. These become especially important at high frequencies or in partially saturated or heterogeneous media.

Experimental work has further confirmed theoretical predictions. For example, Wyllie et al. (1956) measured elastic wave velocities in both synthetic and natural porous media at ultrasonic frequency, demonstrating wave velocities increase with fluid saturation compared to dry samples. In mixed fluid conditions, such as water and gas, wave velocities decrease due to the lower compressibility and density of gas. Then, Shumway (1960) highlighted how porosity, grain size, and rigidity govern sound speed and absorption in marine sediments, providing key insights for acoustic modelling in geophysics and seafloor mapping. Meanwhile, in situ measurements have provided additional insights. Hamilton (1970) investigated compressional and shear wave velocities in marine sediments, concluding that almost all open-ocean sediments have finite rigidity, allowing them to transmit shear waves. Building on this, Hamilton (1971) proposed elastic and viscoelastic models for water-saturated porous media and showed that these mediums exhibit elastic behaviour under small stresses. These pioneering studies laid the groundwork for understanding the effects of pore fluids on elastic wave propagation. A combination of theoretical studies, experimental investigations, and in situ measurements is essential to achieve a comprehensive understanding of the subject.

Since then, the development of elastic wave property studies has been greatly influenced by advancements in understanding pore fluid effects. Building on Biot’s poroelastic theory, White (1975) developed an extension that addresses its limitations and incorporates additional mechanisms relevant to partially saturated and patchy-saturated media. This model accounts for heterogeneities in fluid distribution within pores, unlike Biot's assumption of uniform saturation. White's model highlights the influence of fluid heterogeneity on wave attenuation and velocity, particularly at seismic frequencies (~20–50 Hz), where wave-induced fluid flow between gas pockets and the liquid matrix causes significant energy loss.

Dutta et al. (1979) confirmed White’s theory, demonstrating that attenuation is primarily caused by wave-induced flow at gas-water interfaces, resulting in viscous energy dissipation. Further work by Dvorkin and Nur (1998) showed that patchy saturation leads to a steady increase in P-wave velocity with saturation, while homogeneous saturation shows minimal changes until near full saturation, where it sharply rises. This study also found that Poisson’s ratio is highly sensitive to saturation patterns, providing insights into the stiffness and fluid distribution of sediments.

Experimentally, Cadoret et al. (1998) observed that drying leads to patchy fluid distribution, while depressurisation at high saturations results in homogeneous distribution, causing hysteresis in wave velocities and quality factors during imbibition and drainage. Barriere et al. (2012) and El-Husseiny et al. (2019) further explored this behaviour, highlighting that pore complexity, such as microcracks, amplifies the effects of patchy saturation. Lower porosity and permeability also lead to inhomogeneous fluid distributions in sandstone pores (Si et al., 2016).

Patchy saturation creates fluid pressure gradients that promote wave-induced fluid flow (WIFF), a key dissipation mechanism responsible for velocity dispersion and seismic attenuation (Chapman et al., 2021; Horikawa et al., 2021; Oh et al., 2011). Müller et al. (2010) categorised WIFF mechanisms into three scales: global flow, corresponding to Biot's (1956a, 1956b) intrinsic attenuation mechanism, which is significant at seismic frequencies—especially in unconsolidated sediments—and at ultrasonic frequencies (>100 kHz) in rocks; pore-scale squirt flow, active at both ultrasonic and seismic frequencies, driven by grain-scale microcracks; and mesoscopic flow, significant at seismic frequencies in patchy saturations.

Mesoscopic-scale heterogeneities in gas-water saturation, influenced by capillary pressure and dry frame properties like permeability, drive seismic attenuation and velocity dispersion in partially saturated porous rocks (Chapman et al., 2021). At the sub-microscopic scale, elastic waves in hydrate-bearing sediments cause pressure differences between the sand framework and porous hydrate grains, leading to viscous fluid movement called sub-microsquirt flow (Sahoo et al., 2019). Additionally, gas bubble resonance contributes to energy loss by amplifying energy loss when wave frequencies match the natural resonance frequency of gas bubbles in the sediment (Smeulders and Van Dongen, 1997). These loss mechanisms are illustrated in Figure 1.2.

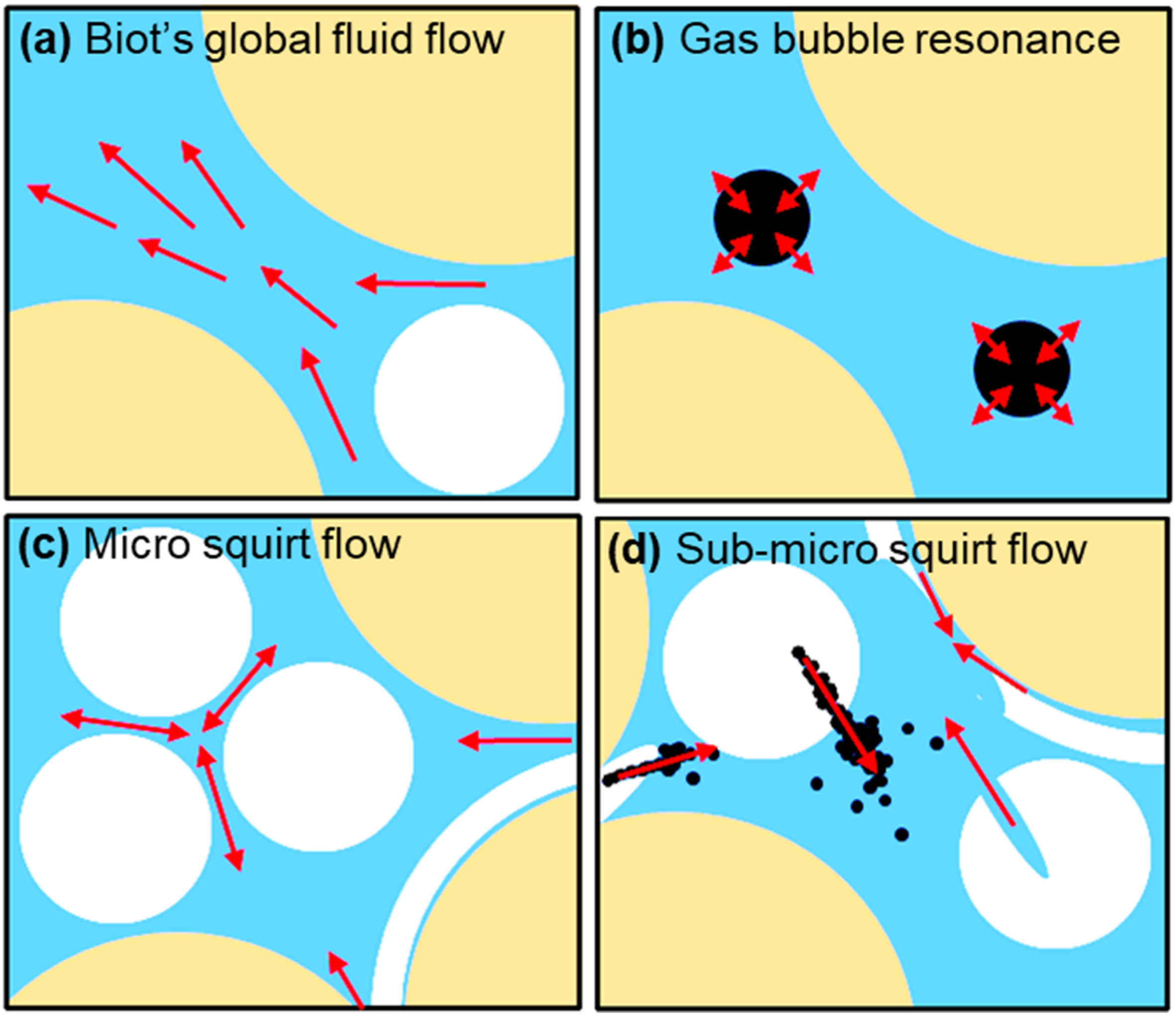

Figure 1.2 Illustration of the attenuation mechanisms. (a) Biot's global fluid flow, (b) gas bubble resonance, (c) micro squirt flow caused by pores with varying aspect ratios formed during ice formation or hydrate growth, and (d) sub-microsquirt flow resulting from gas and water inclusions within hydrates. Yellow represents sediment grains, black indicates gas, cyan shows water, and white denotes gas hydrate/ice. Adapted from Sahoo et al. (2019).

P-wave velocity is affected by various sediment properties such as porosity, grain size, rigidity, depth, and pressure (Buckingham, 2005; Dong et al., 2021; Hamilton and Bachman, 1982; Wyllie et al., 1956), and pore fluid variations (Ecker et al., 2000; Knight and Nolen-Hoeksema, 1990; H. Li et al., 2020; Timur, 1968; White, 1975). In saturated mediums, high porosity generally lowers velocity due to the compressibility of pore water, especially at low pressure (Zimmer et al., 2002). Grain size also plays a role, with larger grains resulting in lower velocities (Hare and Hay, 2018).

Fluid saturation significantly impacts P-wave velocity. Near full saturation, velocity sharply increases, consistent with Biot-Gassmann theory (Astuto et al., 2023; Sutiyoso et al., 2024). For mixed fluid phases, gas compressibility reduces velocity, while water-dominated saturation increases it (Wyllie et al., 1956). In gas-sand reservoirs, velocity initially decreases with increasing water saturation up to ~75-80%, then increases sharply towards full saturation due to reduced fluid compressibility (Domenico, 1974; Knight and Nolen-Hoeksema, 1990). In dry or partially saturated sand, P-wave velocity follows a power-law relationship with depth and stress, remaining lower than fully saturated conditions (Emerson and Foray, 2006). Observations highlight a three-stage velocity trend: a rise between 20-30% water saturation, slower increases up to 80%, followed by a dramatic jump near full saturation (King et al., 2000). Heterogeneities in gas-saturated pores may destabilise P-waves (Gu et al., 2021). In addition, higher confining pressures reduce the effects of fluid saturation on P-wave velocity, which may limit the effectiveness of hydrocarbon detection methods at elevated pressures (Si et al., 2016).

P-wave velocities slightly increase, while S-wave velocities show more pronounced growth with rising confining pressure and axial stress (Schumann et al., 2014). Crack conditions also affect velocity: fluid-filled cracks increase V_P more than V_S, while weak material in cracks reduces both (Hudson, 1981). V_P/V_S ratios, or the ratio of P-wave and S-wave velocities which is one of the indicator of sediment properties, increase under lower effective pressures (Zimmer et al., 2002). Sorting and pre-consolidation affects these ratios by altering sediment porosity: finer grains fill pore spaces during sorting, while pre-consolidation compacts the matrix. These ratios can aid to distinguish overpressure (where the ratio increases) or gas saturation (where the ratio decreases), as gas reduces V_P without affecting V_S (Prasad, 2002).

Elastic wave velocity changes also depend on pore structure. Homogeneous pores result in lower irreducible fluid saturations, while compliant pores like microcracks stiffen under patchy fluid conditions, increasing velocity through wave-induced squirt flow (El-Husseiny et al., 2019). Pore fluid also modifies velocity trends; for example, water with dissolved gas like tap water shows a positive correlation between V_P and saturation, while de-aired water yields stable, high velocities due to uniform pore structures (Gu et al., 2021). These insights emphasise the role of fluid distribution, pore geometry, and saturation in controlling seismic velocities, highlighting their importance for geophysical applications such as reservoir characterisation and overpressure detection.

The propagation, and consequently the attenuation, of elastic waves in marine sediments is influenced by a number of mechanisms, such as the relative movement between mineral frame and pore fluid (squirt flow), and the intrinsic losses (Ayres and Theilen, 2001; Best and McCann, 1995; Winkler and Nur, 1982). Murphy (1982) observed attenuation peaks at 85% water saturation in Massillon sandstone and Vycor porous glass for extensional waves, with energy loss dominated by viscous fluid flow at high saturation and capillary effects at low saturation. Building on that, Murphy (1984) introduced partial gas saturation in sandstones and observed a linear decrease in shear attenuation with gas content, while extensional attenuation shows nonlinear dependence on saturation levels. At low saturations (water saturation < 10%), attenuation increases slightly due to electrochemical effects and capillary forces, at intermediate saturations (water saturation between 10% and 70%), a plateau in attenuation suggests local fluid flow mechanisms at the pore scale, and at high saturations (water saturation > 70%), attenuation behaviour is dominated by global flow mechanisms due to patchy saturation (Cadoret et al., 1998; Gardner, 1962; White, 1986). Water saturation significantly increases compressional wave attenuation compared to velocity (Oh et al., 2011).

Attenuation due to the local squirt flow is proportional to the product of frequency and viscosity (Best and McCann, 1995; Gurevich, 2002; Marketos and Best, 2010; Mavko and Nur, 1975). In water-saturated media, P-wave attenuation is mainly influenced by local fluid flow. The non-zero bulk modulus of water enhances P-wave transmission, significantly increasing attenuation due to interactions between the fluid and solid phases (Li et al., 2024).

Pride et al. (2004) suggested that attenuation in sedimentary rocks mainly stems from mesoscopic heterogeneity (larger than individual pores but smaller than the wavelength), including lithological variations (stiffness differences creating fluid pressure gradients) and patchy saturation (pressure differentials from immiscible fluid patches). Marín-Moreno et al. (2017) found that the presence of gas hydrate can lead to squirt flow, resulting in higher attenuation even at seismic frequencies in a three-phase system. Variations in pore fluid exert a stronger influence on attenuation than changes in the rock frame (Rubino and Holliger, 2012).

Porosity and permeability control attenuation by influencing fluid distribution and flow mechanisms. High-porosity rocks exhibit concave attenuation curves, requiring more water for Biot effects, while fully saturated states can reduce attenuation due to uniform fluid distribution. In contrast, low-porosity rocks show notable attenuation only at higher saturations, influenced by micro-cracks and surface tension (El-Husseiny et al., 2019; Oh et al., 2011). Meanwhile, permeability shifts attenuation from microscopic to macroscopic mechanisms as saturation increases (Oh et al., 2011). In sands and soils under low confining pressure (below 5 MPa), smooth contacts allow grains to slip, causing frictional energy loss even under the small strains produced by seismic wave propagation (Barriere et al., 2012; Duffaut et al., 2010). High resolution-imaging techniques, such as X-ray computed tomography has provided valuable insights into fluid distribution, improving prediction accuracy for attenuation and dispersion (e.g., Chapman et al., 2021; Sahoo et al., 2018). These findings highlight the complex interaction between pore-scale phenomena, fluid properties, and elastic waves behaviour, helping to improved understanding of attenuation in saturated media.

1.3.3 Ice saturation effects on elastic properties behaviour

The behaviour of elastic properties in ice-bearing rocks and sediments are of great interest in both geotechnical engineering and environmental sciences (e.g., Bustamante et al., 2023; Kang et al., 2021; Oswell, 2011). These sediments, composed of minerals, water, ice, and air, exhibit complex interactions affecting wave properties.

An initial study by Timur (1968) observed that compressional wave velocity increases as temperature drops below 0°C due to ice formation in water-saturated pores, while minimal changes occur in dry rock, also confirmed in later studies, for instance, Chang et al. (2021), and Park and Lee (2014). Ice forms in larger pores first and significantly increases elastic moduli and compressional wave velocities. Meanwhile, the first recorded ice-bearing sand study was done by Nakano and Arnold (1973) which confirmed previous results that dilatational wave velocities correlate strongly with unfrozen water content in frozen soils. As with the hysteresis in water saturation studies, they also found hysteresis in velocities during freeze-thaw cycles, linked to unfrozen water content changes. Velocities are more sensitive to low ice saturation, whereas damping, reflected in quality factor reductions, is more pronounced near full ice saturation.

Further, Matsushima et al. (2008) observed ultrasonic attenuation peaking at -3°C, inversely correlated with ice content. Grain boundary interactions and scattering due to heterogeneities drive intrinsic and apparent attenuation, respectively. Internal friction, particularly grain boundary relaxation (sliding), is identified as the primary mechanism of acoustic energy loss in warm ice (Meyer et al., 2019).

Theoretical rock physics models have also been influential in studying how pore content affects elastic wave properties, which is also applied in ice-bearing sediment research. A notable example is the Leclaire et al. (1994) model, which extends Biot's theory to predict elastic wave parameters in frozen media. This model incorporates ice parameters into Biot's theory, assuming no direct contact between the sediment matrix and ice that is separated by unfrozen water, except in the limited case of a fully frozen medium. This theoretical framework on three-phase theory became the foundation of later works (e.g., Carcione and Seriani, 1998; Sahoo and Best, 2021).

In frozen soils, ice bonding, particle contact interaction, and nanoscale porosity become key factors influencing the elastic wave properties, with differences between P-waves and S-waves linked to stiffness and ice distribution, specifically for S-waves surpassing the role of confining stress (Matsushima et al., 2016). Dou et al. (2016) observed velocity increases with ice content, while attenuation reached a maximum at partial saturation. The morphology of ice, whether frame-supporting or pore-floating, significantly influences wave velocity and attenuation, with temperature playing a crucial role in these transitions. As temperature increases, it amplifies P-wave attenuation and causes a shift in the central frequency of S-waves, altering the sediment's mechanical and acoustic properties (Li and Matsushima, 2024).

Helgerud et al. (2009) compared the elastic properties in ice and methane hydrate, finding similar P- and S-wave velocities but different responses in shear moduli. This finding supports using ice as an analogue for gas hydrates, particularly in P-wave analysis. This comparison builds on the work of Helgerud et al. (1999), who developed an effective medium model for elastic wave velocities in marine sediments containing gas hydrates, considering the impact of gas hydrates on sediment elastic moduli. Comparing gas hydrates and ice-bearing sediments is significant because of the importance of both in scientific and industrial contexts.

Initially, gas hydrate studies gained interest due to their potential to block pipelines in the natural gas industry (Lv et al., 2018; Nixdorf and Oellrich, 1997). More recently, research momentum has increased because of their potential as an untapped energy resource (Klauda and Sandler, 2005; Kvenvolden, 1988; Makogon, 2010), their role in geological hazards (Hjort et al., 2022; Maslin et al., 2010; Ning et al., 2012), and their interaction with climate change (Kvenvolden, 1999; MacDonald, 1990; Nisbet, 1990; Xu et al., 2001). Given these factors, studies on gas hydrate-bearing sediment are more common than those on ice-bearing sediments. However, with global warming accelerating permafrost degradation, which is a major carbon reservoir partly in the form of gas hydrate, the relationship between gas hydrate-bearing and ice-bearing sediments has become increasingly relevant.

Gas hydrate-related experiments are often time-consuming, costly, and complicated by the challenge of obtaining natural samples (Ning et al., 2012; Spangenberg et al., 2018). Therefore, using ice-bearing sediment data offers a practical alternative for studying hydrates. Besides similarities in elastic wave velocities (Helgerud et al., 2009), ice and hydrates share comparable hydrogen bonding properties (Ning et al., 2012). Nevertheless, differences remain. For instance, shear and Young’s moduli vary between the two (Helgerud et al., 1999; Ning et al., 2012). Ning et al. (2012) also found that gas hydrates exhibit isotropic elasticity, unlike ice. Geomechanically, gas hydrate has brittle strength, while ice demonstrates higher uniaxial strength due to deviations from the tetrahedral structure of its water molecules (Jendi et al., 2015). Furthermore, gas hydrate introduces more variability and potential attenuation due to its cage-like structure (Liang et al., 2019).

While pure ice and gas hydrate have some differences, experiments with ice-sediment mixtures in permafrost research show distinct behaviour compared to pure ice. When the ice-to-sediment ratio is low, sediments significantly influence or even control mechanical behaviour (Arenson et al., 2007; Moore, 2014). Therefore, comparing gas hydrate-bearing and ice-bearing sediments is complex and requires further study to fully understand their differences.

Thoroughly understanding these differences not only enhances the possibility of using ice as an analogue for gas hydrates but also allows for direct comparison of results, taking advantages of abundant existing data on gas hydrates. Since gas hydrate and ice can form similar morphologies, ice-sand mixtures can also act as a 'quick look' model to understand the behaviour of gas hydrate-sand systems (Heeschen et al., 2020).

1.3.4 Frequency-dependent behaviour

Velocity and attenuation of elastic waves vary across frequencies, affecting measurements from seismic surveys, sonic well-logging, and ultrasonic experiments. Understanding frequency dependence, particularly velocity dispersion (the variation of velocity with frequency), is essential for comparing results from different methods (Kolsky, 1964). Correcting for this frequency dependence ensures consistency between ultrasonic, sonic, and seismic velocity measurements (Zimmer, 2003). With seismic surveys and well-logs increasingly used for shallow, unconsolidated sediments, particularly employing broader frequency bandwidths for improved resolution, understanding dispersion mechanisms in such sediments has become increasingly important (Zimmer, 2003).

Müller et al. (2005) expanded the analysis of wave propagation into low- and high-frequency regimes, showing that low-frequency limiting velocities are governed by the harmonic average of the bulk modulus due to fluid pressure equilibration, while high-frequency (no-flow) velocities are determined by the Hill's (1952) average as a result of constrained fluid motion and increased stiffness (Gei and Carcione, 2003; Müller and Gurevich, 2005). At intermediate frequencies, wave dispersion becomes significant, and attenuation peaks due to dynamic fluid interactions, marking the transition between these regimes (White, 1975). From a fluid mobility perspective, the ability of pore fluid to move and equilibrate under stress—controlled by the ratio of matrix permeability to fluid viscosity—is critical. High mobility supports pressure equilibrium and validates low-frequency assumptions, while low mobility leads to frequency-dependent effects, especially in low-permeability rocks such as shales and siltstones (Batzle et al., 2006).

Compressional wave velocity increases significantly at higher frequencies due to the frequency-dependent behaviour of the bulk modulus (Dutta et al., 1979). Partially saturated media show strong frequency dependence in the kilohertz range, while dry rocks remain nearly independent of frequency beyond 0.1 Hz (Murphy, 1982; Williams et al., 2002). In water-saturated rocks, seismic velocities increase with frequency due to fluid viscosity and pore structure, as predicted by Biot's theory, whereas ultrasonic measurements indicate an unrelaxed state for partially saturated rocks (Li et al., 2020; Zimmer, 2003). Phase velocity shows negative dispersion at high frequencies (0.3–1.0 MHz) and positive dispersion at lower frequencies (<200 kHz), consistent with Biot’s and Buckingham's (2000) Grain-Shearing models (Kimura, 2011; Lee et al., 2007). Attenuation peaks occur at sonic frequencies due to squirt flow (Müller et al., 2010), while attenuation in water-saturated sandy sediments increases non-linearly at high frequencies (0.3–1.0 MHz), with scattering as the primary mechanism (Lee et al., 2007). Grain size also affects velocity dispersion: larger grains show a decrease in velocity at high frequencies but display a temporary velocity increase between 80–140 kHz. For grains larger than 0.2 mm, velocity decreases again (Kimura, 2011).

1.4 Background for ice-bearing sediment and permafrost

Permafrost, often composed of ice-bearing sediment, is a critical component of the cold regions, impacting both infrastructure stability (Hjort et al., 2018) and global climate dynamics (Schuur et al., 2015). The behaviour of near-surface ground layers in cold regions is shaped by periodic and variable atmospheric and microclimatic conditions, causing disturbances such as subsidence (thermokarst), landslides, and frost heave (Williams, 1995). As the permafrost region warms, carbon emissions are projected to rise due to degradation processes (Meredith et al., 2022). Elastic wave properties related to ice content are one of several valuable tools for monitoring and addressing these environmental challenges (Hilbich et al., 2022).

By definition, ice-bearing sediments are geological material, usually composed of soil or sand, containing partial or full ice saturation within their pore spaces (Andersland and Ladanyi, 2004). The ice forms either through the freezing of pore water (e.g., Li and Matsushima, 2024; Watanabe et al., 2011) or deposition from environmental processes (e.g., Fan et al., 2023; Fu et al., 2022), influencing the physical and mechanical properties of the sediments (Chang et al., 2021; Helgerud et al., 2009).

On the other hand, permafrost can be simply defined as ground (soil or rock) that remains at or below 0°C for at least two consecutive years. Contrary to Muller's (1947) initial description as “permanently frozen ground”, permafrost is better described as “perennially-frozen ground”, as the freezing point of its included water may be depressed below 0 °C (French, 2007). Permafrost thickness ranges from centimetres to hundreds of metres, with ancient layers found in Siberia and Alaska, and younger ones in areas like the Mackenzie Delta (Brown et al., 2002).

The permafrost profile consists of three main layers: the active layer, permafrost layer, and taliks (Figure 1.3; French, 2007). The active layer is a near-surface layer subject to annual thawing and freezing driven by seasonal temperature changes, typically ranging from 2-8 cm in thickness but occasionally exceeds 20 m (Dobiński, 2020). Its transient base, rich in ice, is critical for determining slope stability during thaw events (Shur et al., 2005). Taliks are unfrozen zones within or beneath permafrost that occur due to specific ground conditions, such as geothermal heat or hydrological activity (O'Neill et al., 2020). Additionally, unfrozen water films can exist at ice-soil interfaces or grain boundaries below 0°C, influenced by ice crystal size, impurity concentration, and local environment conditions (Dash et al., 1995). This coexistence of ice and unfrozen water has been explored to better understand their complex interactions (e.g., Kleinberg and Griffin, 2005; Watanabe and Mizoguchi, 2002; Yang et al., 2021).

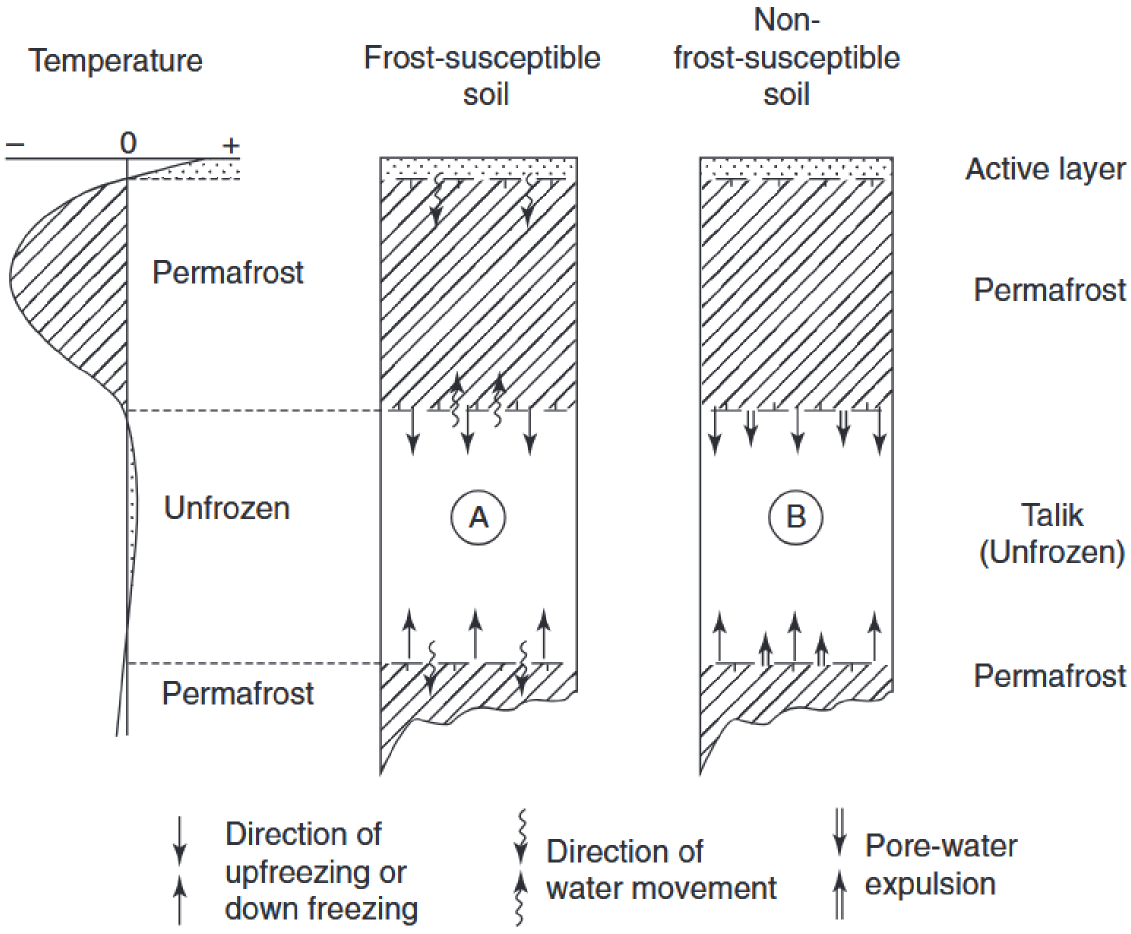

Figure 1.3 Diagram illustrating permafrost profiles and freezing patterns in frost-susceptible and non-frost-susceptible soils. In frost-susceptible soil (A), ice lens growth causes water loss and compaction in the unfrozen zone. In non-frost-susceptible soil (B), porewater expulsion leads to water accumulation and pressure buildup in the unfrozen zone (French, 2007).

Permafrost is also categorised based on its spatial extent into continuous, discontinuous, sporadic, and isolated permafrost. Continuous permafrost, covering 90–100% of the area, is present nearly everywhere except under localised unfrozen zones like lakes and rivers. Discontinuous permafrost, with a 50–90% coverage, consists of frozen ground separated by unfrozen patches. In contrast, sporadic (10–50% coverage) and isolated permafrost (0–10%

coverage) appear as scattered frozen "islands," often located beneath organic-rich, peaty sediments (French, 2007).

In ice-bearing sediment at subzero temperatures, ice primarily exists in two forms: pore ice and segregated ice (Dash et al., 1995). Pore ice consists of small crystallites comparable in size to soil particles. Pore ice tends to cement soil grains together and significantly increase the strength of frozen ground. In contrast, segregated ice features much larger structures, ranging from millimetres to metres, formed through various processes that lead to distinct characteristics.

Recent studies increasingly use the term ‘morphology’ to explain ice distribution within the medium (e.g., Li and Matsushima, 2024; Matsushima et al., 2016). This concept, first proposed by Dvorkin et al. (1999) in modelling high-porosity ocean-bottom sediments, was later adapted for gas hydrate studies by Helgerud et al. (1999). Morphologies are broadly categorised based on how ice interacts with the sediment matrix, which are non-cementing or cementing (Figure 1.4).

Non-cementing morphology occurs when ice grains do not bond to the sediment framework. It can be further divided into: pore-floating ice, which grows freely within the pore space without bridging neighbouring grains (Hu et al., 2014); and load-bearing ice, which connects adjacent grains, thus supporting the sediment frame (You et al., 2024). Meanwhile, cementing morphology occurs when ice bonds directly with sediment grains, either by bonding directly at grain contacts (contact cementing) or by coating the grains with a layer of ice (grain coating) (Best et al., 2013; Ecker et al., 1998; Helgerud et al., 1999).

Understanding the morphological characteristics of ice-bearing sediments is essential for imaging and monitoring ice distribution. Cementing and pore-bridging morphologies significantly enhance the elastic moduli of the sediment, contributing to the structural integrity of the sediment frame. In contrast, pore-floating ice primarily alters the properties of the pore fluid without reinforcing the sediment matrix (Ecker et al., 2000). These distinctions play a crucial role in assessing sediment stability and in interpreting geophysical measurements, as demonstrated by various studies, e.g., Briggs et al. (2017), Buddo et al. (2022), Hilbich et al. (2022), and Kang et al. (2021).

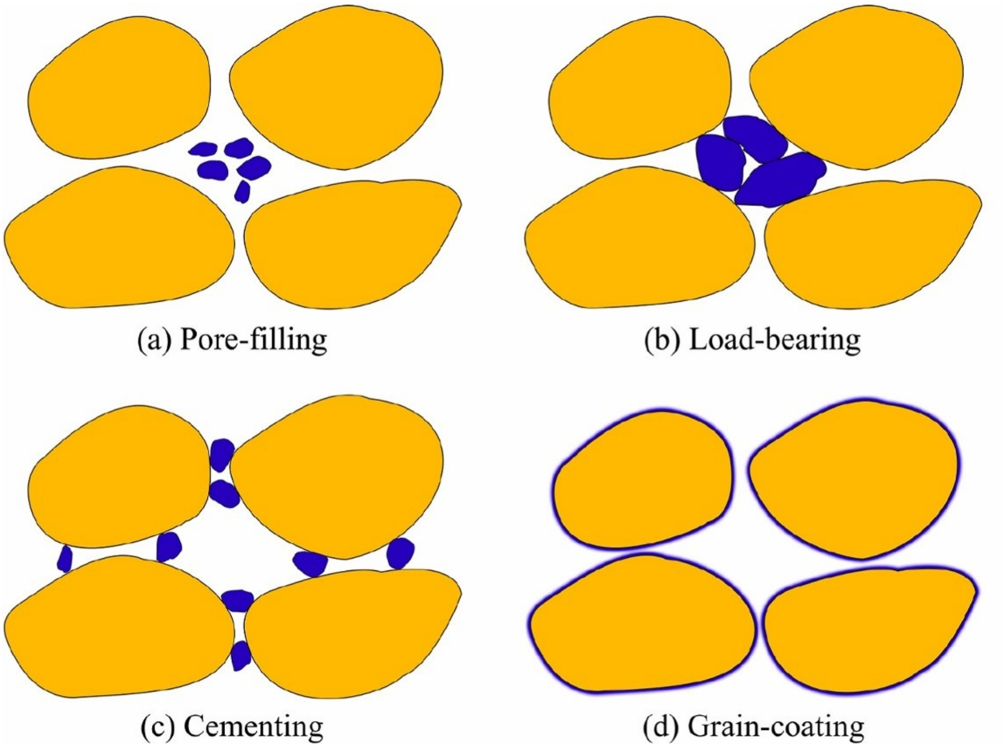

Figure 1.4 Ice morphology within sediment grains: a) pore-filling, b) load-bearing, c) cementing, and d) grain-coating. The size, distribution, and interaction of ice (blue) with sediment grains (brown) affect the elastic wave properties of the soil. Adapted from You et al. (2024).

1.4.1 Geographical distribution and environmental influences

Permafrost underlies approximately 23–25% of the Northern Hemisphere's land area, with extensive coverage in regions such as Russia, Canada, and Alaska (French, 2007), and less than 25% of the Southern Circumpolar Region contains permafrost (Bockheim, 1995). Its vertical extent varies significantly, ranging from fractions of a metre to hundreds of metres (Dobiński, 2020). Permafrost is not limited to terrestrial environments, but also extends to seabed sediments, which are equally vulnerable to rapid degradation, similar to land-based ones (Bustamante et al., 2023; Paull et al., 2022).

The global climate affects the permafrost and vice versa (Anisimov, 1989). Thawing permafrost releases greenhouse gases, primarily methane, stored as methane-ice clathrates at depths exceeding 200 metres within the terrestrial permafrost (MacDonald, 1990) and greater than 300 m within the seabed (Zhang et al., 2017). At shallower depths, methane can exist in the pore spaces of ice (Sloan et al., 2010), which could raise the need for a four-phase effective medium theory to account for the coexistence of free gas, ice, unfrozen water, and sediment grains. This release could intensify global warming, potentially accelerating further permafrost degradation (Nisbet, 1990). Between 2007 and 2016, permafrost temperatures increased by 0.29 ± 0.12 °C due to the amplification of air temperature changes in the Northern Hemisphere (Biskaborn et al., 2019). Over recent decades, Arctic surface air temperatures have increased more than twice the global average, and the warming has been spatially uneven, adding complexity to the issue (Meredith et al., 2022).

Under a 2°C global warming scenario, simulations predict that equilibrium permafrost area could decline by 25–44%, with the continuous permafrost zone suffering the greatest loss, shrinking by 29–67% (Anisimov and Nelson, 1996). By 2100, high-emission scenarios project the release of tens to hundreds of gigatons of carbon from thawing permafrost, posing significant risks to global climate (Meredith et al., 2022).

Given its sensitivity to climate change and its role as a significant carbon deposit, the study of ice-bearing sediments and permafrost is essential. Accelerated warming highlights the urgency of understanding these systems to mitigate detrimental effects on ecosystems, infrastructure, and the global climate.

1.5 The need for and importance of laboratory studies

As explained in Section 1.3, elastic wave behaviour is influenced by a complex interaction of pore fluid phases — water, ice, and air — making controlled laboratory studies important to distinguish these effects. Seismic and acoustic methods, commonly used in resource exploration and climate research, require calibration and validation through controlled experiments to identify the fundamental parameters driving wave propagation (Batzle et al., 2006). For example, inertial mechanisms described by Biot (1956a, 1956b) and local mechanisms such as squirt flow have been extensively studied but remain challenging to isolate without laboratory-based investigations (Dvorkin and Nur, 1998; Mavko and Nur, 1975; Oh et al., 2011; Tisato et al., 2021).Laboratory studies, whether conducted on idealised sediments or natural samples, provide information necessary for refining rock physic models (Ruppel et al., 2019). In addition, while geophysical methods offer non-invasive imaging of subsurface conditions, their accuracy can be improved based on well-calibrated laboratory experiments (Briggs et al., 2017; Wagner et al., 2019). Bridging these gaps requires innovative experimental setups and integrated approaches that combine precise laboratory techniques with field observations to advance understanding and model accuracy.

1.5.1 Challenges of field studies (in-situ measurements)

Field studies face a range of challenges, including logistical, environmental, and methodological constraints. These difficulties often require innovative approaches to data collection and analysis, with laboratory experiments playing a key role in complementing in-situ methods.

Field-based studies, especially in permafrost regions, are often constrained by high costs and logistical difficulties. Accessing remote areas demands significant resources, such as specialised equipment and transportation, making fieldwork both expensive and time-consuming (Wagner et al., 2019). These challenges often restrict studies to specific locations and times, limiting the spatial and temporal resolution of data. This limitation makes it difficult to generalise findings, particularly in environments with heterogeneous conditions, such as gas-saturated reservoirs and permafrost, where properties can vary significantly over short distances (Constable, 2020; Jedari-Eyvazi et al., 2023; Wagner et al., 2019).

For studies using natural cores, maintaining the pristine condition of samples during coring and transportation introduces additional challenges. Changes in temperature and pressure during recovery can alter key properties, such as porosity, permeability, and physical structure, making the samples unrepresentative of their in-situ state (Choi et al., 2014; Spangenberg et al., 2018; Wang et al., 2019). Traditional ice core analysis, often used to study the mechanical properties of ice, faces issues like brine drainage and sampling volume errors (Chang et al., 2021; Hutchings et al., 2015). Even advanced pressure-core technologies cannot fully mitigate these issues (Choi et al., 2014; Schulson et al., 2006). Additionally, such methods are costly and impractical for extensive or long-term studies in cold regions.

To improve accuracy and efficiency, researchers often combine multiple measurement techniques. For example, integrating electrical resistivity tomography with seismic imaging helps map unfrozen water content in permafrost regions (Overduin et al., 2015; Wagner et al., 2019). Similarly, combining P-wave velocity and attenuation data provides a more complete understanding of subsurface properties (Astuto et al., 2023; Emerson and Foray, 2006). While P-wave velocity is sensitive to high saturation levels, its effectiveness decreases at lower saturations, making additional parameters necessary. Attenuation measurements, though essential for studying pore fluid composition and internal heterogeneity, remain overlooked due to challenges in calibration and the lack of robust theoretical models (Oh et al., 2011).

1.5.2 The role and benefits of controlled laboratory experiments

Laboratory experiments play an important role in complementing field studies by providing a controlled environment where researchers can replicate in-situ conditions. These controlled settings make it possible to study material behaviour under various simulated natural conditions. For example, laboratory experiments can vary the water saturation level of unconsolidated sand to explore P-wave propagation under different conditions (e.g., Barriere et al., 2012; Sutiyoso et al., 2024). Similarly, experimental setups enable specific pressure and temperature found in gas hydrate reservoirs and permafrost, allowing detailed studies of their physical properties (Li and

Matsushima, 2024; Yin et al., 2019). This controlled approach reduces the need for recovering natural samples for seismic calibration studies (Wang et al., 2019). Consistent and repeatable experiments also help establish robust relationships between physical properties, such as elastic wave velocity and attenuation (Müller et al., 2010).

Another strength of laboratory experiments is the ability to isolate and analyse specific variables. For instance, controlled studies on partially frozen brine allow precise control over unfrozen brine content by adjusting temperature (Matsushima et al., 2008). In addition, experiments focusing on low hydrate or ice saturations can utilise attenuation measurements, which are more sensitive to small changes in saturation than velocity (Sahoo et al., 2019). These capabilities make laboratory studies invaluable for understanding coupled parameters like velocity and attenuation and for investigating how specific variables interact.

Laboratory studies also play a crucial role in developing and validating theoretical models. For example, laboratory data have been used to improve reservoir models that account for the complex interaction of sediments, hydrates, pore fluids, and gases during production processes (Ruppel et al., 2019). Additionally, these experiments provide insights into the physics of attenuation mechanisms, aiding to interpret seismic wave behaviour in porous media.

Another advantage of laboratory studies is their scalability, which allows experiments across different spatial scales. The studies can be conducted from the micro-scale behaviour of pore spaces to the macro-scale, both of which influence wave propagation (Knight and Nolen-Hoeksema, 1990). This scalability ensures that findings from controlled settings remain relevant to field-scale applications (Waite et al., 2009).

Despite their many benefits, laboratory experiments are not without limitations. Challenges remain in studying phenomena like fluid content, viscosity, and heterogeneity (Barriere et al., 2012). Furthermore, most experiments are limited to a narrow range of lithologies and conditions (Tisato et al., 2021). However, ongoing research continues to address these gaps, making laboratory studies crucial for connecting theoretical models and field observations. By providing baseline data, laboratory experiments help refine the interpretation of geophysical surveys and contribute to a more comprehensive understanding of subsurface processes (Batzle et al., 2006; Spangenberg et al., 2018).

1.6 Relevance and importance of elastic wave measurements

Elastic waves are fundamental in geophysical applications, due to their capabilities in revealing their subsurface properties without altering them (Aki and Richards, 1980; Fanchi, 2010). They are used to determine elastic properties of the near subsurface due to their distinct phase velocities and attenuation, such as lithologies, pore fluid saturation, porosity, and permeability (e.g., Astuto et al., 2023; Dong et al., 2023; Lee et al., 2024; Schumann et al., 2014). Accurate characterisation of sub-seafloor geological features using seismo-acoustic methods is crucial for numerous applications, such as hydrocarbon exploration (e.g., Asada et al., 2022; Ellingsrud et al., 2002), carbon dioxide and energy storage (e.g., Fawad and Mondol, 2021; Li et al., 2020), and marine geotechnical surveys (e.g., pipelines or windfarms) (Le et al., 2014; Reynolds et al., 2017).

One particular importance of water-saturated studies is for understanding soil liquefaction, where saturated sands lose strength and behave like a liquid during an earthquake. Lower P-wave velocities in nearly saturated sands indicate higher liquefaction susceptibility because as pore pressure increases, P-wave velocity decreases, reducing intergranular friction and effective stress (Ishihara et al., 1998). The mechanical stability of clean sands is controlled by effective pressure and porosity, with low effective pressure and high porosity increasing the likelihood of compaction, liquefaction, or shear failure (Zimmer, 2003).

Natural oil reservoirs and subsurface aquifers are typically not fully saturated, requiring seismic data interpretation to account for partial saturation effects (Barriere et al., 2012). P-wave velocity is particularly sensitive to near-full saturation, which may limit geophysical surveys to detecting significant changes only at high saturation levels (Emerson and Foray, 2006). Astuto et al. (2023) also noted that P-wave velocity may be less sensitive to saturation than theoretically predicted, due to variables like pore gas type, fluid characteristics, and soil grain morphology. Combining velocity and attenuation analyses helps overcome these limitations. Attenuation, driven by wave-induced fluid flow (WIFF) mechanisms such as squirt flow and patchy saturation, depends on pore-scale dynamics, confining pressure, and saturation (Müller et al., 2010; Tisato et al., 2021). In high porosity media, attenuation is particularly sensitive to permeability compared to velocity (Lee et al., 2024), offering insights into geological carbon storage for storage assessment and monitoring purposes (Caspari et al., 2014; Zhu et al., 2017).

Understanding the elastic properties of ice-bearing sediments is important for various geophysical applications, such as assessing climate-induced permafrost degradation (Tourei et al., 2024) and exploring carbon-dioxide hydrates as carbon storage alternatives (e.g., Qanbari et al., 2011; Rochelle et al., 2009). Permafrost is highly sensitive to temperature changes, causing subsidence and reduced mechanical strength due to limited ice bonding (Dou et al., 2016). Thawing permafrost can release significant amounts of methane, a potent greenhouse gas, into the atmosphere, amplifying carbon feedback mechanisms (Kvenvolden, 1993; Schuur et al., 2015).

This understanding is beneficial for identifying regions at high risk of hazardous thaw-related hazards (Ni et al., 2021). Such insights can mitigate infrastructure risks (Hjort et al., 2022; Oswell, 2011) and prevent economic losses in permafrost regions (Melvin et al., 2017; Streletskiy et al., 2019). In addition, Arctic sea ice has significantly decreased in area and thickness in recent decades, heightening the need for detailed understanding of ice's physical and mechanical properties, especially in ice-bearing sand (Wagner et al., 2019).

Seismic velocities increase with ice saturation, while attenuation peaks at intermediate levels, reflecting complex ice growth mechanisms beyond simple models (Dou et al., 2016). Advanced rock-physics models and focused studies on unconsolidated permafrost are essential for accurate ice content estimation and geotechnical applications. Non-invasive geophysical methods, such as geophysical imaging, offer high-resolution insights into permafrost characteristics (Wagner et al., 2019).

Additionally, carbon dioxide hydrates offer a promising solution for reducing emissions by storing large volumes of carbon dioxide in stable hydrate structures, complementing existing carbon storage methods (Aminnaji et al., 2024). Ice-bearing sediment can serve as analogue for gas hydrates, which significantly influence climate dynamics and occur in diverse geological settings (Helgerud et al., 2009). Thus, relating elastic wave properties to ice and hydrate content is vital for monitoring and managing these environmental challenges (Fawad and Mondol, 2021; Zheng et al., 2020).

1.7 Methods

This study investigates elastic wave propagation in unconsolidated sediments under water-saturated and ice-bearing conditions in controlled laboratory experiments. The measurements were conducted using an acoustic pulse tube, an instrument that allows waves to propagate in the 1–20 kHz sonic frequency range, which adds significance to the study. In addition to the experimental measurements, rock physics models were used to further explore the mechanisms underlying the P-wave velocity and attenuation.

The following sections begin with an overview of the history and development of geophysical measurements in laboratory settings. Next, I introduce the methods used in this study, with detailed explanations and their applications in Chapters 2 to 4. Chapter 2 focuses on acoustic data processing and calibration, as well as its application to water-saturated sand packs. Chapters 3 and 4 explore the further application of pulse tube measurements in understanding P-wave velocity and attenuation in ice-bearing sands under varying ice saturation and effective pressures.

1.7.1 History and development of laboratory elastic wave experiments

Laboratory experiments have been essential in advancing the understanding of elastic wave propagation in porous media, offering controlled conditions to isolate and study specific variables. The use of ultrasonic pulse method began in the 1940s to measure elastic properties in various materials and mediums, e.g., metal rods (Hughes et al., 1949) and water (Smith and Lawson, 1954). Meanwhile in rocks, Hughes and Jones (1950) measured wave velocities in igneous rocks, and Hughes and Kelly (1952) extended this to sandstone. The work of Wyllie et al. (1956) marked a milestone by applying ultrasonics specifically to sediments, while Gardner et al. (1964) pioneered the measurement of attenuation in sediments under varying pressure and fluid saturations. This study highlighted the complex interactions between wave modes and pore fluids, establishing attenuation as a key focus of laboratory measurements. Later, Toksöz et al. (1979) identified squirt flow and local viscous effects as dominant mechanisms contributing to attenuation, especially under partial saturation, improving the understanding of attenuation in granular media. Ultrasonic experiments gained popularity for their ability to provide high-resolution insights into small-scale phenomena and have since been widely used to study a variety of mediums (e.g., Carcione and Seriani, 1998; Matsushima et al., 2016; Prasad, 2002; Sahoo and Best, 2021; Winkler, 1985).

Generally, the ultrasonic method used for geophysical measurements is classified into two categories: transmission and pulse-echo. In the transmission method, the ultrasonic wave travels from the transmitter to the receiver, and the velocity is determined by dividing the measured arrival time delay by the sample length. It typically uses two axially aligned piezoelectric transducers coupled to opposite ends of the sample. This method is widely used due to its straightforward installation process within high-pressure vessels, making it suitable for measuring rocks and sediments (e.g., Ba et al., 2024; Christ and Park, 2009; Murphy, 1984; Yurikov et al., 2018). While this method is not ideal for measuring attenuation, as it is prone to uncertainties caused by variable coupling of the transducer faces to the rock and calibration samples, attenuation can still be measured using the spectral ratio method, which compares spectral amplitudes at different distances (Mavko et al., 2009). Alternatively, attenuation can be determined by comparing two geometrically identical specimens: a non-dispersive reference specimen and the studied specimen (Bourbie and Zinszner, 1985).

In contrast, the ultrasonic pulse-echo method overcomes transducer coupling issues through self-calibration of signal amplitudes, using the same transmitted pulse for both reference and sample measurements. This is achieved by placing a reflector parallel to the transducer at a known distance and performing a normal incidence reflection experiment on the sample (Ophir et al., 1985). In practice, the sample is sandwiched between buffer rods to create a time window for isolating the two reflections, free from contamination by multiple reflections from surrounding equipment (Sahoo, 2018). The buffer rod and sample assembly are typically cylindrical and must have a sufficient diameter to prevent side-wall reflections caused by the spreading ultrasonic beam due to the longer wave path compared to transmission measurements (McCann and Sothcott, 1992). The pulse-reflection method offers greater repeatability and accuracy than the pulse-transmission method, especially for measuring attenuation. However, the main limitation of both ultrasonic transmission and pulse-echo methods is their very high measurement frequency, which far exceeds field seismic and sonic frequencies, making direct comparison challenging. This technique is widely used to study rock physics, particularly attenuation (e.g., Amalokwu et al., 2014; Sahoo et al., 2019; Winkler, 1985). Both ultrasonic methods are illustrated in Figure 1.5.

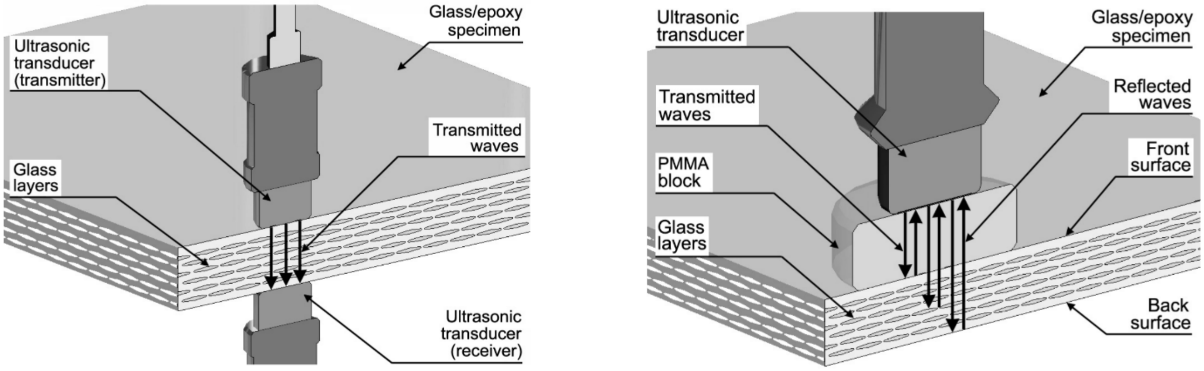

Figure 1.5 Illustration scheme of the ultrasonic testing of transmission (left) and pulse-echo (right) techniques for glass/epoxy specimens. Adapted from Wróbel and Pawlak (2007).

Despite its strength, the ultrasonic method is typically limited to laboratory conditions, with frequencies ranging from 150 kHz to 1 MHz, much higher than those used in field seismic (Hz) and sonic (kHz) applications. The small sample size also restricts laboratory studies of rock heterogeneity and scaling effects at decimetre to metre scales and beyond. This frequency and dimension mismatch has led to the development of other methods, such as the resonant bar (including the Split-Hopkinson Pressure Bar), resonant column, forced-oscillation method, and acoustic pulse tube.

The resonant bar method measures the dynamic elastic properties of solids, such as rocks, under small-strain conditions. Birch and Bancroft (1938) developed this technique by analysing the resonant vibrations of a granite column, establishing its use for sonic frequency measurements. A cylindrical sample is excited until it reaches its natural resonance, enabling the calculation of shear and Young's moduli. Piezoelectric or electromagnetic transducers excite extensional or torsional modes, with attenuation measured from the resonant peak width or decay time. Longer bars produce lower frequencies, so shorter bars are often cemented together due to coring challenges (Born, 1941). However, the resonant bar method has limitations, including measurement difficulties under high-pressure and high-temperature conditions, and challenges in achieving pure shear modes (Wang, 1997). To overcome frequency limits, Tittmann (1977) suggested adding mass to adjust the moment of inertia without changing rigidity. Inspired by this, Nakagawa (2011) designed a modified resonant bar system for smaller samples, similar to the Split-Hopkinson pressure bar.

The conventional Split-Hopkinson pressure bar has been used for decades in high strain material testing to determine properties such as stress, strain, and strain rate (Chen and Song, 2011). It consists of two long, cylindrical bars (input and output bars) with the sample placed between them. A stress wave is generated in the input bar, typically using a striker bar or a gas gun, and propagates through the sample to cause deformation. The transmitted and reflected waves are measured using strain gauges on the bars. Originally developed by Kolsky (1949) and named after Hopkinson (1914), the Split-Hopkinson pressure bar is widely applied in materials science, rock mechanics, and engineering for studying the behaviour of materials under impact or rapid loading conditions (e.g., Lundberg, 1976; Nakagawa, 2011; Stopka et al., 2024; Zhao and Gary, 1996). However, this setup has limitations in low-strain testing and requires complex calibration, particularly to address errors arising from wave dispersion and attenuation in the pressure bar (Davies and Taylor, 1947).

The resonant column is a geotechnical tool commonly used to measure shear wave velocities in soils and rocks by inducing torsional vibrations. Based on the vibration theory of a linearly viscoelastic cylindrical rod, the shear wave velocity is calculated from the resonance frequency of the sample and its drive mechanism (Richart et al., 1970). Although rods with rectangular cross-sections are feasible, cylindrical rods are preferred as they do not necessitate geometric corrections in the torsional excitation mode (Lucet et al., 1991). Resonance frequencies typically range from 17–25 Hz for soft clay soils (Hardin and Drnevich, 1972) to 400 Hz for stiff cemented sands (Avramidis and Saxena, 1990), aligning with frequencies used in marine seismic surveys. Initially developed by Stokoe et al. (1999), the ‘Stokoe’ resonant column primarily applies torsional vibration but can also be modified for flexural vibration, enabling measurements of compressional wave velocity (Cascante et al., 1998). Nowadays, resonant columns are widely used in various contexts, including elastic wave property studies in gas hydrate-bearing sand (e.g., Madhusudhan et al., 2019; Priest et al., 2005).

The forced-oscillation method has become a widely used alternative to ultrasonic techniques for measuring the elastic and anelastic properties of materials due to its frequency range matching field seismic surveys, which simplifies data interpretation for fluid-saturated rocks (Jackson et al., 2011; Mikhaltsevitch et al., 2014). Initiated in the 1960s by Bruckshaw and Mahanta (1961) and Peselnick and Outerbridge (1961) to measure the intrinsic attenuation and elastic moduli of rocks, forced-oscillation experiments initially lacked strain control but were later adjusted to maintain strain amplitudes below 10^{-6} (Mavko, 1979; Winkler and Murphy, 1995), minimising frictional attenuation between grain contacts and aligning with real seismic conditions (Winkler and Nur, 1979). This strain amplitude limit matches field seismic measurements and is a major constraint on laboratory tests of the elastic and anelastic properties of rocks. The method requires a frequency-adjustable force generator, a force sensor, and strain sensors to calculate modulus and attenuation from the stress-strain ratio and phase angle. However, this method rely on traditional electronic sensors, like capacitive transducers and strain gauges, resulting in long measurement times and demands highly homogeneous samples due to limited sensor contact (Mikhaltsevitch et al., 2023).

The acoustic pulse tube, also known as an impedance pulse tube, has been used since the early 1900s, initially for measuring the acoustic impedance of materials in architecture and acoustic design (Pierce, 2019). Over time, this method evolved to measure the dynamic elastic properties of materials (Dubbelday and Capps, 1984). The pulse tube operates as an acoustic waveguide, consisting of a fluid inside a solid cylindrical tube (McCann et al., 2014). Sound velocity and attenuation are measured using samples inside the tube, with acoustic properties determined from wave reflections. For geophysical applications, Biot (1952) demonstrated that in a borehole with elastic walls, the main acoustic wave is a dispersed Stoneley wave, which is the only wave that can travel at low frequencies. Redwood (1960) showed that a rigid-walled, fluid-filled waveguide supports a plane wave travelling with a flat, longitudinal wavefront. Dubbelday and Capps (1984) further theoretically demonstrated that even a steel rod can propagate a compressional wave in a fluid-filled tube with rigid walls, provided the tube-to-sample radius ratio is below 1.001. These findings confirm that a plane wave can propagate inside an acoustic pulse tube.

McCann et al. (2014) applied these principles to measure compressional wave properties in marine sediments at sonic frequencies under varying differential pressures. The study showed that compressional waves derived from Stoneley waves produced results consistent with published ultrasonic measurements, after adjusting the result to equivalent conditions of pressure, temperature, pore fluid salinity, and measurement frequency. The findings also revealed that different jacket materials, such as PVC (primarily used in this thesis), have negligible effects on velocity and attenuation measurement. These details are further discussed in Sections 1.7.2. and 1.7.3.

1.7.2 Preparation of water-saturated and ice-bearing sand

This study focuses on elastic wave propagation in unconsolidated sediment. The samples comprised clay-free quartz sand from Leighton Buzzard, with a mean grain diameter of 100 µm. This grain size was chosen for its similarity to typical sand found in permafrost regions, as reported in numerous studies from Alaska, Siberia, and China (e.g., Fuchs et al., 2018; Liu et al., 2023; Strauss et al., 2012). Using sediment with comparable properties to those found in the field helps minimize scaling effects and enables more direct comparison with field data.

The sand packs were encased using cylindrical jackets and endcaps made of polyvinyl chloride (PVC), allowing measurement in the water-filled pulse tube. This setup allowed the surrounding confining fluid (water) to apply uniform hydrostatic pressure to the sand pack while maintaining acoustic impedance compatibility for wave propagation.

To minimise density and porosity variations within the sample, a standardised preparation method was employed. The sand was oven-dried and tamped into the PVC jacket in successive layers, with the boundaries between layers scratched to avoid impedance contrasts. This approach was based on the ‘Proctor method’ for soil compaction (ASTM, 2007). The porosity of the samples was calculated using a dry mass balance method, with values ranging from 38% ± 0.25% to 42% ± 0.25%. The error margin was derived by comparing porosity measurements from dry bulk density and post-saturation data.

De-ionised water was used to saturate the samples using a combination of vacuum and imbibition methods. The vacuum method removed air from the pores, while the imbibition process relied on capillary pressure at the gas-liquid interface to achieve full saturation (McPhee et al., 2015). Saturation was carried out incrementally, with the PVC jacket tapped during the process to release trapped gas bubbles.

For ice-bearing samples, the fully saturated specimens were frozen at -10°C for 48 hours in a controlled environment. The removal of gas bubbles during saturation ensured the formation of bubble-free ice, which contributed to consistent measurements (McCutchan and Johnson, 2022). Despite the controlled freezing conditions, some unfrozen water may persist within the pores. This includes thin water films bound to grain surfaces, as described by Dash et al. (1995) and Watanabe and Mizoguchi (2002).

Understanding the distribution of water within the sand sample is critical for interpreting pulse tube results. To address this, a novel microwave measurement technique was developed. Microwave methods, commonly used to measure soil water content through electrical permittivity or dielectric constant (e.g., Lewandowski et al., 2017; Richards et al., 2014), are non-destructive and preserve sample integrity. Water and ice distribution were monitored by taking microwave readings at regular intervals along the sample length. This non-destructive transmission-based technique achieved an error margin of 5.9% after calibration (Sutiyoso et al., 2024a).

1.7.3 Acoustic pulse tube measurement

The acoustic pulse tube functions as an acoustic waveguide, consisting of a water-filled, thick-walled stainless steel cylindrical tube designed to propagate plane waves (Dubbelday and Capps, 1984; Redwood, 1960). The configuration ensures that higher-order wave modes do not propagate at frequencies below 26 kHz (McCann et al., 2014). The experimental setup can simulate various subsurface conditions corresponding to depths of up to 1 km (Figure 1.6).

The acoustic waves are generated from chirp signal source within the 1–20 kHz range. The time-domain data were transformed into the frequency domain and deconvolved with the chirp source signal to obtain the impulse response. Time-domain gating was also applied to eliminate multiple reflections within the pulse tube. An inversion method was used to estimate the sample's complex velocity. Calibration of the experimental setup followed the method outlined by McCann et al. (2014) by comparing pulse tube measurements with theoretical transmission coefficients. Initial calibration was performed using a nylon rod with well-known acoustic properties. The calibration method was then applied to PVC-jacketed sand packs, producing consistent results. A 3% reduction observed in the jacketed system was applied as a calibration factor. The relative experimental uncertainties were estimated to be ±2.4% for velocity and ±5.8% for attenuation (explained in detail in Chapter 2, Section 2.2.3.3).

Although the acoustic pulse tube had been installed several years prior to this study, I was still able to contribute to its overall development. I tested various experimental setup configurations, beginning with the source signals. Initially, testing and initial measurements were performed using an equalised chirp signal. However, due to measurement inconsistencies, particularly in the frequency spectrum, I experimented with a linear chirp signal generated by a researcher. This new signal reduced variations in frequency spectrum, especially at higher frequencies, by focusing energy more effectively in that range, thereby improving the quality of the acoustic measurements. This signal source was the one mainly used in this study.

Additionally, I assisted in improving the data processing. The inversion method utilised in data processing uses the scattering matrix approach, which involves many parameters to calculate signal reflection and transmission. My main role was to help reviewing the code, ensuring the correct application of arithmetic operators in the updated definitions of reflection and transmission parameters. The final version of the code resulted in more stable results, particularly in attenuation within the frequency spectrum.

I also tested the jacket system used in the pulse tube. Initially, I used a rubber jacket with nylon endcaps to enable sand emplacement within the water-filled pulse tube. However, preparing unconsolidated sand into the rubber jacket presented practical challenges, as the jacket often inflated during sand insertion. This caused uneven tamping, leading to small gaps between the rubber jacket and nylon endcaps. These gaps allowed water from the pulse tube to seep into the sample as confining pressure increased, altering the saturation levels. On several occasions, the sample failed to contain the incoming water, causing it to break and rendering the pulse tube inoperable due to the need for extensive cleaning after sand scattered inside, risking obstruction of wave propagation. I resolved this issue by using a solid PVC tube and endcaps with applied O-rings, ensuring uniform application of confining pressure.

These trial-and-error efforts in the pulse tube setup improved the reliability of measurements for various materials, particularly unconsolidated sand under different saturation conditions, as explored in this study. This process has increased confidence in the quality of the results for further analysis and application.

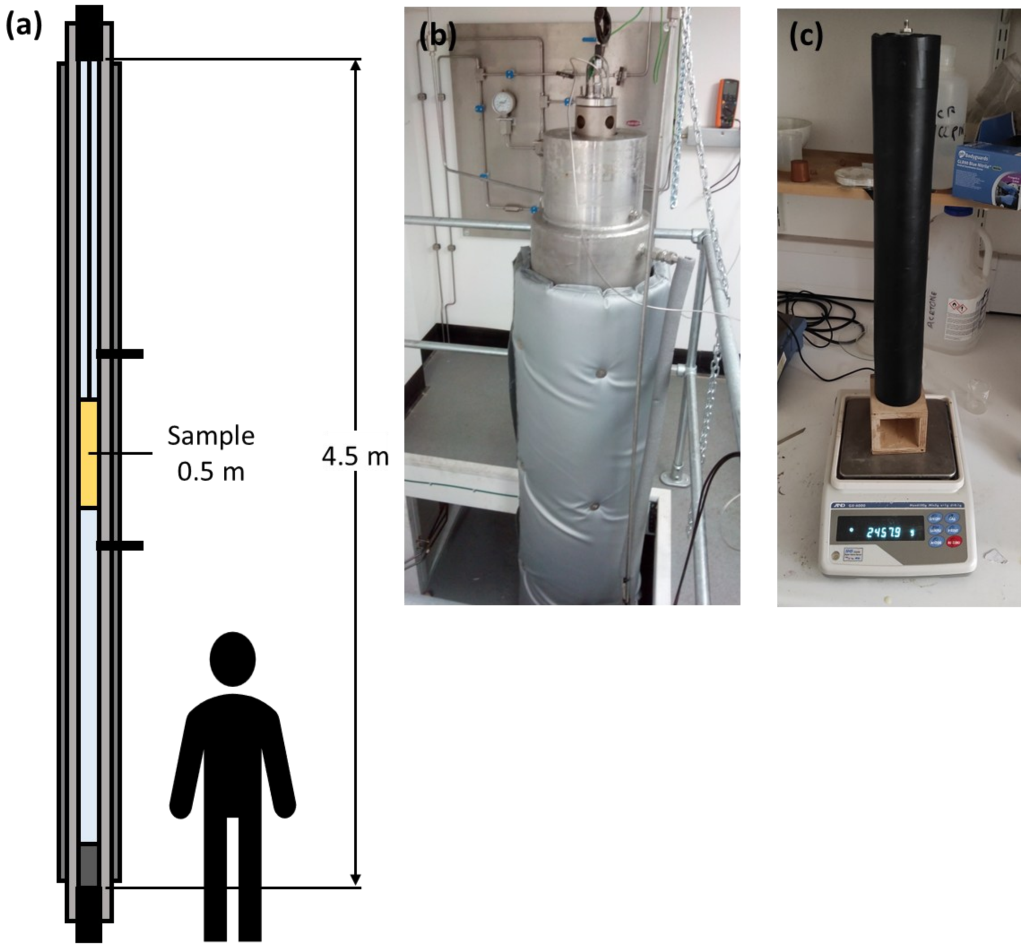

Figure 1. 6 (a) Schematic of the experimental pulse tube setup with human and sample figures for scale (detailed dimensions provided in Chapter 2); (b) Photograph of the top section of the pulse tube with insulation jacket for temperature control; (c) Sample preparation with a weighing scale for reference.

1.7.4 Rock physics theory and modelling and ice estimation

Theoretical studies by Biot (1956a, 1956b) were pioneering in understanding the effects of fluid content on the elastic wave properties of porous media. Biot's theory explains how elastic waves induce frequency-dependent fluid motion relative to the solid matrix, leading to frequency-dependent velocity and attenuation. Later studies explored the effects of gas and liquid distributions, differentiating between uniform and patchy saturations (e.g., Pride et al., 2004; White, 1975).

Biot’s theory is widely recognised for modelling elastic wave propagation in porous media, particularly in unconsolidated sediments. It is applicable in high-frequency conditions, such as laboratory experiments, where Gassmann's theory (1951) is more suitable for low-frequency conditions below 100 Hz. In this study, Biot’s model was compared to experimental results, particularly the Biot-Stoll model (Stoll and Bryan, 1970) as implemented in the hydrate-bearing effective sediment (HBES) model developed by Marín-Moreno et al. (2017). The HBES model builds on Biot's framework by incorporating additional fluid flow mechanisms, such as squirt flow and gas bubble interactions, to better represent complex pore-scale processes.

The HBES model is versatile as it can simulate porous sediments saturated with gas or liquid without requiring hydrate to be present. For the water-saturated study, hydrate saturation was set to zero, allowing the model to predict the effects of water saturation on the acoustic properties. The HBES model was developed from the hydrate effective grain (HEG) model by Best et al. (2013), which accounts for velocity and attenuation dispersion through the clay-squirt flow mechanism (Leurer, 1997; Leurer and Brown, 2008). The HBES incorporates gas bubble resonance effects based on the work of Smeulders and Van Dongen (1997), making it highly suitable for analysing the acoustic properties of sediment. The model employs the Reuss approximation (Reuss, 1929) to calculate the effective bulk modulus of fluids. In this study, the model was extended to also include the Voigt (Voigt, 1889) and Brie (Brie et al., 1995) approximations, enabling investigation of water and ice distribution on acoustic properties.

Leclaire et al.'s (1994) model was also used to investigate acoustic behaviour in ice-bearing sediments, complementing the HBES model. Both models extend Biot’s theory to predict frequency-dependent velocity and attenuation but differ in how they treat the sediment frame. Leclaire et al. (1994) developed a three-phase model that considers sediment, ice, and unfrozen water coexisting within the system. In the HBES model, pore-filling hydrate/ice is treated as part of the pore fluid, while cementing hydrate/ice is considered part of the sediment matrix. To adapt the HBES model for ice-bearing sediments, the bulk and shear modulus parameters for hydrate grains were replaced with those of ice grains. This adjustment enabled the model to simulate the effects of ice on acoustic velocity and attenuation accurately.

Ice saturation was inferred empirically during the melting process using the elapsed time as the primary parameter. Both rock physics models were applied to this inversion process, incorporating the variability of the melting process through an empirical coefficient (*n*). Velocity and attenuation in the fully melted state provide a baseline to compare with data recorded during melting. The initial ice saturation was assumed to be completely freezing upon entering the pulse tube. The relationship between ice saturation (S_i) and melting time is described by the following equation:

$$S_i = 1 - \left(\frac{t}{T}\right)^n, \tag{1.1}$$

where S_i is ice saturation, t is the elapsed measurement time (in seconds), T is the total time for complete melting (determined by velocity and attenuation at the fully melted state), and n is an empirical parameter expressing the exponential relationship between ice melting and time (McCutchan and Johnson, 2022).

1.7.5 Advantages and challenges in methods

Pulse tube measurements offer several advantages for investigating acoustic properties, particularly due to their larger dimensions, which enable wave propagation at lower frequencies by accommodating larger sample sizes. These larger samples better replicate natural conditions compared to smaller ultrasonic setups, allowing for the study of mesoscopic heterogeneity, while maintaining more control than field-scale seismic methods. This is particularly important because most geophysical laboratory studies operate at ultrasonic frequencies, whereas field measurements typically occur at seismic and sonic frequencies. By operating within the sonic frequency range, the acoustic pulse tube becomes directly relevant to high-resolution seismic surveys and borehole sonic logging, enhancing its potential to support direct interpretation of field data. In contrast, the ultrasonic method, with its much shorter wavelength, provides higher-resolution insights into micro-scale interaction between phases. This method is particularly effective for studying pore-scale phenomena such as squirt flow (e.g., Li et al., 2024; Si et al., 2016; Tisato et al., 2021; Winkler and Nur, 1979) while using larger samples may average out these fine-scale variations.

The resonant column operates within a similar frequency range to the pulse tube but differs in methodology. Unlike the pulse tube and ultrasonic methods, the resonant column does not directly measure wave propagation. Instead, it calculates wave velocities by deriving dynamic material properties from the torsional (twisting about the central axis) and flexural (bending along the sample's length) vibrations (Cascante et al., 1998; Priest et al., 2005). This approach assumes the sample is homogeneous and isotropic, which may not represent materials with heterogeneities or multiple phases, such as melting ice-bearing sediment. Effective moduli used in calculations may fail to represent the interactions between phases. Meanwhile, the pulse tube directly measures wave propagation within the samples, allowing it to detect heterogeneities at scales relevant to the propagating wavelength. Even smaller-scale heterogeneities, albeit spatially averaged, can be identified (Best et al., 2013; Huang et al., 2009). Additionally, resonant column is reported to have higher uncertainty in measuring attenuation (Best et al., 2013).

The use of chirp signals in the pulse tube, spanning frequencies between 1–20 kHz, offers another advantage over single-frequency approaches. This frequency range covers a significant range of the sonic spectrum, where attenuation peaks are known to occur due to squirt flow mechanisms (Müller et al., 2010). Such broad frequency coverage is particularly beneficial for attenuation measurements and allows for the validation of theoretical models across a wide frequency range.

Despite these advantages, pulse tube measurements face certain challenges. The large size of the tube, while ideal for measuring samples relevant to kHz frequencies, requires careful operating to ensure accurate and consistent results. One common issue is the presence of gas bubbles in the water-filled tube, particularly at the bottom of the sample. These bubbles significantly degrade wave propagation, which directly reduce measurement accuracy (Xue et al., 2023). This issue can be mitigated by systematically increasing confining pressure to dissolve the bubbles (Enns et al., 1965) or by pushing the bubbles upward and releasing them through the top cap of the pulse tube.

Achieving uniform distribution of ice and water in such large samples is another challenge, especially at partial saturations, where patchy distributions may occur. Non-uniform saturation can create heterogeneous zones of water and ice, leading to local variations in acoustic properties. These inconsistencies can complicate the interpretation of velocity and attenuation data. In this study, water distribution was monitored using an experimental microwave method, which ensured uniform ice and water saturation. However, direct monitoring within the pulse tube would provide an even more detailed understanding of the distribution's effects on acoustic measurements.

Another challenge is the distortion of acoustic signals within the pulse tube, primarily caused by multiple reflections from the side-wall ports and end caps. Introducing additional instruments to monitor fluid distribution inside the samples, while advantageous, would further amplify these distortions. To address this issue, time-domain gating and deconvolution techniques were applied to isolate the direct waveforms. This approach effectively minimised the impact of reflections and improved signal clarity. However, it also eliminated portions of the data, which might otherwise provide additional insights.

1.8 Introduction of the study

This study investigates elastic wave propagation in water-saturated and ice-bearing sand packs, focusing on how water and ice saturation influence acoustic wave velocity and attenuation at sonic frequencies. By using pulse tube measurements, the study explores a potential method for estimating water and ice saturation indirectly, which is crucial for applications like carbon storage and permafrost monitoring (Fawad and Mondol, 2021; Tourei et al., 2024; Wagner et al., 2019). The experimental results provide valuable insights into the dynamic changes in velocity and attenuation during ice melting in sand, highlighting on interactions between ice, water, and sediment grains. These findings are relevant to thawing permafrost, where velocity changes can indicate reduced strength and potential risks such as carbon release or infrastructure failures (Carcione and Seriani, 1998; Hjort et al., 2018; Li and Matsushima, 2024).

The study also compares laboratory findings with field measurements, offering a benchmark for future research on acoustic wave behaviour in saturated media. In addition, it evaluates the strengths and limitations of existing rock physics models, identifying opportunities for model refinement and development. Overall, this work contributes to understanding acoustic wave propagation in frozen and saturated sediments, providing a foundation for future research in permafrost dynamics.

1.9 Thesis Overview

I begin this thesis by introducing the study and outlining the research aims and scope. This is followed by a review of the elastic wave properties of water-saturated and ice-bearing sediments. I first present the general concepts of elastic wave properties, including velocity and attenuation, before discussing the characteristics of elastic wave behaviour in saturated sediments. This review includes an overview of studies on wave propagation in such media. Given the relevance of this study, I also provide background information on ice-bearing sediments and permafrost. Then, I address the need for and importance of laboratory investigations. Lastly, I describe the methodology used in this study, including sample preparation, acoustic pulse tube measurements, and the application of rock physics models. This section also highlights the advantages and challenges of the chosen methods.

The remainder of the thesis consists of a collection of self-contained chapters based on individual studies:

Chapter two investigates how water saturation affects wave propagation in unconsolidated sand. This chapter also details the data processing and calibration processes for the pulse tube measurements, estimating relative experimental uncertainties of ±2.4% for velocity and ±5.8%

for attenuation. The results show consistent readings across all samples, with velocity and attenuation significantly influenced by changes in water saturation. Additionally, the distribution of water plays a key role in affecting the elastic wave properties. This chapter is a reformatted version of my published paper: *Sutiyoso, H.S., Sahoo, S.K., North, L.J., Minshull, T.A., Falcon-Suarez, I.H. & Best, A.I. (2024) Laboratory measurements of water saturation effects on the acoustic velocity and attenuation of sand packs in the 1–20 kHz frequency range. Geophysical Prospecting, 1–22. https://doi.org/10.1111/1365-2478.13607*. All experiments and analysis were done by me. Role of the authors: Hanif Sutiyoso (conceptualisation, data curation, formal analysis, investigation, software, visualisation, writing); Sourav Sahoo (conceptualisation, supervision, review and editing); Laurence North (methodology, software); Ismael Falcon-Suarez (review and editing); Tim Minshull (conceptualisation, supervision, funding acquisition, project administration, review and editing); Angus Best (conceptualisation, supervision, funding acquisition, project administration, review and editing).

Chapter three, entitled “Laboratory measurement of sonic (1-20 kHz) P-wave velocity and attenuation during melting of ice-bearing sand”, examines the effects of ice saturation on velocity and attenuation during the melting process under low effective pressures, simulating conditions in the active layer of permafrost. The findings reveal that both velocity and attenuation strongly correlate with ice saturation. However, attenuation is influenced by ice saturation only up to a certain level, in contrast to velocity that is influenced throughout ice saturation levels. The results also demonstrate that ice morphology significantly affects wave propagation. This chapter is a reformatted version of my paper, now under revision after the first round of review, submitted to the Journal of Geophysical Research: Solid Earth. All experiments and analysis were done by me. Role of the authors: Hanif Sutiyoso (conceptualisation, data curation, formal analysis, investigation, software, visualisation, writing); Sourav Sahoo (conceptualisation, supervision, review and editing); Laurence North (methodology, software); Ismael Falcon-Suarez (review and editing); Tim Minshull (conceptualisation, supervision, funding acquisition, project administration, review and editing); Angus Best (conceptualisation, supervision, funding acquisition, project administration, review and editing).

Chapter four, entitled “P-wave velocity and attenuation measurements during the melting process of ice-bearing sand at 1-20 kHz under elevated effective pressures”, explores how ice saturation affects velocity and attenuation under elevated effective pressures, representing the conditions in deeper permafrost layers. The results show that ice content influences velocity and attenuation, particularly at high ice saturations, with the most pronounced effects occurring at lower pressures. Additionally, ice distribution (patchy or uniform) has a greater impact on velocity and attenuation at high pressures compared to ice morphology. The influence of permeability on wave propagation decreases as effective pressure increases. This chapter is a reformatted version of a paper currently in preparation for submission to Geophysical Research Letter. All experiments and analysis were done by me. Role of the authors: Hanif Sutiyoso (conceptualisation, data curation, formal analysis, investigation, software, visualisation, writing); Sourav Sahoo (conceptualisation, supervision, review and editing); Laurence North (methodology); Ismael Falcon-Suarez (review and editing); Tim Minshull (conceptualisation, supervision, funding acquisition, project administration, review and editing); Angus Best (conceptualisation, supervision, funding acquisition, project administration, review and editing).

Chapter five concludes the thesis by summarising the findings, discussing their significance and implications, comparing the experimental results with published studies across various frequencies, and offering suggestions for future research.

Chapter 2 Laboratory measurements of water saturation effects on the acoustic velocity and attenuation of sand packs in the 1–20 kilohertz frequency range

This chapter forms a published paper: Sutiyoso, H.S., Sahoo, S.K., North, L.J., Minshull, T.A., Falcon-Suarez, I.H. & Best, A.I. (2024) Laboratory measurements of water saturation effects on the acoustic velocity and attenuation of sand packs in the 1–20 kHz frequency range. Geophysical Prospecting, 1–22. https://doi.org/10.1111/1365-2478.13607

My contributions to the development of equipment and processing tools include: calibrating the pulse tube using a nylon rod and sediment samples (i.e., sand packs), improving data acquisition (e.g., testing different sound sources to get better results), refining the processing workflow (e.g., debugging and optimising the processing code), and calibrating the microwave equipment (e.g., testing it with various samples).

Abstract

We present novel experimental measurements of acoustic velocity and attenuation in unconsolidated sand with water saturation within the sonic (well-log analogue) frequency range of 1 – 20 kilohertz. The measurements were conducted on jacketed sand packs with 0.5-metre length and 0.069- metre diameter using a bespoke acoustic pulse tube (a water-filled, stainless steel, thick-walled tube) under 10 Megapascal of hydrostatic confining pressure and 0.1 Megapascal of atmospheric pore pressure. We assess the fluid distribution effect on our measurements through an effective medium rock physics model, using uniform and patchy saturation approaches. Our velocity and attenuation (Q^{-1}) are accurate to ± 2.4% and ± 5.8%, respectively, based on comparisons with a theoretical transmission coefficient model. Velocity decreases with increasing water saturation up to ~75% and then increases up to the maximum saturation. The velocity profiles across all four samples show similar values with small differences observed around 70-90% water saturation, then converging again at maximum saturation. In contrast, the attenuation increases at low saturation followed by a slight decrease towards maximum saturation. Velocity increases with frequency across all samples, which contrasts with the complex frequency-dependent pattern of attenuation. These results provide

valuable insights into understanding elastic wave measurements over a broad frequency spectrum, particularly in the sonic range.

2.1 Introduction

Accurate characterisation of sub-seafloor geological features using seismo-acoustic methods is crucial for hydrocarbon exploration (e.g., Asada et al., 2022; Ellingsrud et al., 2002), carbon dioxide and energy storage (e.g., Fawad and Mondol, 2021; Li et al., 2020), and marine geotechnical surveys (e.g., pipelines or windfarms) (Le et al., 2014; Reynolds et al., 2017). These imaging methods can provide useful information on stratigraphy (e.g., folds, faults) and fluid distribution, deriving physical properties from elastic wave velocity and attenuation. Understanding controls on the compressional (P-) and shear (S-) wave properties of marine sediments at sonic frequencies of 1-20 kilohertz (kHz) can help interpretation of high-resolution seismic surveys, such as Chirp sub-bottom profilers operating in the 1–10 kHz frequency range (McCann et al., 2014). In addition, knowledge of these properties at elevated confining pressures and temperatures can help the interpretation of data from borehole sonic logs operating at 10 – 15 kHz in more deeply buried sediments.

P-wave velocity and attenuation are sensitive to fluid content and pore connectivity (Mavko et al., 2009); while S-wave velocity remains insensitive unless fluid density changes. Therefore, most studies focus on P-wave properties when investigating water saturation effects. The relationship between fluid content and elastic wave properties is often complex, representing a challenge to interpreting seismo-acoustic data. This relationship can be quantified in a laboratory setting where environmental conditions can be controlled. For instance, resonant bar studies have shown that partial liquid saturation creates strong attenuation in porous rocks in the kHz range (e.g. Batzle et al., 2006; Chapman et al., 2021; Murphy, 1982). At sonic frequencies, compacted heterogeneous soils evidence similar velocity and attenuation versus water saturation dependencies to rocks (e.g., Barriere et al., 2012; Cadoret et al., 1998; Dong et al., 2023). However, there are few studies on saturation effects at sonic frequencies, especially in unconsolidated sediments with varying water saturation (McCann et al., 2014). Most prior research focused on dry or nearly fully saturated media (Ayres and Theilen, 2001; Prasad, 2002).

Theoretical model studies by Biot and Stoll (e.g., Biot, 1956a, 1956b; Stoll, 1985) and others have investigated fluid content effects on elastic wave properties. Biot's theory describes how elastic waves induce frequency-dependent fluid motion relative to the solid matrix in porous media, influenced by fluid viscosity, density, and rock matrix permeability, leading to frequency-dependent velocity and attenuation. The theory predicts two compressional waves (fast and slow) and a shear wave, with the slow P-wave being highly attenuated and rarely observed (e.g., Bouzidi and Schmitt, 2009). Other theoretical studies have examined gas and liquid distribution effects, whether uniform or patchy (e.g., Pride et al., 2004; White, 1975).

We conducted an experimental study to investigate the effects of water saturation on frequency-dependent compressional wave velocity and attenuation (expressed as the inverse quality factor, Q^{-1}) in unconsolidated sand packs at sonic frequencies. These sand packs are known to conform well to Biot's model description of wave propagation, at least in saturated samples at ultrasonic frequencies (e.g., Klimentos and McCann, 1988). We used a water-filled acoustic pulse tube similar to the one described by McCann et al. (2014) to measure P-wave velocity and attenuation on sediment samples (0.5 m length, 0.069 m diameter) at 1 – 20 kHz. We compared our pulse tube data with an effective medium rock physics model (i.e., the Biot-Stoll model) to understand the underlying mechanisms.

Our measurements can be used to validate frequency-dependent rock physics models, which are important for accurately interpreting subsurface properties. The intermediate (sonic) frequency range that lies between ultrasonic and seismic frequencies is often key to understanding theoretically predicted velocity dispersion and attenuation peaks caused by visco-elastic relaxation that tend to occur in this range (Guerin and Goldberg, 2005; Sahoo and Best, 2021). These models, potentially modified to account for our data, can then be used to interpret field seismic (including the high-resolution method) and borehole sonic log data in relation to pore fluid content analysis. For example, enhanced rock physics models can facilitate monitoring of carbon storage, from the sequestration process, which can introduce patchy saturation, to detecting seabed gas leaks (Azuma et al., 2013; Jedari-Eyvazi et al., 2023).

2.2 Methods

2.2.1 Sample Preparation and Measurement Procedure

The samples comprised clay-free quartz sand from Leighton Buzzard with a mean grain diameter of 100 μm. We used polyvinyl chloride (PVC) material to make cylindrical jackets (outer diameter 0.069 m, inner diameter 0.063 m, length 0.5 m) and endcaps to hold the sand and enable sample emplacement within the water-filled pulse tube (Figure 2.1). The PVC's acoustic impedance is 2.9 x 10^6 kg m^{-2} s^{-1} with a velocity of 2600 m s^{-1} and density of 1120 kg m^{-3} (Selfridge, 1985), similar to that of water-saturated sand: 2.2 - 4.2 x 10^6 kg m^{-2} s^{-1} with a velocity of 1450 – 2200 m s^{-1} and density of 1460 – 1890 kg m^{-3} (Schumann et al., 2014). We sealed both ends of the jacket using 3-cm thick PVC endcaps with attached O-rings. These endcaps were free to move lengthways inside the jacket while maintaining a pressure seal, thus allowing the external surrounding water confining pressure to be applied evenly to the sand pack inside the pulse tube.

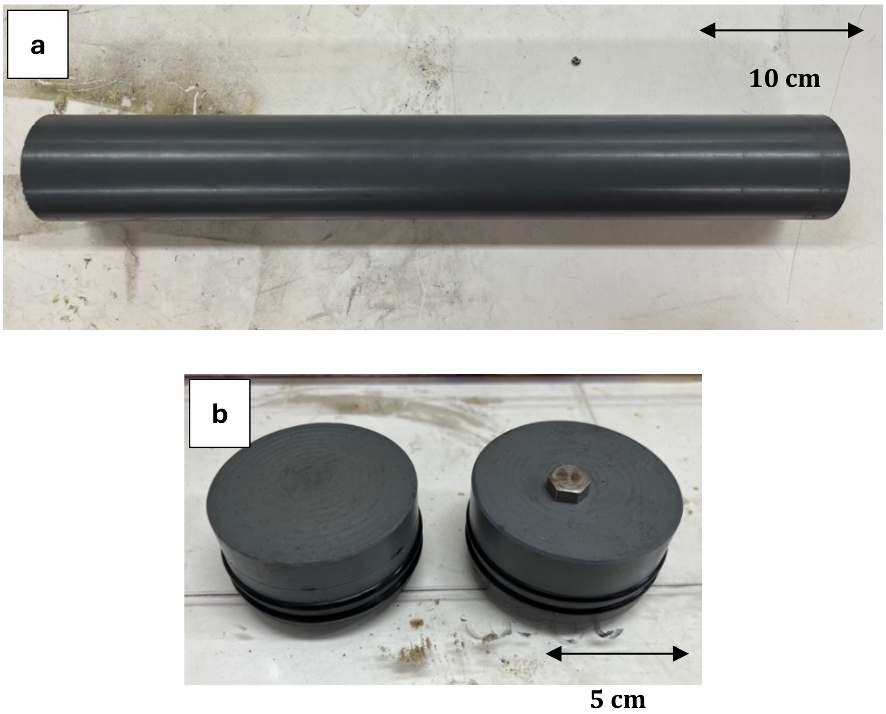

Figure 2.1 Components of jacket system used to hold the sand pack: a) 50 cm length PVC cylinder jacket, and b) top and bottom PVC endcaps with O-ring seals and location of pore fluid vent port (hexagonal nut on top endcap on the right).

To avoid inconsistencies during the preparation of sand packs that could cause significant density and porosity variations along the sample, we developed a repeatable sample preparation procedure. First, we oven-dried the sediment in a 60°C oven for 24 hours, then we tamped and evenly compacted the sand in successive layers into the cylindrical jacket, with the bottom endcap fitted beforehand, mimicking the “Proctor method” for compacting soils (ASTM, 2007). We provide further explanation in Appendix A. Finally, we fitted the top cap to prevent leaks and inserted the dry sample into the pulse tube for measurements under dry conditions.

We measured sample mass and dimensions before each experiment and calculated sample porosity ($\emptyset$) based on grain density and sample densities (ρ_d and ρ_b, respectively), as $\emptyset = 1 - \frac{\rho_b}{\rho_d}$. The porosity of the four samples (A-D) ranges from 38% to 44%, as shown in Table 2.1.

Table 2.1 Experimental parameters of sand pack samples.

Sample	Porosity (%)	Water Saturation (%)	Effective Pressure (MPa)
A	38 ± 0.25	0-100	10
B	40 ± 0.25		
C	44 ± 0.25		
D	42 ± 0.25		0, 1, 5, 10

We used de-ionised water in the water saturation experiments. Firstly, we connected a vacuum pump to the downstream pore fluid port to remove air from the sample. Upon constant vacuum pressure, we opened the upstream port to enable water imbibition from an external reservoir. Simultaneously, we recorded the mass change in the reservoir to estimate the pore water volume, and hence the water saturation (i.e., water to pore volume ratio). We repeated this process to achieve several water saturation steps, up to 30%. Above this point, the vacuum method was inefficient, so we switched to imbibition, allowing better control of the saturation process at a higher saturation range. Imbibition relies on the capillary pore fluid pressure at the interface between the gas and liquid to draw in more liquid until full saturation is reached (McPhee et al., 2015). For each saturation step, we placed the sample vertically in a water-filled acrylic container for 48 hours with the water level just above the top cap with two openings to provide water ingress. We tilted the container to around 45 degrees and rotated the sample every 3 to 4 hours to evenly distribute the water inside the pore space under gravity. Then, we weighed the sample again to measure the added mass of water and new saturation. We aimed to add 50 - 60 mL of water for each saturation step.

As an extra measure to understand the water distribution in the sample, we utilised an experimental microwave scanner (Figure 2.2; Section 2.2.2). If the water distribution was not uniform, we left the sample for another 24 hours for the water to distribute further before being placed in the pulse tube for measurements. We repeated the water addition procedure until the sample was fully saturated for each sample. Please refer to Figure 2.5a for the complete workflow of sample preparation and pulse tube data acquisition.

2.2.2 Water Saturation Monitoring using the Microwave Method

Understanding the water distribution inside the sand sample is essential to interpreting pulse tube results. Hence, we developed a novel microwave measurement technique to achieve that understanding. Microwave methods have been widely utilised to measure the water content of soil, e.g., from measurements of electrical permittivity or dielectric constant (e.g., Richards et al., 2014). They are non-destructive methods and thus can preserve the sample condition.

We used a free-space, contactless, microwave method to monitor the water distribution utilising a vector network analyser with two spot-focusing, curved antennae in the 1 – 6 GHz frequency range. We used a PicoVNA 106 Quad RX with a frequency resolution under 10 kHz. In general, a Vector Network Analyser (VNA) is used to test materials by applying a test signal to the materials, measuring the reflected and transmitted signals, and then comparing them to the test signal. In our method, we only used the transmission signals to determine the water saturation. The system was connected to a PC to run the measurements using PicoVNA2 software (Figure 2.2a & 2.2b).

This microwave method requires an accurate calibration between the measured dielectric permittivity and the actual water content of the soil (Ghodgaonkar et al., 1990), so we conducted an in-house calibration. We obtained reference values for the dielectric permittivity of saturated and dried samples in the 1-6 GHz frequency range using a shorted coaxial cell, consisting of a coaxial structure where the inner conductor is short-circuited to the outer conductor at one end to maximise the microwave reflection, which is critical for determining accurately the dielectric properties of the sample material. The cell, with an internal diameter of 16 mm and a centre conductor diameter of 7 mm, measures 55 mm in axial length (Figure 2.2c). The cell calibration was performed using a multiple-offset short method (Glasser, 1978).

Leighton Buzzard sand was saturated with RO water in a container outside the coaxial calibration cell, and then lightly compacted into the coaxial cell for measurement. Subsequently, the saturated sample underwent oven drying at 60°C for 48 hours and was re-measured to determine the dielectric constant for the dry sample. The cell and its contents were weighed in both saturated and dry states to calculate saturation and pore volume gravimetrically, assuming a grain density of 2650 kg m^{-3}. The pore volume of the sample was 42%, typical of uncompacted sand, with a water saturation of 88.75%. We calibrated the system by measuring the dielectric constant of dry and fully saturated sand, 2.5 and 22.6 F m^{-1}. Peak picking of wideband transmitted signal arrival time is used to calculate group velocity and hence dielectric constant. A comparison between the dielectric constant for dry sand and air obtained with the coaxial cell and antenna measurement system allowed us to deduce error bounds for the antenna system, conservatively set at a 10% error margin. We used these dielectric constant values to obtain the water saturation as described in Appendix B.

We monitored the water distribution in the PVC-jacketed sand samples by conducting a microwave reading at 5 cm intervals down the length of all samples after each water addition step. We defined the distribution from the standard deviation of the measured water saturations down the sample. If the standard deviation of saturation values determined in the sample was over 15%, we left the sample for another 24 hours to let the water evenly distribute and repeated the readings until the requirement was fulfilled. An example of the water distribution of the sample at several saturation levels is provided in Figure 2.3.

As the saturation increases, a more uniform water distribution becomes easier to achieve due to higher relative permeability, allowing the fluid to distribute more easily. At most saturations, the bottom half of the sample (0-25 cm) tends to saturate first due to the influence of gravity on the imbibition process. This phenomenon is particularly clear at intermediate saturations, as illustrated by the orange and yellow lines in Figure 2.3. This higher saturation extends from 5-10 cm (orange lines) and up to 25 cm (yellow lines), potentially affecting the acoustic properties at higher frequencies where the acoustic wavelength is shorter than the region of higher saturation. To assess this effect, we calculated the wavelength from the velocity and frequency (wavelength = velocity / frequency). We found that the lengths of the regions with higher saturation correspond to the wavelength for frequencies higher than 12 kHz (~11 cm wavelength; orange line) and 6 kHz (~21 cm wavelength; yellow line). Further discussion of the effect of variable water saturation at different frequencies is provided in Section 2.3.1.

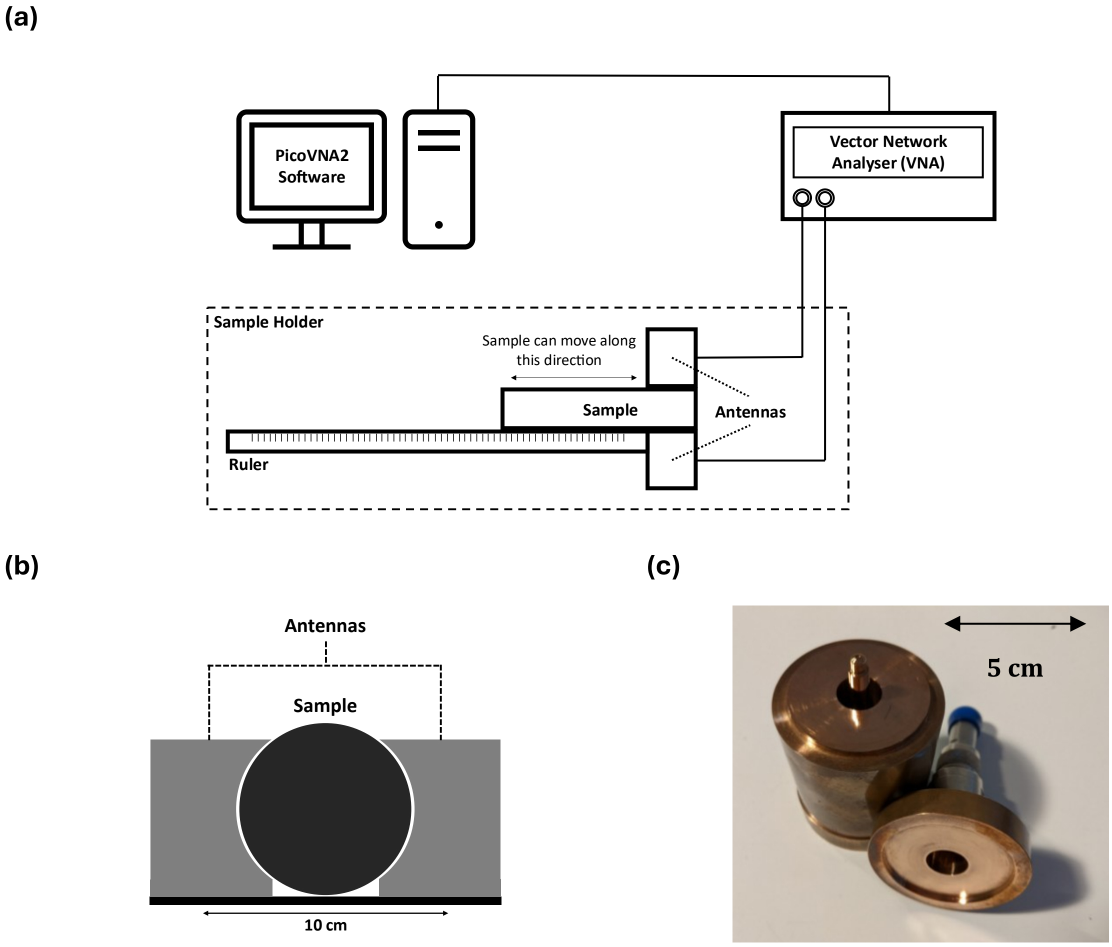

Figure 2.2 Block diagram of the experimental microwave setup: a) complete setup connecting to computer, and b) side-view of the microwave setup. c) Coaxial cell used for calibration measurements. Photographs of the microwave setup are provided in Appendix D.

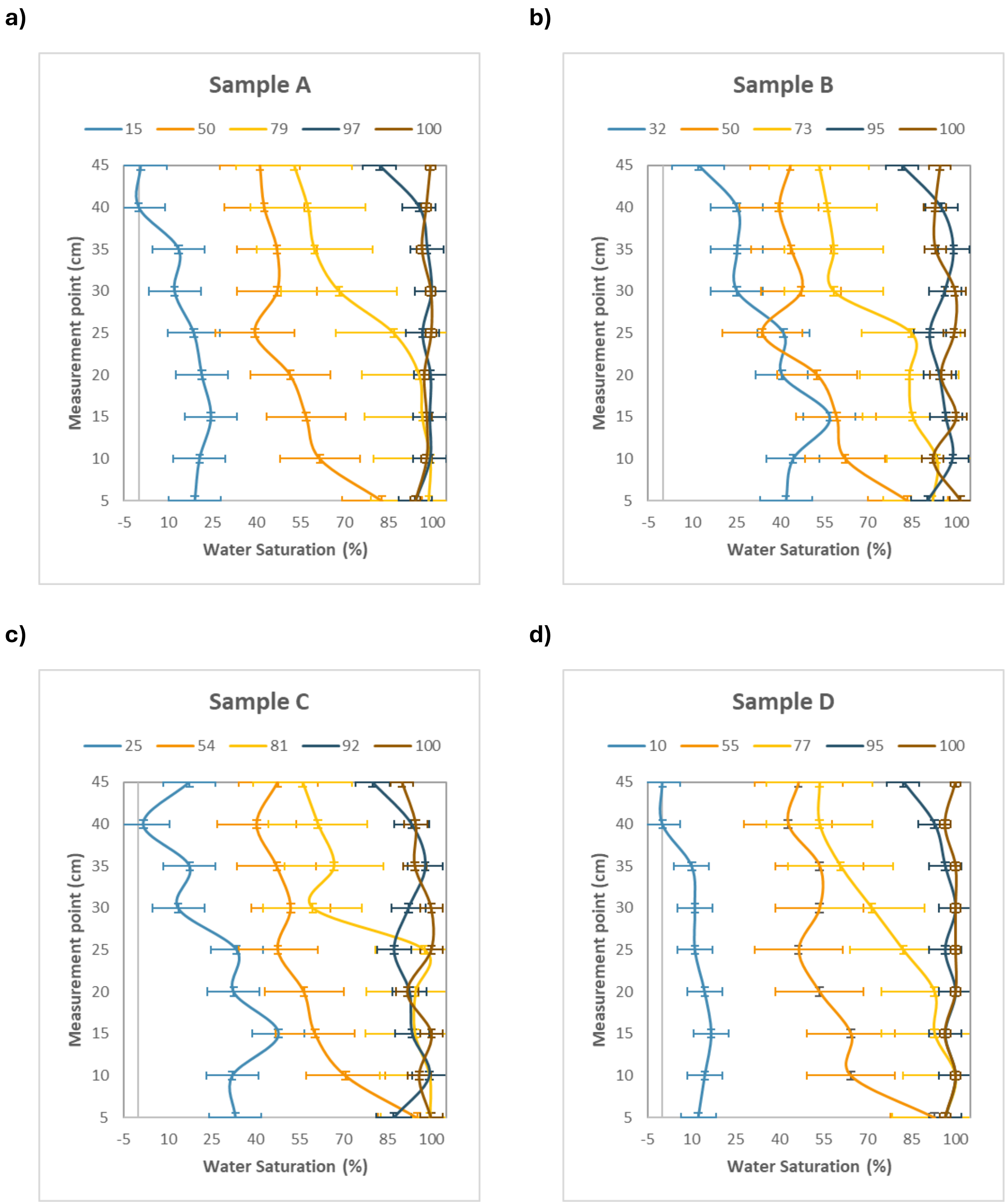

Figure 2.3 Water saturation distributions for progressively increasing % sample saturations (see legend) using the microwave transmission system for all samples with error bars at various saturations (a, b, c, d). The readings are every 5 cm along the sample. The top (50 cm) and bottom (0 cm) measurements are not calculated due to the influence of the PVC end caps on microwave readings. The standard deviation for each sample is 9.9, 10.9, 12, and 9.5% (Sample A to D). The differences between the microwave readings and the water saturation values calculated from sample weight are 6.0, 6.2, 6.6, and 4.8% (Sample A to D).

2.2.3 Acoustic Pulse Tube

2.2.3.1 Experimental Apparatus

The acoustic pulse tube utilises an acoustic waveguide concept consisting of a water-filled, thick-walled, stainless steel cylindrical tube. This setup is common for investigating acoustic properties of materials using the theory of axially propagating plane waves in a fluid-filled, rigid-walled waveguide. The pulse tube has a waveguide diameter of 0.07 m, and no higher modes will propagate at frequencies less than 26 kHz (McCann et al., 2014). McCann et al. (2014) also argued based on the theory of Dubbelday and Capps (1984) that plane waves propagate in the sediment-jacket system. The ratio of the tube radius to the sample radius should be smaller than 1.03 for a low-impedance material, such as our sediment-jacketed system. In our experiment, the ratio is 1.014, below this critical value.

We conducted the experiment using a 4.5 m long pulse tube at the National Oceanography Centre (NOC), Southampton (Figure 2.4). The tube has an inner diameter of 0.07 m with the capacity to hold a sample with a diameter of 0.069 m. The designed maximum confining pressure of the pulse tube vessel is 60 MPa, though for this study, we only tested at a confining pressure below 12.5 MPa. A water circulation jacket that wraps the vessel is connected to a temperature control unit, allowing an experimental temperature within the range of -5 to 55°C. We performed the measurements for all samples at a controlled temperature of 4°C and a confining pressure of 10 MPa with a pore fluid port connected to the sample vented to atmospheric pressure through the pulse tube top cap, thus giving an effective (differential) pressure of c. 10 MPa, analogous to subsurface depths of about 1 kilometre in the earth. We also performed measurements on sample D at increasing effective pressures (Table 2.1).

A bespoke acoustic piezo-electric transducer located at the bottom of the pulse tube insonified the jacketed sample in the 1-20 kHz range using variable-frequency chirp signals (i.e., within the working frequency of well logs). The pulse tube has two hydrophones installed through side-wall ports at a spacing of 1.2 m. The sample is suspended between the hydrophones, hanging from the top cap through the pore fluid line. We acquired the data using an Agilent 30 MHz Function/Arbitrary Wave generator producing a 6-second 20 kHz chirp synchronised to a LeCroy WaveSurfer 200 MHz Oscilloscope to display and record the output. We stacked the readings 16 times to improve the signal-to-noise ratio.

The confining and pore pressure are controlled by an ISCO EX-100D syringe pump system. To minimise undesired distortions of the signal associated with trapped air, first, we slowly lowered the jacketed sample into the tube using the pore fluid pipe, ensuring no air bubbles were trapped at the bottom of the sample. Then, we systematically increased the confining pressure and opened valves in the top cap of the pulse tube to release any air trapped inside the sample. Lastly, we closed the pulse tube with its top cap and slowly elevated (~0.01 MPa/s) the confining pressure to the target pressure. We stabilised the pulse tube system for ~2 hours to let the sand sample equilibrate. After completing the measurements, we released the confining pressure at the same rate as before to prevent the sample from experiencing any stress-release-induced damage before removing the sample. Additionally, we measured the water-filled pulse tube without any sample as a reference for the acoustic data processing and calibration.

2.2.3.2 Acoustic Data Processing

The measurements comprised time series of signal amplitude (voltage) from the sample at each saturation and from the water-filled pulse tube. The time-domain data were transformed into the frequency domain using a Fast Fourier Transform (FFT) to then deconvolve the raw signals with the chirp source signal, thus obtaining the impulse response. The stimulus is monochromatic (i.e., single frequency), thus the equations used in the processing are evaluated at each frequency coincident with those of the FFT of the measured gated time domain signal.

We applied time-domain gating to eliminate multiple reflections from the pulse tube endcaps, although any reflections that coincide temporally with the time-domain gate may degrade results. These are typically proximal reflections from geometrical changes in the pulse tube, for instance, the hydrophone ports along the pulse tube. Figures 2.5b and 2.6 show the data processing workflow and examples of the raw and processed time-domain data.

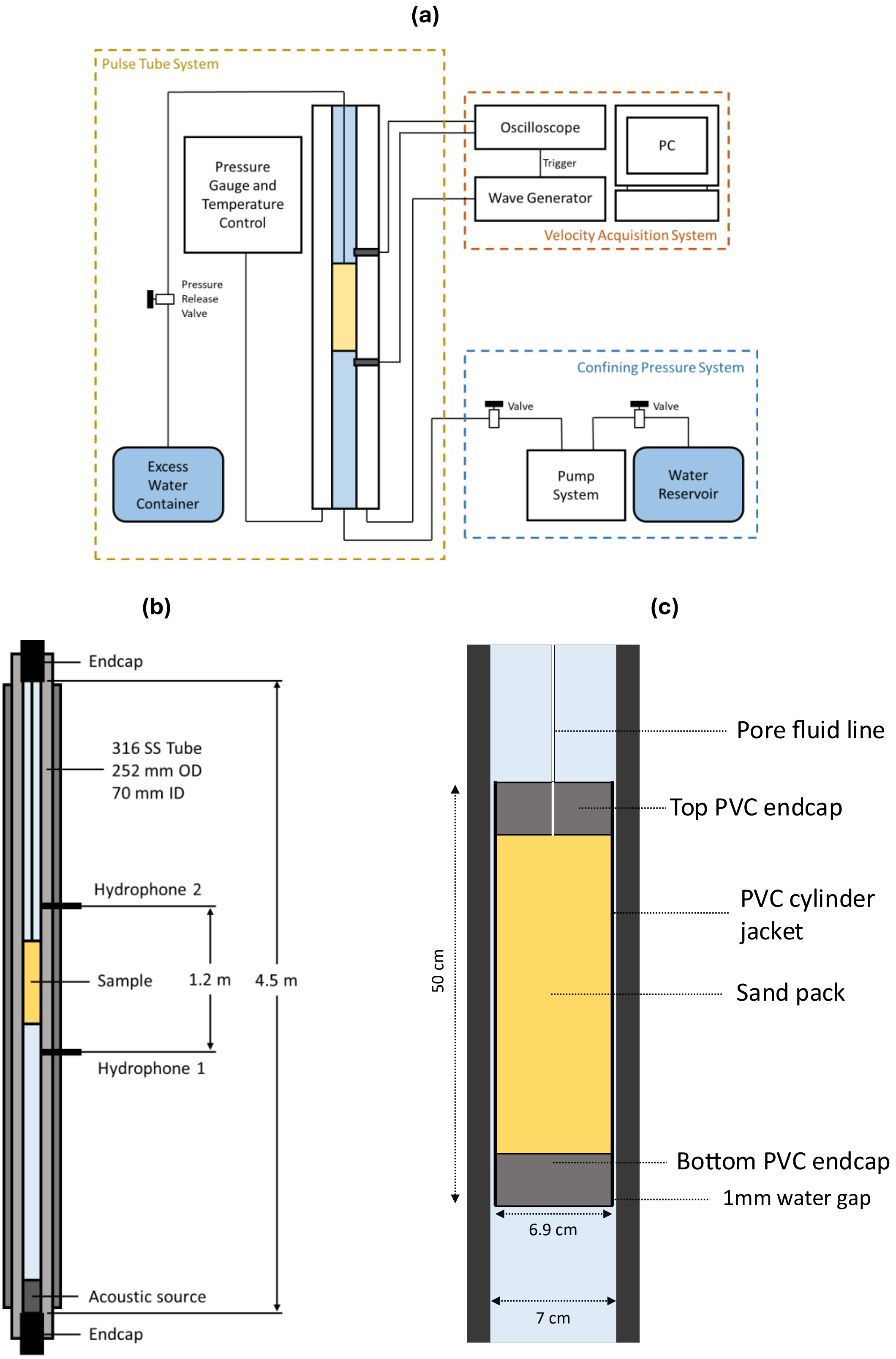

Figure 2.4 Diagram of the experimental pulse tube setup: a) Schematic diagram of pulse tube with pressure system and data acquisition setup, b) Dimensions of the pulse tube in detail, and c) Detail of the PVC-jacketed sample inside the pulse tube with pore fluid line (vented via high-pressure lead-throughs in the top cap of the pulse tube).

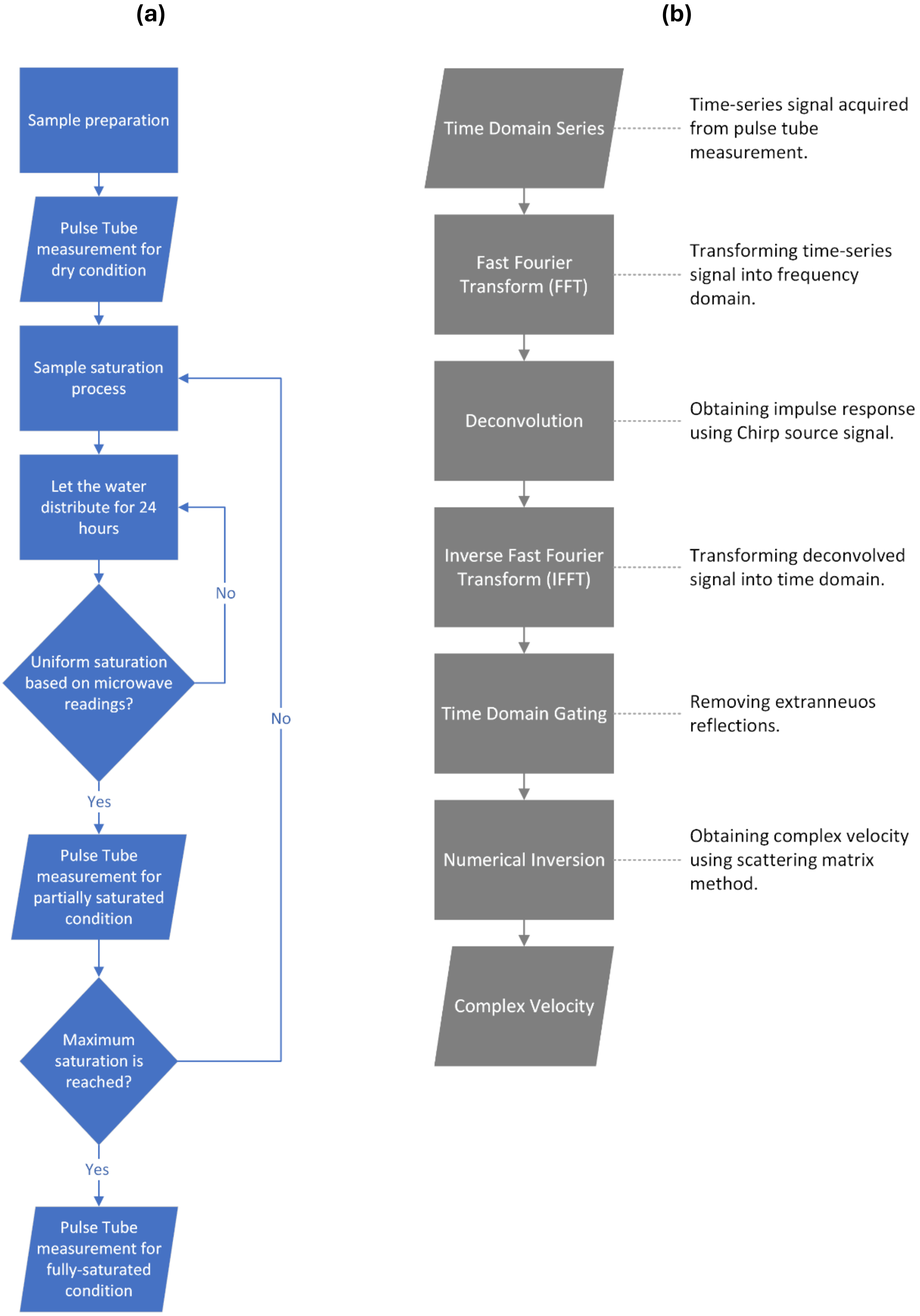

Figure 2.5 Workflow diagrams for: (a) sample preparation and pulse tube data acquisition, and (b) data processing steps (with description) to obtain the acoustic wave properties.

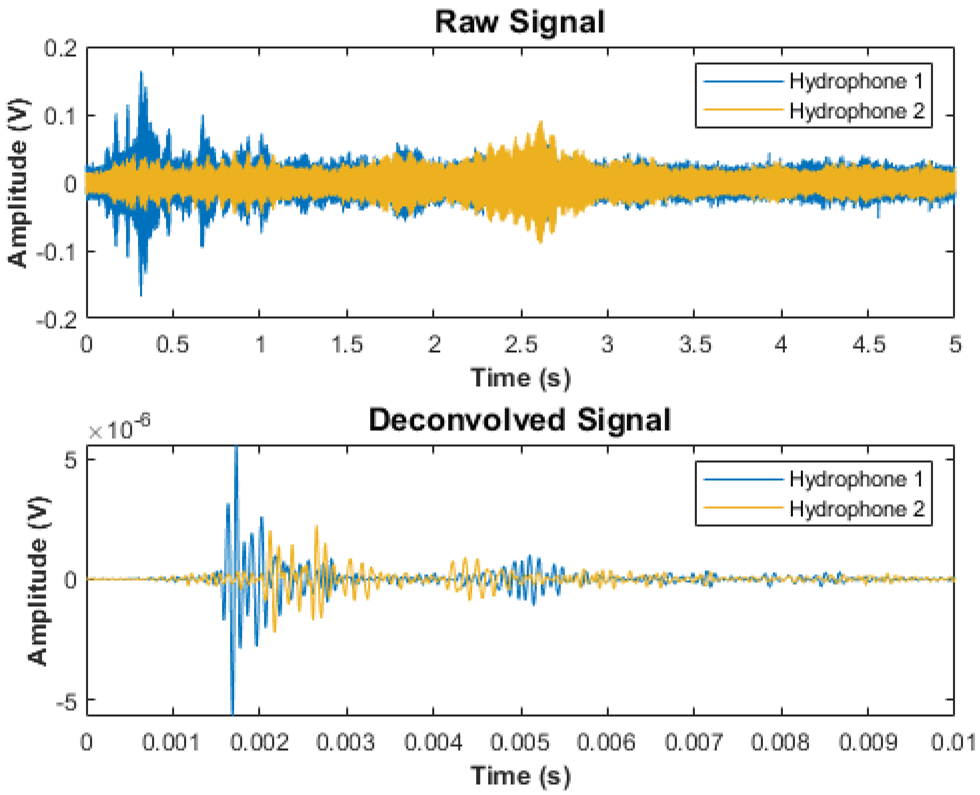

Figure 2.6 An example of raw and deconvolved time-domain acoustic data on a jacketed sand sample (Sample D) from pulse tube measurements. The positions of hydrophones 1 and 2 are shown in Figure 2.4. Further examples for different samples are provided in Appendix D.

We used nonlinear inversion to minimise the following objective function, which uses an initial value estimated using the time domain signal, thus deriving the complex velocity of the sample. We assumed a linear time-invariant system to ensure the input and output are scaled by the same value. We also assumed a plane wave propagation so that shear moduli of the sample (i.e., sand pack) and end caps may be neglected, resulting in a one-dimension transmission line system without any propagation at the sidewalls, multiple paths, or shear-wave coupling. The main objective function is provided in Equation 2.1, while the analytical descriptions are provided in Equations 2.2-2.13 and illustrated in Figure 2.7.

$$Objective\ function = |R_{1mod} - R_{1obs}| + |R_{2mod} - R_{2obs}| \tag{2.1}$$

$$R_{1mod} = \frac{m_1}{m_{1ref}} \tag{2.2}$$

$$R_{2mod} = \frac{m_2}{m_{2ref}} \tag{2.3}$$

$$R_{1obs} = \frac{M_1}{M_{1ref}} \tag{2.4}$$

$$R_{2obs} = \frac{M_2}{M_{2ref}} \tag{2.5}$$

With m_1 and m_2 as follows:

$$m_1 = Ph_1 \left[(1 + \gamma_{w1}^2 S_{11c1}) + \gamma_{w1}^2 \gamma_s^2 S_{21c1} S_{12c1} S_{11c2} \sum_{n=0}^{n=\infty} \gamma_s^{2n} \, S_{22c1}^n S_{11c2}^n \right] \tag{2.6}$$

$$m_2 = Ph_2 \left[(\gamma_{w1} \gamma_{w2} \gamma_s S_{21c1} S_{21c2}) \sum_{n=0}^{n=\infty} \gamma_s^{2n} \, S_{22c1}^n S_{11c2}^n \right] \tag{2.7}$$

By using the concept of infinite geometric series, we could simplify Equations 2.6-2.7 into Equations 2.8-2.9.

$$m_1 = Ph_1 \left[(1 + \gamma_{w1}^2 S_{11c1}) + \frac{\gamma_{w1}^2 \gamma_s^2 S_{21c1} S_{12c1} S_{11c2}}{1 - \gamma_s^2 S_{22c1} S_{11c2}} \right] \tag{2.8}$$

$$m_2 = Ph_2 \left[\frac{\gamma_{w1} \gamma_{w2} \gamma_s S_{21c1} S_{21c2}}{1 - \gamma_s^2 S_{22c1} S_{11c2}} \right] \tag{2.9}$$

And m_{1ref} and m_{2ref} as follows:

$$m_{1ref} = Ph_1 \tag{2.10}$$

$$m_{2ref} = Ph_2 \gamma_{w1} \gamma_{w2} \gamma_{w3} \tag{2.11}$$

P is the incident stimulus, *h_1* and *h_2* are the hydrophones transfer functions. γ is the transmission coefficient and *S* represents the scattering matrix. Small *m* stands for the inversion model while big *M* stands for the actual measurement with ref notation referring to water-filled tube condition (without sample).

Lastly, by taking the ratio R_{1mod} and R_{2mod}, we could remove *P*, *h_1* and *h_2*, as provided in Equations 2.12-2.13. The complete description of the scattering parameters is provided in Appendix C.

$$R_{1mod} = (1 + \gamma_{w1}^2 S_{11c1}) + \frac{\gamma_{w1}^2 \gamma_s^2 S_{21c1} S_{12c1} S_{11c2}}{1 - \gamma_s^2 S_{22c1} S_{11c2}} \tag{2.12}$$

$$R_{2mod} = \frac{1}{\gamma_{w3}} \frac{\gamma_s S_{21c1} S_{21c2}}{1 - \gamma_s^2 S_{22c1} S_{11c2}} \tag{2.13}$$

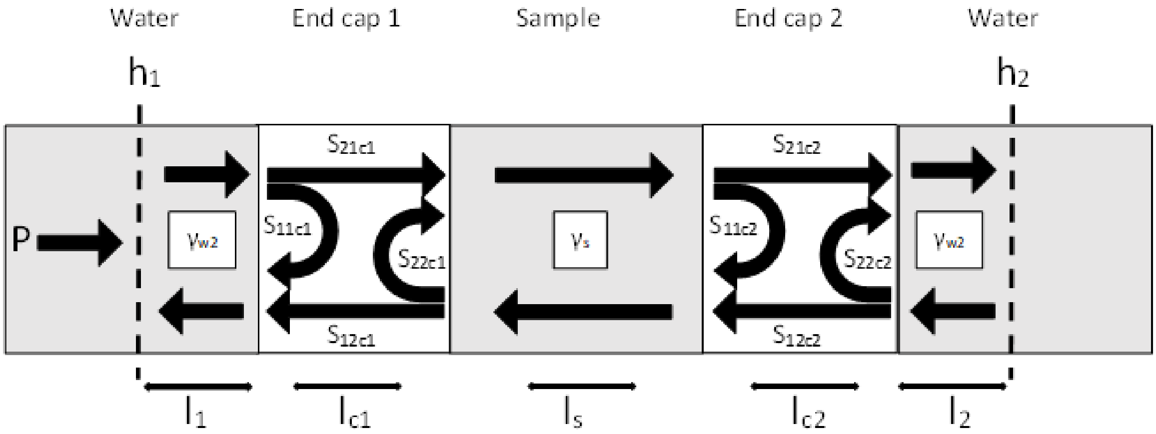

Figure 2.7 Description of scattering parameters used in the idealised transmission line (scattering matrix) model of the acoustic pulse tube that are included in the numerical inversion. Refer to Appendix C for the mathematical definition of symbols.

We calculated the attenuation Q^{-1} from the real and imaginary velocity output of the scattering matrix method using Equation 14 (Mavko et al., 2009).

$$Q^{-1} = \frac{1 - e^{-2\pi \frac{v_1}{v_2}}}{2\pi} \tag{2.14}$$

where v_1 and v_2 are the real and imaginary velocities, respectively.

2.2.3.3 Acoustic Pulse Tube Calibration

The calibration process involved several steps. First, we determined the velocity and attenuation errors by comparing the pulse tube and theoretical transmission coefficients (McCann et al., 2014). The theoretical model predicts the sample's response based on plane wave transmission through an infinite plate of finite thickness *L* and the acoustic impedance of the sample I_2 inside a fluid with acoustic impedance I_1 as defined in Equations 2.15-2.17. We determined the error bounds as the parameter values at which the sum of squares of the residuals between experimental and theoretical transmission coefficients reached 10% higher than the best-fit solution.

$$T = \frac{4 I_1 I_2}{(I_1 + I_2)^2 e^{i k_2 L} - (I_1 - I_2)^2 e^{-i k_2 L}} \tag{2.15}$$

$$k_2 = 2\pi \left(\frac{f}{V_2} - \frac{if}{2 Q V_2} \right) \tag{2.16}$$

$$I_2 = \rho_2 \frac{2\pi f}{k_2} \tag{2.17}$$

where *T* is the transmission coefficient of compressional waves, k_2 is the wavenumber of the sample, V_2 is the velocity of the sample, and *f* is frequency.

Firstly, we used a material with well-known properties, i.e., a nylon rod, to calibrate our method. Then, we used the same method on the PVC jacketed sand packs. The comparisons are in good agreement based on R^2 (or the coefficient of determination) values of 0.95 and 0.89, showing that 95% and 89% of the variance of the experimental data was accounted for by the theoretical model for nylon and PVC-jacketed samples, respectively (Table 2.2 and Figure 2.8).

Table 2.2 Errors of pulse tube measurements on two samples calculated from the comparison of pulse tube transmission coefficient with theoretical models. R^2 is the coefficient of determination for the transmission loss (Figure 2.8).

Sample	**Velocity (m s^{-1})**	**Attenuation (Q^{-1})**	**R^2**
Nylon	± 1 %	± 3.9 %	0.95
PVC with sand	± 2.4 %	± 5.8 %	0.89

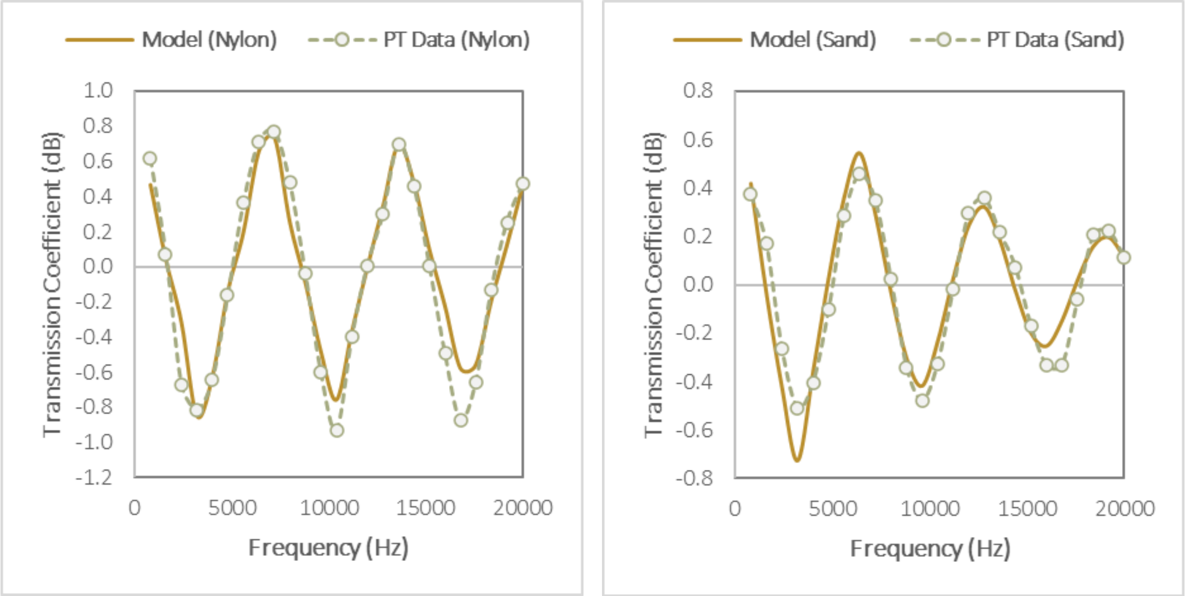

Figure 2.8 Experimental and theoretical transmission loss coefficient spectra (in dB) for nylon (left) and jacketed sand (right) at an effective pressure of 10 MPa and temperature of 4°C. Dashed lines with points represent pulse tube data and solid lines represent the theoretical result from the transmission model.

The error is slightly higher in the PVC-jacketed sample compared to the nylon rod, perhaps because of the multi-layered system of the jacketed sample, i.e., end caps and PVC tube with the sample inside. This layering could affect the propagating wave by introducing complexity in the scattering matrix calculation, compared to the solid nylon rod without any jacket and end caps.

Next, we compared our data to those reported by Selfridge (1985) for nylon at ultrasonic frequencies. We converted Selfridge's ultrasonic data to sonic frequency, i.e., from 0.5 MHz to 10 kHz, using Equation 2.18 from Kolsky (1964).

$$Vp(f_1) = Vp(f_2)\left[1 + \frac{1}{\pi Q}\ln\left(\frac{f_1}{f_2}\right)\right], \tag{2.18}$$

where $Vp(f_1)$, $Vp(f_2)$ are the nylon compressional wave velocities at frequencies f_1 and f_2 respectively, and Q is the quality factor measured by Selfridge, which is assumed constant in the frequency range from f_1 to f_2.

Table 2.3 Acoustic properties of nylon from pulse tube measurements and from the ultrasonic measurements of Selfridge (1985).

Pulse tube observation		**Ultrasonic P-wave observation**	
Velocity (m s^{-1})	**Q^{-1}**	**Velocity (m s^{-1})**	**Q^{-1}**
2546 ± 25	0.008 ± 0.0005	2600	0.006
Velocity comparison			
Pulse tube (m s^{-1})		**Corrected ultrasonic measurement (m s^{-1})**	
2546 ± 25		2561.1	

As shown in Table 2.3, the measured and the predicted velocities of nylon are 2546 and 2561 m s^{-1}, indicating a good agreement with a difference of around 1%. Lastly, we also explored the effect of the jacket system on acoustic property measurement by comparing the acoustic velocity of water inside the pulse tube and the PVC jacket. We used an empty pulse tube to calculate the water velocity from the propagation time from hydrophone 1 to hydrophone 2. Then, we compared the measured water velocity inside and outside the jacketed sample. The results showed a 3% reduction in velocity due to the jacket system (i.e., 1374 ± 21 and 1419 ± 22 ms^{-1} for water velocity in the PVC jacket and empty pulse tube, respectively). Meanwhile, attenuation shows < 0.001 (or < 7%) difference. For additional comparison, we calculated the acoustic speed in water at 4°C and 10 MPa pressure using equations from Belogol'skii et al. (1999). The theoretical estimate (i.e., 1432 m s^{-1}) is ~1% higher than the acoustic velocity measured in the pulse tube. As a result, we have adopted a calibration factor of 1.03 for measurements using the

PVC jacket and estimate that our relative experimental uncertainty is ± 2.4% and ± 5.8% for velocity and attenuation, respectively.

2.2.4 Theoretical Modelling

The elastic wave properties of water-saturated sediments and rocks can vary significantly with frequency (Williams et al., 2002). Velocity dispersion, i.e., the change in velocity with frequency, is related to attenuation through the principle of causality (e.g., Kolsky, 1964). The velocity and attenuation of elastic waves can be measured over a wide frequency range, including seismic surveys, sonic well-logging, and ultrasonic laboratory experiments. Therefore, it is essential to understand the entire frequency dependence to enable comparison of measurements from various techniques.

Across various theoretical explanations of elastic wave propagation in porous media, particularly unconsolidated sediment, Biot's theory (Biot, 1956a, 1956b) is commonly used (e.g., Cadoret et al., 1998; Chotiros, 1995; Williams et al., 2002). This theory was developed to predict the frequency-dependent velocity and attenuation due to the fluid viscosity and the inertial interaction between pore fluid and sediment matrix. Biot's theory is relevant in unconsolidated sediments (or sand packs) and high-porosity rocks in the high-frequency limit, as opposed to the low-frequency limit (i.e., below 100 Hz) where Gassmann's theory suffices (Gassmann, 1951). Therefore, we compared Biot's model with our laboratory results, in particular the Biot-Stoll model (Stoll and Bryan, 1970) that is incorporated in the hydrate-bearing effective sediment (HBES) model of Marín-Moreno et al. (2017). We used this particular model because it includes additional complex fluid flow mechanisms within the Biot porous medium concept, namely squirt flow and gas bubble interaction.

The HBES model is generally applicable to porous sediments with gas/liquid saturating fluids and does not require hydrate to be present. We used this model (with a hydrate saturation of zero) to predict how gas bubbles affect velocity and attenuation. The model is able to calculate P- and S-wave velocity and attenuation. The model was developed from the Hydrate Effective Grain (HEG) model of Best et al. (2013), which predicts velocity and attenuation dispersion based on the clay-squirt flow mechanism in marine sediment (Leurer, 1997; Leurer and Brown, 2008). This mechanism is incorporated in the Biot-Stoll fluid flow model to predict the frequency-dependent acoustic properties in sediment and rocks as a function of pore content. The HBES model extended the HEG model by adding the effects of gas. The model included gas bubble resonance effects, based on the work of Smeulders and Van Dongen (1997), which makes this model suitable for our study.

To address how pore fluid distribution affected our experimental data, we extended the modelled velocity and attenuation by varying the effective fluid bulk modulus calculated using the Voigt (Voigt, 1889), Brie (Brie et al., 1995) and Reuss (Reuss, 1929) techniques. This extension allowed us to vary the patchiness. In addition, we explored the sensitivity of the results to permeability and gas bubble radius variations. Firstly, we varied the patchiness parameter in the model to match our experimental data using the input parameters in Table 2.4. Then, we used the best-fit model to explore the permeability and gas bubble radius effects by varying permeability from 0.01 to 10 Darcys and the gas bubble radius from 0.0001 – 10 mm (see Table 2.5).

The fixed parameters used in the HBES model were selected based on a combination of direct measurements, literature values, and calibration to experimental data. Porosity (0.41) and grain diameter (10^{-4} m) were measured directly from the sand samples. The critical porosity was set to 0.38, based on Best et al. (2013), representing the threshold above which pore space begins to dominate the mechanical behaviour of the sediment. Although the measured porosity slightly exceeds this value, the model remains valid in this range and fits the experimental data well, though it may slightly underestimate frame stiffness in loosely packed conditions. Grain-scale elastic properties—bulk modulus (36 GPa), shear modulus (45 GPa), and density (2650 kg/m^3)—were adopted from Simmons (1965), a widely accepted reference for quartz-rich sands. The coordination number of 9, from Murphy (1982), assumes a random close-packed structure, providing a reasonable estimate of frame stiffness for moderately compacted sands. Tortuosity was set to 3 (Berryman, 1981), reflecting moderate pore network complexity typical of well-sorted sands.

Table 2.4 Fixed input parameters used in the HBES model.

Parameters		**Value**	**Reference**
	Effective pressure	10^6 Pa	Experimental setup
	Temperature	4°C	
Sand grain properties			
	Bulk modulus	36 x 10^9 Pa	Simmons (1965)
	Shear modulus	45 x 10^9 Pa	
	Density	2650 kgm^{-3}	
	Diameter	10^{-4} m	Measured
	Coordination number	9	Murphy (1982)
Sand sediment properties			
	Porosity	0.41	Measured
	Critical porosity	0.38	Best et al. (2013)
	Tortuosity	3	Berryman (1981)

Table 2.5 Gas bubble radius size used in the HBES model.

Gas bubble type	Gas bubble radius (m)
Nanobubble	10^{-7}
Microbubble	10^{-6}, 10^{-5}
Fine bubble	10^{-4}
Medium bubble	10^{-3}
Coarse bubble	10^{-2}

We calculated the difference between the experimental and modelled values to find the best fit using an objective function (Equation 2.19) at each step of the modelling process. We minimised the objective function to find the best-fit water distribution (patchiness), permeability, and gas bubble radius parameters. When we varied one parameter, we held the other two parameters constant until we found the best fit. For instance, we varied the patchiness parameter first by holding the permeability and gas bubble radius constant.

$$Objective\ function = \frac{|V_{experimental} - V_{modelled}|}{V_{experimental}} + \frac{|Q^{-1}_{experimental} - Q^{-1}_{modelled}|}{Q^{-1}_{experimental}} \quad (2.19)$$

2.3 Results and Discussion

2.3.1 Variation of Velocity and Attenuation

P-wave velocity (V_p) increases with frequency across all samples (A-D), with Sample D showing the least variation (Figure 2.9). Attenuation patterns are more complex: Sample A shows a significant decrease with frequency, Samples B and C exhibit more complex behaviour, and Sample D shows little variation, particularly above 4.5 kHz. There are significant variations with saturation level, particularly in V_p. Fully saturated sand packs consistently show the highest V_p, as expected, while attenuation displays more variation with frequency. Results for each sample at all saturation levels (S_w) are in Appendix D.

We observe V_p peaks in Sample A (12.5-17.5 kHz at S_w = 100%) and Sample B (10-12.5 kHz at S_w = 50%). The variation in Sample A can be attributed to patchiness, as observed by others at full saturation (Dvorkin and Nur, 1998; Tserkovnyak and Johnson, 2002). Sample A also displays increase attenuation in the same frequency range, supporting the interpretation because patchiness may introduce more attenuation (Cadoret et al., 1998). The variation in Sample B can also be attributed to patchy saturation (Figure 2.3). Higher saturations extend 5-10 cm from the bottom of the sample, which could affect V_p in the frequency range of the peak, where the wavelength is approximately 11 cm. Variations in both velocity and attenuation towards both ends of the frequency spectrum resulting from processing artefacts due to the time-gating process (Section 2.2.3.2), particularly impacting the lower frequencies, as seen in the case of Sample C below 2.5 kHz.

Velocity and attenuation both increase with saturation at all pressure levels (Figure 2.10), after a small initial reduction in velocity from S_w = 0% to about S_w = 50%. However, the rate of increase varies, particularly for V_p at S_w = 75-100%, with higher pressures showing larger increases. This trend is due to the compaction of air bubbles within pores near to full saturation, significantly increasing velocity (Dvorkin and Nur, 1998). Attenuation increases similarly with saturation at all pressures. At lower saturation levels (e.g., S_w < 50%), attenuation may be affected by local flow mechanisms; however, at higher saturation, attenuation can be associated with patchy fluid distribution. Additionally, at sufficiently high frequencies (i.e., sonic frequencies), unrelaxed pores can increase attenuation (Cadoret et al., 1998; El-Husseiny et al., 2019; Mavko and Nolen-Hoeksema, 1994).

P-wave velocity increases and attenuation decreases with increasing effective pressure (Figure 2.11). Using relative value (compared to the 0 MPa condition), we highlighted the impact of effective pressure on both acoustic parameters. Sample compaction progressively increases from 0 to 10 MPa due to micro-crack closure and grain movement to be a closer pack, reflecting a non-linear V_p trend at S_w = 100% (He et al., 2021; Horikawa et al., 2021; Prasad, 2002). The compaction effect is masked by the fluid distribution effect at intermediate S_w (e.g., S_w = 50% in Figure 2.11) because the bulk modulus of the samples is dominated by the effective fluid modulus. The dry sample exhibits the greatest attenuation reduction with increasing pressure, particularly from 1 to 5.5 MPa, due to initial cracks closure and reduced gas pocket volumes (e.g., Li et al., 2014; Zhang et al., 2022). In addition, only grain contact squirt flow is present in the dry sample, whereas partial and fully saturated samples also experience other attenuation mechanisms, such as mesoscopic fluid flow, Biot flow, and gas bubble scattering.

In the dry sample, gas predominates in the pores, with residual water present only at grain contacts, in microcracks, and adsorbed on grain surfaces. Fully saturated samples have minimal residual gas saturation. However, in 50% water-saturated samples, two co-existing fluids in the pores lead to gas bubble formation in the water. Gas bubble resonance effects might affect attenuation in 50% water-saturated samples, giving a different trend than dry and fully saturated samples. Pore-scale fluid flow mechanisms might also affect the behaviour at intermediate saturations (Winkler and Nur, 1979; Zhan et al., 2022).

a)

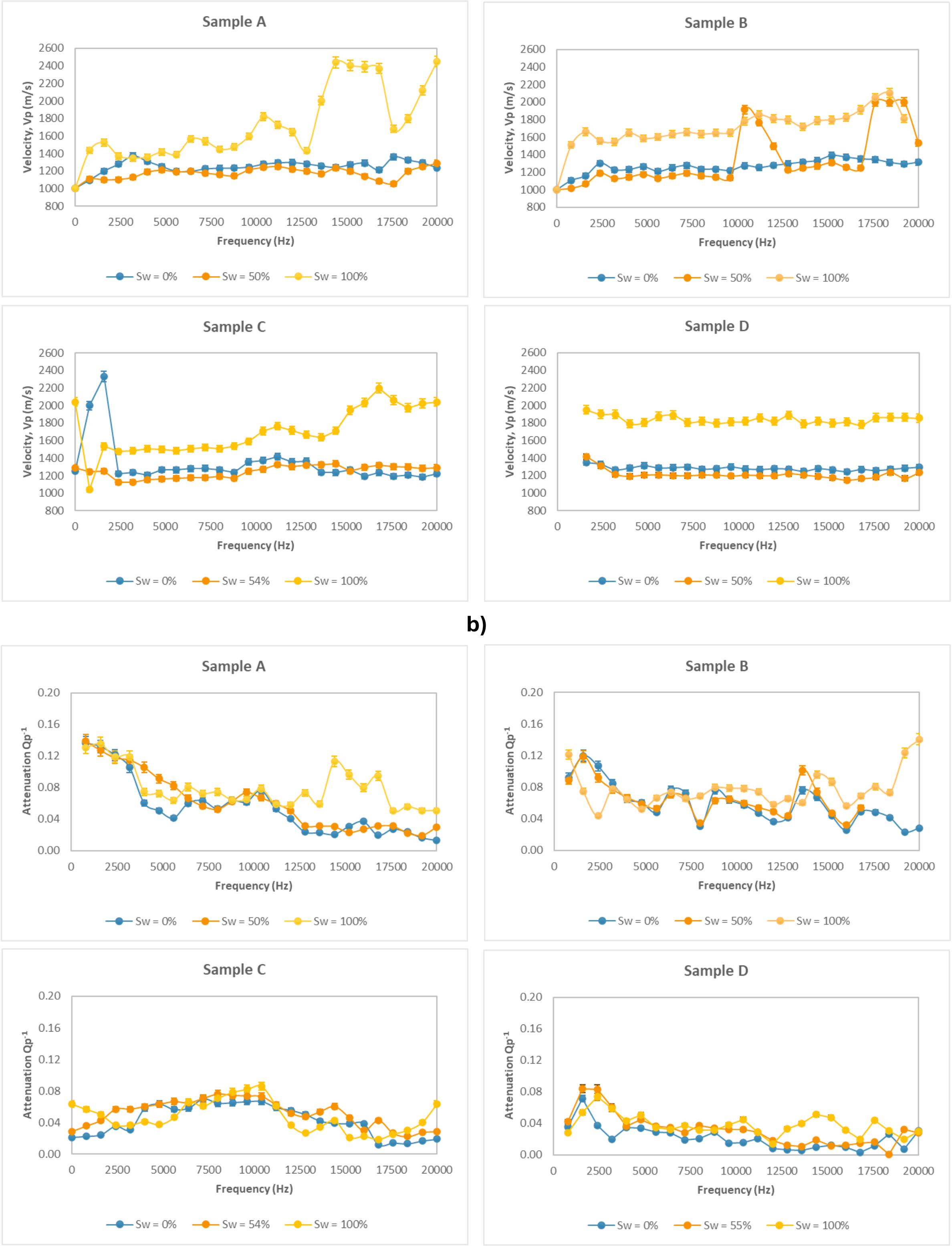

Figure 2.9 Measured variations in P-wave velocity (V_p) and attenuation (Q_p^{-1}) across the acoustic pulse tube frequency range of 1-20 kHz at three saturation levels: dry (0%), partially saturated (~50-55%), and fully saturated (100%). The effective pressure was 10 MPa and the temperature was 4°C.

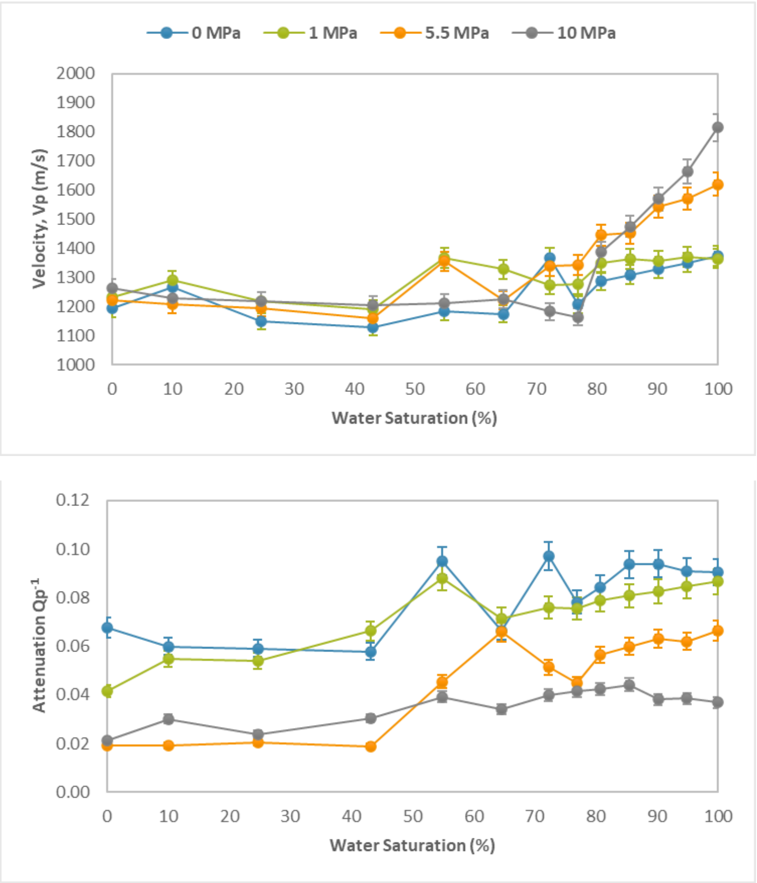

Figure 2.10 Variation in measured P-wave velocity and attenuation with water saturation at 10 kHz at effective pressures between 0 – 10 MPa indicated in the legend in Sample D at a temperature of 4°C.

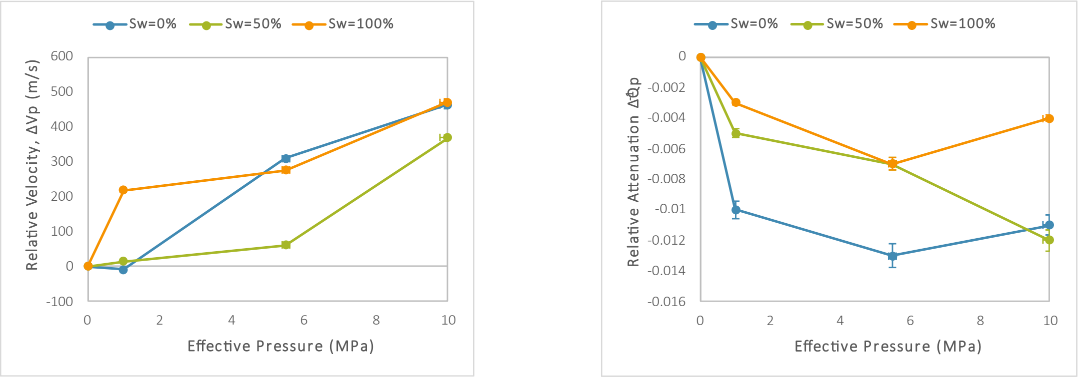

(a)

(b)

Figure 2.11 Variations in relative velocity and attenuation with effective pressure at 10 kHz in Sample D at three water saturations of 0%, 50%, and 100%. The velocity and attenuation at 0 MPa were used as the reference values. The temperature was 4°C.

We present data from four samples to explore the water saturation effect on acoustic parameters (Figure 2.12). V_p consistently decreases with saturation up to S_w ~75%, then increases up to full saturation, with the main differences occurring at $S_w > 70\%$. V_p increases at S_w ~80% for Samples A and D and at S_w ~70% for Samples B and C. However, attenuation varies significantly between samples, with Sample D exhibiting a lower average value.

The V_p variation with saturation resembles that previously observed for homogeneous saturations, characterised by a decrease followed by a sharp increase (e.g., Dvorkin and Nur, 1998). For homogeneous saturations, the compressibility of the water-gas mixture is similar to that of air across most saturation levels. In this range, velocity decreases due to changes in density. However, as full saturation is approached (around S_w ~75% in this study), the compressibility of the mixture approaches that of water, leading to a sharp increase in bulk modulus, stiffness, and, consequently, velocity. Attenuation behaviour is influenced by fluid flow mechanism. At lower saturations (S_w = 0–75%), microscopic fluid flow controls attenuation (Alkhimenkov et al., 2020; Cadoret et al., 1998), while at the highest saturations, macroscopic mechanisms such as the Biot effect dominate. At full saturation, most samples exhibit a decrease in attenuation, attributed to minimal to no fluid movement between pores, reducing energy loss (Li et al., 2020; Oh et al., 2011).

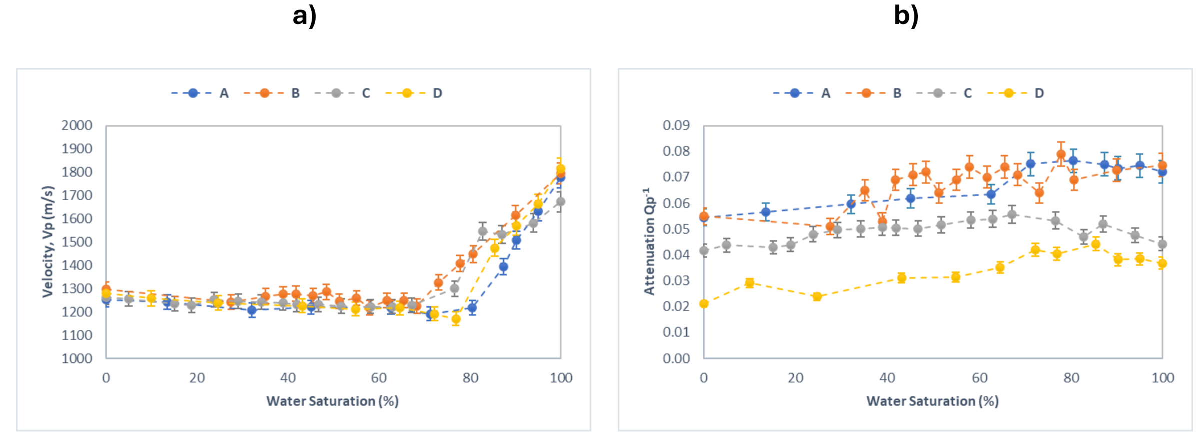

Figure 2.12 Variations in (a) P-wave velocity and (b) attenuation with water saturation at 10 kHz, for the four samples. The measurements were conducted at an effective pressure of 10 MPa and a temperature of 4°C.

2.3.2 Comparison with rock physics modelling

2.3.2.1 Water distribution

The Voigt and Reuss models serve as the upper (patchy saturation) and lower (uniform saturation) bounds for fluid bulk modulus, with Brie's model (Brie et al., 1995) considered a more realistic estimate for patchy saturation (Mavko et al., 2009). We adjusted Brie's calibration constant (*e*), representing saturation patchiness (Lee and Collett, 2006; Papageorgiou et al., 2016), to fit our experimental data. As *e* increases, the model approaches uniform saturation, closely resembling the Reuss approximation at *e* > 30. In contrast, as *e* decreases, a patchier distribution is represented, closely approaching the Voigt approximation at *e* = 1.

Our velocity data are better explained by uniform than by patchy gas saturation, with a good fit to the Brie model for *e* ranging from 5 to 10 (Figure 2.13). From dry to ~75% saturation, the velocity data align well with the *e* = 10 prediction, while at higher saturations (75% - 100%), the best fit lies between *e* = 10 and *e* = 20, suggesting a fluid distribution change as saturation increases. Our attenuation data are better explained by the Brie model with a higher *e* value (*e* > 20), particularly below 70% saturation. At higher saturations, the data are scattered, which complicates the interpretation. Nevertheless, the data from Sample C are closely aligned with the Brie model result for *e* = 10-20. Full plots for all samples can be found in Appendix D.

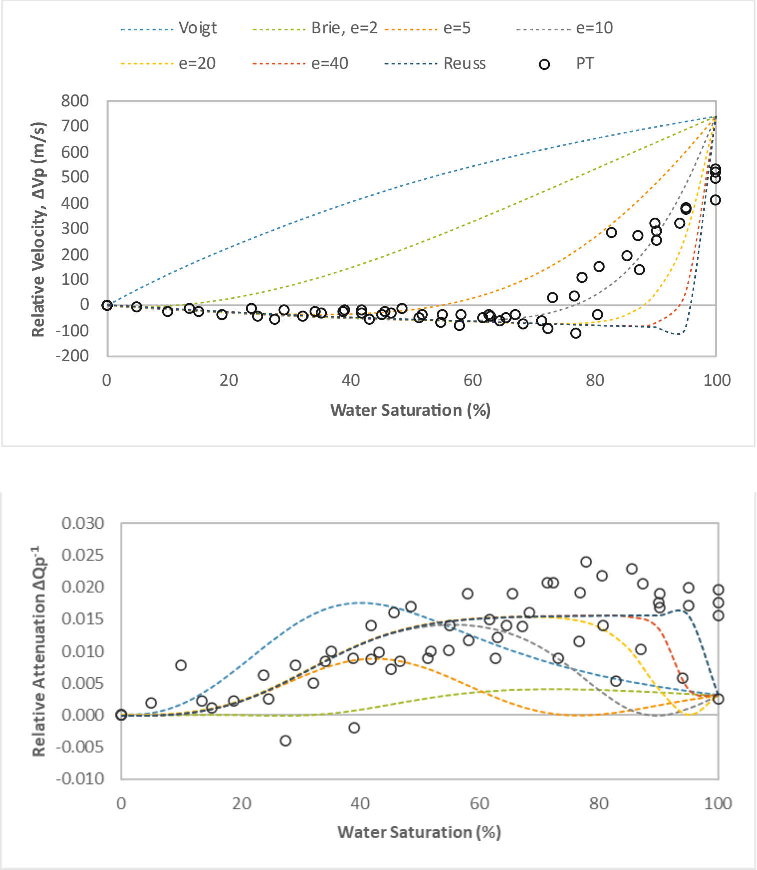

Figure 2.13 Variations of relative velocity and attenuation with saturation for all samples at 10 kHz, referenced to the measured parameters at Sw=0%, compared to HBES model predictions (with the extension of various fluid bulk modulus approximations) under the permeability of 5 Darcys and gas bubble radius of 0.1 mm. The measurements and predictions were conducted under an effective pressure of 10 MPa and a temperature of 4°C.

2.3.2.2 Permeability

We explored the effect of permeability changes by varying the model's permeability from 0.01 to 10 Darcy. These simulations are done to match our unconsolidated sand sample data at a centre frequency of 10 kHz, under an effective pressure of 10 MPa, and using Brie's coefficient of e = 10 (Figure 2.14a). Velocities are higher and vary less with saturation at higher permeabilities, but the differences are too small to be resolved by our data (Figure 2.14b).

In contrast, attenuation varies significantly with permeability across all saturations (Figure 2.14a). Attenuation increases with permeability, particularly below 2.5 Darcy, with higher permeabilities shifting the attenuation peak from higher to lower saturations, deviating from our data above 85% saturation. These changes are most noticeable at permeabilities above 5 Darcys. Based on objective function minimisation, our data best align with the model results for a permeability around 5 Darcy which falls within the measured range of 1 – 8.4 Darcys for a clean quartz sand pack (Wei et al., 2022; West, 1995).

2.3.2.3 Gas bubble radius

Before exploring the gas bubble radius effect on the acoustic properties, we calculated the pore throat size (a) for our samples to determine the applicable radius range. Stoll (1974) found that pore throat size values range from one-sixth to one-seventh of the mean grain diameter (d), while Hovem and Ingram (1979) calculated it as follows: $a = \emptyset d/[3(1-\emptyset)]$, where $\emptyset$ represents the porosity. Employing both approaches, the result is 0.014 – 0.017 mm.

We used six gas bubble sizes to represent various bubble types (Table 2.5). However, the results are indistinguishable below 1 mm radius, with significant differences only for the 10 mm radius (Figure 2.15), which is much larger than the calculated pore throat size. The model predictions with a larger gas bubble radius also deviate from our pulse tube data. Through objective function minimisation, we determined that the best-fitting gas bubble radius is around 0.001 – 0.01 mm, with a 0.1 mm radius also fitting well. Therefore, our data are consistent with bubble sizes no larger than 0.1 mm, explaining the lack of discernible gas bubble resonance effects on attenuation around our simulated gas bubble sizes, especially at 10 kHz (Gong et al., 2010).

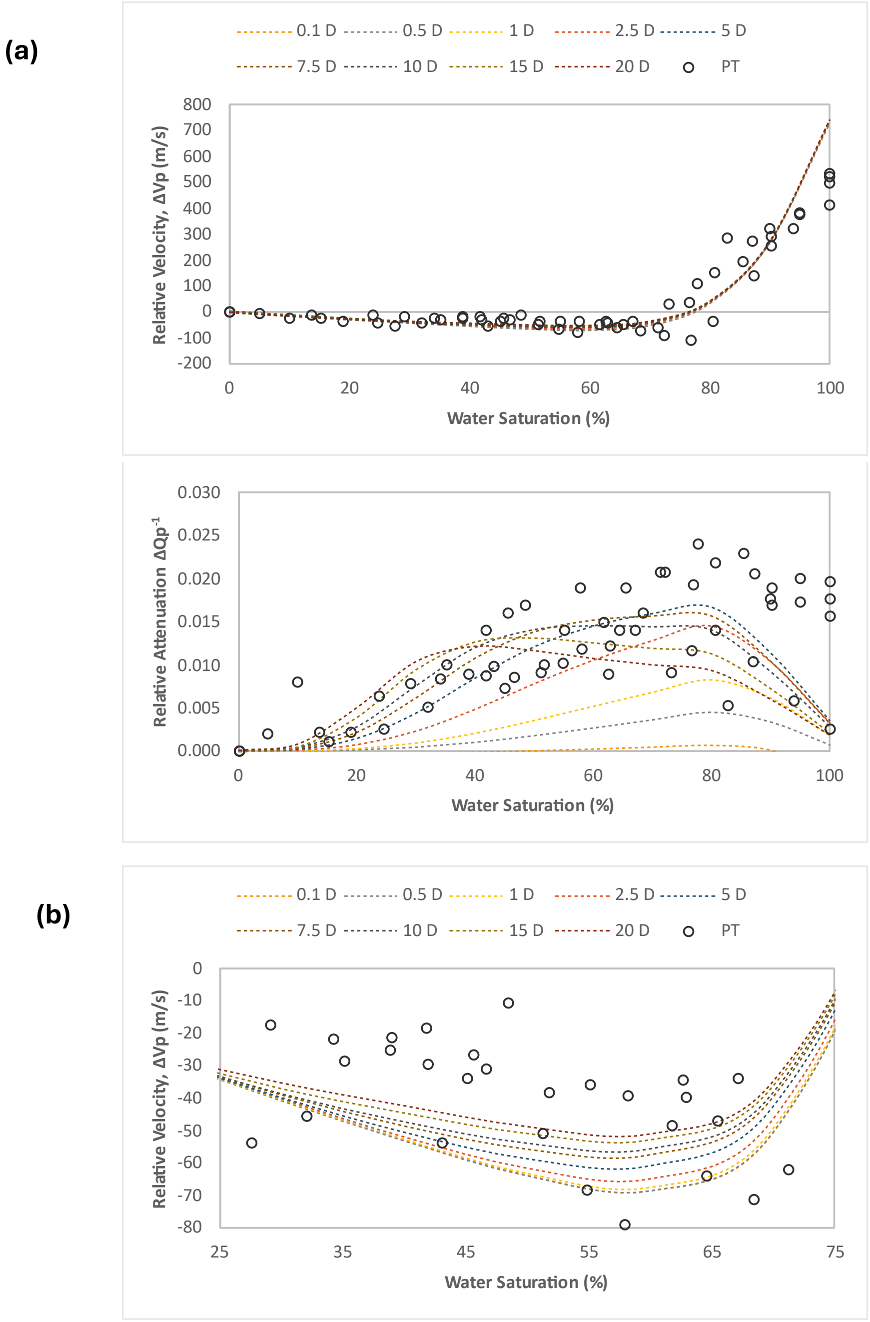

Figure 2.14 a) Variations of relative velocity and attenuation with saturation for all samples at 10 kHz, referenced to the measured parameters at S_w=0%, compared to the HBES model at various permeabilities. b) The same models and data plotted with an expanded vertical scale. The measurements and simulations were conducted at an effective pressure of 10 MPa and a temperature of 4°C.

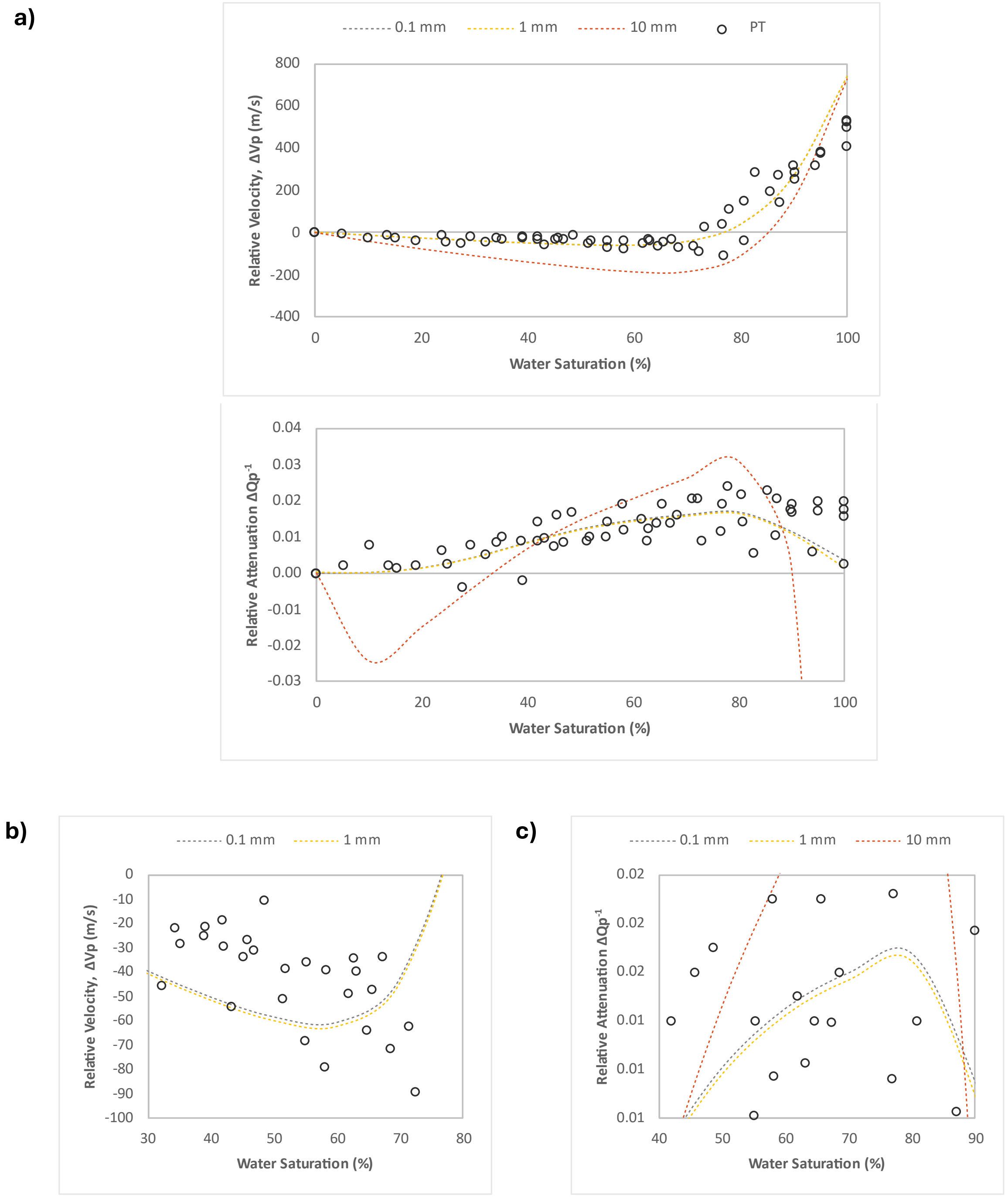

Figure 2.15 a) Variations of relative velocity and attenuation with saturation for all samples at 10 kHz, referenced to the measured parameters at S_w=0%, compared to the HBES model at various gas bubble radii. b) and c) The same models and data plotted with an expanded vertical scale. The 0.0001 – 0.01 mm results are not shown because they are indistinguishable from the 0.1 mm results. The measurements and simulations were conducted at an effective pressure of 10 MPa and a temperature of 4°C.

2.4 Limitation of study and future direction

We selected a sample size that ensured that the sample length (i.e., 0.5 m) extended at least half of the wavelength at the lowest frequency, which for a velocity of 1200-1300 m s^{-1} is 0.75-0.81 m at 1.6 kHz so that the measurements captured well the sample characteristics. We conducted these lab experiments to imitate natural conditions as closely as possible and to inform field measurements and the development of robust inversion techniques. However, our experiments focus on a single sand pack, whereas field conditions may involve variations in grain size distribution and lithology. In addition, field conditions may include different types of gases with various saturations as part of the pore fluid. Also, we observe variations, particularly in attenuation, that can be attributed to changes in the distribution of pore fluid within the sample. These limitations highlight potential directions for future research.

2.5 Conclusion

This study presents novel laboratory experimental measurements of P-wave velocity and attenuation Q_p^{-1} on four quartz sand packs in the frequency range 1 – 20 kHz. We conducted the experiments at mostly an effective pressure of 10 MPa and temperature 4°C as a function of air/water saturation using a novel, bespoke acoustic pulse tube. The method provides consistent measurements for PVC-jacketed samples accurate to ± 2.4 % and ± 5.8 % for velocity and attenuation, respectively. We investigated the acoustic properties under varying frequencies, effective pressures, and water saturations. Velocity consistently increases with frequencies, while attenuation patterns vary across samples.

Velocity increases with effective pressure and attenuation decreases, at all water saturations. Dry and fully saturated samples show more pronounced velocity increases than partially saturated ones, while the dry samples show the largest attenuation decreases. Velocities decrease with increasing saturation until around 75% saturation and then increase towards full saturation. In contrast, attenuation initially increases with saturation and later slightly decreases towards full saturation.

We also looked at the effects of patchy saturation, permeability, and gas bubble resonance by comparing predictions from theoretical models to our experimental results. Our samples match better with more uniform saturation models, as represented by $5 < e < 20$ in Brie et al.'s (1995) equation. Our data are best matched using a permeability of around 5 Darcys, which is a reasonable value for unconsolidated fine sand. Our data are matched by a gas bubble radius no higher than 0.1 mm. Table 6 summarises the key findings from the experiments and modelling.

These results offer valuable insights into understanding elastic wave measurements in a broad frequency spectrum. The pulse tube used in this study is a laboratory measurement system working in the sonic frequency range, which can fill the gap in laboratory scale measurements in the sonic frequency range.

Table 2.6 Summary of the experiments and modelling key findings on acoustic properties to tested parameters.

Parameters	**Velocity**	**Attenuation Q^{-1}**
Experimental data analysis		
Frequency	Generally increased, particularly at full water saturation.	Complex relationship but mainly decreased to slight variation.
Effective pressure	Increased, particularly in dry and full water saturation.	Decreased with significant reduction from 1 to 5.5 MPa*.
Water saturation	Decreased until around 75% saturation, then increased until full saturation.	Increased until around 75% saturation, then slightly decreased until full saturation**.
Modelling comparisons		
Water distribution	The experimental data matched well with the tested model using Brie approximation (e=10).	
Permeability	The experimental data matched well with the tested model using a permeability value of 5 Darcys.	
Gas bubble radius	The experimental data matched well with the tested model using gas bubble radius values from 0.0001 - 0.1 mm.	

* Based on tested effective pressure steps, i.e., 0, 1, 5.5, and 10 MPa.

** One sample showed little to no variation from 75% to full saturation.

Chapter 3 Laboratory measurement of sonic (1-20 kHz) P-wave velocity and attenuation during melting of ice-bearing sand

This chapter forms a published paper: Sutiyoso, H.S., Sahoo, S. K., North, L.J., Falcon-Suarez, I.H., Minshull, T.A., & Best, A I. (2024). Laboratory measurement of sonic (1-20 kHz) P-wave velocity and attenuation during melting of ice-bearing sand. Journal of Geophysical Research: Solid Earth, 130. DOI: https://doi.org/10.1029/ 2024JB030465

My contributions to the development of equipment and processing tools include: calibrating the pulse tube using a nylon rod and sediment samples (i.e., sand packs), improving data acquisition (e.g., testing different sound sources to get better results), refining the processing workflow (e.g., debugging and optimising the processing code), and calibrating the microwave equipment (e.g., testing it with various samples).

Abstract

We measured the acoustic properties of ice-bearing sand packs in the laboratory using an acoustic pulse tube within the frequency range of 1-20 kHz, similar to sonic well-logs. We analysed how wave velocity and attenuation (the inverse of quality factor) change with ice saturation during melting. We found strong frequency-dependent correlations for both acoustic parameters with ice saturation. For any frequency within the studied range, velocity decreases and attenuation increases as the ice melts. We used rock physics models with three-phase approaches to assess our experimental results. The comparison highlights the influence of ice formation location, sediment frame permeability, and gas content on both velocity and attenuation. Our results pave the way for monitoring ice saturation from sonic measurements as ice saturation has contrasting effects on velocity and attenuation and the effects vary with frequency. Overall, this research contributes to a better understanding of the acoustic response of ice-bearing sediments and provides valuable insights for various applications, including permafrost monitoring and gas hydrate dissociation studies.

3.1 Introduction

Understanding the elastic properties of ice-bearing sediments is crucial for various geophysical applications, such as understanding climate-induced permafrost degradation (Tourei et al., 2024) and its interaction with gas hydrate deposits (e.g., Guerin and Goldberg, 2002; Ruppel and Kessler, 2017; Lin et al., 2018). As permafrost thaws, it can release significant amounts of methane, a potent greenhouse gas primarily stored as gas hydrates (Kvenvolden, 1993), into the atmosphere. This process would exacerbate global warming (e.g. Kvenvolden, 1993; Schuur et al., 2015), and impact structure stability (e.g., Hjort et al., 2022). Thus, relating elastic wave properties to ice or hydrate content is key for monitoring and managing these environmental challenges.

Elastic wave properties, such as velocity and attenuation, can be measured across a broad frequency spectrum depending on the spatial scale required, that is, from seismic surveys and sonic well-logging to ultrasonic laboratory experiments. Frequency controls the degree of velocity dispersion (e.g., Ahmed et al., 2022; Oda et al., 1990; O'Hara, 1985), which is related to attenuation through the causality principle (Kolsky, 1964). Therefore, understanding frequency dependence is essential for comparing acoustic data across different spatial scales.

Compressional wave velocity and attenuation are both sensitive to pore fluid content (e.g., Barriere et al., 2012; Berryman, 1981; Knight and Nolen-Hoeksema, 1990; Rubino and Holliger, 2012). The relationship between elastic wave properties and pore fluid content is often complex in nature, potentially requiring multiple measurement techniques and costly in-situ observations to achieve a thorough understanding. To address this challenge, controlled laboratory experiments offer a viable alternative. However, these studies are commonly performed at ultrasonic frequencies (150 kHz to 1 MHz), where properties may differ from those measured in the field using seismic (~100 Hz) and sonic logging (~10-25 kHz) methods. Likewise, laboratory studies on ice-bearing rocks have focused on linking geophysical and geomechanical properties at ultrasonic frequencies (e.g. Chang et al., 2021; Matsushima et al., 2008), which are also relevant to gas hydrate-bearing sediments due to the similarity in compressional wave characteristics between hydrate and ice (Best et al., 2013; Helgerud et al., 2009). However, to bridge the gap between ultrasonic laboratory experiments and field seismic surveys of permafrost (e.g. Bustamante et al., 2023; James et al., 2021; Wagner et al., 2019), further studies at sonic frequencies are needed.

Theoretical rock physics models have been influential in studying how pore content affects elastic wave properties, particularly in ice/cryosphere research (e.g., Leclaire et al., 1994; Li and Matsushima, 2024). These models can be either two-phase: sediment and pore fluid, or three-phase: sediment, ice (or hydrate), and pore fluid (e.g., Leclaire et al., 1994; Marín-Moreno et al., 2017). Current models accounting for velocity dispersion are primarily based on Biot's theory (Biot, 1962; Biot, 1956b) and are applied to unconsolidated sediments and porous rocks. A notable example is Leclaire et al. (1994)'s model, which extends Biot's theory to predict elastic wave parameters in frozen media. This model incorporates ice parameters into Biot's theory, assuming no direct contact between the sediment matrix and ice that is separated by unfrozen water, except in the limited case of a fully frozen medium. Rock physics models developed for gas hydrate studies can also explain ice-bearing sediment cases due to the similarity in gas hydrate and ice properties (Gabitto and Tsouris, 2010; Helgerud et al., 2009; Marín-Moreno et al., 2017; Pearson et al., 1983).

In this study, we present and assess a novel experimental dataset of compressional (P-) wave velocity and attenuation of sand packs as a function of ice saturation across the 1-20 kHz frequency range. Our results show that P-wave velocity and its attenuation depend on both saturation and frequency. Using LeClaire's model (Leclaire et al., 1994) and the hydrate-bearing effective sediment (HBES) approach (Marín-Moreno et al., 2017), we analyse our findings to better understand the mechanisms driving our experimental observations and provide new insights for improving ice content estimations from field measurements.

3.2 Methods

3.2.1 Sample preparation and description

We used clay-free Leighton Buzzard sand with a mean grain diameter of 100 μm in a 0.5 m long polyvinyl chloride (PVC) cylindrical pipe with an outer diameter of 0.069 m (Figure 3.1a). The acoustic impedance of the PVC material is 2.9 x 10^6 kg m^{-2} s^{-1}, derived from a velocity of 2,600 m s^{-1} and a density of 1,120 kg m^{-3} (Selfridge, 1985). Meanwhile, the acoustic impedance of the sand pack is 2.2 – 6.8 x 10^6 kg m^{-2} s^{-1}, derived from velocities of 1,450 – 3,600 ms^{-1} and densities of 1,460 – 1,890 kgm^{-3}, covering both water-saturated (lower impedance) and ice-bearing states (higher impedance) (Kang et al., 2021; Schumann et al., 2014). We sealed both ends of the pipe with PVC endcaps to ensure hydrostatic pressure was uniformly applied across the sand pack during the experiment.

We prepared the samples by pouring the sand into the PVC pipe (fitted with the bottom endcap) and tamping it in successive layers for even compaction. To prevent impedance contrasts between layers, we evenly scratched the top part of each layer. Once the sand was fully compacted in the pipe, we saturated the sample by flowing a pre-calculated amount of de-ionised water into the sand pack within the pipe, increasing the sample saturation by ~10%, stepwise. Before proceeding with the freezing, we measured the acoustic properties of the water-saturated sample in the pulse tube to provide baseline measurements of the acoustic properties at water-saturated or fully-melted conditions.

For this experiment, we prepared two samples (denoted as Samples 1 and 2), with their properties shown in Table 3.1. We estimated the empirical porosity (ϕ) by wet-dry mass balance, and then using the bulk dry density (ρ_b) estimated for each sample and the average density of the solid grain (ρ_s), we contrasted the empirical values with the theoretical porosity (ϕ_T) resulting from $\phi_T = 1 - \rho_b/\rho_s$, which assumes full saturation. These estimates resulted in ice saturation discrepancies of ~6% and ~7% for Samples 1 and 2, respectively, which are the experimental uncertainties associated with the saturation process due to non-connected porosity (e.g., Falcon-Suarez et al., 2024).

Table 3.1 Sand pack sample properties.

ID	Porosity	Sample bulk density (g/cm^3)
Sample 1	0.408 ± 0.01	1.611 ± 0.033
Sample 2	0.413 ± 0.01	1.613 ± 0.033

For the ice-bearing sand preparation, we froze the samples in a freezer at a controlled temperature of -10°C for 48 hours to ensure maximum conversion of pore fluid to ice. Releasing gas bubbles during sand saturation helped minimise bubble formation during ice formation, ensuring more consistent laboratory measurements (McCutchan and Johnson, 2022). We used a non-destructive microwave measurement technique to image ice distribution in Sample 2 as it thawed gradually at a controlled room temperature of 19°C (Figure 3.1b). This technique captured changes in dielectric permittivity associated with ice melting, allowing us to estimate ice content with an approximate error of 5.9% (Sutiyoso et al., 2024; Chapter 2). Measurements were taken at 2 cm intervals along the sample length and repeated at multiple time points during the thawing process. These data enabled us to visualise the spatial and temporal progression of ice melting, supporting the interpretation of velocity and attenuation changes related to varying ice content.

3.2.2 Pulse tube measurement

We conducted the experiment using a 4.5-metre-long acoustic pulse tube at the National Oceanography Centre (NOC) Southampton (Figure 3.1c & 3.1d). The tube uses an acoustic waveguide concept, consisting of a water-filled, thick-walled, stainless steel cylindrical tube as the waveguide to axially propagate plane waves, as also argued by McCann et al. (2014) based on the theory of Dubbelday and Capps (1984). An acoustic piezo-electric transducer located at the bottom insonifies the sample within the 1-20 kHz range using variable frequency chirp signals (Appendix E). We performed the measurements at a confining pressure (P_c) of 2.5 MPa, and atmospheric pressure (P_p) (i.e., effective pressure, $P_{eff} = P_c - P_p \sim 2.5$ MPa) and a controlled temperature of 19°C, for all samples. This experimental setup is analogous to the melting of permafrost active layer and to gas hydrate dissociation (Dobiński, 2020; Voronov et al., 2016).

The measurements consisted of a time series of signal amplitude in voltage from the sample throughout the ice saturation. We used a Fast Fourier Transform method to obtain the impulse response by deconvolving the raw signals with the source. Then, we applied time-domain gating to eliminate multiple reflections from the pulse tube endcaps. Lastly, we used an inversion model incorporating the scattering matrix method to determine complex velocity and attenuation. Examples of measured and deconvolved signals are shown in Figure 3.2, and details of the processing workflow are provided in Chapter 2 as well as North and Best (2015) and Sutiyoso et al. (2024).

The pulse tube geometry constrains wave propagation to a quasi-plane (lowest order) wave mode below the cut-off frequency for higher-order modes (Wilson et al., 2003), in this case, approximately 20 kHz. This quasi-plane mode allows the pulse tube to directly measure plane or body wave propagation within the samples. This has been confirmed with finite element modeling (FEM) and measurements of materials with known elastic properties, for example, Nylon 66 (see Appendix E).

The calibration process involves comparing pulse tube measurements with theoretical transmission coefficients to determine velocity and attenuation errors. The error bounds are defined as the parameter values where the sum of squares of the residuals between experimental and theoretical coefficients reached 10% higher than the best-fit solution (McCann et al., 2014). Our experimental uncertainties are ±2.4% and ±5.8% for velocity and attenuation, respectively. Experimental results agreed with ultrasonic measurements when projected into the sonic range using a standard linear solid model, which accounted for attenuation and velocity dispersion. This analysis confirmed that similar compressional waves propagated through the material in both methods. Additionally, the velocity of the water-filled PVC jacket was compared with both the water-filled pulse tube and the theoretical model by Belogol'skii et al. (1999), also showing strong agreement. This consistency indicates that the same compressional waves travel through the pulse tube. Both calibration procedures are explained in detail by North and Best (2015) and Sutiyoso et al. (2024).

Anomalous results are observed both in calibration measurements and FEM below frequencies corresponding to a ratio of propagating wavelength to sample length of ½. FEM shows this effect only for rigid solids (with a significant shear modulus). We interpret this as the result of the pistonlike movement of the sample within the pulse tube, resulting in significant viscous losses in the thin water layer between the sample and the pulse tube walls. The FEM results are provided in the Appendix E.

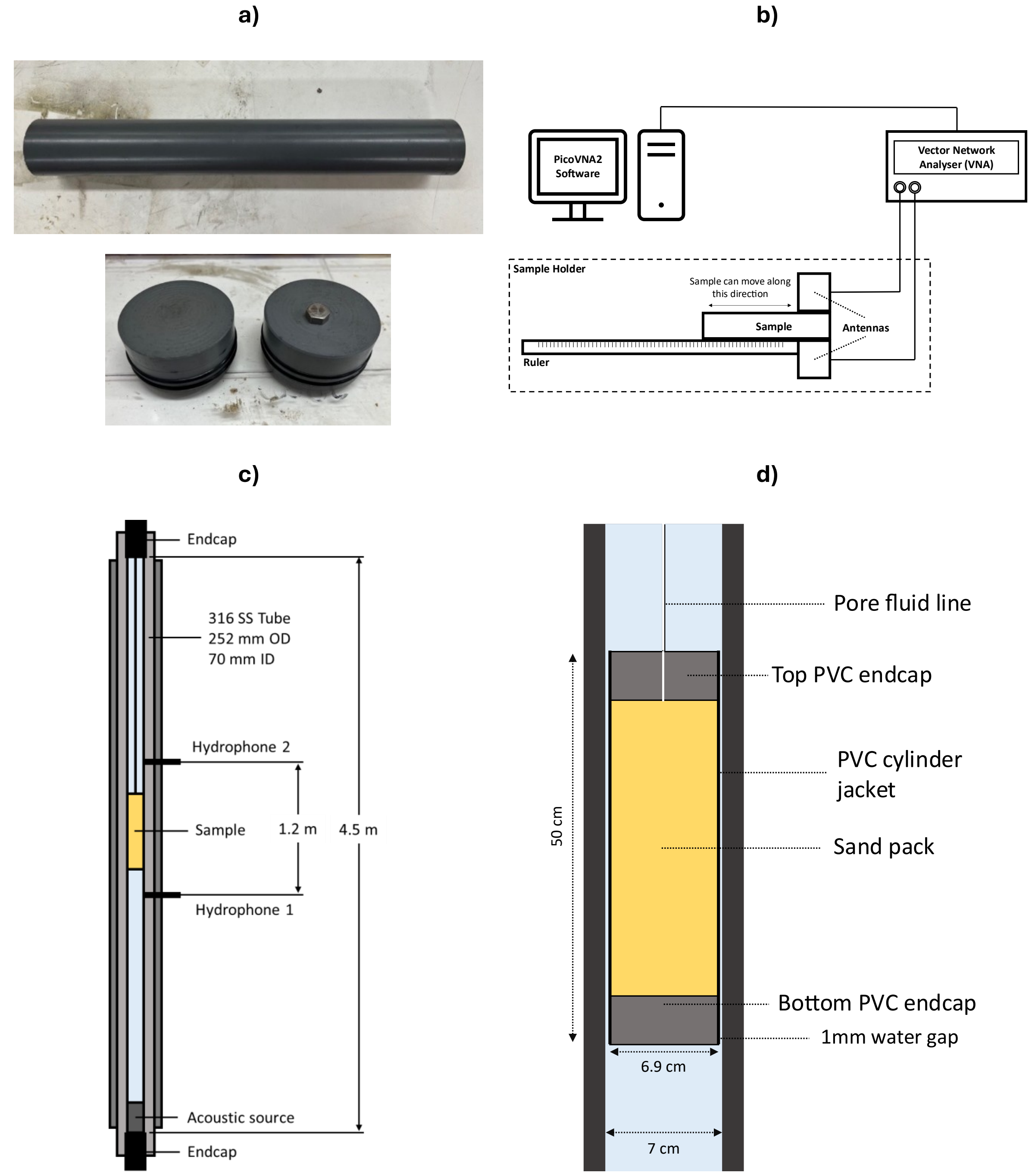

Figure 3.1 Experimental setup: a) 50 cm length PVC cylinder jacket and PVC endcaps; b) Schematic diagram of pulse tube with pressure system and data acquisition setup, b) Block diagram of the experimental microwave setup, c) Dimensions of the pulse tube and its components, and d) Detail of the PVC-jacketed sample inside the pulse tube with pore fluid line (vented via high-pressure lead-throughs in the top cap of the pulse tube).

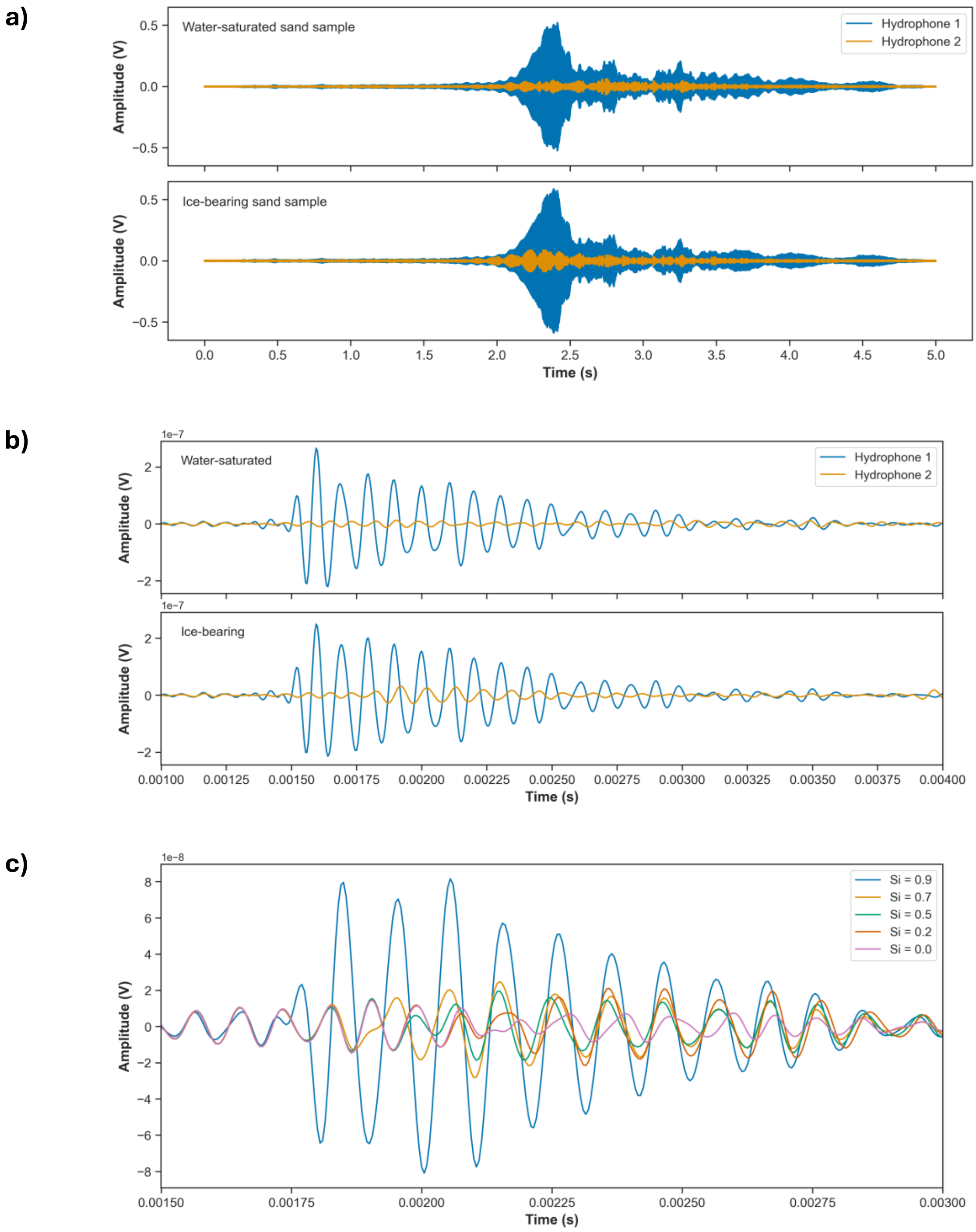

Figure 3.2 An example of: a) recorded time series (raw) and b) deconvolved signals from pulse tube measurement for the water-saturated (fully melted state) and ice-bearing (fully frozen state) sand samples from the readings of both hydrophone readings (refer to Figure 3.1c for hydrophone positions), and c) exploded view of deconvolved signals from hydrophone 2 at different ice saturation (S_i).

3.2.3 Ice saturation estimates and modelling

We established a baseline by measuring the velocity and attenuation of the sample fully saturated in water but before freezing (i.e., melted state, $S_i = 0$). Then, we assumed $S_i = 1$ when the sample entered the pulse tube, although keeping in mind that some unfrozen water might still be present, such as thin water films bound to grains (Dash et al., 1995; Watanabe and Mizoguchi, 2002). However, the melting process started before our first measurement due to the time required to reach the target pressure in the pulse tube. Thus, we predicted the velocity and attenuation at full saturation using a regression model. The estimated ice saturation is derived from the following empirical relationship (Equation 3.1).

$$S_i = 1 - \left(\frac{t}{T}\right)^n, \tag{3.1}$$

where S_i is ice saturation, t is the elapsed measurement time (in seconds), T is the total time for complete melting (determined by velocity and attenuation at the fully melted state), and n is an empirical parameter expressing the exponential relationship between ice melting and time (McCutchan and Johnson, 2022). We estimated n from the best fit of our experimental results to the rock physics models of Leclaire et al. (1994) and Marín-Moreno et al. (2017). Both models incorporate Biot's theory to predict frequency-dependent velocity and attenuation but consider the solid frame differently. Biot's theory (Biot, 1962; Biot, 1956b) is a widely used model for unconsolidated sediments (e.g., Cadoret et al., 1998; Chotiros, 1995; Williams et al., 2002), which accounts for the frequency dependence of the acoustic attributes due to fluid viscosity and inertial interaction between pore fluid and sediment matrix.

Leclaire et al. (1994) extended Biot's theory to predict elastic wave parameters in frozen media. This model uses a three-phase approach where the sediment matrix, ice, and unfrozen water can coexist, incorporating ice parameters into Biot's theory. The model assumes no direct contact between sediment matrix and ice due to thin water film formation around sediment grains, except for the fully frozen media case. Marín-Moreno et al. (2017) proposed the hydrate-bearing effective sediment (HBES) model, which was developed from Best et al.'s (2013) hydrate effective grain model. This model predicts velocity and attenuation dispersion based on the clay-squirt flow mechanism in sediment (Leurer, 1997; Leurer and Brown, 2008) by incorporating the Biot-Stoll fluid flow model (Stoll and Bryan, 1970). It calculates acoustic properties using the complex bulk modulus of both the pore fluid (water, gas, and pore-filling (PF) hydrate) and the solid phases (sediment grains and cementing hydrate). HBES uses the Reuss approximation (Reuss, 1929) to calculate the effective fluid bulk modulus. We extended the model by adding the Voigt and Brie approximations (Brie et al., 1995; Voigt, 1889) to explore the effect of ice distribution on the acoustic properties. We used Brie's coefficient (*e*) equal to 5, which positioned Brie's approximation between Voigt's and Reuss' (Brie et al., 1995). To apply the HBES model to ice-bearing sediments, we simplified the model by assuming there is no gas and fluid inclusion inside the ice grains, and we replaced the bulk and shear modulus parameters of hydrate grains with those of ice grains (5.5 GPa and 2.7 GPa, respectively) from the average values reported by Chang et al. (2021), reflecting updated measurements at sub-zero temperatures. These values are crucial for modelling ice-bearing sediments where ice contributes to load-bearing strength and modifies wave properties (see model inputs in Table 3.2).

First, we compared both models with the experimental data to determine the best fit. Using the best-fit model, we varied morphology, permeability, gas saturation, and gas bubble size. The initial settings were 100% pore-filling morphology, 1 Darcy permeability, and 0% gas saturation. We adjusted one parameter at a time, keeping the others constant, until the objective function (Equation 3.2) showed minimal improvement, indicating the best fit. The function works well if velocity and attenuation vary by similar factors, which holds true for the current dataset. However, if both parameters exhibited significantly different variation magnitudes, one parameter could disproportionately influence the objective function.

$$Objective\ function = \frac{\left|V_{experimental} - V_{modelled}\right|}{V_{experimental}} + \frac{\left|Q^{-1}_{experimental} - Q^{-1}_{modelled}\right|}{Q^{-1}_{experimental}} \tag{3.2}$$

Table 3.2 Fixed and case-dependent input parameters used in the model runs (case-dependent parameters only used in HBES model runs).

Parameter	Value	Units	Reference
Fixed input parameters			
Experimental conditions			
Effective pressure	2.5×10^6	Pa	
Temperature	19	°C	
Sand sediment properties			
Porosity without ice	0.41		Measured
Critical porosity	0.38		
Sand grain bulk modulus	36×10^9	Pa	Simmons (1965)
Sand grain shear modulus	45×10^9	Pa	Simmons (1965)
Sand grain density	2650	kgm^{-3}	Simmons (1965)
Sand grain diameter	1×10^{-4}	m	Best et al. (2013)
Coordination number	9		Murphy (1982)
Tortuosity	3		Berryman (1981)
Ice grain properties			
Ice bulk modulus	5.5×10^9	Pa	Chang et al. (2021)
Ice shear modulus	2.7×10^9	Pa	Chang et al. (2021)
Case-dependent input parameters			
Pore-filling concentration	0.0 – 1.0		
Sand frame permeability	0.25 – 10	Darcy	
Gas saturation	0 – 0.05		
Gas bubble radius	0.01 – 10	mm	

3.3 Results

3.3.1 Inferring ice saturation

Figure 3.3a shows ice melting early began from both the top (35-45 cm) and bottom (0-5 cm) sections (e.g., at S_i = 0.95), where the melting progressed faster compared to the middle part of the column (e.g., S_i = 0.76 and 0.48). The microwave image represents only Sample 2, but we assume the distribution will be similar in both samples due to similarity in properties. Ice in the middle-to-bottom section (5-15 cm) melted more slowly, especially as saturation dropped to S_i = 0.28, before stabilising at low ice saturation levels (e.g., S_i = 0.06). The ice saturation averaged over the sample against melting time (Figure 3.3b), shows an exponential decay in ice saturation over time (a steep initial drop that slows around 180 minutes). We compared these measurements with an ice melting model (Equation 3.1) using different *n* values, representing an empirical parameter. Most data points fit well within the curves for *n* = 1.0 – 1.4, suggesting this range best captures the observed melting behaviour.

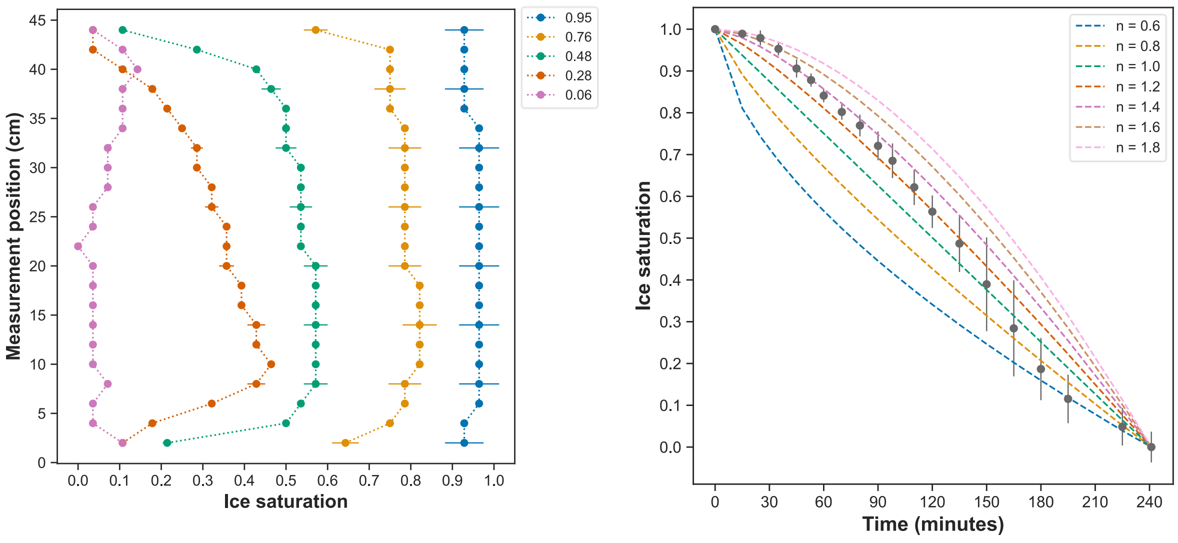

a)

b)

Figure 3.3 Ice saturation measurement using the microwave imaging setup during melting at 19°C (room temperature). a) A representative subset of ice distribution along the sample core at various saturations. Readings are taken every 2 cm along the sample, excluding the measurements near the top (50 cm) and bottom (0 cm) due to the interference from the PVC end caps. The legend values represent the average ice saturation of the entire sample. b) Ice saturation (averaged throughout the core) against melting time, with *n* represents an empirical parameter.

To determine the empirical parameter *n*, we considered two things: the best fit of experimental data to the modelled results using the objective function (Equation 3.2, with results shown in

Table 3.3) and how well the predicted experimental values at $S_i = 1$ (based on regression models) fit with the modelled results.

We found that experimental velocity best fit with the models using $n = 1.1 – 1.3$ (Figure 3.4a). In Appendix E, we show that $n < 1.1$ overestimates velocities at $S_i = 1$ but matches the attenuation, while $n > 1.3$ underestimates velocities at $S_i = 1$ and leads to significant deviations in attenuation at $S_i > 0.6$. From the microwave data, we calculated $n = 1.2 \pm 0.1$ (Figure 3.3b), which is consistent with our model fits. Thus, we adopted $n = 1.2$ for the remainder of the discussions (see Appendix E for full comparisons between the experimental results and model predictions).

Table 3.3 Calculation of objective function to compare experimental and modelled velocity and attenuation. A lower value indicates a better fit.

Model	**Objective function at n =**				
	1	**1.1**	**1.2**	**1.3**	**1.4**
HBES – Voigt	0.38	0.36	0.35	0.36	0.38
HBES – Brie	0.52	0.51	0.50	0.53	0.57
HBES – Reuss	0.68	0.65	0.65	0.68	0.72
LeClaire	0.48	0.49	0.50	0.49	0.47

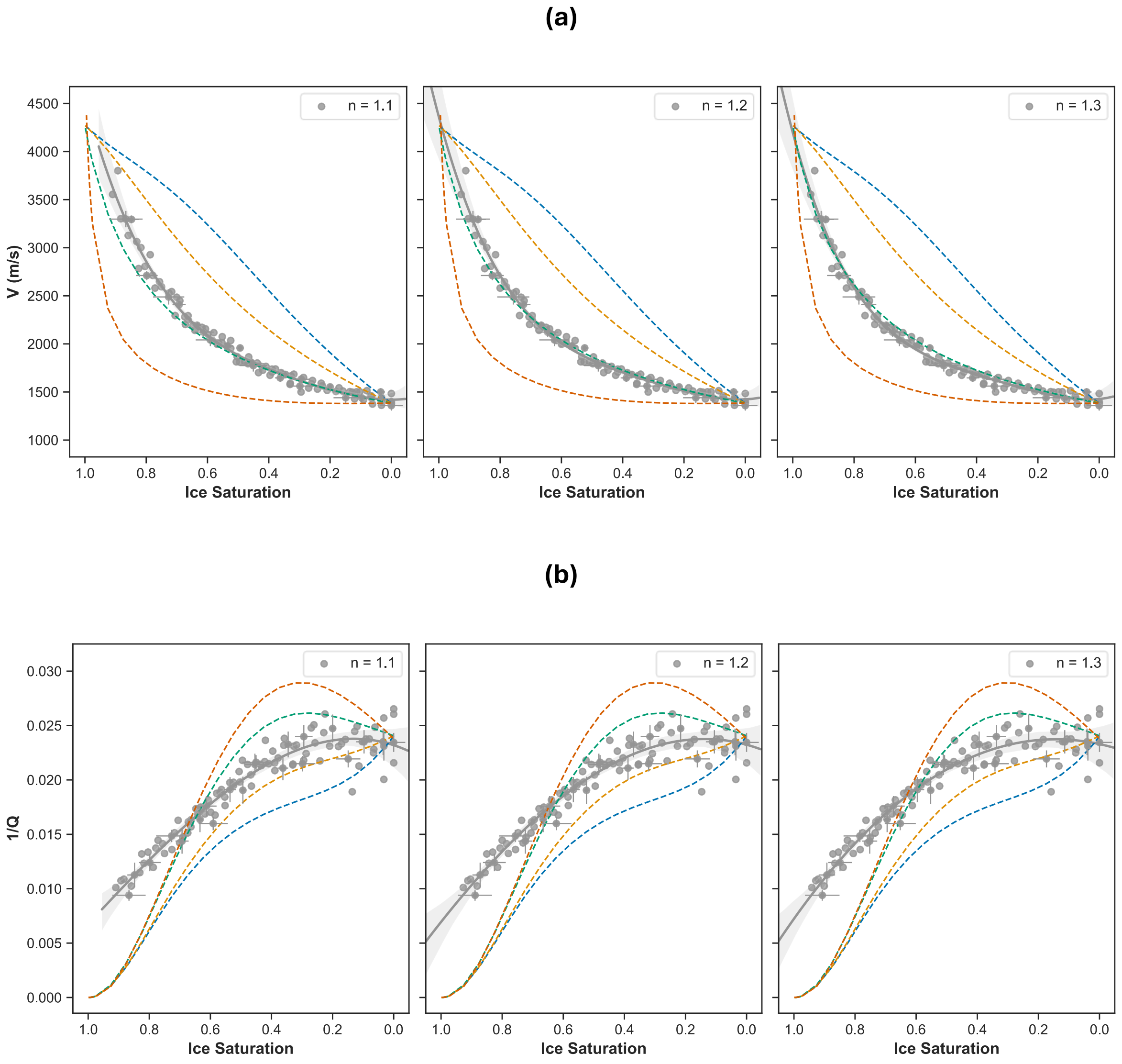

Figure 3.4 Empirical parameter (*n*) fitting of measured data (grey dots) of a) velocity and b) attenuation to HBES with Reuss, Brie, and Voigt approximations (blue, yellow, and green dotted lines, respectively) and LeClaire (red dotted lines) models. Grey solid lines represent the respective regression models to each dataset with averaged R^2 of 0.98 and 0.93 for velocity and attenuation, respectively. Cross error bars are shown at every 0.05 decrement of ice saturation (S_i).

3.3.2 Acoustic properties of ice-bearing sediment during the ice melting process

Velocity decreases with decreasing ice saturation, showing similar values for both samples, although Sample 2 exhibits a slightly smaller velocity (by ~1%) between S_i = 0.2–0.7 (Figure 3.5a). Velocity drops rapidly when $S_i > 0.5$, reflecting the loss of stiffness provided by ice. As ice acts as a solid bonding agent between grains, its presence significantly enhances the elastic moduli of the sediment. Therefore, as ice melts and is replaced by water, which has a lower elastic modulus, the overall stiffness of the sample decreases, leading to a sharp velocity reduction. At lower ice saturation ($S_i < 0.5$), the rate of velocity decline diminishes, indicating that remaining ice contributes less to stiffness.

In contrast, attenuation generally increases with decreasing ice saturation, especially at higher ice saturations ($S_i = 0.4–0.9$), then increases more slowly at lower saturation. This behaviour can be attributed to the increasing mobility of pore fluids and enhanced viscous damping as ice melts. At high ice saturation, the transition from cementing ice to partially unfrozen conditions introduce more compliant grain contacts, promoting internal friction and energy loss. As the ice fraction decreases further, attenuation continues to rise due to squirt flow and fluid movement within the interconnected pore network, though the rate slows because the system becomes more homogeneously water saturated. Both samples exhibit similar attenuation, with variations observed at $S_i < 0.2$, likely associated with variable ice distribution. The rates of change in velocity and attenuation confirm that ice saturation significantly affects both properties at higher saturation ($S_i > 0.5$), consistent across both samples, although attenuation analysis shows more variation (Figure 3.5b).

Using the regression models, we capture the non-linear response of velocity and attenuation during the melting process. We used third-degree polynomial models for both datasets. The models capture the trend fairly well at most saturation levels with R^2 (or the coefficient of determination) values of 0.98 for velocity and 0.93 for attenuation, indicating the models account for 98% and 93% of the experimental data variance. Increasing the polynomial degree did not significantly improve the fit.

The two samples show that velocity is only weakly frequency-dependent at all saturations but varies more significantly at higher saturations (Figure 3.6a), likely due to ice/water distribution effects. On average, velocity increases with frequency by ~3% over the 3.2-20 kHz bandwidth, with the highest increase (~6%) at $S_i > 0.9$. However, at $S_i \sim 0.7$, velocity tends to decrease with frequency, showing a ~5% decline over the same bandwidth. Note that we determined the cut-off frequency (3.2 kHz) to ensure that at least half of the wavelength should propagate through the sample (0.5 m in length) to provide accurate measurements. At 1.6-2.4 kHz, the half-wavelengths at high saturation for both samples are ~0.63-0.69 m, longer than the sample. At 3.2 kHz, the half-wavelengths are ~0.44-0.47 m, shorter than the sample, thus fulfilling the requirements.

Attenuation is more sensitive to frequency, especially above 8 kHz in the high saturation range (Figure 3.6b). Significant attenuation dips occur around 10–12 kHz at low saturation ($S_i \sim 0–0.3$) and around 17–19 kHz at intermediate to high saturation ($S_i \sim 0.5 – 0.7$) in both samples. The variations in attenuation, particularly at higher frequencies, can be attributed to patchiness or heterogeneous ice distribution (Matsushima et al., 2016). This observation is supported by the fact that the sensitivity of attenuation to frequency increases with the ice melting, showing consistent patterns across both samples. The wavelengths at these frequencies are below 0.1 m, indicating patchiness on a similar scale. Similar variations near fully melted conditions have also been observed in water-saturated sediment studies at full saturation (e.g., Dvorkin and Nur, 1998; Tserkovnyak and Johnson, 2002).

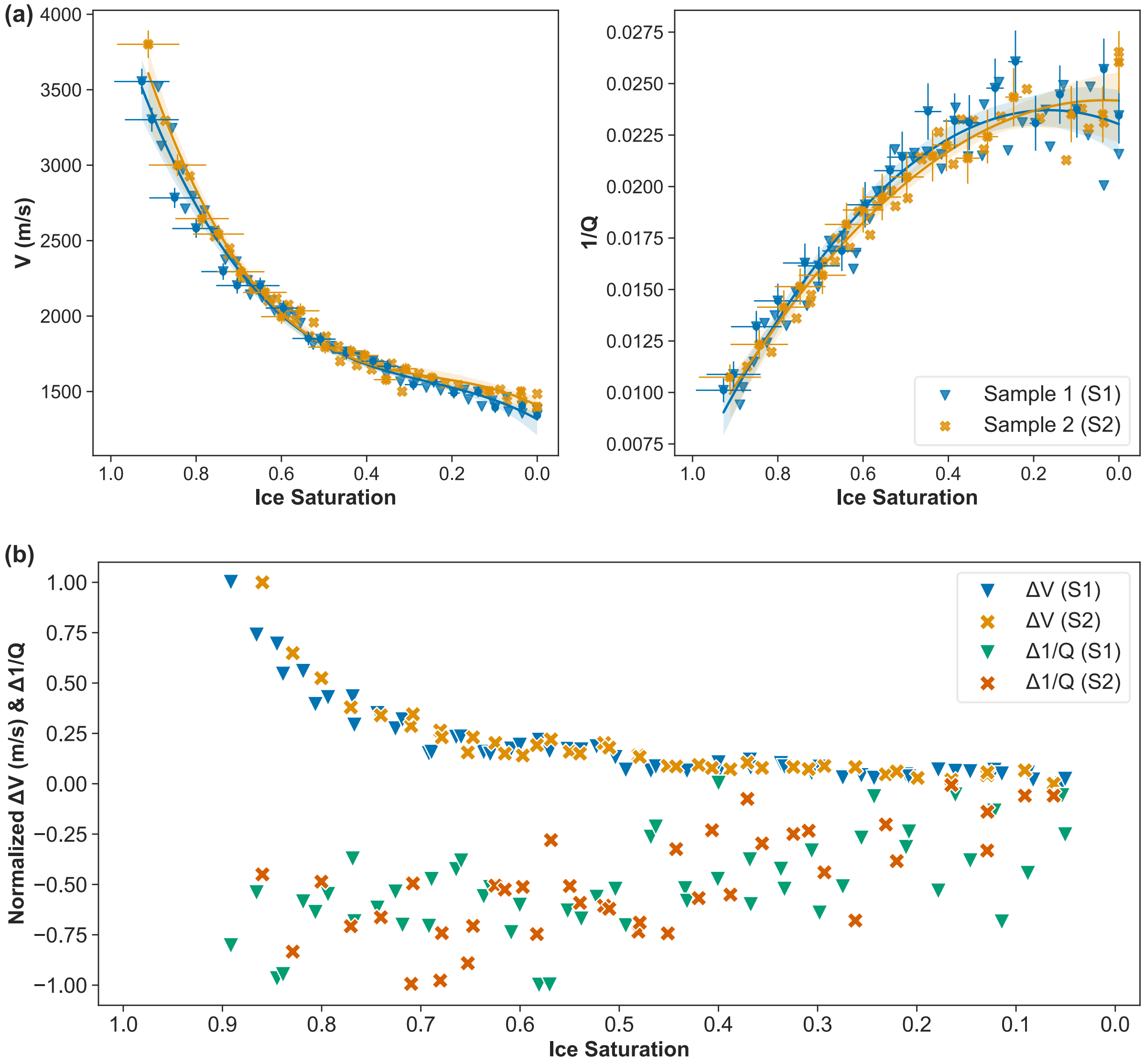

Figure 3.5 (a) Variations in velocity (V) and attenuation (1/Q) across ice saturations during melting at 10 kHz and 2.5 MPa. Samples 1 and 2 are prepared similarly with 100 μm Leighton Buzzard sand (porosity of 0.408 and 0.413). Solid lines and shaded areas represent regression models with R2 of 0.98 and 0.93 for velocity and attenuation datasets, respectively. Cross error bars are shown at every 0.05 decrement of ice saturation (Si) reflect ~6% and ~7% uncertainties for Samples 1 and 2, associated with the saturation process, likely due to non-connected porosity and possible volumetric expansion. (b) Rate of changes of velocity and attenuation with decreasing Si, normalized to their values at Si = 0. Positive values indicate a decrease, and negative values indicate an increase in acoustic properties with decreasing Si.

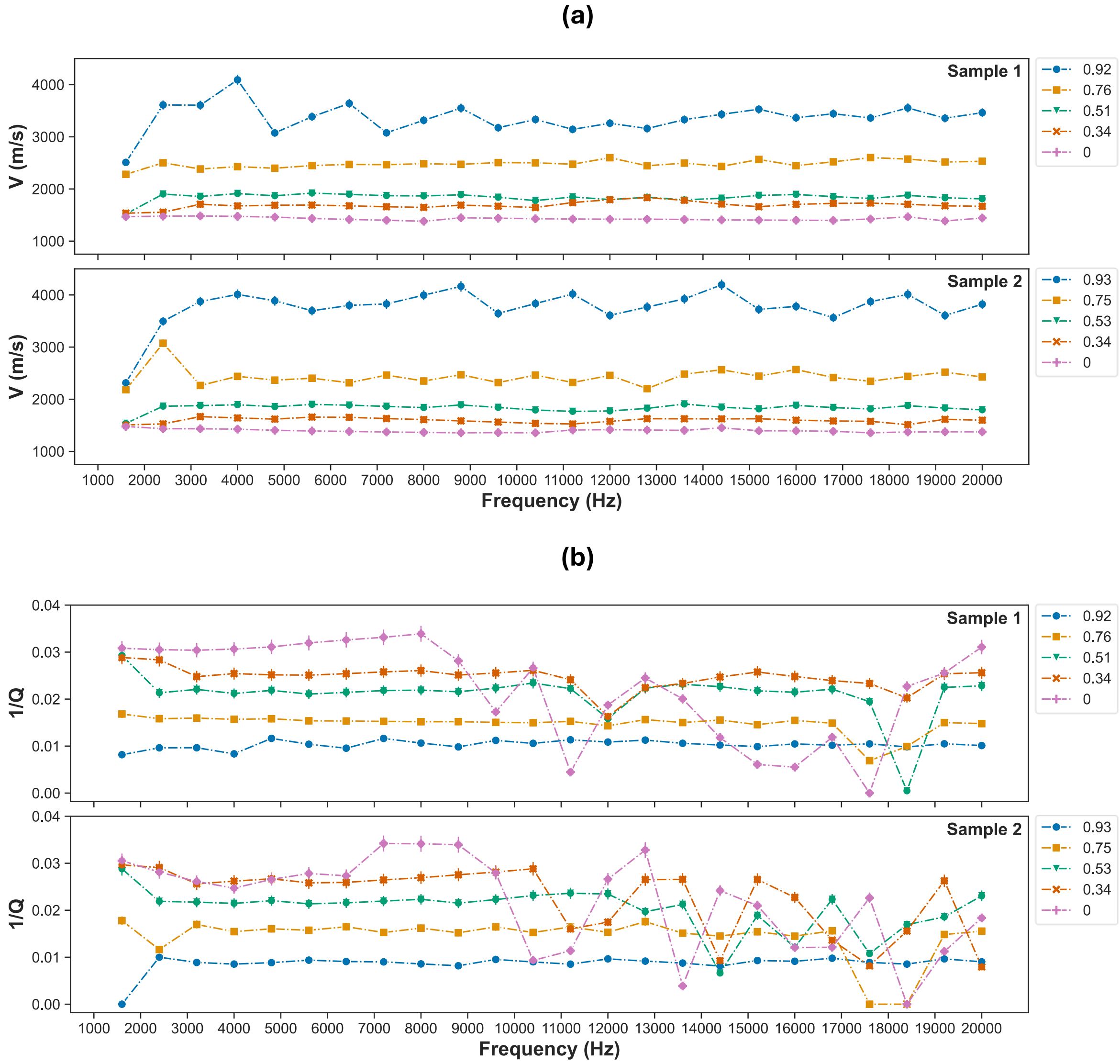

Figure 3.6 Variations in a) velocity and b) attenuation in frequency spectra at selected ice saturation levels (shown in legends) for Sample 1 and 2. Error bars are shown at each frequency at all saturations. Some error bars are not visible due to smaller than the data points.

The similarity in velocity and attenuation values and patterns across both samples demonstrates the consistency in sample preparation and measurements, thereby validating the basis for further analysis. We used correlation analysis to explore how velocity and attenuation relate to ice saturation at different frequencies, especially due to the pulse tube's ability to measure a range of frequencies (Figure 3.7).

Velocity strongly correlates with changes in ice saturation, with correlation values mainly above 0.85, especially at frequencies above 4 kHz. The correlation values are statistically significant for the entire frequency range, exceeding the 99% confidence line. Both samples show similar correlation values, with minor differences observed at frequencies below 4 kHz, which are mainly under the cut-off frequency of 3.2 kHz.

Attenuation also strongly correlates with changes in ice saturation, albeit negatively. Unlike velocity, correlation values for attenuation are higher at the lower frequency band (~2–9 kHz), exceeding the 99% confidence line. At frequencies above 10 kHz, correlations are mainly significant with 90% confidence. The weakest correlation is near the highest frequency band (> 19 kHz). Correlation values for attenuation in both samples are similar but less converged than those for velocity, with higher values observed in Sample 2, particularly at lower frequencies.

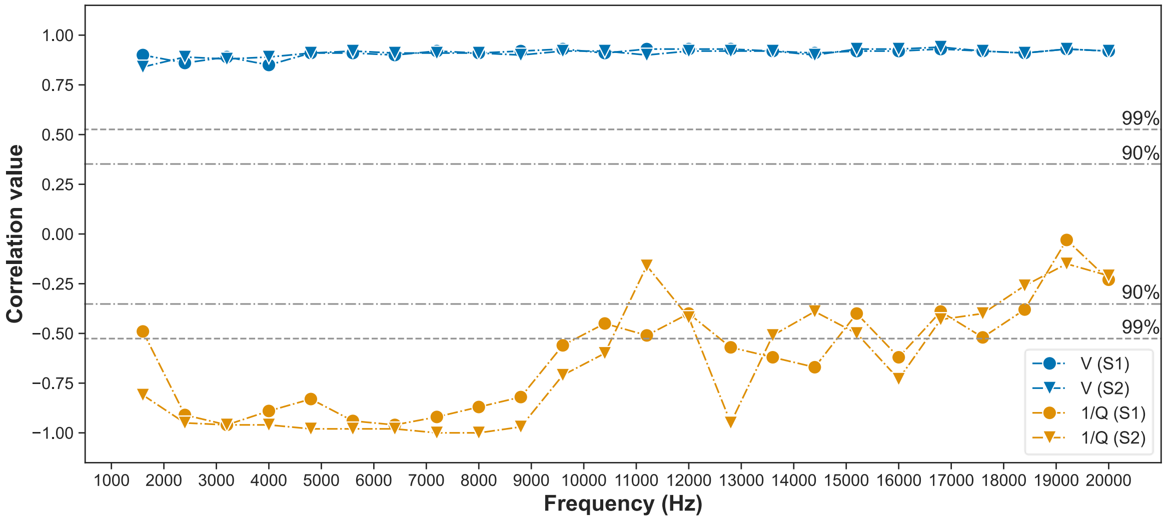

Figure 3.7 Correlation values of velocity and attenuation with ice saturation across the frequency band for both samples. V and 1/Q represent velocity and attenuation, and S1 and S2 represent Sample 1 and 2.

We selected velocity and attenuation at four representative frequencies—3.2, 12.8, 16.8, and 20 kHz—to explore their correlation levels, spanning both below and above the 90% and 99% confidence thresholds (Figure 3.8). Figures for all frequencies can be found in Appendix E, which shows consistency across both samples at all frequencies. This analysis is more relevant to attenuation because of its complex variation with frequency, unlike velocity which shows similar correlation values across the frequencies.

Attenuation initially increases with decreasing ice saturation until S_i ~ 0.4 for both samples. Beyond this saturation level, attenuation varies differently at each frequency (Figure 3.8b). At 3.2 kHz (99% confidence level), attenuation continues to increase. At 12.8 kHz, differences between the samples are pronounced, with Sample 1 showing more variation than Sample 2. Despite the similar correlation values above the 99% confidence line, we observed differences at S_i ~ 0.3. At 16.8 kHz (90% confidence level), attenuation remains constant in average with decreasing ice saturation from S_i ~ 0.5 to 0. Sample 1 shows more variation than Sample 2, but the trends are similar. At 20 kHz, where correlations do not reach the 90% confidence cut-off, trends differ between samples. In Sample 1, attenuation increases until S_i ~ 0.2 before dipping significantly and stabilising up to $S_i = 0$. In contrast, the attenuation of Sample 2 decreases from $S_i \sim 0.5$ to 0.3, stabilises from $S_i \sim 0.3$ to 0.1, then increases again up to $S_i = 0$.

The analysis highlights the importance of selecting an appropriate range of frequencies to accurately capture frequency-dependent behaviours within ice-bearing sediments. Velocity shows similar sensitivity to changes in ice content across all frequencies. However, attenuation is more sensitive to changes in ice content at higher frequencies due to smaller wavelengths that approach the size of the heterogeneities. At lower frequencies, attenuation shows a steady, predictable change with ice content because longer wavelength perceives the medium as homogeneous, unlike higher frequencies, where the wavelengths are comparable to the heterogeneities and show their presence more clearly.

Understanding these mechanisms at the correct frequencies enhances our ability to monitor and predict changes in ice-bearing sediments, which has broader implications for fields like quantifying ice content in permafrost and its monitoring (e.g. Hilbich et al., 2022; Lin et al., 2018). For example, in sub-bottom profilers, higher frequencies may lead to increased energy scattering and reduced sub-bottom penetration in areas with partially melted seabed permafrost.

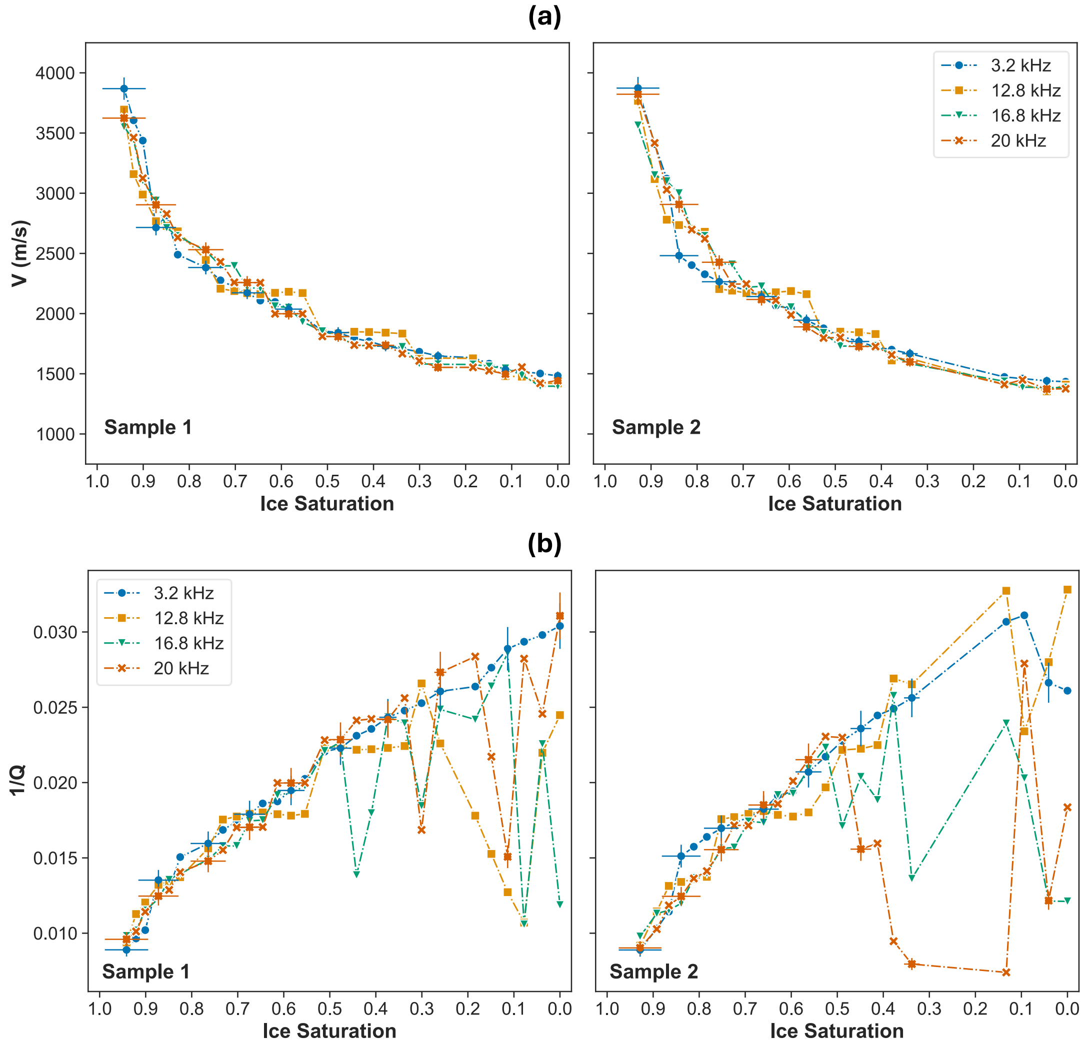

Figure 3.8 Variations in a) velocity and b) attenuation with ice saturations during the melting process of both samples at the selected frequency of 3.2, 12.8, 16.8, and 20 kHz. Cross error bars are shown at every 0.1 decrement of ice saturation (S_i).

3.4 Modelling insight

3.4.1 Three-phase models

Both experimental data and model predictions show that velocity decreases with decreasing ice saturation, although at different rates (Figure 3.9). The models represent a three-phase approach to predicting the velocity and attenuation, with the LeClaire model representing the least uniform ice distribution (i.e., patchy ice distribution), while the HBES-Reuss model represents the most uniform ice distribution. The HBES-Brie model represents conditions between both of these end-member predictions. The LeClaire model predicts the fastest velocity decrease at S_i = 1.0 to ~0.8, followed by HBES with Voigt, Brie, and Reuss approximations, respectively. Our data aligns well with the HBES–Voigt model, which may suggest moderate to patchy ice distribution, though at S_i < 0.5, the data sometimes falls between the HBES–Voigt and LeClaire models. This pattern could suggest that at this saturation range the system behaves like a three-phase system with sufficient ice and water with the sand matrix. However, at higher ice saturations, ice grains may interlock, thus limiting relative motion between the three phases, which is also found by Sahoo et al. (2019) in a hydrate-bearing sediment cases, similar in terms of characteristic to our ice study.

Attenuation predictions from the models show various patterns. The LeClaire and HBES–Voigt models predict an increase in attenuation as saturation decreases from S_i = 1.0 to 0.3, followed by a decrease up to S_i = 0, with LeClaire's prediction showing a higher rate of decrease. Meanwhile, HBES–Brie and Reuss models mainly show a continued increase in attenuation as saturation decreases. LeClaire's model shows the highest attenuation at S_i = 0.3 and the lowest at S_i = 1.0, mainly due to squirt flow loss (Guerin and Goldberg, 2005). For HBES predictions, the lowest attenuation is observed at S_i = 1.0, while the highest at S_i = 0.3 for Voigt, and at S_i = 0 for Brie and Reuss approximations. Our experimental results fall between HBES–Voigt and Brie predictions, particularly at S_i < 0.6. At S_i > 0.6, the experimental attenuation is higher than the predictions.

Based on the objective function comparison, we chose the HBES model with Voigt approximation for further discussion, supported by Best et al. (2013), who found that LeClaire's model works better for S-waves rather than P-waves, which we used in this study.

3.4.2 Ice formation morphology

We investigated how the location of ice formation affects velocity and attenuation using the HBES model. This model can consider different morphologies, a term commonly used in hydrate formation, where ice forms either as part of the pore fluid (pore-filling, *PF*) or as cementing ($C = 1 - PF$) that strengthens the sediment matrix. We tested pore-filling concentrations from 0 to 1 in increments of 0.1, focusing on the figures relevant to our experimental data (Figure 3.10). Results from the complete simulation are provided in Appendix E.

Velocity decreases with decreasing ice saturation, with similar trends across PF scenarios. Higher PF concentrations generally show lower velocity, but the differences are not significant, particularly at intermediate saturations (S_i = 0.8 to 0.4). Higher PF concentrations show a higher velocity decrease with decreasing ice saturation, particularly at S_i > 0.8. Experimental velocities align well with the 1.0 PF scenario particularly at S_i > 0.6 and intersect with lower PF scenarios at S_i = 0.6 to 0.4. However, the velocity differences due to different PF concentrations are still within the variation of the experimental velocity, particularly at the intermediate saturation, because trend-wise, the experimental velocity matches the higher pore-filling concentration, particularly for the high decrease rate at high ice saturation (S_i = 1.0 to 0.8).

Attenuation in all scenarios increases with decreasing ice saturation, with different rates for each PF concentration scenario. Lower PF concentration leads to lower attenuation. Changes in attenuation across PF concentrations are caused by changes in viscous drag between the solids (i.e., ice grains) and global fluid flow as per Biot's attenuation mechanism (Marín-Moreno et al., 2017). Experimental attenuation fits better with the higher PF scenario; however, at $S_i < 0.6$, the experimental attenuation varies. Meanwhile, at $S_i > 0.6$, the experimental attenuation intersects with the predicted attenuation with lower PF concentrations (PF = 0.6 – 0.9), which may suggest that some of the ice may form around the sand grain rather than fully in the pore fluid.

3.4.3 Permeability

Velocity barely varies with changes in the sediment frame's permeability across all ice saturation (Figure 3.11). At $S_i = 0$, lower permeability predicts lower velocities with about a difference of ~50 m/s between the 0.25 and 10 Darcy (D) scenarios. At $S_i = 1.0$, velocities from all permeability scenarios converge to a similar value. Therefore, lower permeability predicts a higher decrease in velocity with ice saturation.

At permeabilities below 1 D, attenuation increases with decreasing ice saturation up to $S_i \sim 0.4$, then slightly decreases up to $S_i = 1$. For higher permeabilities, attenuation increases continuously up to $S_i = 1$. The peak of attenuation shifts to lower ice saturation as permeability increases up to 2.5 D. All permeability scenarios under-predict attenuation at $S_i > 0.6$ when compared to experimental attenuation. However, experimental attenuation falls between the 0.5 and 0.75 D predictions at $S_i < 0.6$. This range is within the permeability values of ice-bearing sand in permafrost environments, which range approximately from 0.05 to 10 D (Kleinberg and Griffin, 2005; Lacelle et al., 2022). The permeability value represents the permeability of the sediment frame without ice ($S_i = 0$). At higher ice saturation, permeability is expected to decrease due to reduced pore spaces from ice formation. In contrast, at lower ice saturations, permeability is expected to increase as more open spaces become available, leading to higher attenuation due to global fluid flow. These changes are particularly significant at $S_i > 0.4$, which may indicate a shift in ice morphology around this saturation level (see in Appendix E).

3.4.4 Gas saturation and bubble size

Predicted velocity changes slightly with varying gas saturation (S_g) at different ice saturations (Figure 3.12a). The most significant difference occurs at maximum ice saturation, where lower gas saturation generates higher velocity. On average, velocities at lower gas saturations ($S_g < 0.025$) are similar, while higher gas saturation produces a visibly lower velocity. Our experimental data best fits the predicted velocity without any gas present ($S_g = 0$).

Predicted attenuation differs in value with a similar trend with varying gas saturation at different ice saturation. Attenuation increases with gas saturation, and the variations are more pronounced than those in velocity. The increase in attenuation due to increased gas saturation aligns with our experimental attenuation. At $S_i = 0.6$, experimental attenuation intersects with the predicted attenuation at $S_g = 0$, then at $S_i > 0.8$, experimental attenuation intersects with the predicted attenuation at $S_g > 0.01$. This may suggest that high experimental attenuation, particularly at $S_i > 0.6$, could be due to a small concentration of gas. At high ice saturation, most pore water is frozen; therefore, leaving gas within the pores. However, as the ice melts, more pore water becomes available, increasing the concentration gradient between water and gas, thus increasing the gas solubility, making the gas easier to dissolve into water, particularly under high effective pressure (Sander, 2015).

We also explored how gas bubble size affects velocity and attenuation. To determine the appropriate bubble size range, we calculated the pore throat size (*a*) for our samples. Stoll (1974) found that pore throat sizes typically range from one-sixth to one-seventh of the mean grain diameter (*d*). Meanwhile, Hovem and Ingram (1979) provided the formula as follows: $a = \emptyset d/[3(1-\emptyset)]$, where $\emptyset$ is porosity. Using both methods, we calculated the pore throat size between 0.014 – 0.023 mm.

We tested four gas bubble sizes to represent microbubble (0.01 mm), fine bubble (0.1 mm), medium bubble (1 mm), and coarse bubble (10mm) (Figure 3.12b). Predicted velocity remains consistent across all bubble sizes, and attenuation shows no significant change for bubble radii below 1 mm. A significant change in predicted attenuation occurs at the bubble size of 10 mm, however, it exceeds both our experimental attenuation and the calculated pore throat size. Overall, the experimental results align with bubble sizes no larger than 0.1 mm, which explains the lack of noticeable gas bubble resonance effects on attenuation for the predicted bubble sizes (Gong et al., 2010).

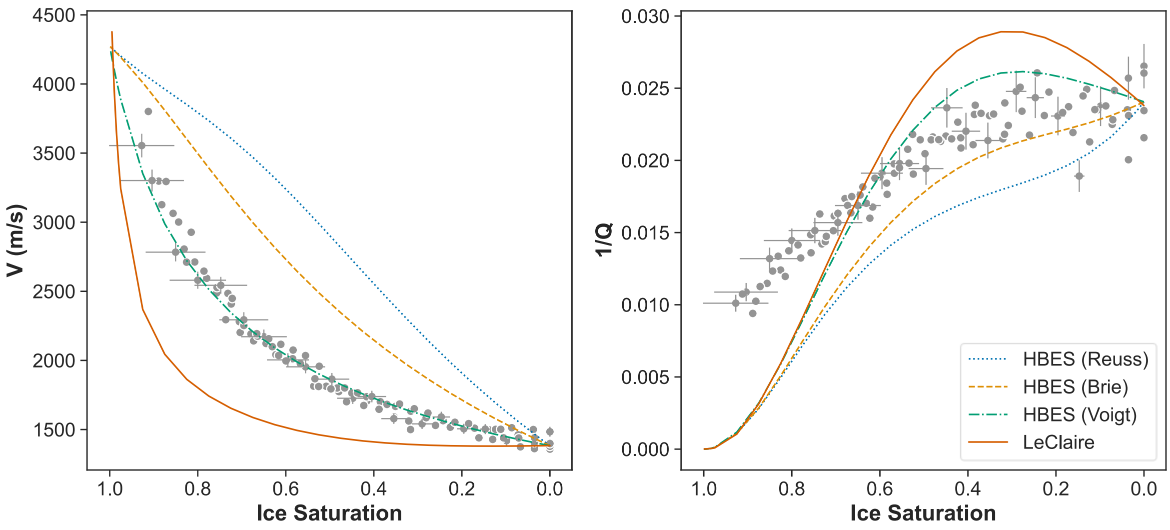

Figure 3.9 Comparison of velocity (left) and attenuation (right), at 10 kHz and 2.5 MPa effective pressure, against HBES (with various effective fluid bulk modulus approximations) and LeClaire models across ice saturation during the melting process. Grey dots represent the experimental data, and dashed lines represent the models (as shown in the legend). Cross error bars for the experimental dataset are shown at every 0.05 decrement of ice saturation (S_i).

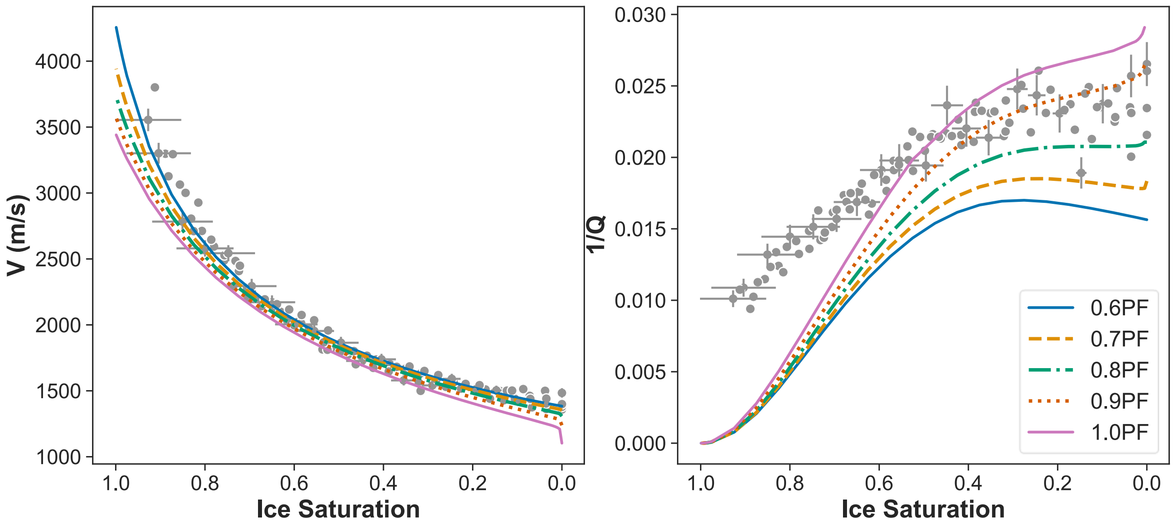

Figure 3.10 Comparison of velocity (left) and attenuation (right), at 10 kHz and 2.5 MPa effective pressure, against HBES model with selected pore-filling (PF) concentrations across ice saturation during the melting process. Grey dots represent the experimental data, and dashed lines represent the models (as shown in the legend). Cross error bars for the experimental dataset are shown at every 0.05 decrement of ice saturation (S_i).

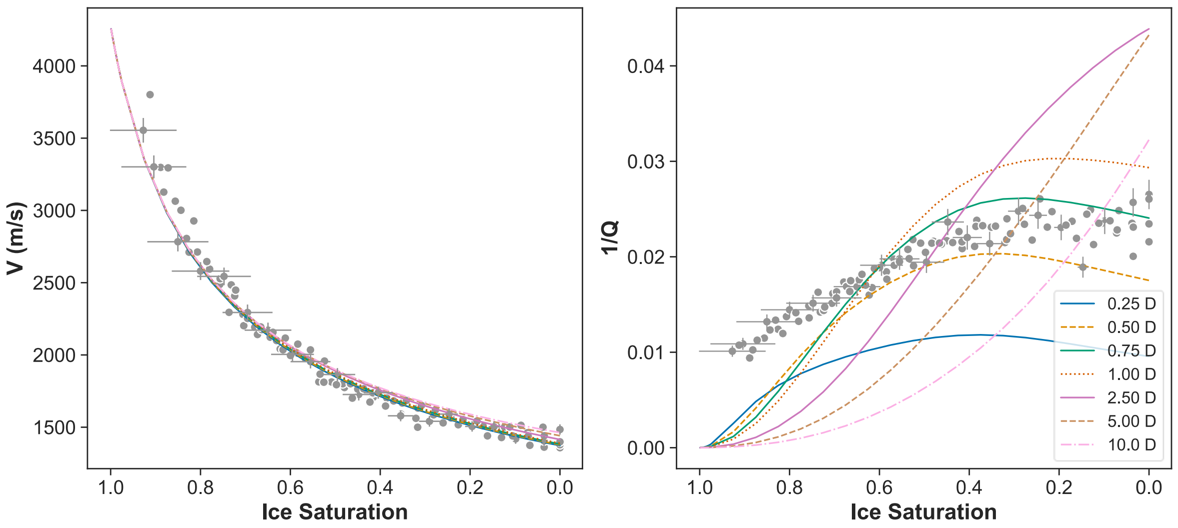

Figure 3.11 Comparison of velocity (left) and attenuation (right), at 10 kHz and 2.5 MPa effective pressure, against HBES model with various permeability values across ice saturation during the melting process. Grey dots represent the experimental data, and dashed lines represent the models (as shown in the legend). Cross error bars for the experimental dataset are shown at every 0.05 decrement of ice saturation (S_i).

3.5 Discussion

Ice distribution affects the acoustic attributes of sediments; but also, its location with respect to grains within the porous medium. This study shows that as ice melts, velocity decreases while attenuation increases, which agrees with previous ice melting/thawing studies (e.g., Matsushima et al., 2016; Yang et al., 2021). We observe that velocity is more sensitive to ice saturation (S_i) changes in the high S_i range ($S_i > 0.6$). This effect might be related to ice forming at grain contact above a certain S_i, leading to combined cementation and pore clogging phenomena that, in turn, increased the stiffness of the sand frame. At low saturations, ice effect on velocity may be less pronounced due to inclusion in the pore fluid, so changes in velocity are less significant.

On the other hand, attenuation increases with ice melting down to $S_i \sim 0.4$, then it stabilises. At higher saturation, the introduction of water coexisting with ice increases viscous drag, thus increasing the attenuation. However, once the saturation reaches $S_i \sim 0.4$, further melting may not significantly change the fluid dynamics, as there is already enough water present to reach a steady state. In addition, at high frequencies (e.g., sonic frequencies), unrelaxed pores may contribute to attenuation (Cadoret et al., 1998; Mavko and Nolen-Hoeksema, 1994). Similar changes have been observed in the studies of ice-bearing and gas-hydrate bearing sediments (e.g., Li and Matsushima, 2024; Sahoo and Best, 2021). The sensitivity of both velocity and attenuation to ice content suggests that these parameters could be used to estimate ice content in the field, particularly at high saturation where both parameters are equally sensitive.

Estimation can be performed through direct comparison with field measurements (e.g., well-log data) or enhance by supervised machine learning (e.g., Bustamante et al., 2024; Singh et al., 2021), where laboratory data are used to train models to predict ice content from field measurements. However, a larger data set is needed to provide effective training and testing processes.

We have ensured that the measurements well capture the sample characteristics by considering its length (i.e., 0.5 m) relative to the sonic wavelength. However, our focus on a homogeneous sand pack may contrasts with the field conditions where permafrost may be composed of sediment with varying grain sizes and lithologies. The volumetric expansion caused by melting ice could also affect the measurements. As ice melts and contracts, it may introduce errors in saturation estimation. In addition, there could still be some unfrozen water present after the freezing process in the form of thin water films (Dash et al., 1995; Watanabe and Mizoguchi, 2002). We have included error bars in our figures to address these potential issues.

These limitations suggest future research directions, such as investigating different sediment types, scaling up to field samples, and employing real-time monitoring to better understand ice and water distribution in the sample.

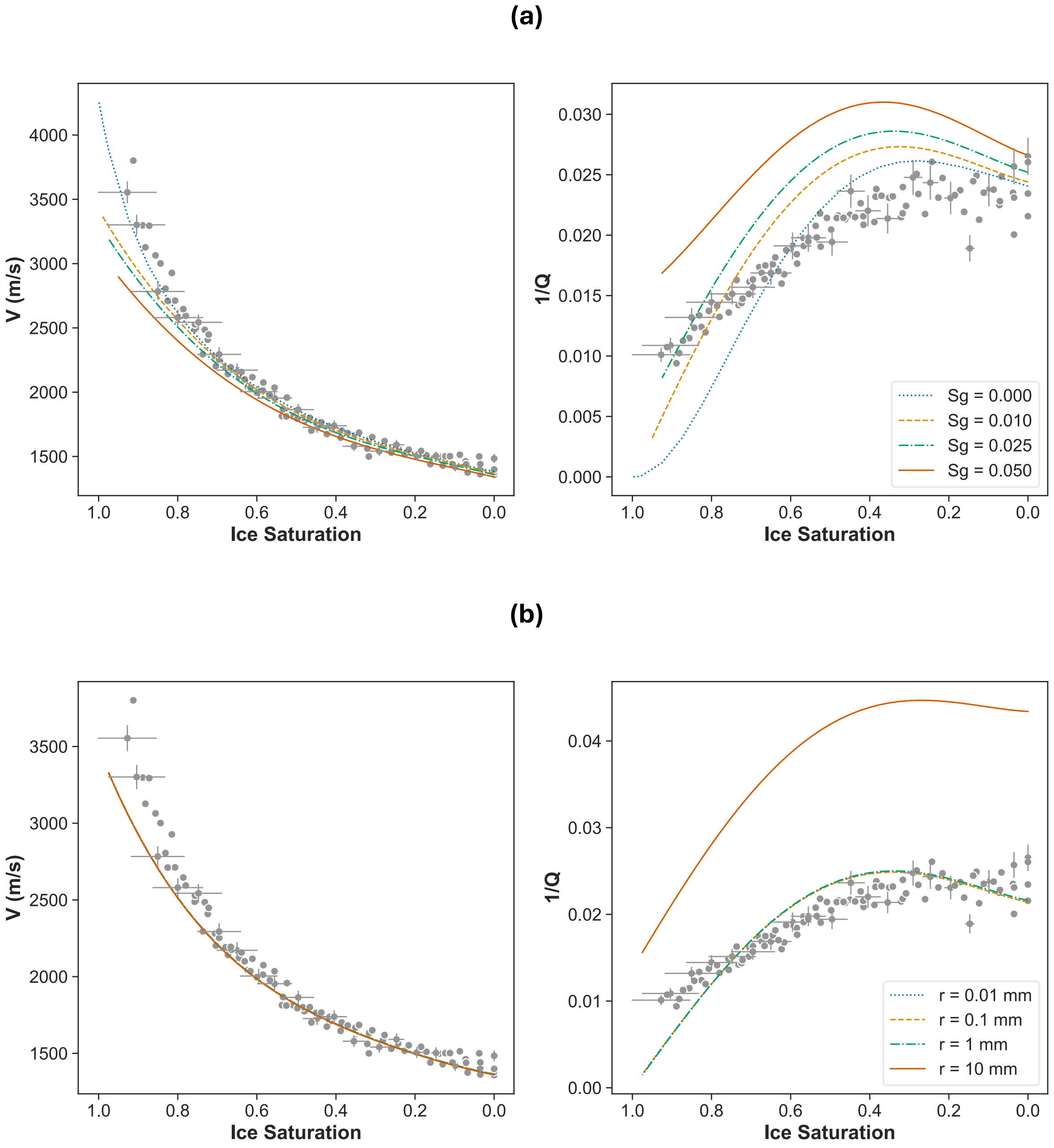

Figure 3.12 Comparison of velocity (left) and attenuation (right), at 10 kHz and 2.5 MPa effective pressure, against HBES model with various a) gas saturation (S_g) with a gas bubble size of 0.01 mm, and b) gas bubble size (r) with $S_g = 0.025$, across ice saturation during the melting process. The r = 0.01 – 0.1 mm curves are not shown due to having similar values with the r = 1 mm curve. Grey dots represent the experimental data, and dashed lines represent the models (as shown in the legend). Cross error bars for the experimental dataset are shown at every 0.05 decrement of ice saturation (S_i).

3.6 Conclusion

This study enhances the understanding of frequency-dependent acoustic behaviours in ice-bearing sands at sonic frequencies, addressing gaps in how P-wave velocity and attenuation respond to varying ice saturations, which is important for studying permafrost and gas hydrate stability, particularly in the light of climate change.

Our findings show that while P-wave velocity consistently correlates with ice saturation across all frequencies, attenuation demonstrates higher sensitivity at higher frequencies. This difference is important for selecting optimal frequencies for subsurface monitoring of ice-bearing sediments. By comparing experimental results with three-phase models, we identified that the HBES model with Voigt approximation better represents patchy ice distributions, providing a more accurate framework for interpreting field data.

These findings offer potential practical applications in improving geophysical survey designs for permafrost regions which may also deposit gas hydrates (incorporating potent greenhouse gases like methane), allowing more accurate estimations of ice content and sediment stability. Future studies could expand on these results by integrating field-scale data and refining models to account for complex pore fluid interactions, further improving the understanding of ice content in permafrost for monitoring purposes.

Chapter 4 The effect of pressure on acoustic (1 - 20 kHz) velocity and attenuation during the melting of ice-bearing sand

This chapter is currently in final preparation for submission to Geophysics: Advances in Rock Physics.

My contributions to the development of equipment and processing tools include: calibrating the pulse tube using a nylon rod and sediment samples (i.e., sand packs), improving data acquisition (e.g., testing different sound sources to get better results), refining the processing workflow (e.g., debugging and optimising the processing code), and calibrating the microwave equipment (e.g., testing it with various samples).

Abstract

Acoustic velocity and attenuation are influenced by ice and water saturations in ice-bearing sediments and can vary with frequency. This study investigates how ice melting in ice-bearing sand affects both acoustic parameters under effective pressures of 2.5, 5.0, and 7.5 megapascals, simulating thawing permafrost conditions at depths of up to 450 metres below the surface. As the ice melts, velocity decreases and attenuation increases, with the most significant changes occurring at lower pressures. Both acoustic properties show frequency-dependent characteristics, especially at higher frequencies. Comparisons with three-phase Biot models suggest that velocity is mainly affected by ice distribution, while attenuation is also influenced by ice morphology (pore-filling versus cementing ice) and the permeability of the solid frame. This study's lower-frequency acoustic measurements offer field-relevant insights, highlighting the role of ice saturation, distribution, and morphology in predicting acoustic behaviour in ice-bearing sediments for permafrost monitoring.

4.1 Introduction

The elastic properties of ice-bearing sand packs is of great interest in both geotechnical engineering and environmental sciences, particularly concerning permafrost (e.g., Bustamante et al., 2023; Kang et al., 2021; Oswell, 2011). Permafrost, or permanently frozen ground, is a critical component of the cryosphere, impacting infrastructure stability (e.g., Hjort et al., 2018) and global climate dynamics (e.g., Schuur et al., 2015). As the permafrost region warms, methane emissions from permafrost degradation are expected to rise (Meredith et al., 2022). Thus, linking elastic wave properties to ice content is key for monitoring and addressing these environmental challenges (Hilbich et al., 2022).

Elastic wave velocity and attenuation vary with frequency and such variations affect interpretations of results from seismic surveys and sonic logging that are based on laboratory experiments. Understanding frequency dependence, particularly velocity dispersion (the variation of velocity with frequency), is crucial for comparing results from different methods (Kolsky, 1964). These properties are also sensitive to pore fluid content (e.g., Emerson and Foray, 2006; Rubino and Holliger, 2012; Sutiyoso et al., 2024). While laboratory studies offer valuable insights, most are conducted at ultrasonic frequencies (150 kHz to 1 MHz; e.g., Dou et al., 2016; Li and Matsushima, 2024; Matsushima et al., 2016) that differ from those of field measurements, highlighting the need for more research at frequencies closer to those of field measurements, such as sonic frequencies, used in borehole logging.

The concept of ‘morphology’ is increasingly used to describe ice distribution in sediment, highlighting its role in influencing the mechanical and acoustic properties of ice-bearing sediments (e.g., Li and Matsushima, 2024; Matsushima et al., 2016). First introduced by Dvorkin et al. (1999) for high-porosity ocean-bottom sediments and later adapted for gas hydrates by Helgerud et al. (1999), ice morphologies are categorised into non-cementing and cementing types based on their interaction with the sediment matrix. In non-cementing morphology, ice does not bond to the sediment framework. Within this category, pore-floating ice grows freely in pore spaces without connecting grains, while pore-bridging ice connects adjacent grains, contributing to frame support (Hu et al., 2014; Priest et al., 2009). Cementing morphology involves ice bonding directly to sediment grains, either at grain contacts (contact cementing) or as a coating around grains (grain coating) (Best et al., 2013; Ecker et al., 1998; Helgerud et al., 1999). Cementing morphologies often enhance load-bearing capacity, significantly influencing the elastic properties of sediment. The concept of morphology provides a framework for interpreting experimental and field observations of ice-bearing sediments.

Theoretical rock physics models, including those based on Biot's theory, are commonly used to study how pore content affects wave properties in ice-bearing sediments. These models range from two-phase systems (sediment and pore fluid) to three-phase systems (sediment, ice or hydrate, and pore fluid) (e.g., Leclaire et al., 1994; Marín-Moreno et al., 2017). Models developed for gas hydrates can also be applied to ice-bearing sediments due to the similarities in their characteristics (Helgerud et al., 1999), offering a framework for predicting elastic wave behaviour in frozen media.

Permafrost can extend to 365 m below the surface (Dobiński, 2020) with estimated pressures ranging from 4.9 to 6.2 MPa (Kawasaki et al., 1983). Therefore, understanding how pressure affects the elastic properties of ice-bearing sediments is important for accurately interpreting geophysical data with depth in permafrost environments. In our previous work (Chapter 3; Sutiyoso et al., 2025), we explored the elastic wave properties of ice-bearing sands, but the dataset was limited to single pressure measurements. This study addresses that limitation by investigating the elastic wave properties of ice-bearing sand using an acoustic pulse tube under multi-depth conditions within the sonic frequency range (1-20 kHz), which is more relevant to permafrost layers. This setup enables us to measure changes in acoustic velocity and attenuation, providing insights into the interaction between ice and sand during melting under varying pressures and frequencies. Comparing our experimental results with three-phase rock physics models enhances our understanding of the mechanisms behind our observations, which could aid in estimating ice content from geophysical field measurements.

4.2 Materials and Methods

4.2.1 Ice-bearing sand sample

We used clay-free Leighton Buzzard sand (mean grain diameter of 100 μm), chosen for its similarity to the size of typical permafrost sands (e.g., Fuchs et al., 2018; Liu et al., 2023; Strauss et al., 2012). The sand was packed in a 0.5 m long PVC pipe, sealed with PVC endcaps to enable uniform confining pressure (Appendix F). The acoustic impedance of the PVC material is 2.9 x 10^6 kg m^{-2} s^{-1} (Selfridge, 1985), while the impedance of the sand pack ranges from 2.2 to 6.8 x 10^6 kg m-^{2} s^{-1}, depending on whether it is water-saturated or ice-bearing (Kang et al., 2021; Schumann et al., 2014).

To prepare the sample, we poured sand into the PVC pipe, compacting it in layers for even compaction and scratching the surface between layers to minimise impedance contrasts. The porosity of the sand pack was 41 ± 0.1%, calculated from the wet-dry mass balance, with uncertainties determined through error propagation. Once compacted, we gradually added a pre-calculated amount of de-ionised water and tapped the pipe to release air bubbles. This process helped in reducing gas bubbles in the ice, resulting in more consistent laboratory measurements (McCutchan and Johnson, 2022). After fully saturating the sample, we sealed it and let the water distribute for 24 hours. Then, we froze the sample at -10°C for 48 hours. Further details about the sample preparation can be found in Appendix F.2.

We inferred ice saturation based on the elapsed melting time during measurements (Appendix F.3). We established a baseline by measuring velocity and attenuation in the fully melted state (S_i = 0). Ice saturation was calculated using an empirical relationship that incorporates elapsed melting time and an empirical parameter derived by comparing the experimental results with rock physics models (explained further in Section 4.2.3) and minimising an objective function.

4.2.2 Pulse tube measurements

We measured velocity and attenuation (inverse quality factor, 1/Q) using a 4.5-metre-long acoustic pulse tube with variable-frequency chirp signals with the range of 1-20 kHz. The tube uses a stainless-steel cylinder filled with water to propagate plane waves along its axis, based on an acoustic waveguide concept (Redwood, 1960). A piezoelectric transducer at the bottom insonified the sample within the same frequency range. We collected acoustic measurements at effective pressures of 2.5, 5.0, and 7.5 MPa under a controlled temperature of 19°C, simulating conditions similar to thawing permafrost at depths of approximately 150 – 450 m, assuming a permafrost density of 1700 kg/m^3 (Kawasaki et al., 1983). While permafrost has been reported to extend to depths of up to 365 m (Dobiński, 2020), a higher-pressure limit was selected to account for geological variability (e.g., higher sediment densities) and to provide a conservative upper bound. This temperature setting reflects an extreme surface warming scenario (Kim et al., 2024).

At each pressure level, we allowed the sample to thaw during the measurement process, enabling us to track changes in wave properties as the ice gradually melted. After completing the measurements at one pressure, we let the sample rest for 24 hours to reduce residual effects from compression under confining pressure, then re-froze it to restore the initial frozen condition before moving to the next pressure step. This approach ensured comparable starting conditions across all pressure levels and helped minimise the influence of prior pressure on the acoustic responses. Our measurements covered the full melting process, from frozen to completely thawed states. This experimental approach ensures the results remain applicable to a wide range of natural permafrost conditions, including regions with thick permafrost or elevated overburden stress.

For the measurements, we recorded signal amplitude in voltage across the ice saturation stages. Then, we applied Fast Fourier Transform to deconvolve the raw signals using time-domain gating to eliminate extraneous reflections, and then applying an inversion model using the scattering matrix method to calculate complex velocity and attenuation. The relative experimental uncertainty was ±2.4% for velocity and ±5.8% for attenuation. Further details on the experimental setup and data processing are given by Sutiyoso et al. (2024) (Chapter 2).

To ensure accurate measurement, we determined cut-off frequencies based on the requirement that at least half of the wavelength must propagate through the 0.5-metre-long sample. We calculated wavelengths by dividing velocity by frequency. The frequencies that meet this requirement are 4.0 kHz for 2.5 MPa data and 4.8 kHz for the 5 and 7.5 MPa data, resulting in half-wavelengths of 0.41-0.50 m. Below these frequencies, the half-wavelengths exceed the sample length, and thus may not represent the entire sample condition. Aside from frequency dependence analysis, we mainly focus on the experimental results at 10 kHz, which is the mid-bandwidth frequency of 1 – 20 kHz range.

4.2.3 Rock physics models

We used two rock physics models to investigate the mechanisms underlying the melting process in ice-bearing sand. The first, developed by Leclaire et al. (1994), extends Biot's (1956) theory to predict elastic wave behaviour in frozen media using a three-phase system of sediment matrix, ice, and unfrozen water. This model assumes no direct contact between the sediment and ice due to a thin water film around the grains, except in fully frozen conditions. The second model is the hydrate-bearing effective sediment (HBES) model (Marín-Moreno et al., 2017), which treats pore-filling ice as part of the pore fluid and cementing ice as part of the sediment frame. Both models incorporate Biot’s theory to account for frequency-dependent velocity and attenuation, but they differ in their treatment of the sediment frame. We extended the HBES model by incorporating additional effective medium approximations by Brie et al. (1995) and Voigt (1889), alongside the existing Reuss (1929) approximation, to calculate fluid bulk moduli and assess how ice distribution affects acoustic properties.

We investigated the effect of ice morphology on acoustic velocity and attenuation, defined as a combination of pore-filling (PF) and cementing ice (C = 1 – PF). The HBES model incorporates a load-bearing scheme by treating cementing ice as part of the sediment frame, using the Voigt-Reuss-Hill average for bulk and shear moduli, as described by Ecker et al. (2000). Unlike the classic load-bearing scheme by Dvorkin et al. (1999) and Helgerud et al. (1999), which models ice as replacing sand grains in the sediment pack, the HBES model emphasises cementing ice coating grains or bonding at grain contacts, without replacing sand grains. Unlike gas hydrate, ice lacks microporosity—pores smaller than a micron that drive squirt-flow—resulting in less contribution to attenuation under stress (Best et al., 2013). Thus, we consider the pore-filling and cementing morphologies sufficient to capture the underlying mechanism of acoustic parameters in ice-bearing sediments.

We adapted the HBES model for ice-bearing sediments by substituting hydrate parameters with those of ice and assuming that ice has no gas or fluid inclusions in the ice grains (non-microporous). The model inputs are provided in Table 4.1.

Table 4.1 Fixed and case-dependent input parameters used in the model runs (case-dependent parameters are used only in HBES model runs).

Parameter	Value	Units	Reference
Fixed input parameters			
Experimental conditions			
Effective pressure	2.5 – 7.5 x 10^6	Pa	
Temperature	19	°C	
Sand sediment properties			
Porosity without ice	0.41		Measured
Sand grain bulk modulus	36 x 10^9	Pa	Simmons (1965)
Sand grain shear modulus	45 x 10^9	Pa	Simmons (1965)
Sand grain density	2650	kgm^{-3}	Simmons (1965)
Sand grain diameter	1 x 10^{-4}	m	Best et al. (2013)
Coordination number	9		Murphy (1982)
Tortuosity	3		Berryman (1981)
Ice grain properties			
Ice bulk modulus	5.5 x 10^9	Pa	Chang et al. (2021)
Ice shear modulus	2.7 x 10^9	Pa	Chang et al. (2021)
Case-dependent input parameters			
Pore-filling concentration	0.6 – 1.0		
Sand frame permeability	0.3 – 1.1	Darcy	

4.3 Results

4.3.1 Experimental measurements

Velocity decreases as the ice melts (or as ice saturation, S_i, decreases) across all effective pressure conditions (Figure 4.1a, left). The most significant decline in velocity occurs at higher ice saturation (S_i > 0.5), while the rate of decline slows down as the ice approaches fully melted condition (S_i = 0). At maximum ice saturation, velocities at 2.5 and 5 MPa are similar and slightly higher than at 7.5 MPa. However, at the lowest saturation (S_i = 0), velocity is highest at 7.5 MPa, followed by 5 MPa and then 2.5 MPa, as expected for water saturated sand packs (Zimmer et al., 2002). Comparing the velocities at maximum and minimum saturations reveals that the 2.5 MPa case experiences the greatest reduction in velocity as the ice melts, followed by the 5 and 7.5 MPa cases. This indicates that ice content has a greater influence on the elastic properties of sediments at lower pressure. Additionally, the decrease in velocity at 2.5 MPa is more gradual compared to the higher pressures, suggesting that differences in effective pressure may affect how ice interacts with the sand matrix.

Attenuation increases as ice melts from maximum saturation to $S_i \sim 0.2$ at 2.5 MPa, and to $S_i \sim 0.7$ for the 5 and 7.5 MPa cases, after which attenuation remains relatively constant up to $S_i = 0$ across all pressures, with some variation at 5 and 7.5 MPa (Figure 4.1a, right). These patterns show a shift in the attenuation peak from lower to higher ice saturation with increasing effective pressure. This observation suggests that at higher effective pressure, the sand grains are more compact due to closer grain contact, making the sand matrix more resistant to deformation as the ice melts (Zimmer, 2003).

Across ice saturation levels, the 2.5 MPa data consistently show the highest attenuation, followed by the 5 and 7.5 MPa data. At $S_i > 0.7$, attenuation values are similar across all pressures, within the range of data variability. However, as the ice melts, the gap in attenuation widens between the 2.5 MPa case and the higher-pressure cases. In terms of rate of change, the 2.5 MPa data exhibit the most significant increase in attenuation as ice melts, followed by the 5 and 7.5 MPa cases, consistent with the stronger effect of ice melting on velocity at lower effective pressures.

The volumetric expansion of ice may introduce errors in saturation estimation (French, 2007), along with the potential unfrozen water in the form of thin films (Dash et al., 1995; Watanabe and Mizoguchi, 2002). To account for these uncertainties, we have included error bars in our figures, based on a conservative 9% error estimate that considers these sources of error (French, 2007).

The non-linear behaviour of both velocity and attenuation as the ice melts are best fit using fourth-degree polynomial models for all effective pressures. These models captured the trend fairly well, with R^2 (coefficient of determination) values of 0.99, 0.98, 0.98 for velocity and 0.94, 0.82, 0.79 for attenuation at 2.5, 5, and 7.5 MPa, respectively. The R^2 values indicate that the models account for 98-99% and 79-94% of the variance in the experimental velocity and attenuation data (see Figure 4.1a). The lower R^2 values for attenuation at 5 and 7.5 MPa are largely due to greater variance at intermediate saturations ($S_i \sim 0.6$ - 0.2). We found that increasing the polynomial degree did not significantly improve the fit.

We also explore the relationship between velocity and attenuation (Figure 4.1b). As velocity increases, attenuation decreases across all effective pressures, consistent with both theoretical and experimental observations (e.g., Li and Matsushima, 2024; Yang et al., 2021). This effect is related to the matrix stiffening (i.e., sand with high ice saturation or with increased effective pressures), which allows acoustic wave to transmit more efficiently, thereby reducing energy loss (Li and Matsushima, 2024; Zimmer et al., 2002). The trends are relatively similar across all pressures, showing a non-linear relationship, especially due to the varying rate of change at high and low ice saturations. The data point values for each pressure are visibly separated, indicating that by measuring both velocity and attenuation, the effects of pressure and ice saturation can be distinguished. However, it is important to note that the effect of pressure on velocity is smaller compared to that of ice saturation, requiring a significant pressure contrast to differentiate the effects. In contrast, attenuation is more sensitive to pressure effects, complementing the velocity data and suggesting that ice saturation may be inferred from both acoustic parameters.

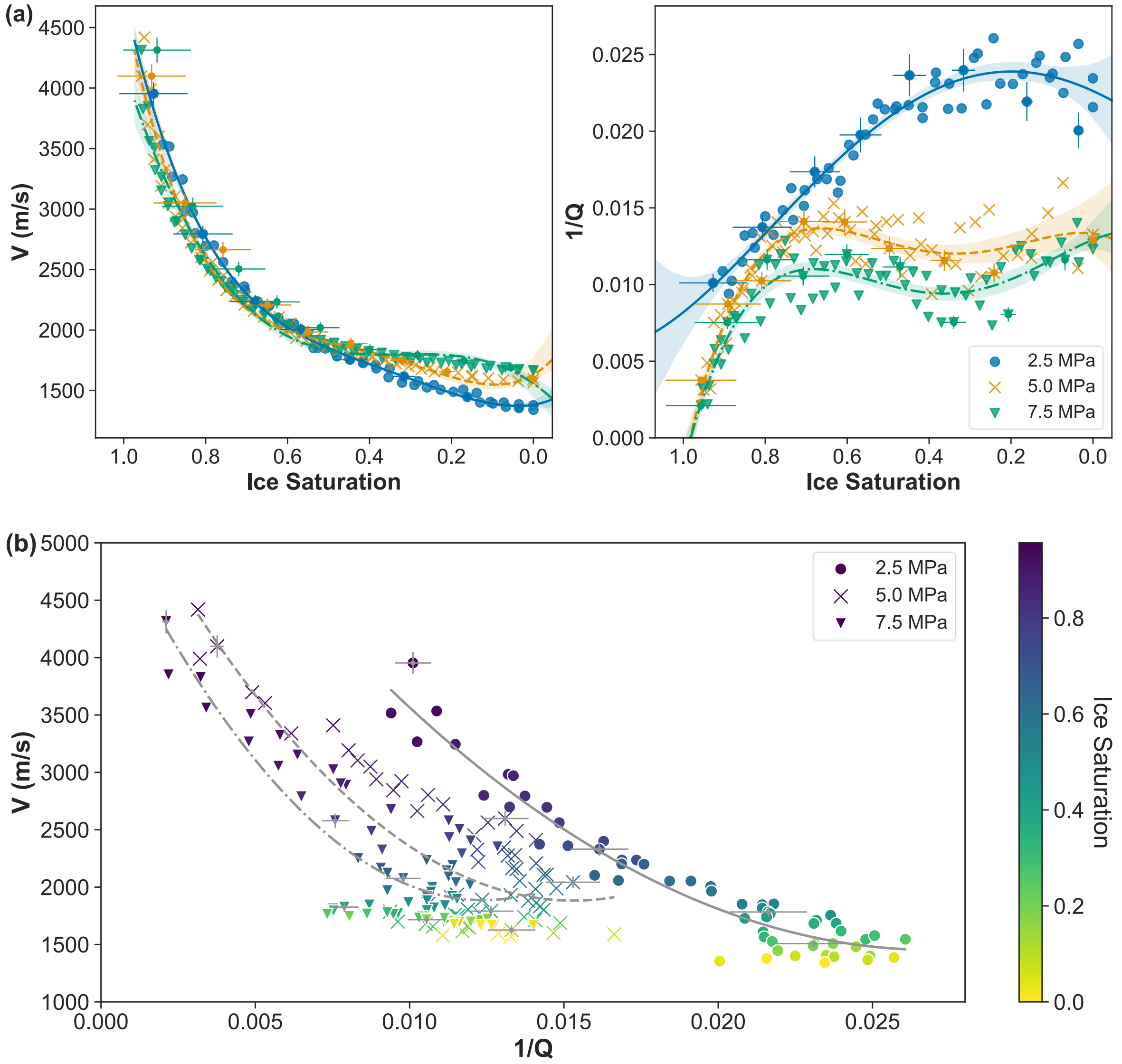

Figure 4.1 Variations in P-wave velocity and attenuation at 10 kHz plotted: a) across ice saturations during the ice melting process at various effective pressures, with lines and shaded areas representing fourth-order regression models with R^2 of 0.99, 0.98,

0.98 for velocity and 0.94, 0.82, 0.79 for attenuation at 2.5, 5, and 7.5 MPa, respectively; and b) between each other, with lines representing second-order polynomial regression models with R^2 of 0.94, 0.72, and 0.72 at 2.5, 5, and 7.5 MPa, respectively. Cross-error bars are plotted every 10 data points in (a) and every 15 data points in (b).

Velocity varies slightly with frequency at all effective pressures, with more variation observed at higher ice saturations, for example, at S_i ~ 0.9 (Figure 4.2a). Small velocities occur at around 1.5 kHz at all pressures, which can be excluded from the analysis due to the cut-off frequency. We observed similar peaks around 18 kHz across all pressures, which could be caused by variations in ice distribution in the scale of 0.1 m, as inferred from the wavelength at that frequency. Aside from these variations, velocity remains relatively constant within this frequency range.

However, velocity exhibits unique frequency-dependent behaviour at high saturations, as velocity decreases with frequency at S_i > ~0.9 and increases at S_i = 0.9 to 0.8 (Figure 4.2c). This velocity increase may result from the squirt flow mechanism, where melting ice leads to a partially connected framework with water pockets, creating a strong contrast between the solid framework and water-filled pores. High-frequency waves cannot equilibrate pressure differences quickly due to restricted pore spaces, leading to a stiffer response and higher velocity (Müller et al., 2010). This effect is more pronounced at higher pressures (5.0 and 7.5 MPa), which may be due to greater grain contact, increasing the stiffness contrast between the solid framework and water-filled pores.

Attenuation varies more with frequency, especially at higher ice saturations at 2.5 MPa and at most saturations at 5 and 7.5 MPa (Figure 4.2b). Attenuation is generally lowest at high saturation (S_i ~ 0.9) across the entire frequency range, indicating that high saturations uniformly reduce attenuation. At intermediate saturations (S_i ~ 0.6 to 0.3), attenuation increases with more noticeable variations at specific frequencies. For instance, at this saturation range, low attenuation values occur around 3-4 kHz at 5 and 7.5 MPa. At S_i = 0, attenuation reaches its highest values, with similar frequency variations compared to the intermediate saturation. Above 5 kHz, attenuation varies similarly across all pressures. We observed noticeable peaks around 13-14 kHz, followed by dips around 15 kHz. These variations at higher frequencies may be influenced by small-scale heterogeneities, as also seen in the velocity data.

We also evaluated the relationship between the acoustic parameters and ice saturation at each frequency using Spearman's rank correlation (Figure 4.2d). This analysis evaluates the frequency dependency—sensitivity of each measurement frequency—to changes of ice saturation, leveraging the multi-frequency capability of the acoustic pulse tube.

Velocity correlates strongly with changes in ice saturation (r > 0.81), consistently exceeding the 99% confidence level across all frequencies and effective pressures. As ice saturation decreases, velocity also decreases, as confirmed by the positive correlation. In contrast, attenuation shows more complex patterns. It generally correlates negatively with ice saturation, indicating that attenuation increases as ice saturation decreases. Attenuation measured at 2.5 MPa exhibits stronger correlation values on average than at 5 and 7.5 MPa.

Attenuation exhibits its strongest and most consistent correlations between 5 and 10 kHz, particularly at 7 kHz, where all correlation values surpass the 99% confidence threshold. Across most frequencies, attenuation patterns are similar at all effective pressures, except in the lower frequency band (~2 to 5 kHz), where differences are more pronounced. At 2.5 MPa, attenuation shows strong negative correlation in this frequency range, while at higher pressure, correlations are weaker correlations (ranging from weakly positive to near zero). These differences may reflect attenuation values approaching the system's detection limit (< 0.01 or Q > 100) at 5 and 7.5 MPa, which is still relevant since attenuation magnitudes of most importance in applied geophysics are above 0.01 (e.g., Allmark et al., 2018; Parolai et al., 2022). However, we can exclude the correlation values from this range due to the cut-off frequency.

In summary, velocity strongly correlates with ice saturation across the frequency band, while attenuation exhibits its strongest correlation at lower frequencies, particularly around 7 kHz. These results highlight the importance of selecting an appropriate frequency range to effectively capture frequency-dependent mechanisms related to ice content in ice-bearing sediments. Optimising measurement frequencies improves our ability to monitor and predict changes in frozen grounds, with broader applications for quantifying and monitoring ice content in permafrost regions (e.g., Hilbich et al., 2022; Lin et al., 2018).

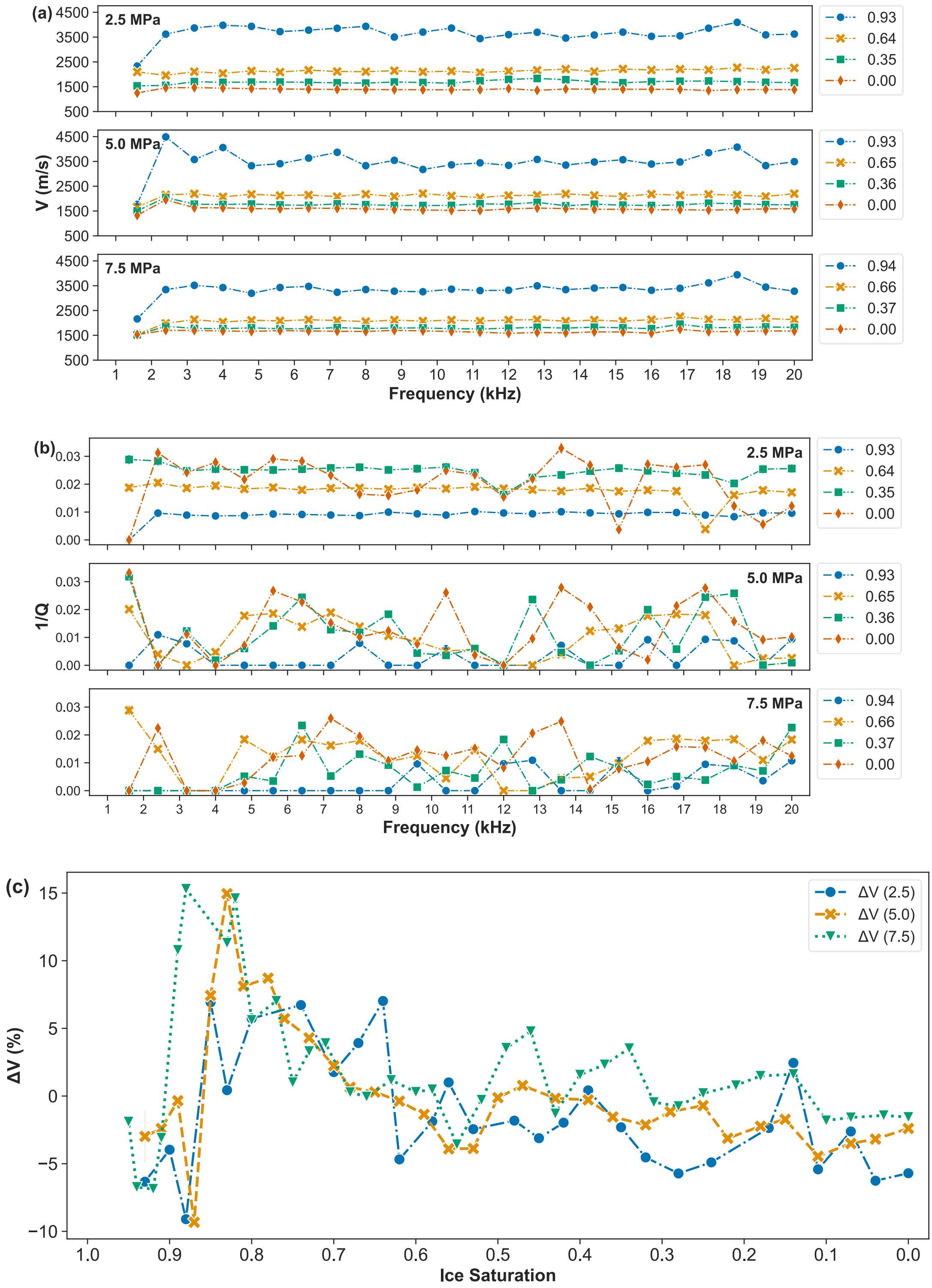
(a)
2.5 MPa
5.0 MPa
7.5 MPa
V (m/s)
4500
3500
2500
1500
500
0.93
0.64
0.35
0.00
0.93
0.65
0.36
0.00
0.94
0.66
0.37
0.00
1 2 3 4 5 6 7 8 9 10 11 12 13 14 15 16 17 18 19 20
Frequency (kHz)
(b)
1/Q
0.03
0.02
0.01
0.00
2.5 MPa
5.0 MPa
7.5 MPa
0.93
0.64
0.35
0.00
0.93
0.65
0.36
0.00
0.94
0.66
0.37
0.00
1 2 3 4 5 6 7 8 9 10 11 12 13 14 15 16 17 18 19 20
Frequency (kHz)
(c)
ΔV (%)
15
10
5
0
−5
−10
ΔV (2.5)
ΔV (5.0)
ΔV (7.5)
1.0 0.9 0.8 0.7 0.6 0.5 0.4 0.3 0.2 0.1 0.0
Ice Saturation

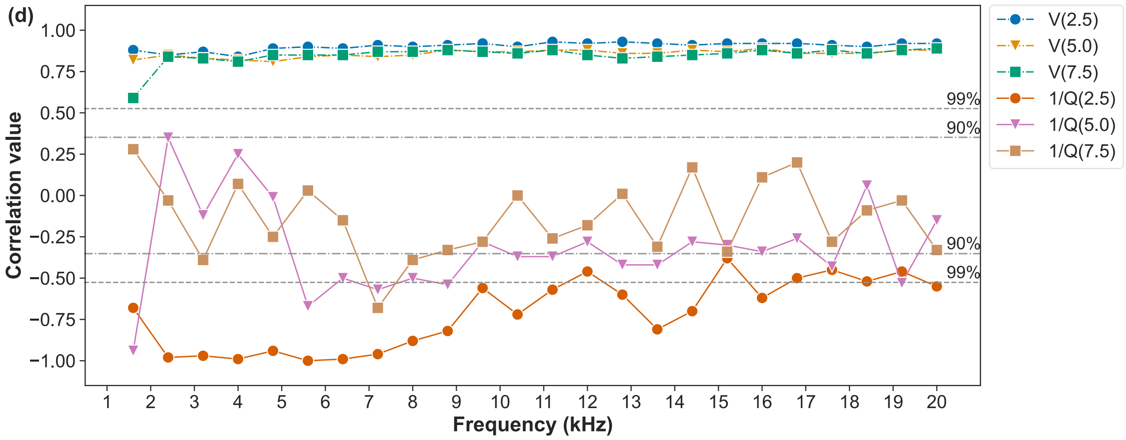

Figure 4.2 Experimental measurements of a) P-wave velocity and b) attenuation frequency spectra (1-20 kHz) at selected saturations (as shown in the legend). c) Percentage changes in velocity across the frequency spectrum at various saturations. d) Correlation values of velocity and attenuation with ice saturation across the frequency spectra at various effective pressures. V and 1/Q represent velocity and attenuation, while 2.5, 5.0, and 7.5 represent effective pressures in megapascals (MPa).

4.3.2 Insight from modelling

All modelled velocities decrease as ice melts, with varying rates at each effective pressure (Figure 4.3a). The LeClaire model predicts the steepest decrease at high saturation ($S_i > 0.8$), followed by the HBES models with Voigt, Brie, and Reuss approximations. These differences reflect how ice distribution affects velocity—LeClaire assumes the most heterogeneous (patchy) distribution, while HBES-Reuss represents the most uniform, with Voigt and Brie in between.

At 2.5 MPa, the experimental velocities align well with the HBES-Voigt model, particularly at intermediate saturations ($S_i = 0.8$ to 0.4), but shift towards the LeClaire model at lower saturation ($S_i < 0.2$). At 5 and 7.5 MPa, experimental velocities are still in good agreement with HBES-Voigt at most saturation but closer toward the LeClaire model than at 2.5 MPa. At high saturations ($S_i >$ 0.9), experimental velocities are the closest to the HBES-Brie and Reuss predictions.

These comparisons suggest that ice is more uniformly distributed during early melting ($S_i > 0.8$), and becomes increasingly heterogeneous as saturation decreases. Higher effective pressure causes experimental velocities to shift closer to the LeClaire prediction at intermediate saturations (e.g., $S_i = 0.8$ to 0.4), likely due to pressure-induced changes in pore structure (Zimmer et al., 2002). As grain contact increases under higher pressure, ice in smaller pore spaces may melt at different rates compared to larger spaces, where the availability of pore fluid to transfer heat differs, promoting uneven melting rates (Abbasi et al., 2022; De Lemos, 2012).

All modelled attenuations increase with melting, although the trends are less straightforward than for velocities (Figure 4.3b). At 5 and 7.5 MPa, attenuation increases from $S_i = 1.0$ to ~0.4, then levels off or decreases. At 2.5 MPa, similar patterns only occur in the LeClaire and HBES-Voigt models, while the HBES-Brie and Reuss models show near-continuous increases. While ice distribution affects velocity at all pressures, attenuation becomes less sensitive to distribution at higher pressures in the HBES models. We also observed shifts in modelled attenuation peaks, although different from the experimental trends. For example, the HBES-Voigt peak shifts from lower to higher ice saturation as effective pressure increases, moving from $S_i = 0.125$ at 2.5 MPa to $S_i = 0.375$ at 7.5 MPa.

At 2.5 MPa, experimental attenuation aligns well with HBES-Voigt at low saturations ($S_i < 0.6$), but exceeds model predictions at higher saturations, possibly indicating an additional loss mechanism beyond Biot theory. At 5 and 7.5 MPa, the experimental trends become more complex. Experimental attenuation is higher than predicted at $S_i > 0.6$, and more variable at lower saturations, but still closer to the HBES models.

While both models provide insight into the velocity and attenuation trends, differences suggest that additional mechanisms may be at play. To explore further, we investigated the effects of ice morphology and the sediment frame’s permeability using the HBES-Voigt model, which showed the best fit to experimental data. The following discussion focuses on attenuation, as velocity does not change significantly with either parameter. Velocity results are provided in Appendix F.

Modelled attenuation increases as pore-filling (PF) concentration increases across all saturations and pressures (Figure 4.3c). At 2.5 MPa, this effect is strongest, especially at low ice saturations ($S_i < 0.4$). Experimental attenuation aligns well with the higher PF concentration at low saturations ($S_i < 0.6$), suggesting a transition from cementing (C = 1 – PF) at higher saturation to pore-filling at lower saturations. This trend is less pronounced at higher pressures. The pore-filling mechanisms offer insight into how acoustic properties are affected, particularly at lower ice saturations where the formation is potentially less uniform.

Modelled attenuation also varies with permeability at most ice saturations ($S_i < 0.8$) across all pressures (Figure 4.3d). Higher permeability leads to higher attenuation, especially at low saturation ($S_i < 0.4$), consistent with Biot’s global flow theory, where greater relative motion between the solid matrix and viscous fluid leads to higher attenuation. Experimental attenuation mostly corresponds to permeabilities of 0.3-0.6 D, which is reasonable for tightly packed ice-bearing sand similar to permafrost conditions (typically around 0.01 – 1.01 D, as reported by Sizemore and Mellon, 2008). The increase in permeability may explain the distinct increase in experimental attenuation at lower ice saturation ($S_i < 0.3$), especially at 7.5 MPa. As ice melts, liquid water content and permeability increase due to more spaces becoming available

(Mahabadi et al., 2019), thus allowing greater pore fluid movement relative to solid grains, which consequently increases attenuation (Lee et al., 2024).

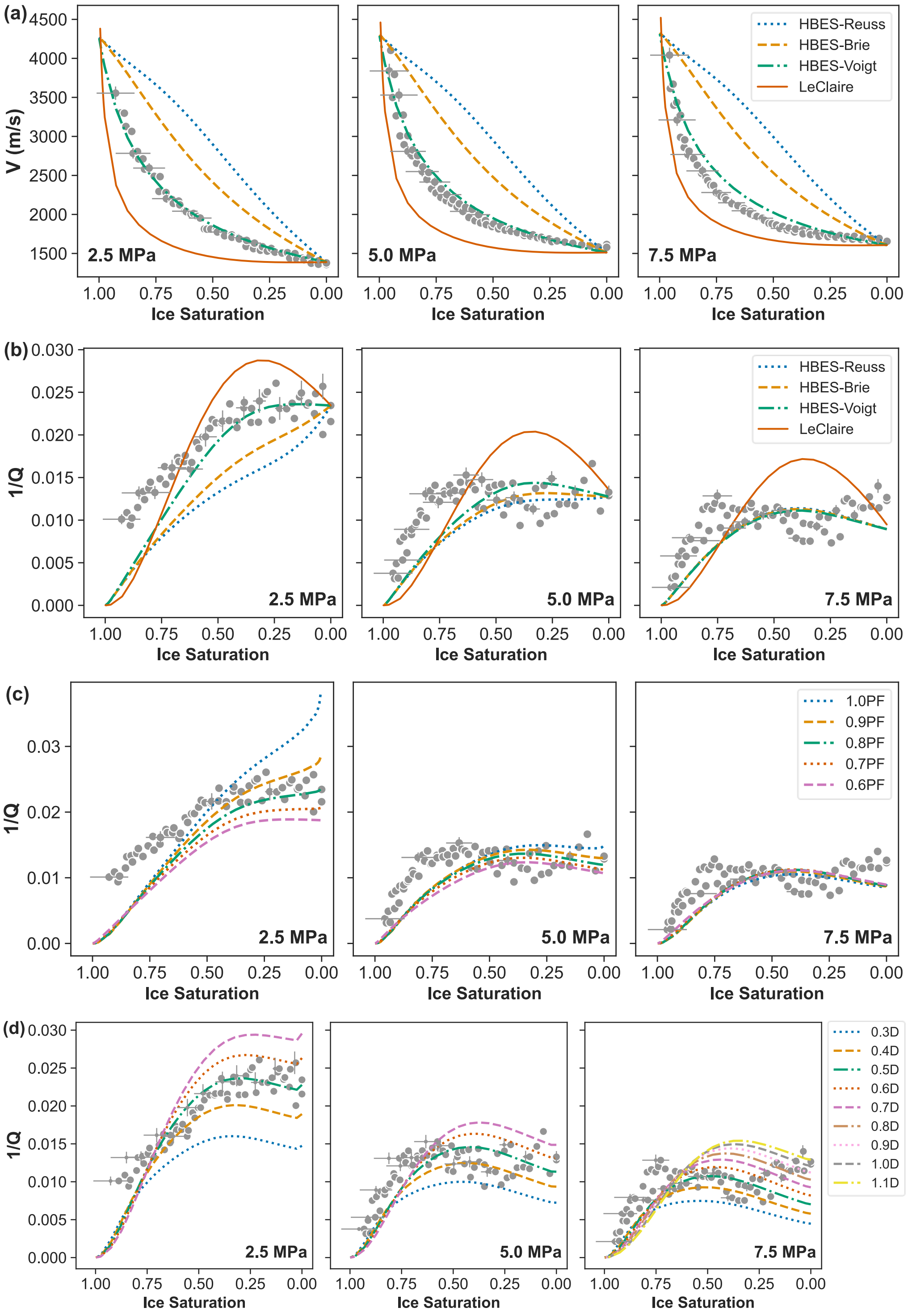

Figure 4.3 Comparison of experimental data and model results for P-waves at 10 kHz: a) velocity and b) attenuation (pore-filling concentration, PF = 1.0, permeability = 0.5 D); c) attenuation at different PF (with the remainder of Si as cementing ice, i.e., 1 - PF); and d) attenuation at different permeabilities for PF = 1.0. Results in c) and d) are modelled using the HBES model with Voigt approximation. Cross error bars are plotted every 15 experimental data points.

4.4 Discussion

Ice content in ice-bearing sand affects both acoustic velocity and attenuation (at 10 kHz) across all tested effective pressures. As ice melts, velocity decreases and attenuation increases, consistent with previous studies at ultrasonic frequencies (e.g., Matsushima et al., 2016; Yang et al., 2021) and with our earlier work (Chapter 3; Sutiyoso et al., 2024b). This study expands on those findings by examining how different pressures influence these acoustic properties. For instance, while the sensitivity of velocity to ice saturation remains relatively consistent across all pressures, velocity exhibits a steeper decrease at 2.5 MPa, particularly in the intermediate saturation range. In contrast, attenuation is more pressure-dependent. The lowest pressure (2.5 MPa) displays greater sensitivity, especially at higher ice saturations. This effect could be linked to the influence of effective pressure. At low pressure, the sand may experience more strengthening from ice formation, thus losing more structural support as the ice melts (i.e., decreasing frame bulk modulus), which affects both velocity and attenuation even down to fully melted conditions ($S_i = 0$). These findings highlight the value of conducting multi-depth acoustic measurements in ice-bearing sediments.

At lower effective pressures, grain-to-grain contacts are less forceful, allowing ice to exert greater mechanical influence (Alkire and Andersland, 1973). Since water expands when it freezes, the resulting ice could dilate the sand pack, especially at lower pressures. This effect is also observed with gas hydrates (e.g., Priest et al., 2021). Consequently, ice melting causes the largest acoustic shift at 2.5 MPa. At higher pressure (5.0 and 7.5 MPa), stronger grain contacts diminish the influence of ice in supporting the matrix.

Another interesting point is that ice may directly support the sand frame only up to a certain point, approximately $S_i > 0.6$, especially if there is dilation due to volume expansion upon freezing of water. Velocity data show an inflection point (where velocities under all effective pressures intersect) at $S_i \sim 0.6–0.7$. This observation may suggest that load-bearing ice is significant for $S_i > 0.6$. Across pressures, attenuation at $S_i > \sim 0.7–0.8$ shows similar values, likely because Biot-type flow is minimal when inter-pore channels are blocked, resulting in small but finite losses. Since ice is non-microporous, attenuation is essentially controlled by Biot global fluid flow, thus reducing sub-microporous squirt flow mechanisms. Therefore, attenuation changes are dominated by permeability evolution.

These interpretations also raise the possibility that attenuation behaviour is linked not only to ice content but also to its morphology, as also shown in gas-hydrate studies (e.g., Sahoo and Best, 2021). At low saturations, ice is likely pore-filling, while at high saturations it may act as a cementing or load-bearing phase. This transition can influence how Biot flow and frame stiffness evolve with pressure and melting. Therefore, attenuation may serve as an indirect diagnostic of ice morphology as well as quantity.

Velocity strongly correlates with ice saturation across the entire frequency range (1-20 kHz), while attenuation correlates more strongly at lower frequencies, particularly around 7 kHz. This could result from slightly higher attenuation around 7 kHz falling within the detectable range for the pulse tube. Variation at higher frequencies may also be attributed to the heterogeneities of water and ice distribution caused by the thawing process. At these frequencies, attenuation becomes more sensitive to changes in ice content because the shorter wavelengths are comparable in scale to the heterogeneities, making them more apparent. In contrast, at lower frequencies, the longer wavelengths average out these small-scale variations, resulting in a smoother and more predictable relationship between attenuation and ice content (Sutiyoso et al., 2025). These complementary behaviours strengthen the potential of velocity and attenuation as dual indicators to estimate ice content in field scenarios, such as well-logging application at similar frequencies (Hearst and Nelson, 1985).

It is also noteworthy that attenuation values at higher pressures and lower saturations were sometimes close to the upper detection threshold of the system ($Q > 100$), suggesting that subtle changes in permeability or wave-induced fluid flow may have gone undetected. This limitation implies that attenuation is more effectively used as a monitoring tool in lower-pressure or higher-saturation settings where Biot flow is more active.

While this study tests a range of effective pressures, allowing for insights into multi-depth conditions (approximately 150 – 450 m below the surface, depending on the sediment density), we acknowledge that our use of a homogenous sand pack may differ from the field condition, where sediment is often composed of varying grain sizes and lithologies. Additionally, sand tends to dilate under pressure, potentially causing small changes in porosity under different pressures. While tracking sample strain would clarify this mechanism, the current pulse tube design restricts internal instrumentation due to space constraints and potential interference with wave propagation.

Another point worth considering is the potential dependence of acoustic response due to freezing and melting histories (Dou et al., 2016; Li and Matsushima, 2024). Ice distribution during melting may not perfectly reverse that during freezing, especially if drainage pathways, air entrapment, or dilation effects differ. Such hysteresis could influence acoustic properties and should be tested in future experiments.

These limitations suggest future research directions, including investigating different sediment types, applying these techniques to field samples, and measuring complementary parameters for a more thorough understanding. Ultimately, the goal is to implement these findings for real-time monitoring of permafrost environments.

4.5 Conclusions

A novel acoustic pulse tube was used to investigate the effect of ice content on velocity and attenuation in ice-bearing sands during melting, across a frequency range of 1–20 kHz, as a function of effective pressure (2.5, 5.0 & 7 MPa). The results serve as an analogue for permafrost conditions at depths between approximately 150 and 450 m.

As shown in Chapter 3 (Sutiyoso et al., 2025), ice content significantly affects the acoustic properties of the sediment. Here, we have shown that this velocity decrease occurs at all pressures, with the largest change observed at the lowest effective pressure (2.5 MPa), where weaker grain-to-grain contact allows ice to exert greater influence on the acoustic response. Additionally, attenuation increases as the ice melts, peaking at lower saturations under lower pressures and at higher saturations under higher pressures. This extension of the Chapter 3 findings further highlights the relationship between effective pressure and the acoustic behaviour of ice-bearing sediments.

Both velocity and attenuation exhibit non-linear behaviour with changes in ice content. Their correlation suggests that combining both parameters could potentially be used to infer ice content at given depths within the effective pressure range of 2.5-7.5 MPa. Comparison with Biot three-phase models indicates that ice distribution significantly affects velocity, while attenuation is more influenced by pore structure—reflecting ice morphologies (the proportion of pore-filling to cementing ice) and the sediment frame's permeability—as well as pressure conditions.

Compared to studies at ultrasonic frequencies, the lower-frequency measurements used in this study provide insights at scales relevant to field applications. These findings highlight the importance of understanding ice saturation, distribution, and morphology for accurately predicting acoustic wave behaviour in ice-bearing sediments, with potential applications for permafrost monitoring.

Chapter 5 Conclusion and Recommendation

5.1 Summary of Key Findings

This thesis has presented controlled laboratory experiments using an acoustic pulse tube to study the effects of water and ice saturation on the elastic wave behaviour of unconsolidated sand at sonic frequencies. The key findings are summarised below:

In Chapter 2, compressional wave (P-wave) velocity and attenuation were measured at varying water saturation levels in unconsolidated sand samples within the sonic frequency range (1-20 kHz). Velocity decreases with increasing water saturation up to 75% and then increases at higher saturation levels. Attenuation increases at lower saturation and stabilises near full saturation. These trends are consistent across samples, establishing a reliable foundation for the rest of this thesis. Velocity increases with frequency, while attenuation shows a more complex frequency dependency. Effective pressure further influences these properties, with velocity increasing especially under saturated conditions and attenuation decreasing especially under dry conditions. These findings align with the HBES model (an effective medium rock physics model developed by Marín-Moreno et al., 2017), which was extended to incorporate uniform and patchy saturation. The model also tested various permeability and gas bubble values, offering insights into wave propagation mechanisms in sediments at these frequencies.

In Chapter 3, the experiments demonstrated that ice saturation significantly affects P-wave velocity and attenuation in ice-bearing sands at sonic frequencies. As ice melts, velocity decreases and attenuation increases, especially at higher ice saturations (> 60%), where the most pronounced changes occur. Both velocity and attenuation show frequency-dependent behaviour, with attenuation at lower frequencies being more sensitive to changes in ice saturation. Rock physics models with three-phase approaches (Leclaire et al., 1994; Marín-Moreno et al., 2017) approaches, support these findings. These models highlight the role of ice distribution and morphology, sediment frame permeability, and pore fluid dynamics. Ice distribution has a greater effect on elastic wave properties than ice morphology, while permeability and gas bubbles mainly affect attenuation.

In Chapter 4, P-wave velocity and attenuation were observed in ice-bearing sands during melting under elevated effective pressure (2.5, 5.0, and 7.5 MPa), simulating permafrost conditions. As ice melts, velocity decreases and attenuation increases, with the largest changes at lower pressures, where the stresses at grain-to-grain contacts are smaller, thus allowing ice to exert more influence. Frequency-dependent trends show slight variations in velocity with frequency, while attenuation exhibits significant fluctuations, particularly at intermediate ice saturations and lower frequencies. Three-phase models (Leclaire et al., 1994; Marín-Moreno et al., 2017) identify ice distribution, morphology, and permeability as critical factors influencing the acoustic properties. Ice distribution affects velocity and attenuation similarly across all tested effective pressures. However, the effects of ice morphology and permeability diminish at higher pressures due to matrix compaction. These findings provide insights into melting permafrost conditions at varying depths.

5.2 Discussion and Reflection

The results of this study provide insights into the acoustic wave behaviour of water-saturated and ice-bearing sands under varying conditions. The findings contribute to a better understanding of subsurface systems, for example, carbon dioxide storage, including the injection process that requires monitoring partial gas and water saturation (Fawad and Mondol, 2021; J. Li et al., 2020), and thawing permafrost due to global warming (Paull et al., 2022; Tourei et al., 2024).

The relationship between P-wave velocity and water saturation in sediments is well-documented, particularly in controlled laboratory settings (e.g., Amalokwu et al., 2014; Barriere et al., 2012; He et al., 2021; Si et al., 2016). However, its attenuation counterpart remains overlooked (Oh et al., 2011). While velocity is highly sensitive to changes at high saturation levels (> 70% for nearly homogeneous samples, as demonstrated in this study), it is less sensitive at lower saturations. This highlights the importance of measuring attenuation alongside velocity, as attenuation is more sensitive to changes in pore content at lower water saturations under most water distribution, whether homogeneous or heterogeneous. This study demonstrates this sensitivity and confirms the findings through comparison with a rock physics model at sonic frequencies. Although separating intrinsic and apparent attenuation is challenging (Buckingham, 2005; Matsushima et al., 2017), these findings might give more incentives for more attenuation measurements to complement velocity studies.

Previous studies on wave propagation in ice-bearing sediment have mainly focused on the effects of temperature on ultrasonic frequency measurements (e.g., Carcione and Seriani, 1998; Li and Matsushima, 2024; Matsushima et al., 2008), often using consolidated rather than unconsolidated sediments (e.g., Timur, 1968; Yang et al., 2021). These measurements are popular due to the ease of temperature control in laboratory settings and serve as a key parameter to predict phase changes in water. However, temperature changes do not always lead to uniform or predictable variations in ice saturation, particularly in heterogeneous sediments. This limits the exploration of variations in ice distribution. Moreover, ice-bearing sediments are complex systems that often require a three-phase approach (sediment, ice, water) or even a four-phase approach if free gas is involved, as in permafrost containing gas hydrate deposits. Inferring seismic wave behaviour in the field from ultrasonic frequencies requires further calibration for accurate application. Therefore, ice saturation-based measurements are also important to improve field estimates, especially given the growing concern over thawing permafrost. Since permafrost mainly consists of unconsolidated sediments, such as sand and silt, more measurements in ice-bearing sands are important. This study's focus on sonic wave behaviour in ice-bearing sands makes its findings particularly relevant.

Comparing experimental results with rock physics models, i.e., HBES and LeClaire et al.'s models, helps to understand the underlying mechanisms of wave propagation in water-saturated and ice-bearing sediments. Aside from some differences in values, particularly in attenuation, the theoretical models effectively explain the experimental results, such as water and ice distribution within sediment pores, and parameters like permeability and gas bubbles. These agreements provide confidence that the experimental results can be used to help interpret relevant field data.

Focusing on the ice-bearing experiments, I compared the pulse tube results in sonic frequencies with published studies on velocity and attenuation measurements in ice-bearing and gas hydrate-bearing sediments from different methods at different frequency ranges (Figure 5.1 and 5.2). I also compared the results with logging data from various settings (Figure 5.3). For clarity, I only included pulse tube velocity data at 7.5 MPa, as it shows similar trends to those at lower pressures, albeit with slightly lower values (see Chapter 3). However, for attenuation 1/Q, I included data at 2.5 and 7.5 MPa, which show different trends (see Chapter 4). Unlike Figure 5.1, which separates ice-bearing and gas hydrate-bearing sediment datasets into separate panels, Figure 5.2 combines data from both in a single panel.

Pulse tube data show a clear increase in velocity with ice saturation, particularly at higher saturations (Figure 5.1a). This trend aligns with most studies on ice-bearing sediments, particularly with datasets from Dou et al. (2016) and Spangenberg et al. (2018), which used sand at ultrasonic frequencies. Velocities from Hilbich et al. (2022) and Kang et al. (2021) show a steeper increase in seismic velocity at lower saturations, likely due to variations introduced by sediment mixtures, as also observed by Park and Lee (2014) and Zimmerman and King (1986) with the mixtures of sand, silt, and clay. Differences in velocity may also result from ice distribution or heterogeneity, as observed by Nakano and Arnold (1973), who reported more significant increases at lower saturations with uniform ice distribution. In consolidated samples, Timur (1968) showed a consistent increase in velocity with ice saturation under an effective pressure of ~30 MPa at ultrasonic frequencies, resulting in much higher velocities. This observation indicates that high effective pressure reduces the effects of ice distribution and morphology on velocity, as demonstrated in Chapter 4. Overall, the pulse tube measurements effectively capture the expected acoustic wave behaviour in ice-bearing sediments. The gradual increase in velocity suggests that ice acts primarily as a pore-filling material at lower saturations (Li and Matsushima, 2024).

The velocity trends in gas hydrate-bearing sediments do not differ significantly from those in ice-bearing sediments (Figure 5.1b). Pulse tube data align with trends observed by Spangenberg et al. (2018) and Yun et al. (2005), who experimented with methane hydrate in glass beads and THF hydrate in sand, respectively. However, significant increases at lower saturations, as shown by velocity from Wang et al. (2019), reflect differences in hydrate morphology. Gas hydrate morphology in laboratory studies often is cementing caused by using the excess gas method, where gas is introduced into a partially saturated sediment (e.g., Rake and Pinkert, 2021; Wang et al., 2019). This morphology has more strengthening effect than the non-cementing one, especially in unconsolidated sediment (Priest et al., 2021), which is the case shown by Wang et al. (2019). On the other hand, Spangenberg et al. (2018) also used the excess gas method but followed it by injecting water to trigger the recrystallisation process for redistributing the cementing hydrate into a pore-filling morphology, resulting in a gentler increase in velocity. Despite these differences, velocities in ice-bearing sediments are comparable to those in gas hydrate-bearing sediments. However, the nature of hydrate formation must be considered before making direct comparisons.

Similarly, attenuation (1/Q) is influenced by hydrate morphology, often more significantly than velocity. In ice-bearing sediments, attenuation decreases with increasing ice saturation, as shown by the experimental results and Yang et al. (2021), due to reduced porosity and energy loss during wave propagation (Guerin and Goldberg, 2002; Hamilton, 1972). In contrast, attenuation trends in gas hydrate-bearing sediments vary due to morphological transitions, as shown by Sahoo et al. (2019). The first gradient is due to a transition from pore filling to pore bridging morphology, while the second one is from pore bridging to interpore hydrate framework morphology (Sahoo et al., 2019). These stages were also shown by Best et al. (2013), Guerin and Goldberg (2002), and Priest et al. (2005) albeit at different saturation ranges. While the values are comparable, hydrate morphology must be carefully considered when comparing attenuation in ice-bearing sediment and gas hydrate-bearing sediments.

Gas hydrates contain small microporous inclusions that ice does not, although ice grains may exhibit microporosity, at least on the surface, in the form of microcracks. This results in sub-micro squirt flow as an additional loss mechanism (Marín-Moreno et al., 2017), on top of the already complex mechanisms due to the presence of gas. Gas hydrate formation may also change the way sediment grains interact with water (wettability), potentially making them hydrophobic (water-repelling), as hydrate crystals are less likely to bond with water (Casco et al., 2021; Nguyen et al., 2020). This change in wettability affects fluid movement through sediment, changing permeability and influencing wave attenuation. Such a shift in wettability does not occur during ice formation. However, ice formation can influence permeability changes in a different way. Ice may form in larger pores first, as the freezing temperature of water within porous materials is influenced by pore size, with smaller pores experiencing a depression in freezing point due to the Gibbs–Thomson effect (David et al., 2019).

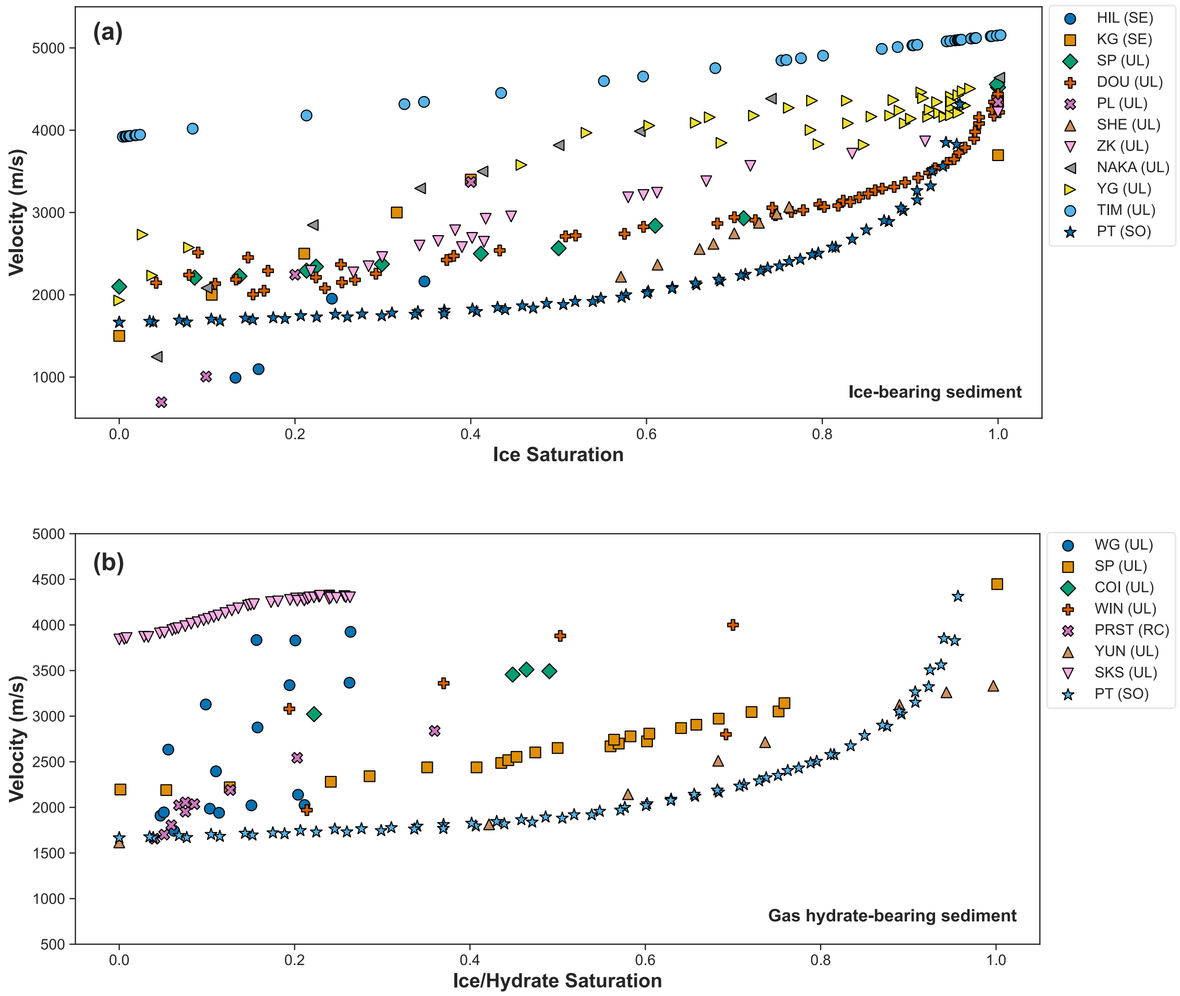

Figure 5.1 Comparison of pulse tube (PT) velocity with published studies in: a) ice-bearing sediments and b) gas hydrate-bearing sediments. The legend lists the codes for the published studies: HIL (Hilbich et al., 2022), KG (Kang et al., 2021), SP (Spangenberg et al., 2018), DOU (Dou et al., 2016), PL (Park and Lee, 2014), SHE (Sheng et al., 2003), ZK (Zimmerman and King, 1986), NAKA (Nakano and Arnold, 1973), YG (Yang et al., 2021), TIM (Timur, 1968), WG (Wang et al., 2019), COI (Choi et al., 2014), WIN (Winters et al., 2007), PRST (Priest et al., 2005), YUN (Yun et al., 2005), and SKS (Sahoo et al., 2019). SE, UL, SO, and RC represent measurements taken at seismic (field survey), ultrasonic, sonic, and seismic (resonant column) frequencies.

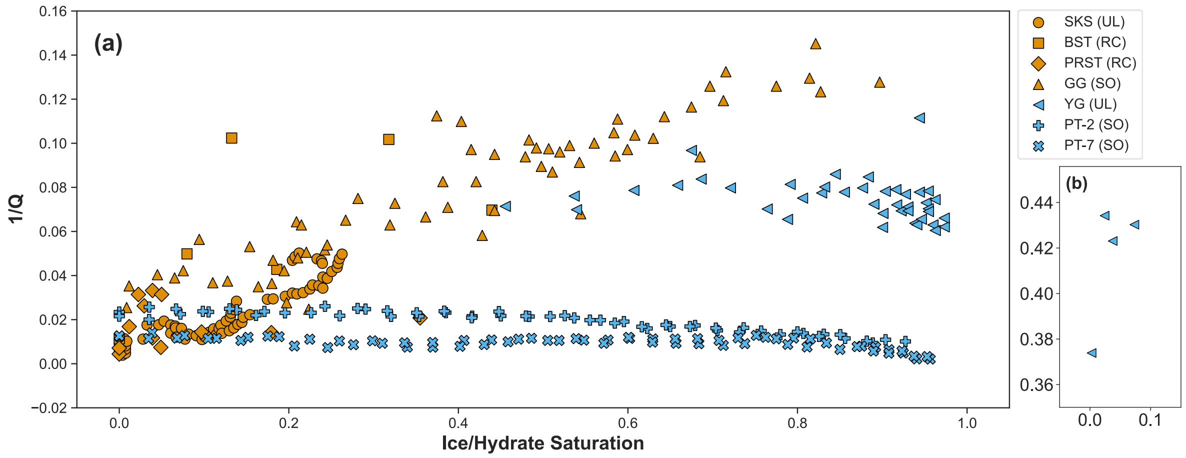

Figure 5.2 a) Comparison of pulse tube attenuation 1/Q to published studies in ice-bearing sediments (blue), and gas hydrate-bearing sediments (brown). b) An inset showing high attenuation from the YG dataset at low saturation, included separately to maintain the clarity of the main panel. The legend lists the codes for the published studies: SKS (Sahoo et al., 2019), BST (Best et al., 2013), PRST (Priest et al., 2005), and YG (Yang et al., 2021). PT-2 and PT-7 represent pulse tube attenuation measurements at effective pressures of 2.5 and 7.5 MPa, respectively. UL, RC, and SO represent measurements taken at ultrasonic, seismic (resonant column), and sonic frequencies, respectively.

In Figure 5.3, the experimental acoustic velocities were compared with field data from sites with confirmed gas hydrate presence: Mallik 2L-38 well (Northern Canada), IODP Expedition 372 - Hole U1518B (Hikurangi Margin), and IODP Expedition 311 - Hole U1328A (Cascadia Margin). These sites differ in sediment composition and environmental settings. The Mallik site mainly consists of sand with small amounts of silt and gravel (Winters et al., 2007). The Hikurangi site is a fault zone, mainly composed of silt and clay, with small portions of sand (Wallace et al., 2019). The Cascadia site is an accretionary prism zone with active cold vents and mainly consists of clay and silt (Riedel et al., 2006).

Both experimental and well-log velocities increase with ice or hydrate saturation, though at different rates. Experimental velocities show a gradual increase at low saturations and a significant rise at higher saturations. In contrast, the Mallik and Cascadia velocities exhibit a steady increase throughout the hydrate saturation range. The Hikurangi dataset displays a steeper increase with saturation, however, this trend is based on a regression model prediction and is limited by the lack of data at higher saturations.

Overall, the gentle increase in experimental velocity at lower saturations aligns well with the logging datasets. Unfortunately, the significant rise at higher saturations observed in the experiments cannot be verified due to limited gas hydrate saturation data in the field. In terms of velocity values, the Mallik site exhibits the highest velocities due to its greater depth (891–1109 m), followed by the Hikurangi site (55–565 m) and the Cascadia site (7–257 m). At lower ice saturations, the experimental velocities are closer to those observed at the Hikurangi and Cascadia sites. Despite some discrepancies in absolute values, the experimental velocities are generally comparable to the well-log velocities. This supports the applicability of the experimental results in detecting and estimating ice and gas hydrate saturation in the field.

However, when applying these findings to real permafrost, it is important to account for the presence of both fresh and saline water, depending on regional and geological conditions. Salinity has minimal effect on P-wave velocity (e.g. a 2.1% increase in clay-rich brine-saturated media at 3.42 M or ~200 g/L, an extreme case) and no effect on attenuation (Jones et al., 1998; Toksöz et al., 1979). However, in ice-bearing media, salinity plays a key role by lowering the freezing point due to hydration shells around solvated ions (Lyu et al., 2020). As ice crystallises, ions are expelled into the remaining water, increasing its electrolyte concentration (King et al., 1988). This requires more energy to complete the phase change (Dou et al., 2016), altering ice formation within the porous medium, especially near full ice saturation. In unconsolidated sediments like the sand used in this study, velocity increases sharply near full freezing due to a uniform phase change. However, in saline conditions, hydration shells delay freezing, resulting in a more gradual velocity change (Lyu et al., 2020).

Reflecting on the methodology, the pulse tube experimental setup proved reliable for measuring acoustic properties in water-saturated and ice-bearing sands. The results align quite well with both published works and field data, as well as theoretical models, despite potential variations introduced by technical factors, such as the use of a jacketed system or achieving uniform water and ice distribution. The controlled experimental environment ensured reproducible results, validating the observed results.

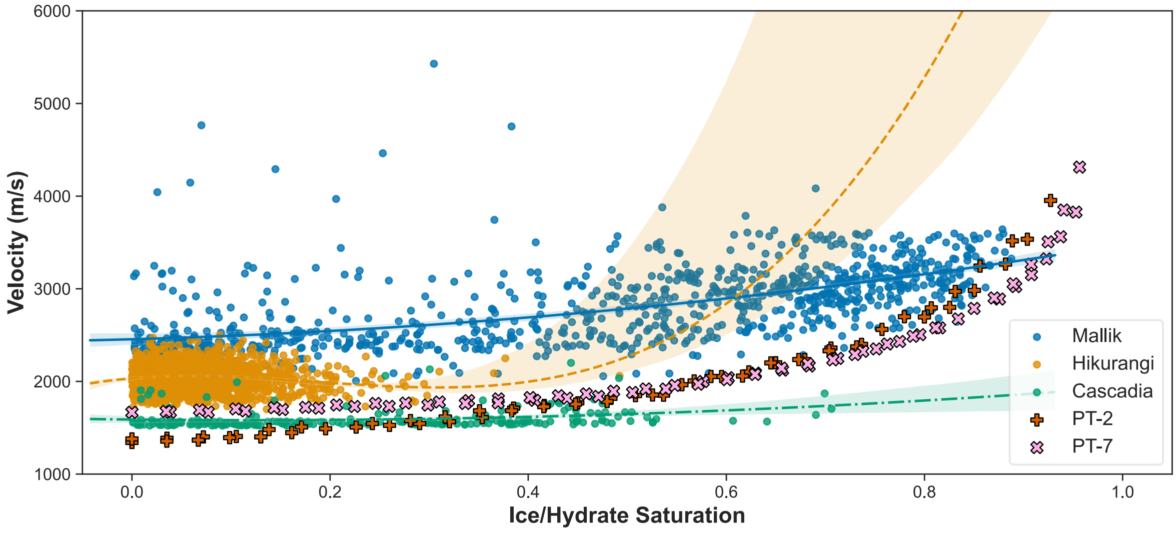

Figure 5.3 Comparison of pulse tube ice velocities with sonic velocities from logging measurements at various gas hydrate-bearing sites. The legend lists the site names. PT-2 and PT-7 represent pulse tube velocities measured at effective pressures of 2.5 MPa and 7.5 MPa, respectively. Sonic velocities are displayed as scatter points, while the lines and shaded areas represent the regression models for each dataset and their 95% confidence intervals.

5.3 Recommendation and Future Work

Building on the findings of this research, several recommendations and directions for future work appear.

Firstly, further investigation is needed to examine how sediment type influences acoustic wave behaviour in ice-bearing sands. For example, using a mixture of sand and silt to mimic the sediment composition of permafrost and sites with confirmed gas hydrate presence, such as the Mallik and Hikurangi sites. This approach could enhance understanding of how sediment composition affects acoustic responses and strengthen the further use of ice-bearing sediments as analogues for gas hydrate-bearing sediments. However, variations in grain size may increase attenuation due to scattering if the different grain-sized sediments are not well intermixed, potentially masking intrinsic attenuation. Addressing this issue might require advanced techniques to separate these effects.

Additionally, exploring the impact of dynamic freezing and thawing cycles on acoustic properties would better simulate natural permafrost conditions. In a thawing permafrost scenario, measuring acoustic properties during melting is sufficient. However, the freezing and thawing cycles may introduce further strengthening or weakening of the sediment matrix. Understanding these effects is essential for assessing sediment stability, with implications for geohazard and infrastructure in cold regions. Such studies could reveal insights into how permafrost systems respond to seasonal and long-term climate changes.

Joint measurement of compressional (P-wave) and shear (S-wave) velocities and attenuation can provide essential insights into the physical and mechanical properties of ice-bearing sediments, critical for effective permafrost monitoring. P-wave properties are more sensitive to fluid characteristics, while S-wave properties respond primarily to solid ice content and morphology (Li and Matsushima, 2024). For instance, cementing ice increases both P- and S-wave velocities, whereas pore-filling ice predominantly affects P-wave velocity with minimal impact on S-waves (Matsushima et al., 2016). Sahoo and Best (2021) also found S-wave attenuation to be more sensitive to morphology transitions in hydrate-bearing sediments. Unlike P-waves, S-wave attenuation is governed by the elastic contrast between ice and sediment grains and is unaffected by squirt flow (Guerin and Goldberg, 2005; Yang et al., 2007). These distinct responses to pore fluids and solid phases offer complementary information for more accurate subsurface characterisation. Moreover, combined analysis of both wave types enables the estimation of elastic moduli—key indicators of mechanical stability—and enhances the reliability of geophysical inversion models (e.g., Kang et al., 2021; Zhang et al., 2023).

Developing imaging techniques to complement the pulse tube is also an important goal. As discussed, the distribution of water and ice within the sediment matrix significantly affects acoustic wave propagation. Using non-invasive imaging methods could improve understanding and help address variations caused by sample heterogeneity. Techniques such as electrical resistivity tomography (ERT) or fibre optic imaging could be synchronised with acoustic measurements to provide detailed insights. However, introducing additional equipment into the pulse tube could disrupt propagating waves, leading to variations that need to be considered carefully.

Lastly, applying this research to field settings would help bridge the gap between laboratory findings and real-world scenarios. Once the acoustic responses of various sediment types are established, the next step should involve natural samples, particularly from thawing permafrost (due to its urgency) and gas hydrate deposits (due to their complexity). Although recovering natural cores can introduce disturbances that may alter their in-situ state, measuring these samples would enhance the interpretation of pulse tube data. This could improve its applicability to field measurements, such as logging activities and sub-bottom profiler surveys, which operate in similar sonic frequency ranges.

5.4 Concluding Remarks

This study has enhanced the understanding of acoustic wave behaviour in water-saturated and ice-bearing sands. It provides insights into how water saturation, ice content, and acoustic properties interact under various effective pressures across a wide range of sonic frequencies. By combining experimental measurements with theoretical models, the research has addressed the underlying mechanisms of these systems and addressed gaps in existing knowledge, particularly regarding the indirect estimation of ice saturation in sediments. Additionally, comparisons of the experimental results with published studies confirm the validity of the findings.

The findings hold significant implications for permafrost studies, providing a foundation for improved monitoring techniques in the context of a warming climate. The methodologies and results presented here also open direction for interdisciplinary collaboration, linking geophysics, engineering, and environmental science to address challenges arising from permafrost degradation.

In conclusion, this work not only contributes to the field of permafrost acoustics but also establishes a groundwork for future research and practical applications. As the understanding of subsurface processes continues to grow, the insights gained from this study will remain valuable in advancing scientific efforts to effectively understand permafrost environments.

Appendix A Application of Proctor Method

We used the Proctor method to prepare sand packs with consistent properties. The Proctor method, or proctor soil compaction test, is commonly used to find the optimal level of moisture for soil and the maximum dry density based on a determined compaction and is applicable to soils and soil-aggregate mixtures. The test achieved grain compaction using a hammer with a known energy. The sample is made up a several layers, each one tamped and compacted using hammer. The calculation of Proctor's compaction energy (*E*) was adapted based on the number of layers (n_L), number of hammer blows (n_B), weight of hammer (*w*), height of fall (*h*) and mold volume (*vol*), calculated using Equation A.1 below:

$$E = \frac{n_L n_B w h}{vol} \tag{A. 1}$$

We kept the same number of layers, bowls, hammer weight, and fall height for all samples. The compaction energy calculation is important if we need to use different sample sizes. By adjusting the parameters as needed, we can keep the same compaction energy, thus keeping various samples at a similar compaction. The parameters are provided in Table A.1.

Table A.1 Sand compaction method: a) Examples from Proctor method based on ASTM D1557 / AASHTO T180 and b) modified Proctor method with adjusted parameters used in this study.

Compaction Energy (Joules)	Layers	Blows	Hammer Weight (kN)	Fall Height (m)	Mould Volume (m^3)	Remarks
76.808	3	25	0.025	0.305	0.007	[a)] Proctor 6-inch test
172.818	3	25	0.025	0.305	0.003	[a)] Proctor 4-inch test
165.687	5	26	0.012	0.15	0.001	[b)] Current experiment

Appendix B Calculation of Microwave Method

The processing of microwave data consisted of deconvolution, an inverse method to calculate the dielectric constant of the sample and its conversion to water saturation. The transmitted signal time series of the saturated sample was deconvolved with the transmitted signal time series from the dry sample to eliminate the effect of the sample jacket and dry sand, focusing on the water content of the sample. Then, we utilised a non-linear least squares optimisation method provided by MATLAB to do an inverse calculation to obtain the dielectric constant of the sample. The inverse method was conducted by comparing the deconvolved signal to a wave propagation model (Equation B.1; Pozar, 2012).

$$\gamma = e^{\frac{-i\omega L\sqrt{\varepsilon_r}}{c}} \tag{B.1}$$

where γ is the theoretical transmission or propagation coefficient, ω is the angular frequency, L is the distance between two antennas, ε_r is the relative dielectric constant of the sample and c is the speed of light in free space. The relative dielectric constant of the sample was converted into water saturation by utilising the dielectric constant of the dry and fully saturated sand from the calibration measurement. The conversion followed Equation B.2.

$$S_w = \frac{S_{w_{sat}} - S_{w_{dry}}}{\varepsilon_{r_{sat}} - \varepsilon_{r_{dry}}} \left(\varepsilon_r - \varepsilon_{dry}\right) \tag{B.2}$$

with S_w is the calculated water saturation, ε_r, $\varepsilon_{r_{sat}}$, $\varepsilon_{r_{dry}}$ are dielectric constant of the measured sample, fully saturated sand and dry sand, respectively, and $S_{w_{sat}}$, $S_{w_{dry}}$ are the percentage of water in fully saturated and dry condition, which are 100 and 0, respectively.

Appendix C Description of Scattering Parameters

The scattering parameters of the first end cap are as follows (Equations C.1-C.8):

$$S_{11c1} = \Gamma_{1c1} - (1 - \Gamma_{1c1}^{2})\gamma_{c1}^{2}\Gamma_{2c1}\sum_{n=0}^{n=\infty}\gamma_{c1}^{2n}\,\Gamma_{1c1}^{n}\Gamma_{2c1}^{n} \tag{C.1}$$

$$S_{11c1} = \frac{\Gamma_{1c1} - \gamma_{c1}^{2}\Gamma_{2c1}}{1 - \gamma_{c1}^{2n}\Gamma_{1c1}^{n}\Gamma_{2c1}^{n}} \tag{C.2}$$

$$S_{21c1} = (1 - \Gamma_{1c1})(1 + \Gamma_{2c1})\gamma_{c1}\sum_{n=0}^{n=\infty}\gamma_{c1}^{2n}\,\Gamma_{1c1}^{n}\Gamma_{2c1}^{n} \tag{C.3}$$

$$S_{21c1} = \frac{(1 - \Gamma_{1c1})(1 + \Gamma_{2c1})\gamma_{c1}}{1 - \gamma_{c1}^{2n}\Gamma_{1c1}^{n}\Gamma_{2c1}^{n}} \tag{C.4}$$

$$S_{12c1} = (1 + \Gamma_{1c1})(1 - \Gamma_{2c1})\gamma_{c1}\sum_{n=0}^{n=\infty}\gamma_{c1}^{2n}\,\Gamma_{1c1}^{n}\Gamma_{2c1}^{n} \tag{C.5}$$

$$S_{21c1} = \frac{(1 + \Gamma_{1c1})(1 - \Gamma_{2c1})\gamma_{c1}}{1 - \gamma_{c1}^{2n}\Gamma_{1c1}^{n}\Gamma_{2c1}^{n}} \tag{C.6}$$

$$S_{22c1} = \Gamma_{2c1} - (1 - \Gamma_{2c1}^{2})\gamma_{c1}^{2}\Gamma_{1c2}\sum_{n=0}^{n=\infty}\gamma_{c1}^{2n}\,\Gamma_{1c1}^{n}\Gamma_{2c1}^{n} \tag{C.7}$$

$$S_{22c1} = \frac{\Gamma_{2c1} - \gamma_{c1}^{2}\Gamma_{1c1}}{1 - \gamma_{c1}^{2n}\Gamma_{1c1}^{n}\Gamma_{2c1}^{n}} \tag{C.8}$$

The scattering parameters of the second end cap are as follows (Equations C.9-C.16):

$$S_{11c2} = \Gamma_{1c2} - (1 - \Gamma_{1c2}^{2})\gamma_{c2}^{2}\Gamma_{2c2}\sum_{n=0}^{n=\infty}\gamma_{c2}^{2n}\,\Gamma_{1c2}^{n}\Gamma_{2c2}^{n} \tag{C.9}$$

$$S_{11c2} = \frac{\Gamma_{1c2} - \gamma_{c2}^{2}\Gamma_{2c2}}{1 - \gamma_{c2}^{2n}\Gamma_{1c2}^{n}\Gamma_{2c2}^{n}} \tag{C.10}$$

$$S_{21c2} = (1 - \Gamma_{1c2})(1 + \Gamma_{2c2})\gamma_{c2}\sum_{n=0}^{n=\infty}\gamma_{c2}^{2n}\,\Gamma_{1c2}^{n}\Gamma_{2c2}^{n} \tag{C.11}$$

$$S_{21c2} = \frac{(1 - \Gamma_{1c2})(1 + \Gamma_{2c2})\gamma_{c2}}{1 - \gamma_{c2}^{2n}\Gamma_{1c2}^{n}\Gamma_{2c2}^{n}} \tag{C.12}$$

$$S_{12c2} = (1 + \Gamma_{1c2})(1 - \Gamma_{2c2})\gamma_{c2}\sum_{n=0}^{n=\infty}\gamma_{c2}^{2n}\,\Gamma_{1c2}^{n}\Gamma_{2c2}^{n} \tag{C.13}$$

$$S_{21c2} = \frac{(1 + \Gamma_{1c2})(1 - \Gamma_{2c2})\gamma_{c2}}{1 - \gamma_{c2}^{2n}\Gamma_{1c2}^{n}\Gamma_{2c2}^{n}} \tag{C.14}$$

$$S_{22c2} = \Gamma_{2c2} - (1 - \Gamma_{2c2}^2)\gamma_{c2}^2\Gamma_{1c2} \sum_{n=0}^{n=\infty} \gamma_{c2}^{2n}\,\Gamma_{1c2}^n\Gamma_{2c2}^n \tag{C.15}$$

$$S_{22c2} = \frac{\Gamma_{2c2} - \gamma_{c2}^2\Gamma_{1c2}}{1 - \gamma_{c2}^{2n}\Gamma_{1c2}^n\Gamma_{2c2}^n} \tag{C.16}$$

The reflection coefficients are as follows (Equations C.17-C.20):

$$\Gamma_{1c1} = \frac{Z_{c1} - Z_w}{Z_{c1} + Z_w} \tag{C.17}$$

$$\Gamma_{2c1} = \frac{Z_{c1} - Z_s}{Z_{c1} + Z_s} \tag{C.18}$$

$$\Gamma_{1c2} = \frac{Z_{c2} - Z_w}{Z_{c2} + Z_w} \tag{C.19}$$

$$\Gamma_{2c2} = \frac{Z_{c2} - Z_s}{Z_{c2} + Z_s} \tag{C.20}$$

The acoustic impedances are as follows (Equations C.21-C.24):

$$Z_{c1} = \rho_{c1}v_{c1} \tag{C.21}$$

$$Z_{c2} = \rho_{c2}v_{c2} \tag{C.22}$$

$$Z_w = \rho_w v_w \tag{C.23}$$

$$Z_s = \rho_s v_s \tag{C.24}$$

The transmission coefficients are as follows (Equations 28-33):

$$\gamma_{w1} = e^{-i\omega\frac{l_1}{v_w}} \tag{C.25}$$

$$\gamma_{w2} = e^{-i\omega\frac{l_2}{v_w}} \tag{C.26}$$

$$\gamma_{w3} = e^{-i\omega\frac{l_3}{v_w}} \tag{C.27}$$

$$\gamma_{c1} = e^{-i\omega\frac{l_{c1}}{v_{c1}}} \tag{C.28}$$

$$\gamma_{c2} = e^{-i\omega\frac{l_{c2}}{v_{c2}}} \tag{C.29}$$

$$\gamma_s = e^{-i\omega\frac{l_s}{v_s}} \tag{C.30}$$

Appendix D Supporting Figures for Chapter 2

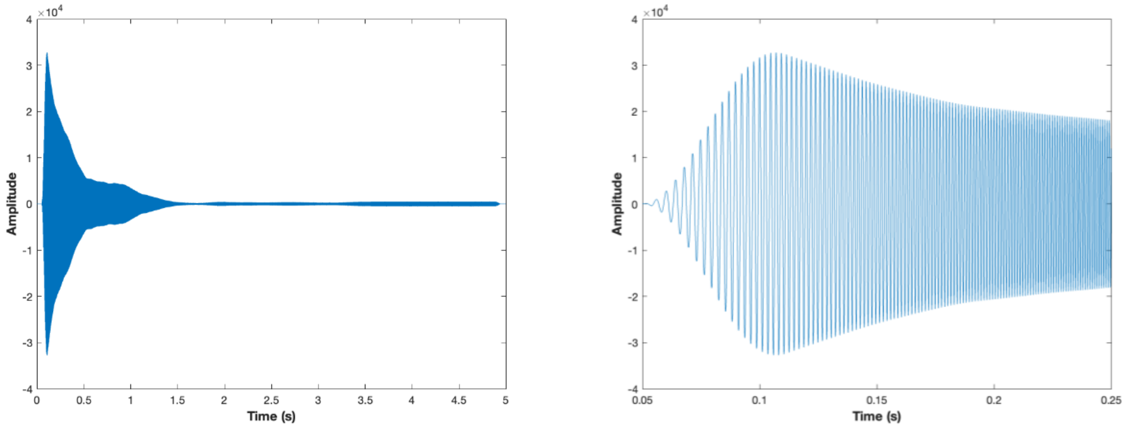

Figure D.1 Example of an acoustic CHIRP source pulse used in the pulse tube: full signal (left) and from 0.05 to 0.25 s (right).

(a)

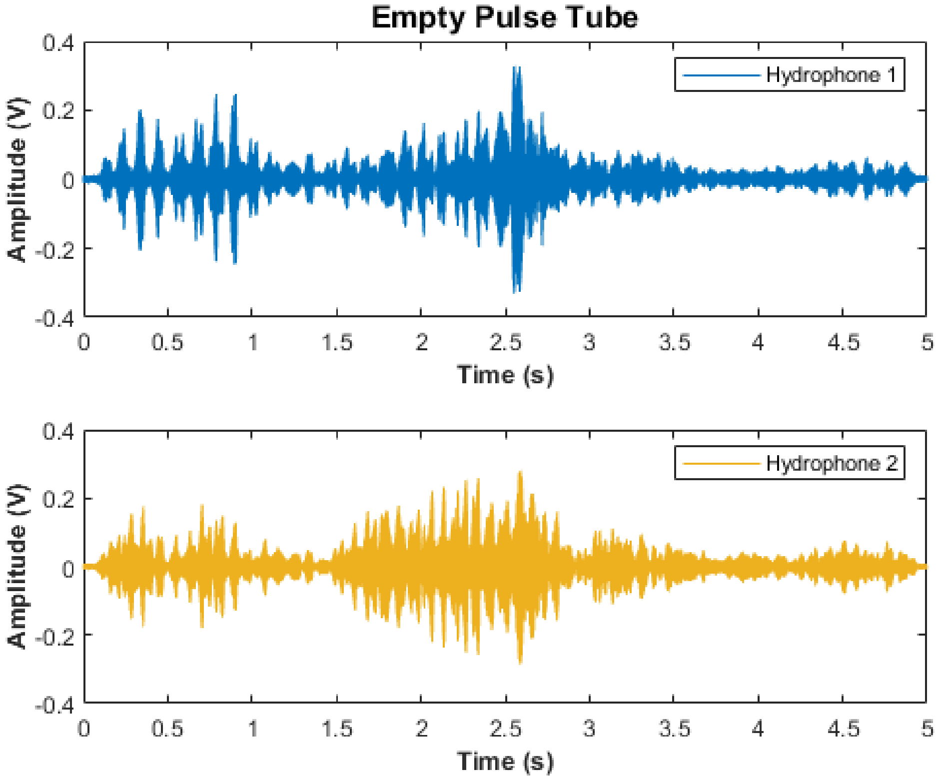

(b)

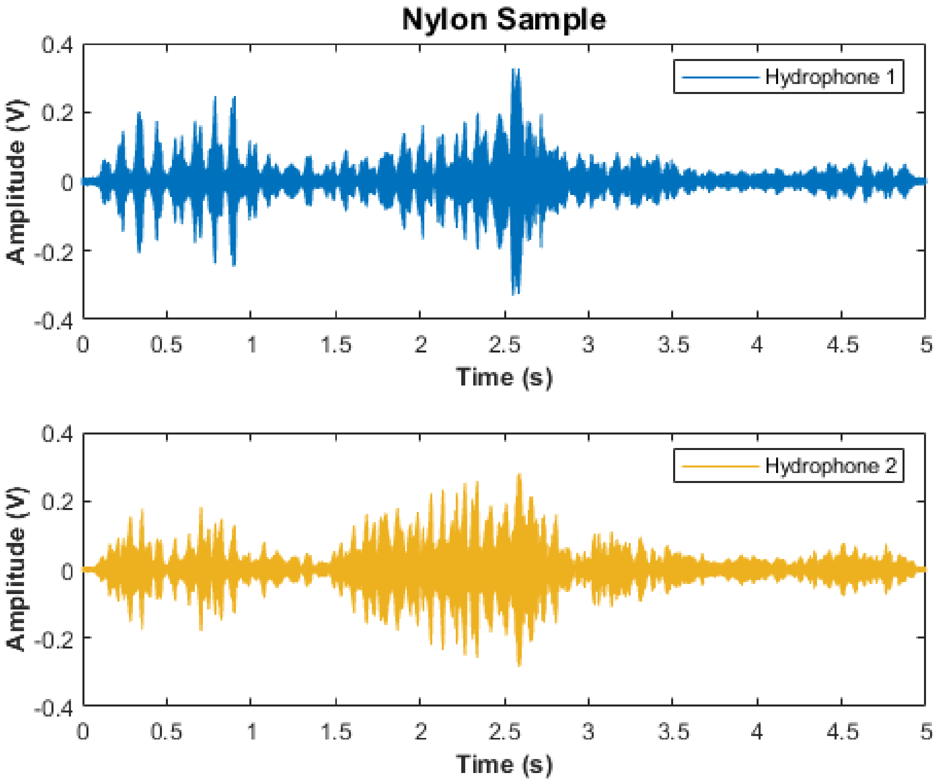
Nylon Sample
Hydrophone 1
Amplitude (V)
0.4
0.2
0
-0.2
-0.4
0
0.5
1
1.5
2
2.5
3
3.5
4
4.5
5
Time (s)
Hydrophone 2
Amplitude (V)
Time (s)

(c)

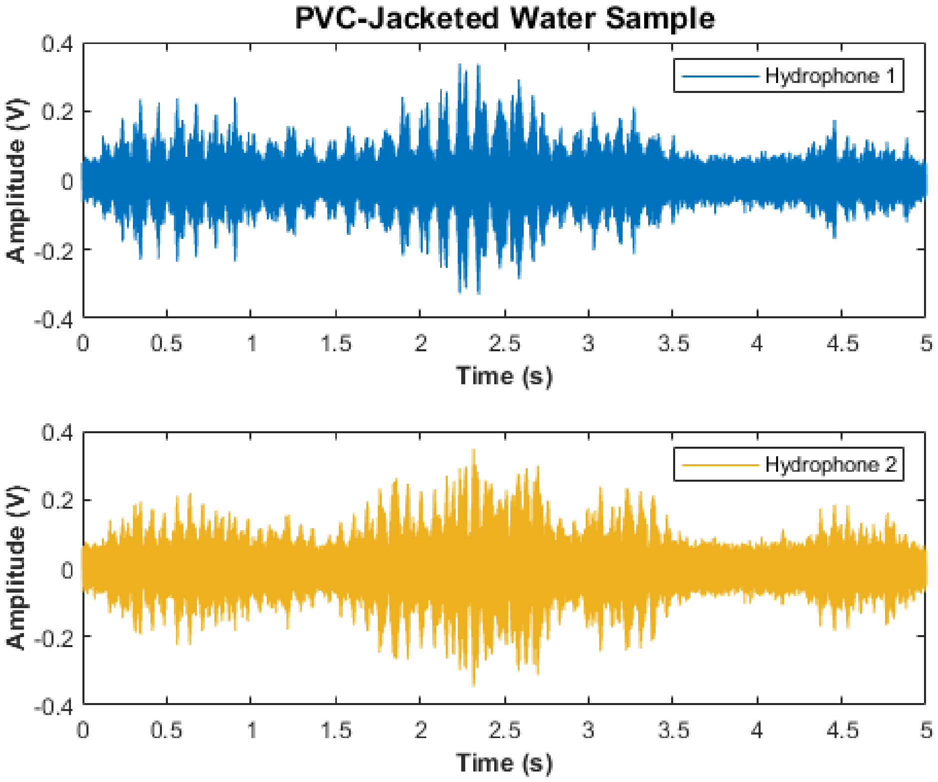
PVC-Jacketed Water Sample
Hydrophone 1
Amplitude (V)
0.4
0.2
0
-0.2
-0.4
0
0.5
1
1.5
2
2.5
3
3.5
4
4.5
5
Time (s)
Hydrophone 2
Amplitude (V)
Time (s)

(d)

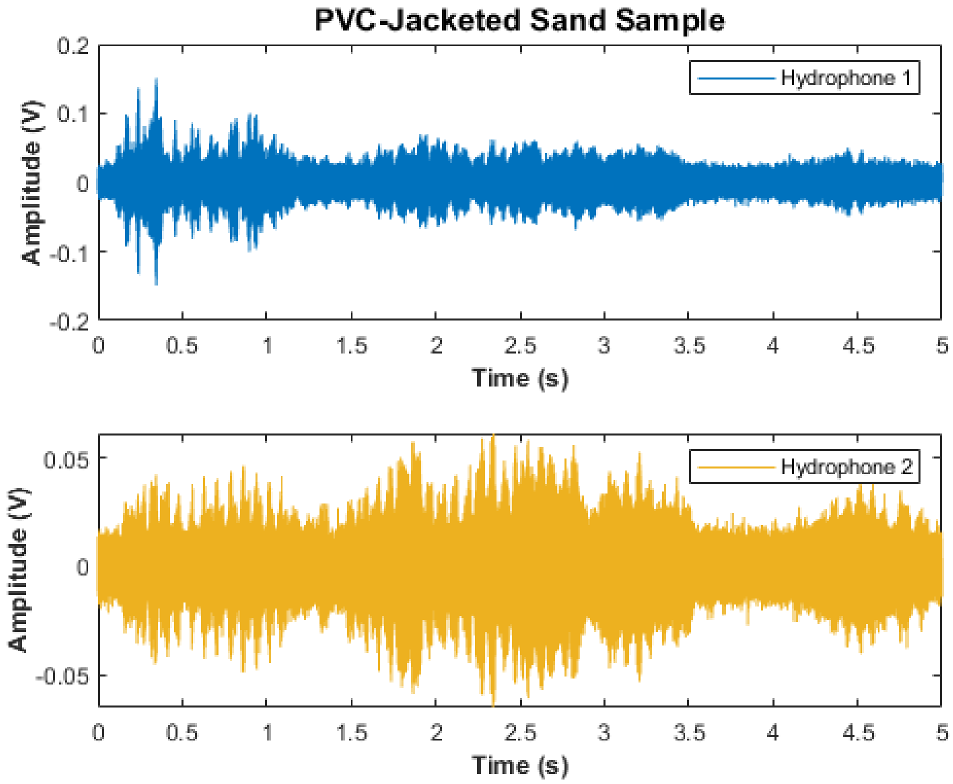

Figure D.2 Recorded time series signal from pulse tube measurement of a) empty pulse tube, b) nylon sample, c) PVC-jacketed water sample, and d) PVC-jacketed sand sample.

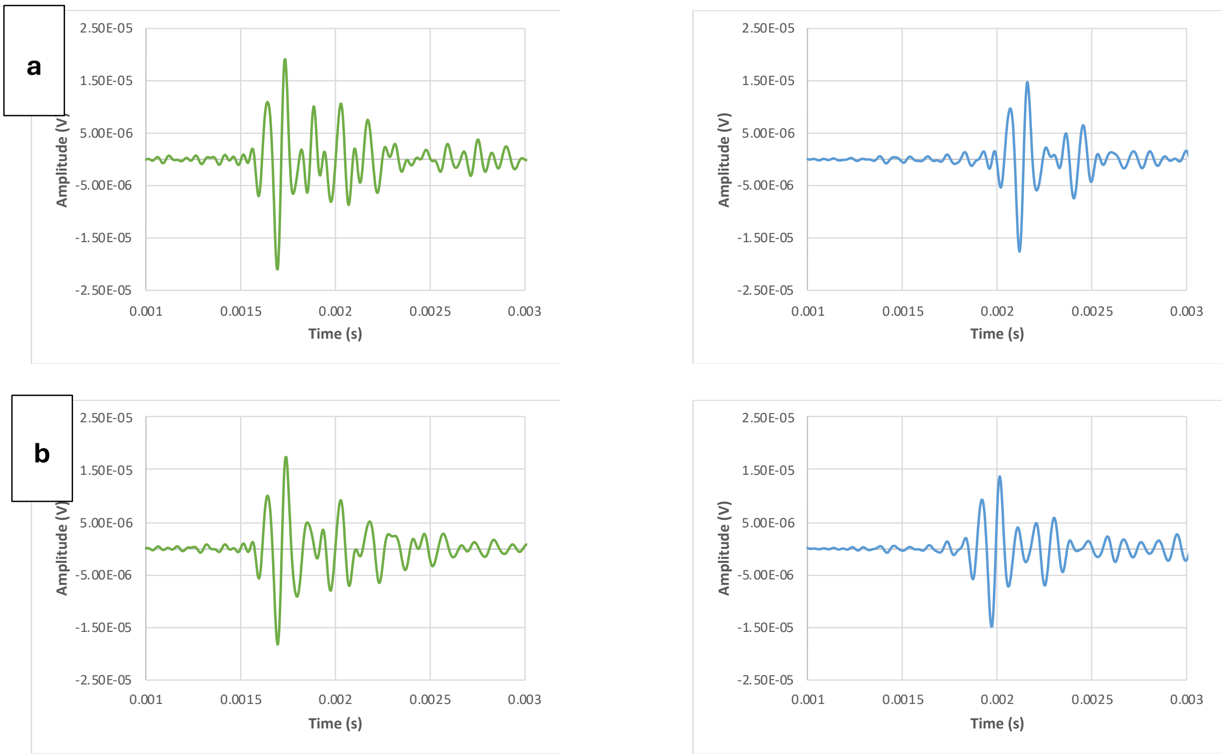

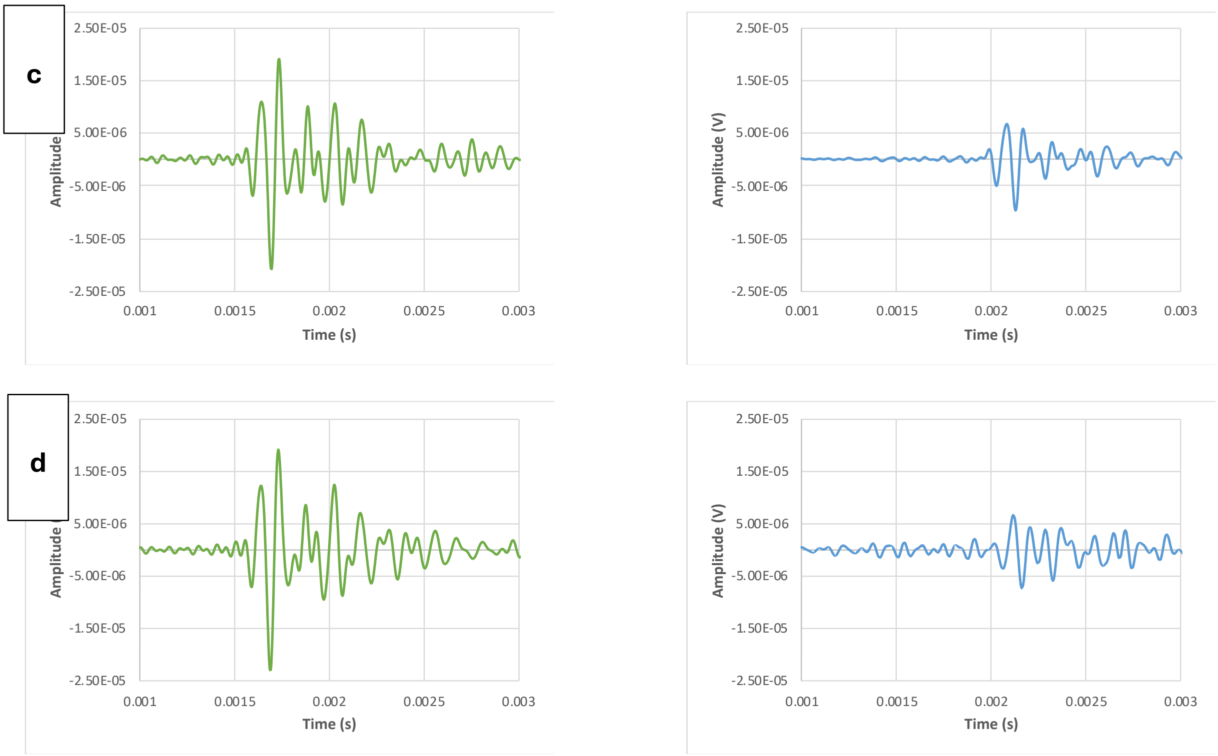

Figure D.3 Examples of deconvolved acoustic pulse tube signals from 0.001 to 0.003 s of: a) empty pulse tube, b) nylon sample, c) water-filled PVC jacket and d) PVC-jacketed sand. Left side (green lines) represent hydrophone 1, and right side (blue lines) are for hydrophone 2. See Figure 2.4b for location of hydrophones.

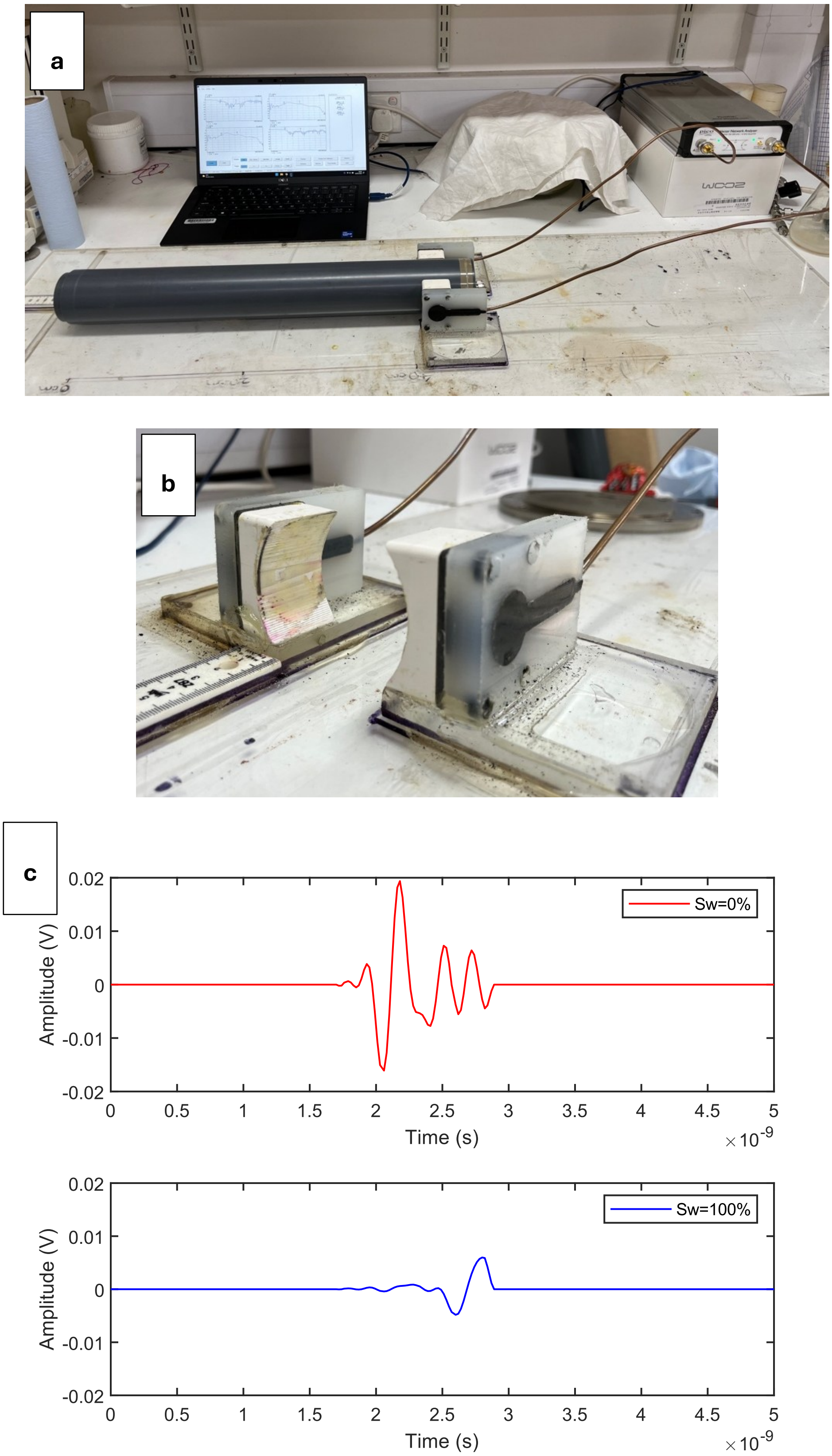

Figure D.4 Microwave method experimental setup: a) Photo of the microwave system with PVC-jacketed sand sample, b) Details of the antennas, and c) Examples of processed transmitted signals at dry (S_w=0%) and fully saturated (S_w=100%) conditions.

Figure D.5 Variations in P-wave velocity (Vp) and attenuation Q-1 across a frequency range of 1-20 kHz, with legends at each plot represent the saturation levels. The measurements were conducted under an effective pressure of 10 MPa and a temperature of 4°C.

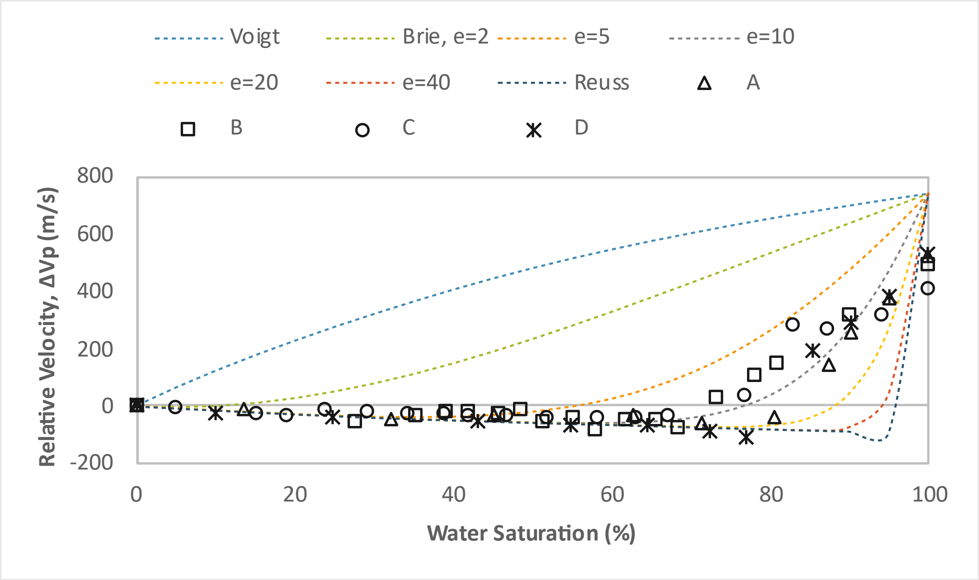

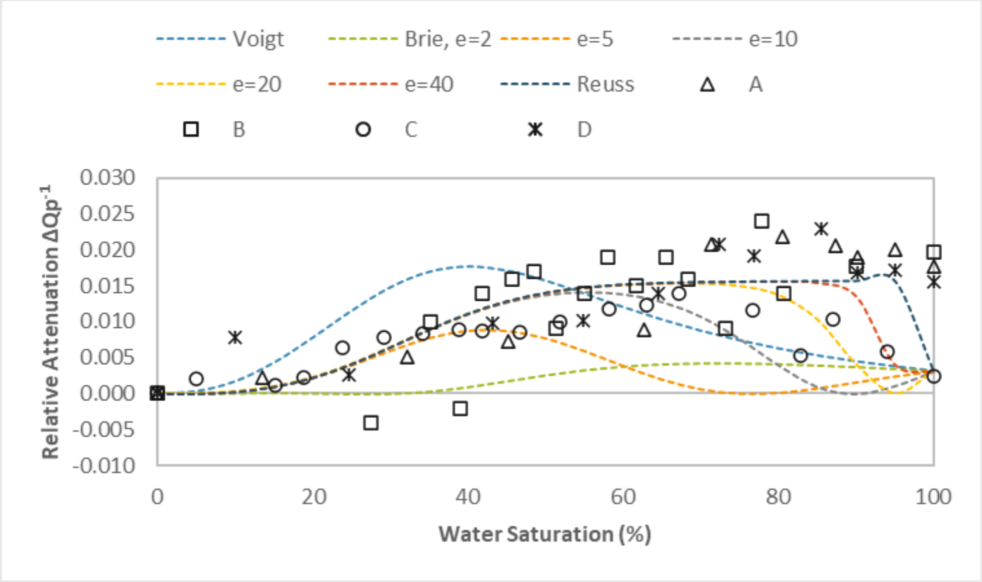

Figure D.6 Comparison of acoustic pulse tube data at 10 kHz (across all samples, indicated in the legend as A-D), illustrating relative velocity and attenuation, referenced to the measured parameters at Sw=0%, against HBES model predictions at varying fluid saturation patchiness using Brie's fluid bulk modulus model parameter e (values indicated in legend) (Brie et al., 1995; Marín-Moreno et al., 2017; Reuss, 1929; Voigt, 1889). The measurements and simulations were conducted under an effective pressure of 10 MPa and a temperature of 4°C.

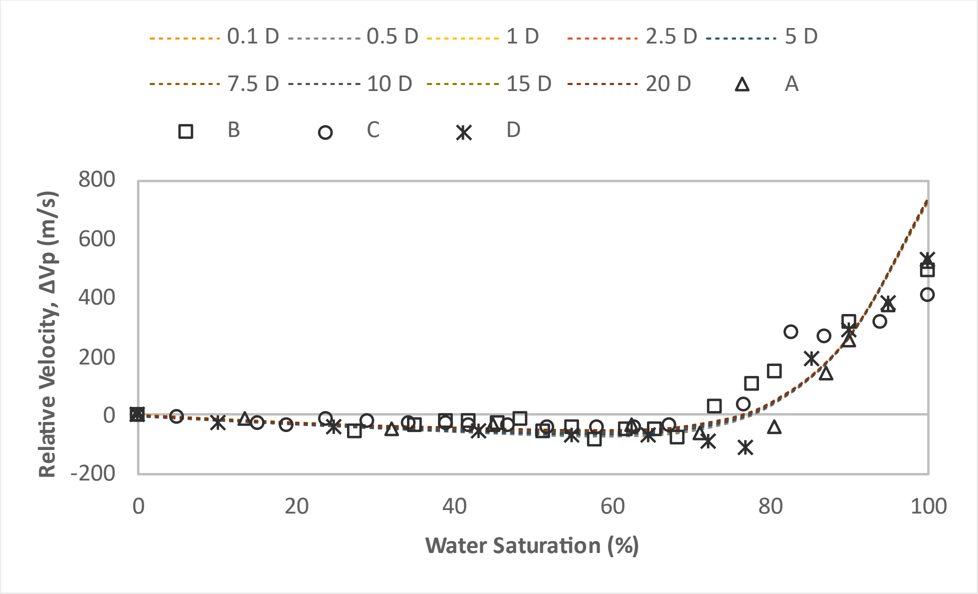

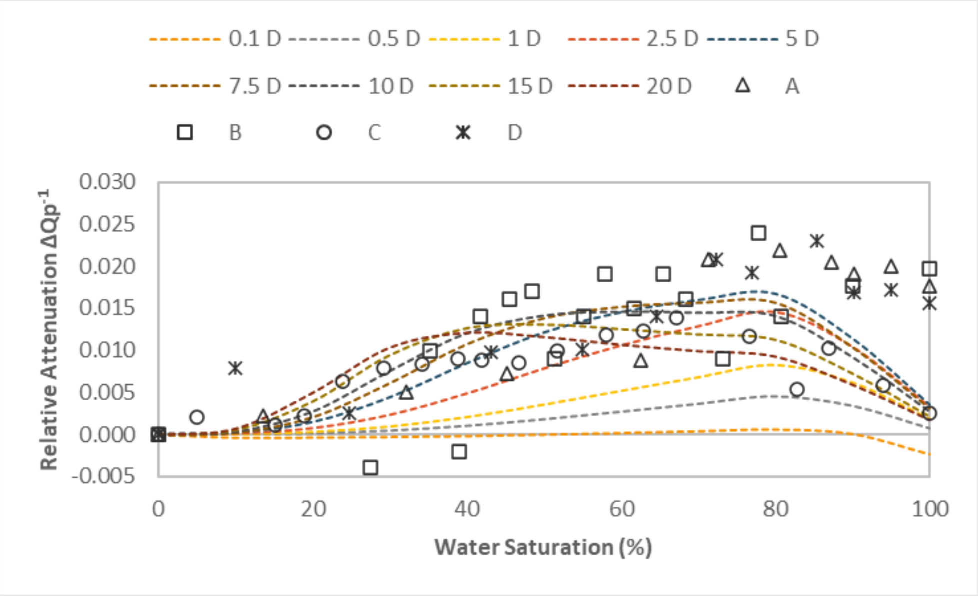

Figure D.7 Comparison of acoustic pulse tube data at 10 kHz (across all samples, indicated in the legend as A-D), illustrating relative velocity and attenuation, referenced to the measured parameters at S_w=0%, against HBES model predictions at varying permeabilities (values indicated in legend) (Marín-Moreno et al., 2017). The measurements and simulations were conducted under an effective pressure of 10 MPa and a temperature of 4°C. The gas bubble radius is 0.1 mm.

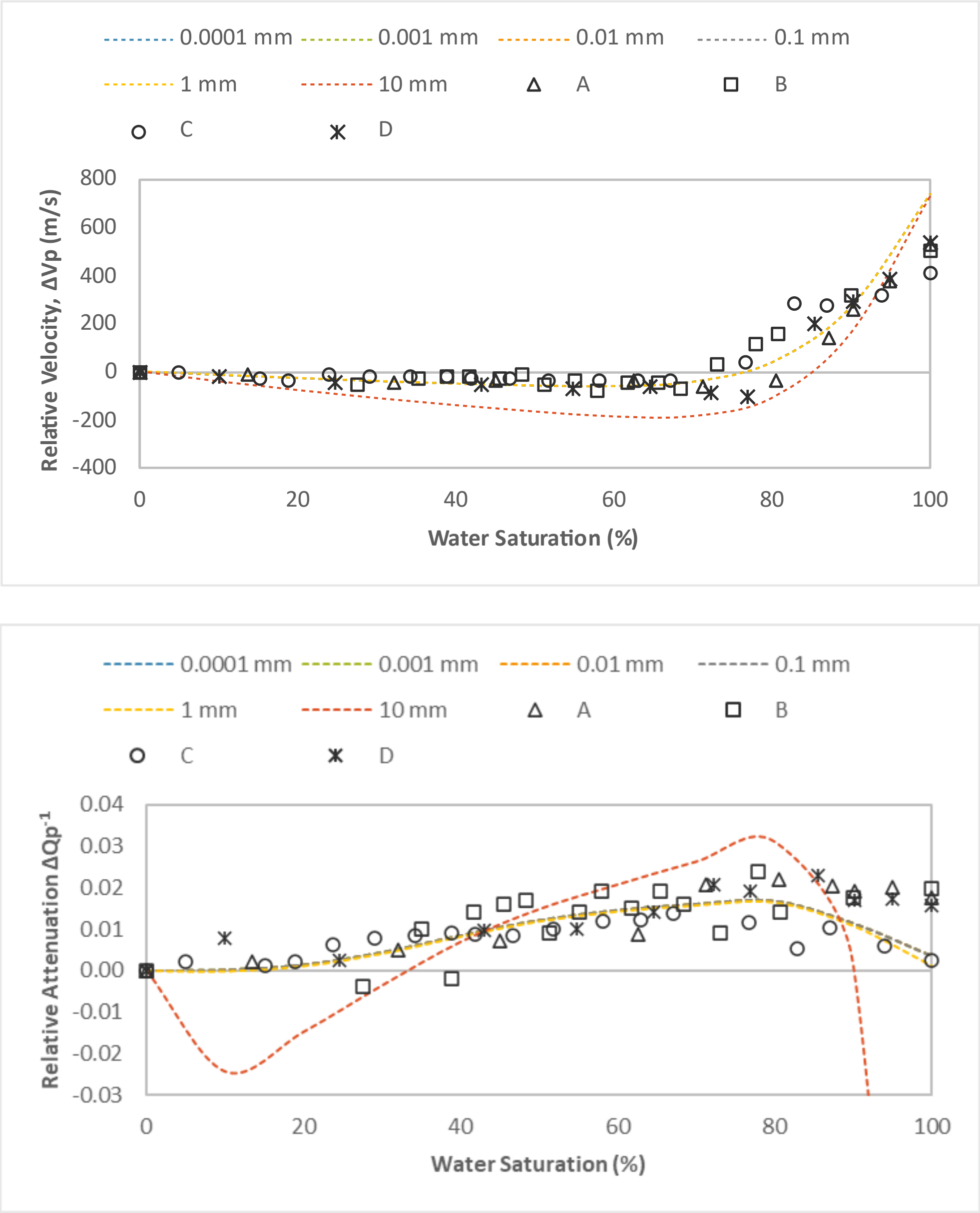

Figure D.8 Comparison of acoustic pulse tube data at 10 kHz (across all samples, indicated in the legend as A-D), illustrating relative velocity and attenuation, referenced to the measured parameters at Sw=0%, against HBES model predictions at varying gas bubble radius (values indicated in legend) (Marín-Moreno et al., 2017). The measurements and simulations were conducted under an effective pressure of 10 MPa and a temperature of 4°C. The permeability is 5 Darcys.

Appendix E Supporting Figures for Chapter 3

E.1 Introduction

In this appendix, I provide additional details about our experiment and full data plots referenced in the main manuscript. Figure E.1 presents an example of the sound sources used in the experiment. Figure E.2 shows broader coverage of the fitting of parameter n to the rock physics models (Leclaire et al., 1994; Marín-Moreno et al., 2017), with n ranging from 0.5 to 1.9. In Figure E.3, we show how measurements at different frequencies affect the changes in velocity and attenuation as the ice melts. Figure E.4 shows morphology modelling using the HBES model, with lower pore-filling (PF) concentration (or higher cementing (C) concentration, where C = 1 - PF). Finally, Figure E.5 provides the changes in sediment frame permeability as ice content decreases.

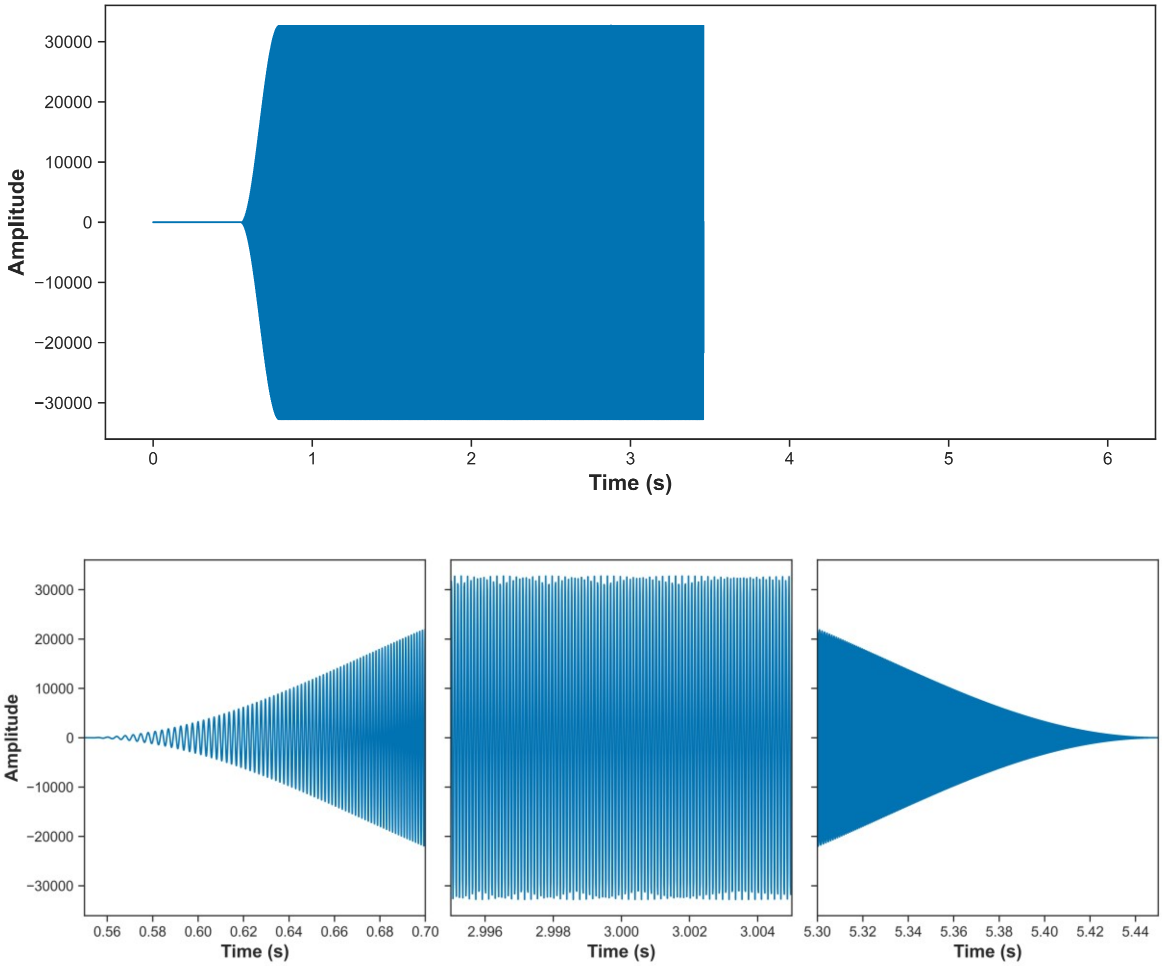

Figure E.1 An example of an acoustic Chirp source pulse used for the pulse tube measurements: full signal (top) and various time-cropped signals (bottom).

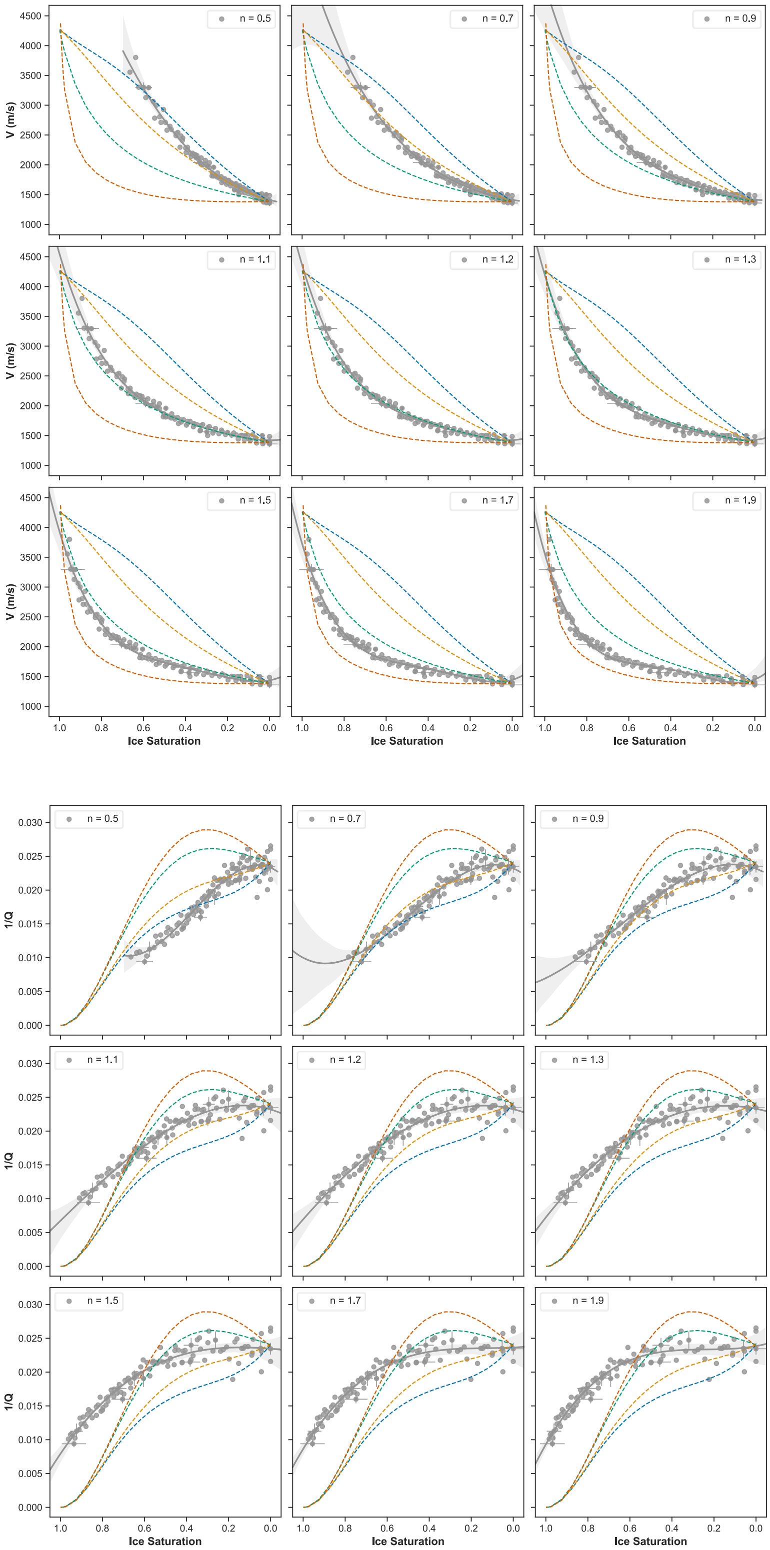

Figure E.2 Empirical parameter (n) fitting of measured data (grey dots) of velocity (top) and attenuation (bottom) to HBES model with Reuss, Brie, and Voigt approximations (blue, yellow, and green dotted lines, respectively) and LeClaire model (red dotted lines) (Brie et al., 1995; Leclaire et al., 1994; Marín-Moreno et al., 2017; Reuss, 1929; Voigt, 1889). Grey solid lines represent the respective regression models to each dataset with averaged R^2 of 0.98 and 0.93 for velocity and attenuation, respectively. Cross error bars are shown at every 0.05 decrement of ice saturation.

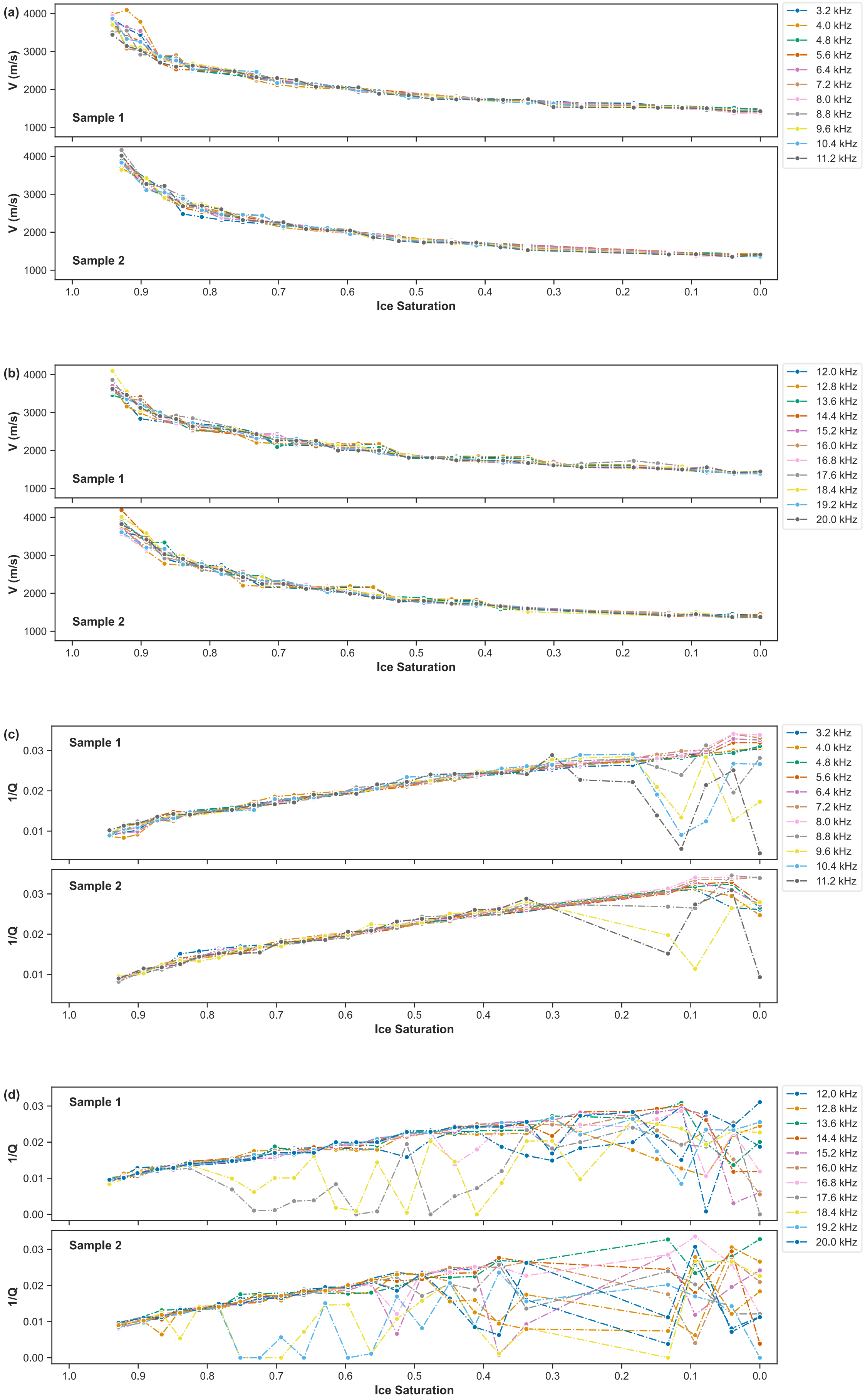

Figure E.3 Variations in velocity (a-b) and attenuation (c-d) across ice saturations during the melting process for both samples at various frequencies (shown in legends).

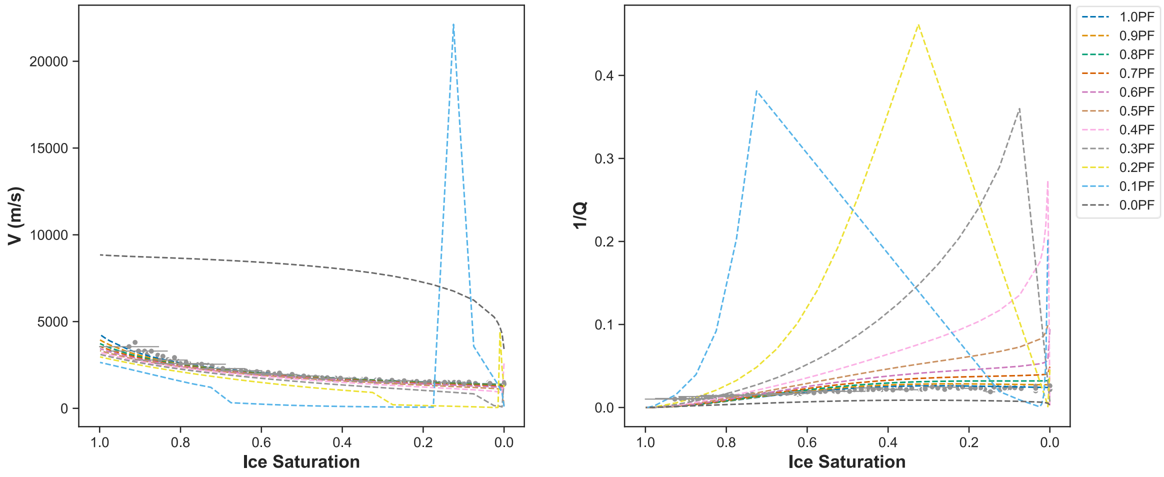

Figure E.4 Comparison of velocity (left) and attenuation (right) at 10 kHz against HBES model (Marín-Moreno et al., 2017) with pore-filling (PF) concentrations across ice saturation during the melting process. Grey dots represent the experimental data, and dashed lines represent the models (as shown in the legend).

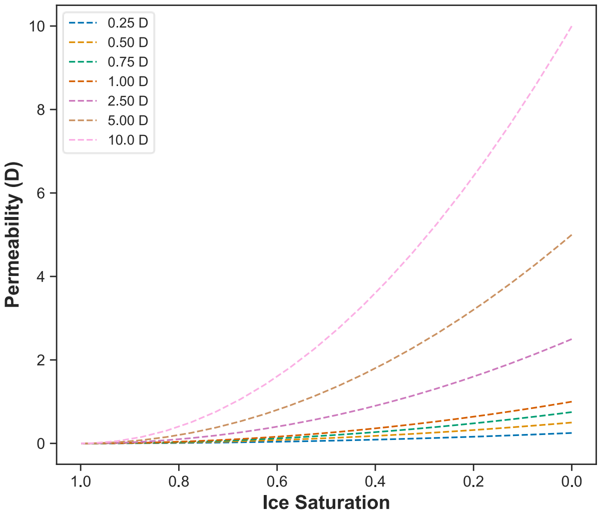

Figure E.5 Variations of modelled permeability using the HBES model (Marín-Moreno et al., 2017) across ice saturation during the melting process. Values in the legend represent the permeability of the sediment frame (without any ice formed or water-saturated state).

Appendix F Supporting Information for Chapter 4

F.1 Introduction

This appendix section provides additional information about our experiment and the full data plots referenced in the main manuscript. Text F.2 includes details on sample preparation and error/uncertainty calculations. Text F.3 describes the method used to estimate ice saturation, based on materials in Chapter 3. Figure F.1 shows the PVC jacket components used in the experiment. Figure F.2 presents the comparison outlined in Text F.3. Figure F.3 illustrates velocity modelling under various pore-filling (PF) concentrations and permeabilities using the HBES model. Table F.1 presents the objective function results from the comparisons in Figure F.2.

F.2 Sample preparation

The samples were prepared by pouring the sand into the PVC pipe and compacting it layer by layer. Both ends of the pipe were sealed with PVC caps, which had rubber O-rings that maintained a seal while allowing the surrounding fluid (water) to apply even hydrostatic pressure on the sand (Figure F1). The top of each layer was lightly scratched to avoid impedance differences between layers. The process was repeated until the pipe was fully compacted, leaving room for the top cap. We saturated the sand by gradually introducing de-ionised water, increasing saturation in steps of around 10%. To remove air bubbles during saturation, the pipe was tapped continuously. Once saturation was achieved, the top cap was sealed, and the sample was left for 24 hours before the water-saturated pulse tube measurement. Uncertainty of the sample's porosity was calculated using error propagation methods. We measured empirical porosity (ϕ) using the wet-dry mass method and compared it with theoretical porosity (ϕ_T) based on bulk dry (ρ_b) and grain (ρ_s) densities, using the formula $\phi_T = 1 - \rho_b / \rho_s$. This approach helped assess uncertainties related to the saturation process due to non-connected porosity, leading to ice saturation errors of ~7%.

F.3 Inferring ice saturation

We first established a baseline by measuring the velocity and attenuation of the sample in its fully melted state ($S_i = 0$) to serve as a comparison for the measurements taken during the melting process. At the start, we assumed an initial ice saturation ($S_i = 1$) when the sample was placed in the pulse tube, though some unfrozen water likely remained, such as thin water films bound to the grains (Watanabe and Mizoguchi, 2002). However, due to the time needed to reach the target pressure in the pulse tube, measurements at full ice saturation ($S_i = 1$) were not possible, as some melting had already occurred. Instead, we used a regression model to estimate velocity and attenuation at full saturation.

We estimated ice saturation based on the melting time during the measurements, applying an empirical relationship (Equation F.1):

$$S_i = 1 - \left(\frac{t}{T}\right)^n, \tag{F.1}$$

where S_i represents ice saturation, t is the time elapsed during measurement (in seconds), T is the total time for complete melting (determined by the velocity and attenuation at the fully melted state), and n is an empirical parameter describing the exponential relationship between ice melting and time. We derived the value of n by comparing experimental results with three-phase rock physics models (Leclaire et al., 1994; Marín-Moreno et al., 2017) using visual comparison and by minimising the objective function (Equation F.2). The function performs well when velocity and attenuation show similar variations, as in the current dataset. However, if their variation magnitudes differ significantly, one parameter may dominate the objective function. Thus, the method is most effective when both parameters vary comparably.

$$Objective\ function = \frac{\left|V_{experimental} - V_{modelled}\right|}{V_{experimental}} + \frac{\left|Q^{-1}_{experimental} - Q^{-1}_{modelled}\right|}{Q^{-1}_{experimental}} \tag{F.2}$$

Figure F.2 illustrates the closest fit between the measured and calculated velocity and attenuation, while Table F.1 provides the objective function outcomes. To determine the empirical parameter n, we considered two factors: the best fit between the experimental data and model predictions using the objective function (Equation F.2), and how well the predicted experimental values at $S_i = 1$ (from regression models) matched the model results. We found that experimental velocity matched the models best when n was 1.2, 1.3, and 1.5 for the 2.5, 5, and 7.5 MPa datasets, respectively. While velocity comparisons are straightforward, the attenuation data required the objective function to better determine the n value.

Figure F.1 PVC jacket system used to enable sample emplacement inside the water-filled acoustic pulse tube: a) 50 cm length PVC cylinder jacket, and b) top and bottom PVC endcaps with O-ring seals, including the location of the pore fluid vent port (shown as a hexagonal nut on the top endcap on the right).

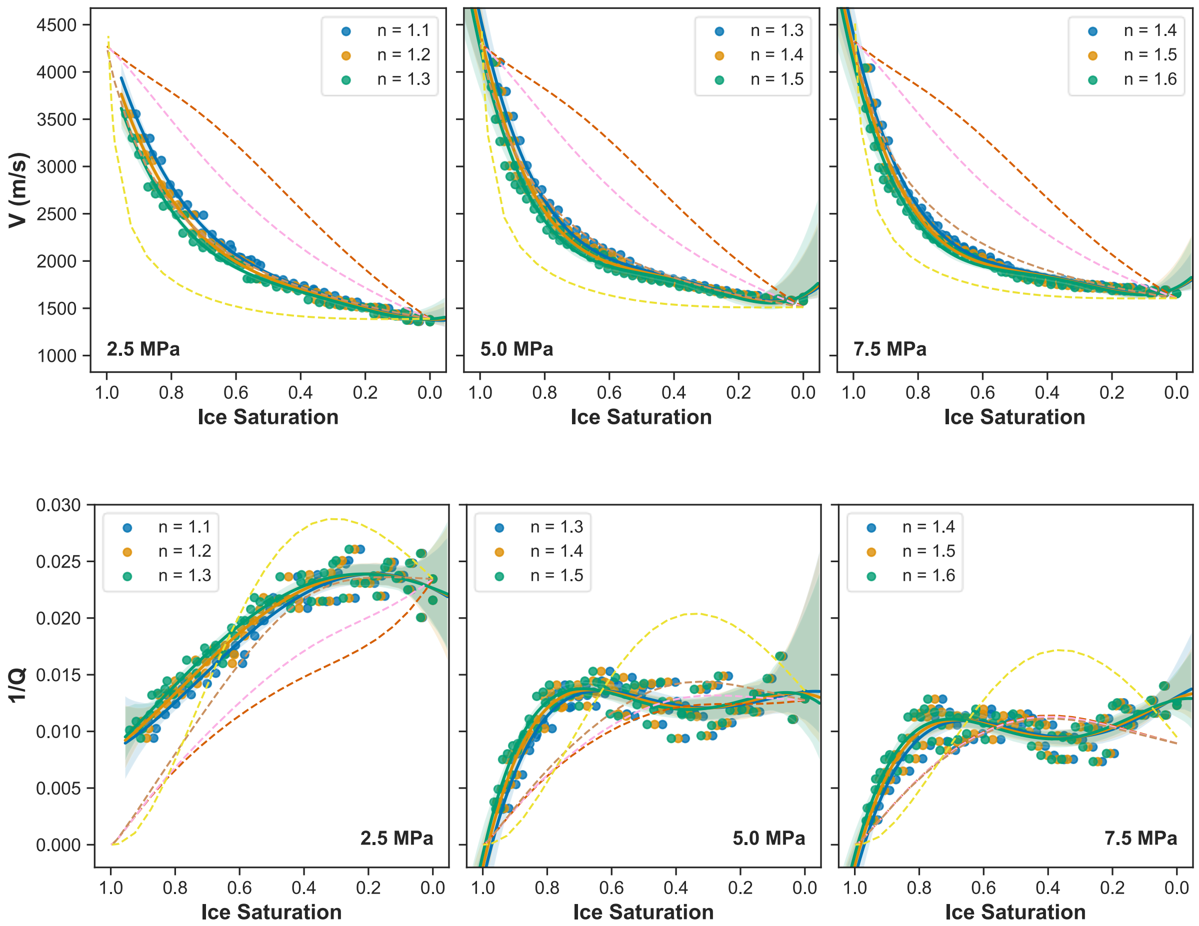

Figure F.2 Empirical parameter (*n*) fitting of measured data at 10 kHz (indicated by the legend) of velocity (top) and attenuation (bottom) to HBES with Reuss, Brie, and Voigt approximations (red, pink, and brown dashed lines, respectively) and LeClaire (yellow dashed lines) models. Blue, orange, and green lines represent the respective regression models for each dataset with averaged R^2 of 0.98 and 0.85 for velocity and attenuation, respectively.

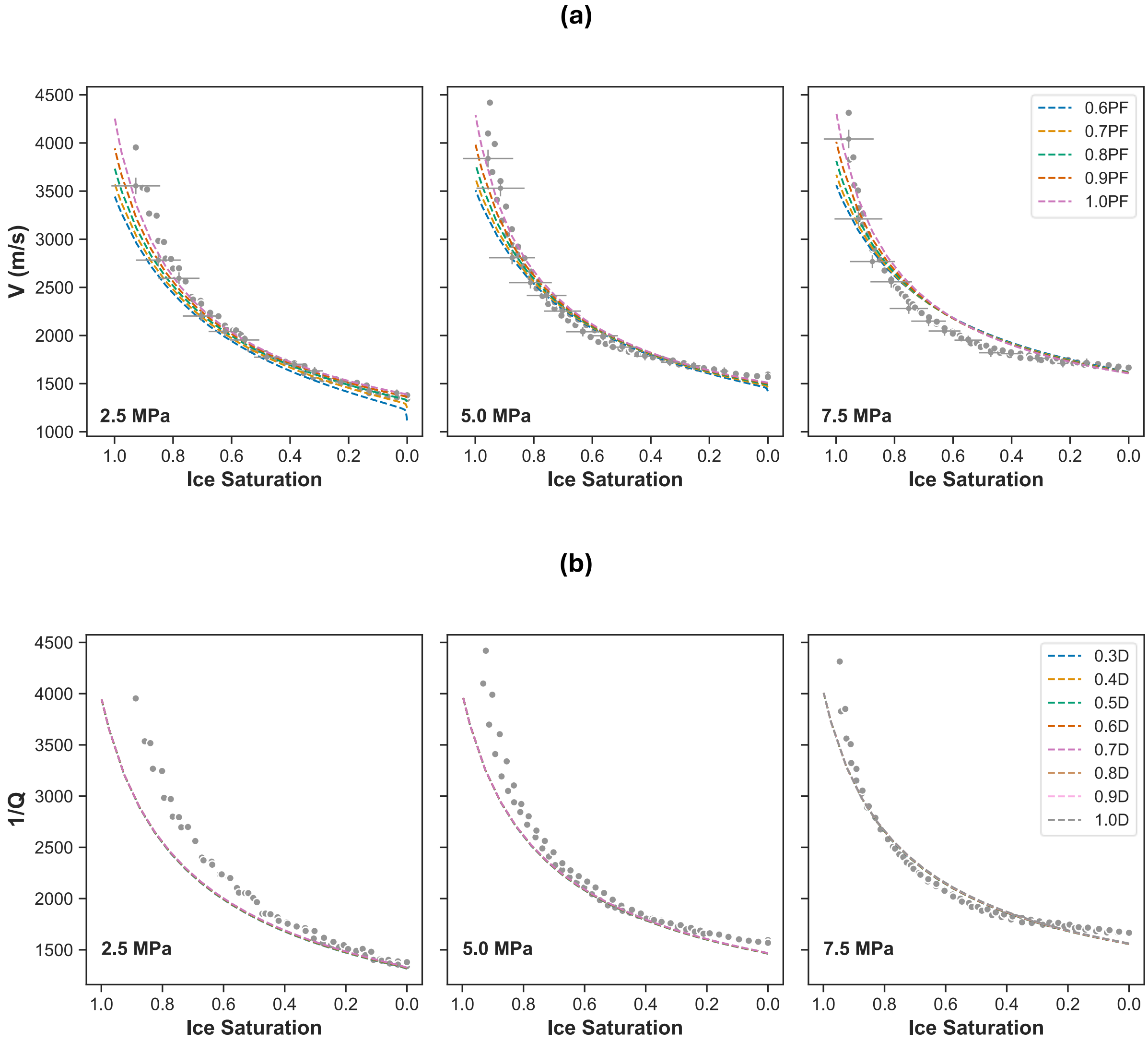

Figure F.3 Comparison of experimental and modelled velocities: a) at various pore-filling (PF) concentrations of ice, and b) at various permeabilities (in Darcies [D] = 1 x 10^{-12} m^2) for PF = 1.0, using the HBES model with Voigt approximations.

Table F.1 Calculation of objective functions to compare experimental and modelled velocity and attenuation. Best fits are indicated by lowest values (underlined).

Dataset	**Objective function at n =**				
	1.1	**1.2**	**1.3**	**1.4**	**1.5**
2.5 MPa	0.359	0.349	0.351	0.359	0.375
5 MPa	0.317	0.416	0.314	0.403	0.333
7.5 MPa	0.721	0.655	0.596	0.531	0.467

List of References

Abbasi, M., Mousavi, S.M., Lee, B.J., Esfahani, J.A., Karimi, N., Mamaghani, M.Y., 2022. Examination of the effects of porosity upon intensification of thermal storage of PCMs in a shell-and-tube type system. Case Studies in Thermal Engineering 33, 101963. https://doi.org/10.1016/j.csite.2022.101963

Ahmed, N., Weibull, W.W., Quintal, B., Grana, D., Bhakta, T., 2022. Frequency-dependent AVO inversion applied to physically based models for seismic attenuation. Geophysical Journal International 233, 234–252. https://doi.org/10.1093/gji/ggac461

Aki, K., Richards, P.G., 1980. Quantitative seismology: Theory and methods.

Alkhimenkov, Y., Caspari, E., Gurevich, B., Barbosa, N.D., Glubokovskikh, S., Hunziker, J., Quintal, B., 2020. Frequency-dependent attenuation and dispersion caused by squirt flow: Three-dimensional numerical study. GEOPHYSICS 85, MR129–MR145. https://doi.org/10.1190/geo2019-0519.1

Alkire, B.D., Andersland, O.B., 1973. The Effect of Confining Pressure on the Mechanical Properties of Sand–Ice Materials. J. Glaciol. 12, 469–481. https://doi.org/10.3189/S0022143000031889

Allmark, C., Curtis, A., Galetti, E., De Ridder, S., 2018. Seismic Attenuation From Ambient Noise Across the North Sea Ekofisk Permanent Array. JGR Solid Earth 123, 8691–8710. https://doi.org/10.1029/2017JB015419

Amalokwu, K., Best, A.I., Sothcott, J., Chapman, M., Minshull, T., Li, X.-Y., 2014. Water saturation effects on elastic wave attenuation in porous rocks with aligned fractures. Geophysical Journal International 197, 943–947. https://doi.org/10.1093/gji/ggu076

Aminnaji, M., Qureshi, M.F., Dashti, H., Hase, A., Mosalanejad, A., Jahanbakhsh, A., Babaei, M., Amiri, A., Maroto-Valer, M., 2024. CO2 Gas hydrate for carbon capture and storage applications – Part 1. Energy 300, 131579. https://doi.org/10.1016/j.energy.2024.131579

Andersland, O.B., Ladanyi, B., 2004. Frozen ground engineering, 2nd ed. ed. Wiley ; ASCE, Hoboken, NJ, [Reston, Va.].

Anisimov, O.A., 1989. Changing Climate And Permafrost Distribution In The Soviet Arctic. Physical Geography 10, 285–293. https://doi.org/10.1080/02723646.1989.10642383

Anisimov, O.A., Nelson, F.E., 1996. Permafrost distribution in the Northern Hemisphere under scenarios of climatic change. Global and Planetary Change 14, 59–72. https://doi.org/10.1016/0921-8181(96)00002-1

Arenson, L.U., Springman, S.M., Sego, D.C., 2007. The Rheology of Frozen Soils. Applied Rheology 17, 12147-1-12147–14. https://doi.org/10.1515/arh-2007-0003

Asada, M., Satoh, M., Tanahashi, M., Yokota, T., Goto, S., 2022. Visualization of shallow subseafloor fluid migration in a shallow gas hydrate field using high-resolution acoustic mapping and ground-truthing and their implications on the formation process: a case study of the Sakata Knoll on the eastern margin of the Sea of Japan. Mar Geophys Res 43, 34. https://doi.org/10.1007/s11001-022-09495-9

ASTM, 2007. Standard Test Methods for Laboratory Compaction Characteristics of Soil Using Standard Effort, ASTM Standard D698. ASTM International.

Astuto, G., Molina-Gómez, F., Bilotta, E., Viana Da Fonseca, A., Flora, A., 2023. Some remarks on the assessment of P-wave velocity in laboratory tests for evaluating the degree of saturation. Acta Geotech. 18, 777–790. https://doi.org/10.1007/s11440-022-01610-9

Avramidis, A.S., Saxena, S.K., 1990. The Modified “Stiffened” Drnevich Resonant Column Apparatus. Soils and Foundations 30, 53–68. https://doi.org/10.3208/sandf1972.30.3_53

Ayres, A., Theilen, F., 2001. Preliminary laboratory investigations into the attenuation of compressional and shear waves on near-surface marine sediments: Attenuation of P- and S-waves. Geophysical Prospecting 49, 120–127. https://doi.org/10.1046/j.1365-2478.2001.00243.x

Azuma, H., Konishi, C., Xue, Z., 2013. Introduction and Application of the Modified Patchy Saturation for Evaluating CO2 Saturation by Seismic Velocity. Energy Procedia 37, 4024–4032. https://doi.org/10.1016/j.egypro.2013.06.302

Ba, J., Wei, Y., Carcione, J.M., Adam, L., Tang, G., 2024. Stress and frequency dependence of wave velocities in saturated rocks based on acoustoelasticity with squirt-flow dissipation. Geophysical Journal International 236, 1753–1763. https://doi.org/10.1093/gji/ggae020

Barriere, J., Bordes, C., Brito, D., Senechal, P., Perroud, H., 2012. Laboratory monitoring of P waves in partially saturated sand. Geophysical Journal International. https://doi.org/10.1111/j.1365-246X.2012.05691.x

Batzle, M.L., Han, D.-H., Hofmann, R., 2006. Fluid mobility and frequency-dependent seismic velocity — Direct measurements. GEOPHYSICS 71, N1–N9. https://doi.org/10.1190/1.2159053

Belogol’skii, V.A., Sekoyan, S.S., Samorukova, L.M., Stefanov, S.R., Levtsov, V.I., 1999. Pressure dependence of the sound velocity in distilled water. Meas Tech 42, 406–413. https://doi.org/10.1007/BF02504405

Berryman, J.G., 1981. Elastic wave propagation in fluid-saturated porous media II. The Journal of the Acoustical Society of America 70, 1754–1756. https://doi.org/10.1121/1.387193

Berryman, J.G., 1980. Confirmation of Biot’s theory. Applied Physics Letters 37, 382–384. https://doi.org/10.1063/1.91951

Best, A.I., McCann, C., 1995. Seismic attenuation and pore-fluid viscosity in clay-rich reservoir sandstones. GEOPHYSICS 60, 1386–1397. https://doi.org/10.1190/1.1443874

Best, A.I., Priest, J.A., Clayton, C.R.I., Rees, E.V.L., 2013. The effect of methane hydrate morphology and water saturation on seismic wave attenuation in sand under shallow sub-seafloor conditions. Earth and Planetary Science Letters 368, 78–87. https://doi.org/10.1016/j.epsl.2013.02.033

Biot, M.A., 1962. Mechanics of Deformation and Acoustic Propagation in Porous Media. Journal of Applied Physics 33, 1482–1498. https://doi.org/10.1063/1.1728759

Biot, Maurice A., 1956a. Theory of Propagation of Elastic Waves in a Fluid-Saturated Porous Solid. I. Low-Frequency Range. Journal of the Acoustical Society of America 28, 168–178. https://doi.org/10.1121/1.1908239

Biot, Maurice A., 1956b. Theory of Propagation of Elastic Waves in a Fluid-Saturated Porous Solid. II. Higher Frequency Range. Journal of the Acoustical Society of America 28, 179–191. https://doi.org/10.1121/1.1908241

Biot, M. A., 1956a. Theory of Propagation of Elastic Waves in a Fluid-Saturated Porous Solid. I. Low-Frequency Range. The Journal of the Acoustical Society of America 28, 168–178. https://doi.org/10.1121/1.1908239

Biot, M. A., 1956b. Theory of Propagation of Elastic Waves in a Fluid-Saturated Porous Solid. II. Higher Frequency Range. The Journal of the Acoustical Society of America 28, 179–191. https://doi.org/10.1121/1.1908241

Biot, M.A., 1952. Propagation of Elastic Waves in a Cylindrical Bore Containing a Fluid. Journal of Applied Physics 23, 997–1005. https://doi.org/10.1063/1.1702365

Birch, F., Bancroft, D., 1938. Elasticity and internal friction in a long column of granite*. Bulletin of the Seismological Society of America 28, 243–254. https://doi.org/10.1785/BSSA0280040243

Biskaborn, B.K., Smith, S.L., Noetzli, J., Matthes, H., Vieira, G., Streletskiy, D.A., Schoeneich, P., Romanovsky, V.E., Lewkowicz, A.G., Abramov, A., Allard, M., Boike, J., Cable, W.L., Christiansen, H.H., Delaloye, R., Diekmann, B., Drozdov, D., Etzelmüller, B., Grosse, G., Guglielmin, M., Ingeman-Nielsen, T., Isaksen, K., Ishikawa, M., Johansson, M., Johannsson, H., Joo, A., Kaverin, D., Kholodov, A., Konstantinov, P., Kröger, T., Lambiel, C., Lanckman, J.-P., Luo, D., Malkova, G., Meiklejohn, I., Moskalenko, N., Oliva, M., Phillips, M., Ramos, M., Sannel, A.B.K., Sergeev, D., Seybold, C., Skryabin, P., Vasiliev, A., Wu, Q., Yoshikawa, K., Zheleznyak, M., Lantuit, H., 2019. Permafrost is warming at a global scale. Nat Commun 10, 264. https://doi.org/10.1038/s41467-018-08240-4

Bockheim, J.G., 1995. Permafrost distribution in the southern circumpolar region and its relation to the environment: A review and recommendations for further research. Permafrost & Periglacial 6, 27–45. https://doi.org/10.1002/ppp.3430060105

Born, W.T., 1941. The Attenuation Constant Of Earth Materials. GEOPHYSICS 6, 132–148. https://doi.org/10.1190/1.1443714

Bourbie, T., Zinszner, B., 1985. Hydraulic and acoustic properties as a function of porosity in Fontainebleau Sandstone. J. Geophys. Res. 90, 11524–11532. https://doi.org/10.1029/JB090iB13p11524

Bouzidi, Y., Schmitt, D.R., 2009. Measurement of the speed and attenuation of the Biot slow wave using a large ultrasonic transmitter. J. Geophys. Res. 114, B08201. https://doi.org/10.1029/2008JB006018

Brie, A., Pampuri, F., Marsala, A.F., Meazza, O., 1995. Shear Sonic Interpretation in Gas-Bearing Sands. Presented at the SPE Annual Technical Conference and Exhibition, p. SPE-30595-MS. https://doi.org/10.2118/30595-MS

Briggs, M.A., Campbell, S., Nolan, J., Walvoord, M.A., Ntarlagiannis, D., Day-Lewis, F.D., Lane, J.W., 2017. Surface Geophysical Methods for Characterising Frozen Ground in Transitional Permafrost Landscapes: Surface Geophysical Methods for Characterising Frozen Ground. Permafrost and Periglac. Process. 28, 52–65. https://doi.org/10.1002/ppp.1893

Brown, J., Ferrians, O., Heginbottom, J.A., Melnikov, E., 2002. Circum-Arctic Map of Permafrost and Ground-Ice Conditions, Version 2.

Bruckshaw, J.M., Mahanta, P.C., 1961. The Variation of the Elastic Constants of Rocsk with Frequency. Geophysical Prospecting 9, 65–76. https://doi.org/10.1111/j.1365-2478.1961.tb01690.x

Buckingham, M.J., 2005. Compressional and shear wave properties of marine sediments: Comparisons between theory and data. The Journal of the Acoustical Society of America 117, 137–152. https://doi.org/10.1121/1.1810231

Buckingham, M.J., 2000. Wave propagation, stress relaxation, and grain-to-grain shearing in saturated, unconsolidated marine sediments. The Journal of the Acoustical Society of America 108, 2796–2815. https://doi.org/10.1121/1.1322018

Buddo, I., Misyurkeeva, N., Shelokhov, I., Chuvilin, E., Chernikh, A., Smirnov, A., 2022. Imaging Arctic Permafrost: Modeling for Choice of Geophysical Methods. Geosciences 12, 389. https://doi.org/10.3390/geosciences12100389

Bustamante, J., Fabien-Ouellet, G., Duchesne, M.J., Ibrahim, A., 2024. Deep-learning viscoelastic seismic inversion for mapping subsea permafrost. Geophysics 89, R339–R353. https://doi.org/10.1190/geo2022-0759.1

Bustamante, J., Fabien-Ouellet, G., Duchesne, M.J., Ibrahim, A., 2023. Understanding seismic velocity variations of subsea permafrost: A sensitivity study. GEOPHYSICS R655–R669. https://doi.org/10.1190/geo2022-0568.1

Cadoret, T., Mavko, G., Zinszner, B., 1998. Fluid distribution effect on sonic attenuation in partially saturated limestones. GEOPHYSICS 63, 154–160. https://doi.org/10.1190/1.1444308

Capelli, A., Kapil, J.C., Reiweger, I., Or, D., Schweizer, J., 2016. Speed and attenuation of acoustic waves in snow: Laboratory experiments and modeling with Biot’s theory. Cold Regions Science and Technology 125, 1–11. https://doi.org/10.1016/j.coldregions.2016.01.004

Carcione, J.M., Mainardi, F., Qadrouh, A.N., Alajmi, M., Ba, J., 2024. Q: A Review. Surv Geophys 45, 1435–1458. https://doi.org/10.1007/s10712-024-09850-y

Carcione, J.M., Seriani, G., 1998. Seismic and ultrasonic velocities in permafrost. Geophysical Prospecting 46, 441–454. https://doi.org/10.1046/j.1365-2478.1998.1000333.x

Cascante, G., Santamarina, C., Yassir, N., 1998. Flexural excitation in a standard torsional-resonant column device.

Casco, M.E., Grätz, S., Wallacher, D., Grimm, N., Többens, D.M., Bilo, M., Speil, N., Fröba, M., Borchardt, L., 2021. Influence of surface wettability on methane hydrate formation in hydrophilic and hydrophobic mesoporous silicas. Chemical Engineering Journal 405, 126955. https://doi.org/10.1016/j.cej.2020.126955

Caspari, E., Qi, Q., Lopes, S., Lebedev, M., Gurevich, B., Rubino, J.G., Velis, D.R., Clennell, M.B., Müller, T.M., 2014. Wave attenuation in partially saturated porous rocks — New observations and interpretations across scales. The Leading Edge 33, 606–614. https://doi.org/10.1190/tle33060606.1

Chang, X., Liu, W., Zuo, G., Dou, Y., Li, Y., 2021. Research on ultrasonic-based investigation of mechanical properties of ice. Acta Oceanol. Sin. 40, 97–105. https://doi.org/10.1007/s13131-021-1890-3

Chapman, S., Borgomano, J.V.M., Quintal, B., Benson, S.M., Fortin, J., 2021. Seismic Wave Attenuation and Dispersion Due to Partial Fluid Saturation: Direct Measurements and Numerical Simulations Based on X-Ray CT. J Geophys Res Solid Earth 126. https://doi.org/10.1029/2021JB021643

Chen, W.W., Song, B., 2011. Conventional Kolsky bars, in: Chen, W., Song, B. (Eds.), Split Hopkinson (Kolsky) Bar: Design, Testing and Applications. Springer US, Boston, MA, pp. 1–35. https://doi.org/10.1007/978-1-4419-7982-7_1

Choi, J.-H., Dai, S., Cha, J.-H., Seol, Y., 2014. Laboratory formation of noncementing hydrates in sandy sediments. Geochem. Geophys. Geosyst. 15, 1648–1656. https://doi.org/10.1002/2014GC005287

Chotiros, N.P., 1995. Biot model of sound propagation in water-saturated sand. The Journal of the Acoustical Society of America 97, 17. https://doi.org/10.1121/1.412304

Chotiros, N.P., Isakson, M.J., 2004. A broadband model of sandy ocean sediments: Biot–Stoll with contact squirt flow and shear drag. The Journal of the Acoustical Society of America 116, 2011–2022. https://doi.org/10.1121/1.1791715

Christ, M., Park, J.-B., 2009. Ultrasonic technique as tool for determining physical and mechanical properties of frozen soils. Cold Regions Science and Technology 58, 136–142. https://doi.org/10.1016/j.coldregions.2009.05.008

Constable, S., 2020. Perspectives on Marine Electromagnetic Methods. Perspectives of ESS 1. https://doi.org/10.1029/2019CN000123

Dash, J.G., Fu, H., Wettlaufer, J.S., 1995. The premelting of ice and its environmental consequences. Rep. Prog. Phys. 58, 115–167. https://doi.org/10.1088/0034-4885/58/1/003

David, R.O., Marcolli, C., Fahrni, J., Qiu, Y., Perez Sirkin, Y.A., Molinero, V., Mahrt, F., Brühwiler, D., Lohmann, U., Kanji, Z.A., 2019. Pore condensation and freezing is responsible for ice formation below water saturation for porous particles. Proc. Natl. Acad. Sci. U.S.A. 116, 8184–8189. https://doi.org/10.1073/pnas.1813647116

Davies, R.M., Taylor, G.I., 1947. A critical study of the Hopkinson pressure bar. Philosophical Transactions of the Royal Society of London. Series A, Mathematical and Physical Sciences 240, 375–457. https://doi.org/10.1098/rsta.1948.0001

De Lemos, M.J.S., 2012. Applications in Hybrid Media, in: Turbulence in Porous Media. Elsevier, pp. 199–352. https://doi.org/10.1016/B978-0-08-098241-0.00011-5

Dobiński, W., 2020. Permafrost active layer. Earth-Science Reviews 208, 103301. https://doi.org/10.1016/j.earscirev.2020.103301

Domenico, S.N., 1974. Effect Of Water Saturation On Seismic Reflectivity Of Sand Reservoirs Encased In Shale. GEOPHYSICS 39, 759–769. https://doi.org/10.1190/1.1440464

Dong, H., Wang, J., Xie, Z., Wang, B., Zhang, L., Shi, Q., 2021. Potential applications based on the formation and dissociation of gas hydrates. Renewable and Sustainable Energy Reviews 143, 110928. https://doi.org/10.1016/j.rser.2021.110928

Dong, J., Sun, H., Zou, D., Yang, H., Jiang, Y., Liu, W., Kan, G., 2023. Model and prediction relationship of sound velocity and porosity of seafloor sediments. Journal of Sea Research 194, 102413. https://doi.org/10.1016/j.seares.2023.102413

Dou, S., Nakagawa, S., Dreger, D., Ajo-Franklin, J., 2016. A rock-physics investigation of unconsolidated saline permafrost: P-wave properties from laboratory ultrasonic measurements. GEOPHYSICS 81, WA233–WA245. https://doi.org/10.1190/geo2015-0176.1

Dubbelday, P.S., Capps, R.N., 1984. Interpretation of sample wave speed measured in an impedance tube. The Journal of the Acoustical Society of America 76, 964–967. https://doi.org/10.1121/1.391217

Duffaut, K., Landrø, M., Sollie, R., 2010. Using Mindlin theory to model friction-dependent shear modulus in granular media. GEOPHYSICS 75, E143–E152. https://doi.org/10.1190/1.3429998

Dutta, N.C., H. Odé, Odé, H., 1979. Attenuation and dispersion of compressional waves in fluid-filled porous rocks with partial gas saturation (White model); Part I, Biot theory. Geophysics 44, 1777–1788. https://doi.org/10.1190/1.1440938

Dvorkin, J., Nur, A., 1998. Acoustic signatures of patchy saturation. International Journal of Solids and Structures 35, 4803–4810. https://doi.org/10.1016/S0020-7683(98)00095-X

Dvorkin, J., Prasad, M., Sakai, A., Lavoie, D., 1999. Elasticity of marine sediments: Rock physics modeling. Geophysical Research Letters 26, 1781–1784. https://doi.org/10.1029/1999GL900332

Ecker, C., Dvorkin, J., Nur, A., 1998. Sediments with gas hydrates: Internal structure from seismic AVO. Geophysics 63, 1659–1669.

Ecker, C., Dvorkin, J., Nur, A.M., 2000. Estimating the amount of gas hydrate and free gas from marine seismic data. GEOPHYSICS 65, 565–573. https://doi.org/10.1190/1.1444752

El-Husseiny, A., Vega, S., Nizamuddin, S., 2019. The effect of pore structure complexity and saturation history on the variations of acoustic velocity as function of brine and oil saturation in carbonates. Journal of Petroleum Science and Engineering 179, 180–191. https://doi.org/10.1016/j.petrol.2019.04.019

Ellingsrud, S., Eidesmo, T., Johansen, S., Sinha, M.C., MacGregor, L.M., Constable, S., 2002. Remote sensing of hydrocarbon layers by seabed logging (SBL): Results from a cruise offshore Angola. The Leading Edge 21, 972–982. https://doi.org/10.1190/1.1518433

Emerson, M., Foray, P., 2006. Laboratory P-wave measurements in dry and saturated sand. Acta Geotech. 1, 167–177. https://doi.org/10.1007/s11440-006-0015-7

Enns, T., Scholander, P.F., Bradstreet, E.D., 1965. Effect of Hydrostatic Pressure on Gases Dissolved in Water. J. Phys. Chem. 69, 389–391. https://doi.org/10.1021/j100886a005

Falcon-Suarez, I.H., Dale, M., Marin-Moreno, H., 2024. Experimental study of geophysical and transport properties of salt rocks in the context of underground energy storage. Geophysical Prospecting 72, 2032–2048. https://doi.org/10.1111/1365-2478.13516

Fan, X., Wang, Y., Niu, F., Li, W., Wu, X., Ding, Z., Pang, W., Lin, Z., 2023. Environmental Characteristics of High Ice-Content Permafrost on the Qinghai–Tibetan Plateau. Remote Sensing 15, 4496. https://doi.org/10.3390/rs15184496

Fanchi, J.R., 2010. Geophysics, in: Integrated Reservoir Asset Management. Elsevier, pp. 71–88. https://doi.org/10.1016/B978-0-12-382088-4.00005-0

Fawad, M., Mondol, N.H., 2021. Monitoring geological storage of CO2: a new approach. Sci Rep 11, 5942. https://doi.org/10.1038/s41598-021-85346-8

French, H.M., 2007. Permafrost, in: The Periglacial Environment. pp. 83–115. https://doi.org/10.1002/9781118684931.ch5

Fu, Z., Wu, Q., Zhang, W., He, H., Wang, L., 2022. Water Migration and Segregated Ice Formation in Frozen Ground: Current Advances and Future Perspectives. Front. Earth Sci. 10, 826961. https://doi.org/10.3389/feart.2022.826961

Fuchs, M., Grosse, G., Jones, B.M., Strauss, J., Baughman, C.A., Walker, D.A., 2018. Sedimentary and geochemical characteristics of two small permafrost-dominated Arctic river deltas in northern Alaska. Arktos 4, 1–18. https://doi.org/10.1007/s41063-018-0056-9

Gabitto, J.F., Tsouris, C., 2010. Physical Properties of Gas Hydrates: A Review. Journal of Thermodynamics 2010, 1–12. https://doi.org/10.1155/2010/271291

Gardner, G.H.F., 1962. Extensional Waves in Fluid-Saturated Porous Cylinders. The Journal of the Acoustical Society of America 34, 36–40. https://doi.org/10.1121/1.1909010

Gardner, G.H.F., Wyllie, M.R.J., Droschak, D.M., 1964. Effects of Pressure and Fluid Saturation on the Attenuation of Elastic Waves in Sands. Journal of Petroleum Technology 16, 189–198. https://doi.org/10.2118/721-PA

Gassmann, F., 1951. Elastic waves through a packing of spheres. Geophysics 16, 673–685. https://doi.org/10.1190/1.1437718

Gei, D., Carcione, J.M., 2003. Acoustic properties of sediments saturated with gas hydrate, free gas and water: Acoustic properties of sediments. Geophysical Prospecting 51, 141–158. https://doi.org/10.1046/j.1365-2478.2003.00359.x

Ghodgaonkar, D.K., Varadan, V.V., Varadan, V.K., 1990. Free-space measurement of complex permittivity and complex permeability of magnetic materials at microwave frequencies. IEEE Trans. Instrum. Meas. 39, 387–394. https://doi.org/10.1109/19.52520

Glasser, L.A., 1978. An Analysis of Microwave De-Embedding Errors (Technical Notes). IEEE Transactions on Microwave Theory and Techniques 26, 379–380. https://doi.org/10.1109/TMTT.1978.1129395

Gong, Y., Cabodi, M., Porter, T., 2010. Pressure-dependent Resonance Frequency for Lipid-coated Microbubbles at Low Acoustic Pressures.

Gu, X., Zuo, K., Tessari, A., Gao, G., 2021. Effect of saturation on the characteristics of P-wave and S-wave propagation in nearly saturated soils using bender elements. Soil Dynamics and Earthquake Engineering 145, 106742. https://doi.org/10.1016/j.soildyn.2021.106742

Guerin, G., Goldberg, D., 2005. Modeling of acoustic wave dissipation in gas hydrate-bearing sediments: ACOUSTIC WAVE DISSIPATION. Geochem. Geophys. Geosyst. 6, n/a-n/a. https://doi.org/10.1029/2005GC000918

Guerin, G., Goldberg, D., 2002. Sonic waveform attenuation in gas hydrate-bearing sediments from the Mallik 2L-38 research well, Mackenzie Delta, Canada. J. Geophys. Res. 107. https://doi.org/10.1029/2001JB000556

Gurevich, B., 2002. Effect of fluid viscosity on elastic wave attenuation in porous rocks. GEOPHYSICS 67, 264–270. https://doi.org/10.1190/1.1451798

Hamilton, E.L., 1972. Compressional-Wave Attenuation In Marine Sediments. Geophysics 37, 620–646. https://doi.org/10.1190/1.1440287

Hamilton, E.L., 1971. Elastic properties of marine sediments. J. Geophys. Res. 76, 579–604. https://doi.org/10.1029/JB076i002p00579

Hamilton, E.L., 1970. Sound velocity and related properties of marine sediments, North Pacific. J. Geophys. Res. 75, 4423–4446. https://doi.org/10.1029/JB075i023p04423

Hamilton, E.L., Bachman, R.T., 1982. Sound velocity and related properties of marine sediments. J. Acoust. Soc. Am. 72, 15.

Hardin, B.O., Drnevich, V.P., 1972. Shear Modulus and Damping in Soils: Measurement and Parameter Effects (Terzaghi Leture). Journal of the Soil Mechanics and Foundations Division 98, 603–624. https://doi.org/10.1061/JSFEAQ.0001756

Hare, J., Hay, A.E., 2018. Attenuation and group speed in water-saturated granular materials at MHz frequencies. The Journal of the Acoustical Society of America 143, 2744–2755. https://doi.org/10.1121/1.5033901

He, W., Chen, Z., Shi, H., Liu, C., Li, S., 2021. Prediction of acoustic wave velocities by incorporating effects of water saturation and effective pressure. Engineering Geology 280, 105890. https://doi.org/10.1016/j.enggeo.2020.105890

Hearst, J.R., Nelson, P.H., 1985. Well logging for physical properties. Mc Graw-Hill Book Co, United States.

Heeschen, K.U., Janocha, J., Spangenberg, E., Schicks, J.M., Giese, R., 2020. The impact of ice on the tensile strength of unconsolidated sand - A model for gas hydrate-bearing sands? Marine and Petroleum Geology 122, 104607. https://doi.org/10.1016/j.marpetgeo.2020.104607

Helgerud, M.B., Dvorkin, J., Nur, A., Sakai, A., Collett, T., 1999. Elastic-wave velocity in marine sediments with gas hydrates: Effective medium modeling. Geophys. Res. Lett. 26, 2021–2024. https://doi.org/10.1029/1999GL900421

Helgerud, M.B., Waite, W.F., Kirby, S.H., Nur, A., 2009. Elastic wave speeds and moduli in polycrystalline ice Ih, sI methane hydrate, and sII methane-ethane hydrate. J. Geophys. Res. 114, B02212. https://doi.org/10.1029/2008JB006132

Hilbich, C., Hauck, C., Mollaret, C., Wainstein, P., Arenson, L.U., 2022. Towards accurate quantification of ice content in permafrost of the Central Andes – Part 1: Geophysics-based estimates from three different regions. The Cryosphere 16, 1845–1872. https://doi.org/10.5194/tc-16-1845-2022

Hill, R., 1952. The Elastic Behaviour of a Crystalline Aggregate. Proceedings of the Physical Society. Section A 65, 349. https://doi.org/10.1088/0370-1298/65/5/307

Hjort, J., Karjalainen, O., Aalto, J., Westermann, S., Romanovsky, V.E., Nelson, F.E., Etzelmüller, B., Luoto, M., 2018. Degrading permafrost puts Arctic infrastructure at risk by mid-century. Nat Commun 9, 5147. https://doi.org/10.1038/s41467-018-07557-4

Hjort, J., Streletskiy, D.A., Doré, G., Wu, Q., Bjella, K., Luoto, M., 2022. Impacts of permafrost degradation on infrastructure 3, 24–38. https://doi.org/10.1038/s43017-021-00247-8

Hopkinson, B., 1914. A method of measuring the pressure produced in the detonation of high explosives or by the impact of bullets. Proceedings of the Royal Society of London. Series A, Containing Papers of a Mathematical and Physical Character 89, 411–413. https://doi.org/10.1098/rspa.1914.0008

Horikawa, T., Katsura, M., Yokota, T., Nakashima, S., 2021. Effects of pore water distributions on *P* -wave velocity–water saturation relations in partially saturated sandstones. Geophysical Journal International 226, 1558–1573. https://doi.org/10.1093/gji/ggab143

Hovem, J.M., Ingram, G.D., 1979. Viscous attenuation of sound in saturated sand. The Journal of the Acoustical Society of America 66, 1807–1812. https://doi.org/10.1121/1.383653

Hu, G., Ye, Y., Liu, C., Best, A., Li, C., 2014. Gas hydrate distribution in sediment pore space and its impact on acoustic properties of hydrate-bearing sediments, in: Proceedings of the 8th International Conference on Gas Hydrates.

Huang, J.-W., Bellefleur, G., Milkereit, B., 2009. Seismic modeling of multidimensional heterogeneity scales of Mallik gas hydrate reservoirs, Northwest Territories of Canada. J. Geophys. Res. 114, B07306. https://doi.org/10.1029/2008JB006172

Hudson, J.A., 1981. Wave speeds and attenuation of elastic waves in material containing cracks. Geophysical Journal International 64, 133–150. https://doi.org/10.1111/j.1365-246x.1981.tb02662.x

Hughes, D.S., Jones, H.J., 1950. Variation of Elastic Moduli of Igneous Rocks with Pressure and Temperature. Bulletin of the Geological Society of America 61, 843–856. https://doi.org/10.1130/0016-7606(1950)61[843:VOEMOI]2.0.CO;2

Hughes, D.S., Kelly, J.L., 1952. Variation Of Elastic Wave Velocity With Saturation In Sandstone. GEOPHYSICS 17, 739–752. https://doi.org/10.1190/1.1437803

Hughes, D.S., Pondrom, W.L., Mims, R.L., 1949. Transmission of Elastic Pulses in Metal Rods. Phys. Rev. 75, 1552–1556. https://doi.org/10.1103/PhysRev.75.1552

Hutchings, J.K., Heil, P., Lecomte, O., Stevens, R., Steer, A., Lieser, J.L., 2015. Comparing methods of measuring sea-ice density in the East Antarctic. Ann. Glaciol. 56, 77–82. https://doi.org/10.3189/2015AoG69A814

Ishihara, K., Huang, Y., Tsuchiya, H., 1998. Liquefaction resistance of nearly saturated sand as correlated with longitudinal wave velocity, in: Poromechanics. CRC Press.

Jackson, I., Schijns, H., Schmitt, D.R., Mu, J., Delmenico, A., 2011. A versatile facility for laboratory studies of viscoelastic and poroelastic behaviour of rocks. Review of Scientific Instruments 82, 064501. https://doi.org/10.1063/1.3592154

Jackson, J.A., Bates, R.L., 1997. Glossary of Geology, Fifth Edition. ed. American Geological Institute.

James, S.R., Minsley, B.J., McFarland, J.W., Euskirchen, E.S., Edgar, C.W., Waldrop, M.P., 2021. The Biophysical Role of Water and Ice Within Permafrost Nearing Collapse: Insights From Novel Geophysical Observations. JGR Earth Surface 126, e2021JF006104. https://doi.org/10.1029/2021JF006104

Jedari-Eyvazi, F., Bayrakci, G., Minshull, T.A., Bull, J.M., Henstock, T.J., Macdonald, C., Robinson, A.H., 2023. Seismic characterization of a fluid escape structure in the North Sea: the Scanner Pockmark complex area. Geophysical Journal International 234, 597–619. https://doi.org/10.1093/gji/ggad078

Jendi, Z.M., Servio, P., Rey, A.D., 2015. Ideal Strength of Methane Hydrate and Ice I $_h$ from First-Principles. Crystal Growth & Design 15, 5301–5309. https://doi.org/10.1021/acs.cgd.5b00829

Jones, S.M., McCann, C., Astin, T.R., Sothcott, J., 1998. The effects of pore-fluid salinity on ultrasonic wave propagation in sandstones. GEOPHYSICS 63, 928–934. https://doi.org/10.1190/1.1444404

Kang, S., Jin, Y.K., Jang, U., Duchesne, M.J., Shin, C., Kim, S., Riedel, M., Dallimore, S.R., Paull, C.K., Choi, Y., Hong, J.K., 2021. Imaging the P-Wave Velocity Structure of Arctic Subsea

Permafrost Using Laplace-Domain Full-Waveform Inversion. JGR Earth Surface 126, e2020JF005941. https://doi.org/10.1029/2020JF005941

Kawasaki, K., Osterkamp, T.E., Jurick, R.W., Kienle, J., 1983. Gravity Measurements in Permafrost Terrain Containing Massive Ground Ice. Ann. Glaciol. 4, 133–140. https://doi.org/10.3189/S026030550000536X

Kim, I.-W., Timmermann, A., Kim, J.-E., Rodgers, K.B., Lee, S.-S., Lee, H., Wieder, W.R., 2024. Abrupt increase in Arctic-Subarctic wildfires caused by future permafrost thaw. Nat Commun 15, 7868. https://doi.org/10.1038/s41467-024-51471-x

Kimura, M., 2011. Velocity dispersion and attenuation in granular marine sediments: Comparison of measurements with predictions using acoustic models. The Journal of the Acoustical Society of America 129, 3544–3561. https://doi.org/10.1121/1.3585841

King, M.S., Marsden, J.R., Dennis, J.W., 2000. Biot dispersion for P- and S-wave velocities in partially and fully saturated sandstones. Geophysical Prospecting 15. https://doi.org/10.1111/j.1365-2478.2000.00221.x

King, M.S., Zimmerman, R.W., Corwin, R.F., 1988. SEISMIC AND ELECTRICAL PROPERTIES OF UNCONSOLIDATED PERMAFROST[1]. Geophysical Prospecting 36, 349–364. https://doi.org/10.1111/j.1365-2478.1988.tb02168.x

Klauda, J.B., Sandler, S.I., 2005. Global Distribution of Methane Hydrate in Ocean Sediment. Energy Fuels 19, 459–470. https://doi.org/10.1021/ef049798o

Kleinberg, R.L., Griffin, D.D., 2005. NMR measurements of permafrost: unfrozen water assay, pore-scale distribution of ice, and hydraulic permeability of sediments. Cold Regions Science and Technology 42, 63–77. https://doi.org/10.1016/j.coldregions.2004.12.002

Klimentos, T., McCann, C., 1988. Attenuation of compressional waves in water?saturated sandstones by intra?pore clay minerals, in: SEG Technical Program Expanded Abstracts 1988, SEG Technical Program Expanded Abstracts. Society of Exploration Geophysicists, pp. 933–935. https://doi.org/10.1190/1.1892402

Knight, R., Nolen-Hoeksema, R., 1990. A laboratory study of the dependence of elastic wave velocities on pore scale fluid distribution. Geophysical Research Letters 17, 1529–1532. https://doi.org/10.1029/GL017i010p01529

Kolsky, H., 1964. Stress waves in solids. Journal of Sound and Vibration 1, 88–110. https://doi.org/10.1016/0022-460X(64)90008-2

Kolsky, H., 1949. An Investigation of the Mechanical Properties of Materials at very High Rates of Loading. Proc. Phys. Soc. B 62, 676–700. https://doi.org/10.1088/0370-1301/62/11/302

Kvenvolden, K.A., 1999. Potential effects of gas hydrate on human welfare. Proc. Natl. Acad. Sci. U.S.A. 96, 3420–3426. https://doi.org/10.1073/pnas.96.7.3420

Kvenvolden, K.A., 1993. Gas hydrates-geological perspective and global change. Rev. Geophys. 31, 173–187. https://doi.org/10.1029/93RG00268

Kvenvolden, K.A., 1988. Methane hydrate — A major reservoir of carbon in the shallow geosphere? Chemical Geology 71, 41–51. https://doi.org/10.1016/0009-2541(88)90104-0

Lacelle, D., Fisher, D.A., Verret, M., Pollard, W., 2022. Improved prediction of the vertical distribution of ground ice in Arctic-Antarctic permafrost sediments. Commun Earth Environ 3, 31. https://doi.org/10.1038/s43247-022-00367-z

Le, T.M.H., Eiksund, G.R., Strøm, P.J., Saue, M., 2014. Geological and geotechnical characterisation for offshore wind turbine foundations: A case study of the Sheringham Shoal wind farm. Engineering Geology 177, 40–53. https://doi.org/10.1016/j.enggeo.2014.05.005

Leclaire, Ph., Cohen-Ténoudji, F., Aguirre-Puente, J., 1994. Extension of Biot's theory of wave propagation to frozen porous media. The Journal of the Acoustical Society of America 96, 3753–3768. https://doi.org/10.1121/1.411336

Lee, J.-W., Kim, J.-S., Hong, C.-H., Oh, T.-M., 2024. Permeability monitoring of underground concrete structures using elastic wave characteristics with modified Biot's model. Sci Rep 14, 22110. https://doi.org/10.1038/s41598-024-73449-x

Lee, K.I., Humphrey, V.F., Kim, B.-N., Yoon, S.W., 2007. Frequency dependencies of phase velocity and attenuation coefficient in a water-saturated sandy sediment from 0.3to1.0MHz. The Journal of the Acoustical Society of America 121, 2553–2558. https://doi.org/10.1121/1.2713690

Lee, M.W., Collett, T.S., 2006. Proceedings of the Ocean Drilling Program, 199 Scientific Results, Proceedings of the Ocean Drilling Program. Ocean Drilling Program. https://doi.org/10.2973/odp.proc.sr.199.2006

Leurer, K.C., 1997. Attenuation in fine-grained marine sediments: Extension of the Biot-Stoll model by the "effective grain model" (EGM). GEOPHYSICS 62, 1465–1479. https://doi.org/10.1190/1.1444250

Leurer, K.C., Brown, C., 2008. Acoustics of marine sediment under compaction: Binary grain-size model and viscoelastic extension of Biot's theory. The Journal of the Acoustical Society of America 123, 1941–1951. https://doi.org/10.1121/1.2871839

Lewandowski, A., Szypłowska, A., Kafarski, M., Wilczek, A., Barmuta, P., Skierucha, W., 2017. 0.05–3 GHz VNA characterization of soil dielectric properties based on the multiline TRL calibration. Meas. Sci. Technol. 28, 024007. https://doi.org/10.1088/1361-6501/28/2/024007

Li, B., Matsushima, J., 2024. Influence of ice properties on wave propagation characteristics in partially frozen soils and rocks: A temperature-dependent rock-physics model. Geophysics 89, MR281–MR295. https://doi.org/10.1190/geo2023-0694.1

Li, G., Li, X., Liu, K., 2024. The control mechanism of P-wave attenuation in unconsolidated porous media. The Journal of the Acoustical Society of America 156, 891–897. https://doi.org/10.1121/10.0028192

Li, H., Zhao, L., Han, D., Gao, J., Yuan, H., Wang, Y., 2020. Experimental study on frequency-dependent elastic properties of weakly consolidated marine sandstone: effects of partial saturation. Geophysical Prospecting. https://doi.org/10.1111/1365-2478.13031

Li, J., Roche, B., Bull, J.M., White, P.R., Davis, J.W., Deponte, M., Gordini, E., Cotterle, D., 2020. Passive acoustic monitoring of a natural CO2 seep site – Implications for carbon capture and storage. International Journal of Greenhouse Gas Control 93, 102899. https://doi.org/10.1016/j.ijggc.2019.102899

Li, X., Dong, L., Zhao, Q., 2014. Seismic modelling study of P-wave attenuation and velocity dispersion in patchy-saturated porous media. J. Geophys. Eng. 11, 065010. https://doi.org/10.1088/1742-2132/11/6/065010

Liang, S., Hall, K.Wm., Laaksonen, A., Zhang, Z., Kusalik, P.G., 2019. Characterizing key features in the formation of ice and gas hydrate systems. Phil. Trans. R. Soc. A. 377, 20180167. https://doi.org/10.1098/rsta.2018.0167

Lin, Z., Pan, H., Fang, H., Gao, W., Liu, D., 2018. High-altitude well log evaluation of a permafrost gas hydrate reservoir in the Muli area of Qinghai, China. Sci Rep 8, 12596. https://doi.org/10.1038/s41598-018-30795-x

Liu, L., Zang, S., Wu, X., Liu, R., Li, T., Zhu, J., Sun, L., Wu, S., Dong, X., Zhang, Z., 2023. Sediment Grain-Size Composition in the Permafrost Region of the Greater Khingan Range and Its Significance as a Material Source. Land 12, 1728. https://doi.org/10.3390/land12091728

Lucet, N., Rasolofosaon, P.N.J., Zinszner, B., 1991. Sonic properties of rocks under confining pressure using the resonant bar technique. The Journal of the Acoustical Society of America 89, 980–990. https://doi.org/10.1121/1.400643

Lundberg, B., 1976. A split Hopkinson bar study of energy absorption in dynamic rock fragmentation. International Journal of Rock Mechanics and Mining Sciences & Geomechanics Abstracts 13, 187–197. https://doi.org/10.1016/0148-9062(76)91285-7

Lv, X., Li, W., Shi, B., Zhou, S., 2018. Study on the blockage mechanism of carbon dioxide hydrate slurry and its microscopic particle characteristics. RSC Adv. 8, 36959–36969. https://doi.org/10.1039/C8RA07259K

Lyu, C., Amiri, S.A.G., Grimstad, G., Høyland, K.V., Ingeman-Nielsen, T., 2020. Comparison of Geoacoustic Models for Unfrozen Water Content Estimation. JGR Solid Earth 125, e2020JB019766. https://doi.org/10.1029/2020JB019766

MacDonald, G.J., 1990. Role of methane clathrates in past and future climates. Climatic Change 16, 247–281. https://doi.org/10.1007/BF00144504

Madhusudhan, B.N., Clayton, C.R.I., Priest, J.A., 2019. The Effects of Hydrate on the Strength and Stiffness of Some Sands. J. Geophys. Res. Solid Earth 124, 65–75. https://doi.org/10.1029/2018JB015880

Mahabadi, N., Dai, S., Seol, Y., Jang, J., 2019. Impact of hydrate saturation on water permeability in hydrate-bearing sediments. Journal of Petroleum Science and Engineering 174, 696–703. https://doi.org/10.1016/j.petrol.2018.11.084

Makogon, Y.F., 2010. Natural gas hydrates – A promising source of energy. Journal of Natural Gas Science and Engineering 2, 49–59. https://doi.org/10.1016/j.jngse.2009.12.004

Marín-Moreno, H., Sahoo, S.K., Best, A.I., 2017. Theoretical modeling insights into elastic wave attenuation mechanisms in marine sediments with pore-filling methane hydrate: Hydrate-Bearing Effective Sediment Model. J. Geophys. Res. Solid Earth. https://doi.org/10.1002/2016JB013577

Marketos, G., Best, A.I., 2010. Application of the BISQ model to clay squirt flow in reservoir sandstones. J. Geophys. Res. 115, 2009JB006495. https://doi.org/10.1029/2009JB006495

Maslin, M., Owen, M., Betts, R., Day, S., Dunkley Jones, T., Ridgwell, A., 2010. Gas hydrates: past and future geohazard? Phil. Trans. R. Soc. A. 368, 2369–2393. https://doi.org/10.1098/rsta.2010.0065

Matsushima, J., Ali, M.Y., Bouchaala, F., 2017. A novel method for separating intrinsic and scattering attenuation for zero-offset vertical seismic profiling data. Geophysical Journal International 211, 1655–1668. https://doi.org/10.1093/gji/ggx391

Matsushima, J., Suzuki, M., Kato, Y., Nibe, T., Rokugawa, S., 2008. Laboratory experiments on compressional ultrasonic wave attenuation in partially frozen brines. GEOPHYSICS 73, N9–N18. https://doi.org/10.1190/1.2827214

Matsushima, J., Suzuki, M., Kato, Y., Rokugawa, S., 2016. Ultrasonic measurements of attenuation and velocity of compressional and shear waves in partially frozen unconsolidated sediment and synthetic porous rock. GEOPHYSICS 81, D141–D153. https://doi.org/10.1190/geo2015-0350.1

Mavko, G., 1979. Frictional attenuation: an inherent amplitude dependence. Journal of Geophysical Research 84, 4769–4775. https://doi.org/10.1029/JB084iB09p04769

Mavko, G., Mukerji, T., Dvorkin, J., 2009. The Rock Physics Handbook, 2nd ed. Cambridge University Press.

Mavko, G., Nolen-Hoeksema, R., 1994. Estimating seismic velocities at ultrasonic frequencies in partially saturated rocks. Geophysics 59, 252–258.

Mavko, G., Nur, A., 1975. Melt squirt in the asthenosphere. J. Geophys. Res. 80, 1444–1448. https://doi.org/10.1029/JB080i011p01444

McCann, C., Sothcott, J., 1992. Laboratory measurements of the seismic properties of sedimentary rocks. SP 65, 285–297. https://doi.org/10.1144/GSL.SP.1992.065.01.22

McCann, C., Sothcott, J., Best, A.I., 2014. A new laboratory technique for determining the compressional wave properties of marine sediments at sonic frequencies and *in situ* pressures: Compressional wave properties of marine sediments. Geophysical Prospecting 62, 97–116. https://doi.org/10.1111/1365-2478.12079

McCutchan, A., Johnson, B., 2022. Laboratory Experiments on Ice Melting: A Need for Understanding Dynamics at the Ice-Water Interface. JMSE 10, 1008. https://doi.org/10.3390/jmse10081008

McPhee, C., Reed, J., Zubizarreta, I., 2015. Chapter 9 - Capillary Pressure, in: McPhee, C., Reed, J., Zubizarreta, I. (Eds.), Core Analysis, Developments in Petroleum Science. Elsevier, pp. 449–517. https://doi.org/10.1016/B978-0-444-63533-4.00009-3

Melvin, A.M., Larsen, P., Boehlert, B., Neumann, J.E., Chinowsky, P., Espinet, X., Martinich, J., Baumann, M.S., Rennels, L., Bothner, A., Nicolsky, D.J., Marchenko, S.S., 2017. Climate change damages to Alaska public infrastructure and the economics of proactive adaptation. Proc. Natl. Acad. Sci. U.S.A. 114. https://doi.org/10.1073/pnas.1611056113

Meredith, M., Sommerkorn, M., Casotta, S., Derksen, C., Ekaykin, A., Hollowed, A., Kofinas, G., Mackintosh, A., Melbourne-Thomas, J., Muelbert, M., Ottersen, G., Pritchard, H., Schuur, E., 2022. The Ocean and Cryosphere in a Changing Climate: Special Report of the Intergovernmental Panel on Climate Change, 1st ed. Cambridge University Press. https://doi.org/10.1017/9781009157964

Meyer, A., Eliseev, D., Heinen, D., Linder, P., Scholz, F., Weinstock, L.S., Wiebusch, C., Zierke, S., 2019. Attenuation of sound in glacier ice from 2 to 35 kHz. The Cryosphere 13, 1381–1394. https://doi.org/10.5194/tc-13-1381-2019

Mikhaltsevitch, V., Lebedev, M., Gurevich, B., 2014. A laboratory study of low-frequency wave dispersion and attenuation in water-saturated sandstones. The Leading Edge 33, 616–622. https://doi.org/10.1190/tle33060616.1

Mikhaltsevitch, V., Lebedev, M., Pevzner, R., Yurikov, A., Tertyshnikov, K., 2023. Low-frequency laboratory measurements of the elastic properties of solids using a distributed acoustic sensing system. Journal of Rock Mechanics and Geotechnical Engineering 15, 2330–2338. https://doi.org/10.1016/j.jrmge.2023.05.002

Moore, P.L., 2014. Deformation of debris-ice mixtures: DEFORMATION OF DEBRIS-ICE MIXTURES. Rev. Geophys. 52, 435–467. https://doi.org/10.1002/2014RG000453

Muller, S.W., 1947. Permafrost : or, permanently frozen ground and related engineering problems. J.W. Edwards, Ann Arbor.

Müller, T.M., Gurevich, B., 2005. Wave-induced fluid flow in random porous media: Attenuation and dispersion of elastic waves. Journal of the Acoustical Society of America 117, 2732–2741. https://doi.org/10.1121/1.1894792

Müller, T.M., Gurevich, B., Lebedev, M., 2010. Seismic wave attenuation and dispersion resulting from wave-induced flow in porous rocks — A review. Geophysics 75. https://doi.org/10.1190/1.3463417

Murphy, W.F., 1984. Acoustic measures of partial gas saturation in tight sandstones. Journal of Geophysical Research 89, 11549–11559. https://doi.org/10.1029/jb089ib13p11549

Murphy, William F., 1982. Effects of partial water saturation on attenuation in Massilon sandstone and Vycor porous glass. The Journal of the Acoustical Society of America 71, 1458–1468. https://doi.org/10.1121/1.387843

Murphy, W.F., 1982. Effects of Microstructure and Pore Fluids on the Acoustic Properties of Granular Sedimentary Materials, Stanford Rock Physics Project report. Stanford University.

Nakagawa, S., 2011. Split Hopkinson resonant bar test for sonic-frequency acoustic velocity and attenuation measurements of small, isotropic geological samples. Review of Scientific Instruments 82, 044901. https://doi.org/10.1063/1.3579501

Nakano, Y., Arnold, R., 1973. Acoustic properties of frozen Ottawa sand. Water Resources Research 9, 178–184. https://doi.org/10.1029/WR009i001p00178

Nguyen, N.N., Galib, M., Nguyen, A.V., 2020. Critical Review on Gas Hydrate Formation at Solid Surfaces and in Confined Spaces—Why and How Does Interfacial Regime Matter? Energy Fuels 34, 6751–6760. https://doi.org/10.1021/acs.energyfuels.0c01291

Ni, J., Wu, T., Zhu, X., Wu, X., Pang, Q., Zou, D., Chen, J., Li, R., Hu, G., Du, Y., Hao, J., Li, X., Qiao, Y., 2021. Risk assessment of potential thaw settlement hazard in the permafrost regions of Qinghai-Tibet Plateau. Science of The Total Environment 776, 145855. https://doi.org/10.1016/j.scitotenv.2021.145855

Ning, F., Yu, Y., Kjelstrup, S., Vlugt, T.J.H., Glavatskiy, K., 2012. Mechanical properties of clathrate hydrates: status and perspectives. Energy Environ. Sci. 5, 6779. https://doi.org/10.1039/c2ee03435b

Nisbet, E., 1990. Climate change and methane. Nature 347, 23–23. https://doi.org/10.1038/347023a0

Nixdorf, J., Oellrich, L.R., 1997. Experimental determination of hydrate equilibrium conditions for pure gases, binary and ternary mixtures and natural gases. Fluid Phase Equilibria 139, 325–333. https://doi.org/10.1016/S0378-3812(97)00141-6

North, L., Best, A., 2015. An Improved High-Spectral Resolution Water Filled Impedance Tube Measurement Method For Marine Sediment Studies, in: Seabed and Sediment Acoustics 2015. Presented at the Seabed and Sediment Acoustics 2015, Institute of Acoustics, Bath. https://doi.org/10.25144/18070

Oda, H., Nishizawa, S., Kusunose, K., 1990. Frequency-dependence of velocity and attenuation of elastic waves in granite under uniaxial compression 133.

Oh, T.-M., Kwon, T.-H., Cho, G.-C., 2011. Effect of Partial Water Saturation on Attenuation Characteristics of Low Porosity Rocks. Rock Mech Rock Eng 44, 245–251. https://doi.org/10.1007/s00603-010-0121-6

O'Hara, S.G., 1985. Influence of pressure, temperature, and pore fluid on the frequency-dependent attenuation of elastic waves in Berea sandstone. Phys. Rev. A 32, 472–488. https://doi.org/10.1103/PhysRevA.32.472

O'Neill, H.B., Roy-Leveillee, P., Lebedeva, L., Ling, F., 2020. Recent advances (2010–2019) in the study of taliks. Permafrost & Periglacial 31, 346–357. https://doi.org/10.1002/ppp.2050

Ophir, J., McWhirt, R.E., Maklad, N.F., Jaeger, P.M., 1985. A Narrowband Pulse-Echo Technique for In Vivo Ultrasonic Attenuation Estimation. IEEE Trans. Biomed. Eng. BME-32, 205–212. https://doi.org/10.1109/TBME.1985.325530

Oswell, J.M., 2011. Pipelines in permafrost: geotechnical issues and lessons ^{1} 2010 R.M. Hardy Address, 63rd Canadian Geotechnical Conference. Can. Geotech. J. 48, 1412–1431. https://doi.org/10.1139/t11-045

Overduin, P.P., Haberland, C., Ryberg, T., Kneier, F., Jacobi, T., Grigoriev, Mikhail.N., Ohrnberger, M., 2015. Submarine permafrost depth from ambient seismic noise. Geophysical Research Letters 42, 7581–7588. https://doi.org/10.1002/2015GL065409

Pandit, B.I., King, M.S., 1979. A study of the effects of pore-water salinity on some physical properties of sedimentary rocks at permafrost temperatures. Can. J. Earth Sci. 16, 1566–1580. https://doi.org/10.1139/e79-143

Papageorgiou, G., Amalokwu, K., Chapman, M., 2016. Theoretical derivation of a Brie-like fluid mixing law: Brie-like fluid mixing law. Geophysical Prospecting 64, 1048–1053. https://doi.org/10.1111/1365-2478.12380

Park, J.-H., Lee, J.-S., 2014. Characteristics of elastic waves in sand–silt mixtures due to freezing. Cold Regions Science and Technology 99, 1–11. https://doi.org/10.1016/j.coldregions.2013.11.002

Parolai, S., Lai, C.G., Dreossi, I., Ktenidou, O.-J., Yong, A., 2022. A review of near-surface QS estimation methods using active and passive sources. J Seismol 26, 823–862. https://doi.org/10.1007/s10950-021-10066-5

Paull, C.K., Dallimore, S.R., Jin, Y.K., Caress, D.W., Lundsten, E.M., Gwiazda, R., Anderson, K., Clarke, J.E.H., Youngblut, S., Melling, H., 2022. Rapid seafloor changes associated with the degradation of Arctic submarine permafrost. Proceedings of the National Academy of Sciences of the United States of America 119, e2119105119–e2119105119. https://doi.org/10.1073/pnas.2119105119

Pearson, C.F., Halleck, P.M., McGuire, P.L., Hermes, R., Mathews, M., 1983. Natural gas hydrate deposits: a review of in situ properties. J. Phys. Chem. 87, 4180–4185. https://doi.org/10.1021/j100244a041

Peselnick, L., Outerbridge, W.F., 1961. Internal friction in shear and shear modulus of Solenhofen limestone over a frequency range of 107 cycles per second. Journal of Geophysical Research (1896-1977) 66, 581–588. https://doi.org/10.1029/JZ066i002p00581

Pierce, A.D., 2019. Acoustics: An Introduction to Its Physical Principles and Applications. Springer International Publishing, Cham. https://doi.org/10.1007/978-3-030-11214-1

Pozar, D.M., 2012. Microwave engineering. Fourth edition. Hoboken, NJ : Wiley, [2012] ©2012.

Prasad, M., 2002. Acoustic measurements in unconsolidated sands at low effective pressure and overpressure detection. GEOPHYSICS 67, 405–412. https://doi.org/10.1190/1.1468600

Pride, S.R., Berryman, J.G., Harris, J.M., 2004. Seismic attenuation due to wave-induced flow: WAVE-INDUCED FLOW LOSSES. J. Geophys. Res. 109. https://doi.org/10.1029/2003JB002639

Priest, J.A., Abbas, M., Hayley, J.L., 2021. The Change in Geomechanical Properties of Gas Saturated Methane Hydrate-Bearing Sand Resulting From Water Saturation. J Geophys Res Solid Earth 126. https://doi.org/10.1029/2021JB022245

Priest, J.A., Best, A.I., Clayton, C.R.I., 2005. A laboratory investigation into the seismic velocities of methane gas hydrate-bearing sand. J. Geophys. Res. 110, 2004JB003259. https://doi.org/10.1029/2004JB003259

Priest, J.A., Rees, E.V.L., Clayton, C.R.I., 2009. Influence of gas hydrate morphology on the seismic velocities of sands. J. Geophys. Res. 114, 2009JB006284. https://doi.org/10.1029/2009JB006284

Qanbari, F., Pooladi-Darvish, M., Hamed Tabatabaie, S., Gerami, S., 2011. Storage of CO2 as hydrate beneath the ocean floor. Energy Procedia 4, 3997–4004. https://doi.org/10.1016/j.egypro.2011.02.340

Rake, L., Pinkert, S., 2021. The ‘excess gas’ method for laboratory formation of methane hydrate-bearing sand: geotechnical application. Sci Rep 11, 22068. https://doi.org/10.1038/s41598-021-00777-7

Redwood, Martin., 1960. Mechanical waveguides; the propagation of acoustic and ultrasonic waves in fluids and solids with boundaries. Pergamon Press, New York.

Reuss, A., 1929. Berechnung der Fließgrenze von Mischkristallen auf Grund der Plastizitätsbedingung für Einkristalle . Z. angew. Math. Mech. 9, 49–58. https://doi.org/10.1002/zamm.19290090104

Reynolds, J., Catt, L., Salaün, G., Knight, P., Cleverly, W., Costa, L., 2017. Integration of Geophysical, Geological and Geotechnical Data for Offshore Wind Farms East Anglia One OWF, Southern North Sea, A Case History. Offshore Site Investigation Geotechnics 8th International Conference Proceeding 1291–1298. https://doi.org/doi:10.3723/OSIG17.1291

Richards, S., Tan, A., Platt, I., Woodhead, I., 2014. Free-space microwave moisture content measurement of moist sand, in: 2014 IEEE Sensors Applications Symposium (SAS). Presented at the 2014 IEEE Sensors Applications Symposium (SAS), IEEE, Queenstown, New Zealand, pp. 145–150. https://doi.org/10.1109/SAS.2014.6798935

Richart, F.E., Hall, J.R., Woods, R.D., 1970. Vibrations of soils and foundations.

Riedel, M., Collett, T.S., Malone, M.J., Expedition 311 Scientists (Eds.), 2006. Proceedings of the IODP, 311, Proceedings of the IODP. Integrated Ocean Drilling Program. https://doi.org/10.2204/iodp.proc.311.2006

Rochelle, C.A., Camps, A.P., Long, D., Milodowski, A., Bateman, K., Gunn, D., Jackson, P., Lovell, M.A., Rees, J., 2009. Can CO $_2$ hydrate assist in the underground storage of carbon dioxide? SP 319, 171–183. https://doi.org/10.1144/SP319.14

Rubino, J.G., Holliger, K., 2012. Seismic attenuation and velocity dispersion in heterogeneous partially saturated porous rocks: Mesoscopic effects and partial saturation. Geophysical Journal International 188, 1088–1102. https://doi.org/10.1111/j.1365-246X.2011.05291.x

Ruppel, C.D., Kessler, J.D., 2017. The interaction of climate change and methane hydrates. Rev. Geophys. 55, 126–168. https://doi.org/10.1002/2016RG000534

Ruppel, C.D., Lee, J.Y., Pecher, I., 2019. Introduction to Special Issue on Gas Hydrate in Porous Media: Linking Laboratory and Field-Scale Phenomena. J. Geophys. Res. Solid Earth 124, 7525–7537. https://doi.org/10.1029/2019JB018186

Sahoo, S.K., 2018. The Effect of Gas Hydrate Saturation and Distribution on the Geophysical Properties of Marine Sediments. University of Southampton, Southampton.

Sahoo, S.K., Best, A.I., 2021. The Influence of Gas Hydrate Morphology on Reservoir Permeability and Geophysical Shear Wave Remote Sensing. JGR Solid Earth 126. https://doi.org/10.1029/2021JB022206

Sahoo, S.K., Madhusudhan, B.N., Marín-Moreno, H., North, L.J., Ahmed, S., Falcon-Suarez, I.H., Minshull, T.A., Best, A.I., 2018. Laboratory Insights Into the Effect of Sediment-Hosted Methane Hydrate Morphology on Elastic Wave Velocity From Time-Lapse 4-D Synchrotron X-Ray Computed Tomography. Geochem. Geophys. Geosyst. 19, 4502–4521. https://doi.org/10.1029/2018GC007710

Sahoo, S.K., North, L.J., Marín-Moreno, H., Minshull, T.A., Best, A.I., 2019. Laboratory observations of frequency-dependent ultrasonic P-wave velocity and attenuation during methane hydrate formation in Berea sandstone. Geophysical Journal International 219, 713–723. https://doi.org/10.1093/gji/ggz311

Sander, R., 2015. Compilation of Henry's law constants (version 4.0) for water as solvent. Atmos. Chem. Phys. 15, 4399–4981. https://doi.org/10.5194/acp-15-4399-2015

Schulson, E.M., Fortt, A.L., Iliescu, D., Renshaw, C.E., 2006. Failure envelope of first-year Arctic sea ice: The role of friction in compressive fracture. J. Geophys. Res. 111, 2005JC003235. https://doi.org/10.1029/2005JC003235

Schumann, K., Stipp, M., Behrmann, J.H., Klaeschen, D., Schulte-Kortnack, D., 2014. *P* and *S* wave velocity measurements of water-rich sediments from the Nankai Trough, Japan: P- and S-wave velocity measurements. J. Geophys. Res. Solid Earth 119, 787–805. https://doi.org/10.1002/2013JB010290

Schuur, E.A.G., McGuire, A.D., Schädel, C., Grosse, G., Harden, J.W., Hayes, D.J., Hugelius, G., Koven, C.D., Kuhry, P., Lawrence, D.M., Natali, S.M., Olefeldt, D., Romanovsky, V.E., Schaefer, K., Turetsky, M.R., Treat, C.C., Vonk, J.E., 2015. Climate change and the permafrost carbon feedback. Nature 520, 171–179. https://doi.org/10.1038/nature14338

Selfridge, A.R., 1985. Approximate Material Properties in Isotropic Materials. IEEE Trans. Son. Ultrason. 32, 381–394. https://doi.org/10.1109/T-SU.1985.31608

Sheng, Y., Peng, W., Wen, Z., Fukuda, M., 2003. Physical properties of frozen soils measured using ultrasonic techniques.

Sheriff, R.E., Geldart, L.P., 1995. Exploration Seismology, 2nd ed. Cambridge University Press, Cambridge. https://doi.org/10.1017/CBO9781139168359

Shumway, G., 1960. Sound Speed And Absorption Studies Of Marine Sediments By A Resonance Method—Part II. GEOPHYSICS 25, 659–682. https://doi.org/10.1190/1.1438749

Shur, Y., Hinkel, K.M., Nelson, F.E., 2005. The transient layer: implications for geocryology and climate-change science. Permafrost & Periglacial 16, 5–17. https://doi.org/10.1002/ppp.518

Si, W., Di, B., Wei, J., Li, Q., 2016. Experimental study of water saturation effect on acoustic velocity of sandstones. Journal of Natural Gas Science and Engineering 33, 37–43. https://doi.org/10.1016/j.jngse.2016.05.002

Simmons, G., 1965. Single Crystal Elastic Constants and Calculated Aggregate Properties 274.

Singh, H., Seol, Y., Myshakin, E.M., 2021. Prediction of gas hydrate saturation using machine learning and optimal set of well-logs. Comput Geosci 25, 267–283. https://doi.org/10.1007/s10596-020-10004-3

Sizemore, H.G., Mellon, M.T., 2008. Laboratory characterization of the structural properties controlling dynamical gas transport in Mars-analog soils. Icarus 197, 606–620. https://doi.org/10.1016/j.icarus.2008.05.013

Sloan, E.D., Koh, C.A., Sum, A.K., 2010. Gas Hydrate Stability and Sampling: The Future as Related to the Phase Diagram. Energies 3, 1991–2000. https://doi.org/10.3390/en3121991

Smeulders, D.M.J., Van Dongen, M.E.H., 1997. Wave propagation in porous media containing a dilute gas–liquid mixture: theory and experiments. Journal of Fluid Mechanics 343, 351–373. https://doi.org/10.1017/S0022112097005983

Smith, A.H., Lawson, A.W., 1954. The Velocity of Sound in Water as a Function of Temperature and Pressure. The Journal of Chemical Physics 22, 351–359. https://doi.org/10.1063/1.1740074

Sondergeld, C.H., Rai, C.S., 2007. Velocity and resistivity changes during freeze-thaw cycles in Berea sandstone. GEOPHYSICS 72, E99–E105. https://doi.org/10.1190/1.2435198

Spangenberg, E., Seyberth, K., Heeschen, K.U., Priegnitz, M., Schicks, J.M., 2018. A *Quick Look* Method to Assess the Dependencies of Rock Physical Sediment Properties on the Saturation With Pore-Filling Hydrate. J. Geophys. Res. Solid Earth 123, 5588–5598. https://doi.org/10.1029/2018JB015855

Stokoe, K.H., Darendeli, M.B., Andrus, R.D., Brown, L.T., Portuguese Society for Geotechnique (SPG), International Society for Soil Mechanics and Geotechnical Engineering, 1999. Dynamic soil properties: Laboratory, field and correlation studies. Presented at the International conference; 2nd, Earthquake geotechnical engineering, A A Balkema;, Lisbon, pp. 811–846.

Stoll, R.D., 1985. Marine sediment acoustics. The Journal of the Acoustical Society of America 77, 12. https://doi.org/10.1121/1.391928

Stoll, R.D., 1974. Acoustic Waves in Saturated Sediments. Presented at the Physics of Sound in Marine Sediments, pp. 19–39.

Stoll, R.D., Bryan, G.M., 1970. Wave Attenuation in Saturated Sediments. The Journal of the Acoustical Society of America 47, 1440–1447. https://doi.org/10.1121/1.1912054

Stoll, R.D., Kan, T.-K., 1981. Reflection of acoustic waves at a water–sediment interface. The Journal of the Acoustical Society of America 70, 9.

Stopka, G., Gieleta, R., Panowicz, R., Wałach, D., Kaczmarczyk, G.P., 2024. High Strain Rate Response of Sandstones with Different Porosity under Dynamic Loading Using Split Hopkinson Pressure Bar (SHPB). Applied Sciences 14, 5347. https://doi.org/10.3390/app14125347

Strauss, J., Schirrmeister, L., Wetterich, S., Borchers, A., Davydov, S.P., 2012. Grain-size properties and organic-carbon stock of Yedoma Ice Complex permafrost from the Kolyma lowland, northeastern Siberia. Global Biogeochemical Cycles 26, 2011GB004104. https://doi.org/10.1029/2011GB004104

Streletskiy, D.A., Suter, L.J., Shiklomanov, N.I., Porfiriev, B.N., Eliseev, D.O., 2019. Assessment of climate change impacts on buildings, structures and infrastructure in the Russian regions on permafrost. Environ. Res. Lett. 14, 025003. https://doi.org/10.1088/1748-9326/aaf5e6

Sutiyoso, H.S., Sahoo, S.K., North, L.J., Falcon-Suarez, I.H., Minshull, T.A., Best, A.I., 2025. Laboratory Measurement of Sonic (1–20 kHz) P-Wave Velocity and Attenuation During Melting of Ice-Bearing Sand. JGR Solid Earth 130, e2024JB030465. https://doi.org/10.1029/2024JB030465

Sutiyoso, H.S., Sahoo, S.K., North, L.J., Minshull, T.A., Falcon-Suarez, I.H., Best, A.I., 2024. Laboratory measurements of water saturation effects on the acoustic velocity and attenuation of sand packs in the 1–20 kHz frequency range. Geophysical Prospecting. https://doi.org/10.1111/1365-2478.13607

Telford, W.M., Geldart, L.P., Sheriff, R.E., 1990. Applied Geophysics, 2nd ed. Cambridge University Press, Cambridge. https://doi.org/10.1017/CBO9781139167932

Timur, A., 1968. Velocity Of Compressional Waves In Porous Media At Permafrost Temperatures. GEOPHYSICS 33, 584–595. https://doi.org/10.1190/1.1439954

Tisato, N., Madonna, C., Saenger, E.H., 2021. Attenuation of Seismic Waves in Partially Saturated Berea Sandstone as a Function of Frequency and Confining Pressure. Front. Earth Sci. 9, 641177. https://doi.org/10.3389/feart.2021.641177

Tittmann, B.R., 1977. Internal Friction Measurements and their Implications in Seismic Q Structure Models of the Crust, in: Heacock, J.G., Keller, G.V., Oliver, J.E., Simmons, G. (Eds.), Geophysical Monograph Series. American Geophysical Union, Washington, D. C., pp. 197–213. https://doi.org/10.1029/GM020p0197

Toksöz, M.N., Johnston, D.H., Timur, A., 1979. Attenuation of seismic waves in dry and saturated rocks: I. Laboratory measurements. GEOPHYSICS 44, 681–690. https://doi.org/10.1190/1.1440969

Tourei, A., Ji, X., Rocha Dos Santos, G., Czarny, R., Rybakov, S., Wang, Z., Hallissey, M., Martin, E.R., Xiao, M., Zhu, T., Nicolsky, D., Jensen, A., 2024. Mapping Permafrost Variability and Degradation Using Seismic Surface Waves, Electrical Resistivity, and Temperature Sensing: A Case Study in Arctic Alaska. JGR Earth Surface 129, e2023JF007352. https://doi.org/10.1029/2023JF007352

Tserkovnyak, Y., Johnson, D.L., 2002. Can one hear the shape of a saturation patch? Geophysical Research Letters 29. https://doi.org/10.1029/2001GL014709

Voigt, W., 1889. Ueber die Beziehung zwischen den beiden Elasticitätsconstanten isotroper Körper. Annalen der Physik 274, 573–587. https://doi.org/10.1002/andp.18892741206

Voronov, V.P., Gorodetskii, E.E., Podnek, V.E., Grigoriev, B.A., 2016. Properties of equilibrium carbon dioxide hydrate in porous medium. Chemical Physics 476, 61–68. https://doi.org/10.1016/j.chemphys.2016.05.031

Wagner, F.M., Mollaret, C., Günther, T., Kemna, A., Hauck, C., 2019. Quantitative imaging of water, ice and air in permafrost systems through petrophysical joint inversion of seismic refraction and electrical resistivity data. Geophysical Journal International 219, 1866–1875. https://doi.org/10.1093/gji/ggz402

Waite, W.F., Santamarina, J.C., Cortes, D.D., Dugan, B., Espinoza, D.N., Germaine, J., Jang, J., Jung, J.W., Kneafsey, T.J., Shin, H., Soga, K., Winters, W.J., Yun, T.-S., 2009. Physical properties of hydrate-bearing sediments. Rev. Geophys. 47, RG4003. https://doi.org/10.1029/2008RG000279

Wallace, L.M., Saffer, D.M., Barnes, P.M., Pecher, I.A., Petronotis, K.E., LeVay, L.J., Expedition 372/375 Scientists (Eds.), 2019. Proceedings of the International Ocean Discovery Program Volume 372B/375, Proceedings of the International Ocean Discovery Program. International Ocean Discovery Program. https://doi.org/10.14379/iodp.proc.372B375.2019

Wang, X.-H., Xu, Q., He, Y.-N., Wang, Y.-F., Sun, Y.-F., Sun, C.-Y., Chen, G.-J., 2019. The Acoustic Properties of Sandy and Clayey Hydrate-Bearing Sediments. Energies 12, 1825. https://doi.org/10.3390/en12101825

Wang, Z., 1997. 3. Seismic Properties of Carbonate Rocks, in: Carbonate Seismology, Geophysical Developments Series. Society of Exploration Geophysicists, pp. 29–52. https://doi.org/10.1190/1.9781560802099.ch3

Watanabe, K., Kito, T., Wake, T., Sakai, M., 2011. Freezing experiments on unsaturated sand, loam and silt loam. Ann. Glaciol. 52, 37–43. https://doi.org/10.3189/172756411797252220

Watanabe, K., Mizoguchi, M., 2002. Amount of unfrozen water in frozen porous media saturated with solution. Cold Regions Science and Technology 34, 103–110. https://doi.org/10.1016/S0165-232X(01)00063-5

Wei, J., Li, J., Zhang, X., Wang, Z., Shi, J., Huang, Z., 2022. Experimental investigation for the dynamic adsorption behaviors of gel system with long slim sandpack: Implications for enhancing oil recovery. Energy Reports 8, 9270–9278. https://doi.org/10.1016/j.egyr.2022.07.057

West, T.R., 1995. Geology Applied to Engineering, 1st Edition. ed. Prentice-Hall.

White, J.E., 1986. Biot-Gardner theory of extensional waves in porous rods. Geophysics 51, 742–745. https://doi.org/10.1190/1.1442126

White, J.E., 1975. Computed Seismic Speeds And Attenuation In Rocks With Partial Gas Saturation. Geophysics 40, 224–232. https://doi.org/10.1190/1.1440520

Williams, K.L., Jackson, D.R., Thorsos, E.I., Dajun Tang, Schock, S.G., 2002a. Comparison of sound speed and attenuation measured in a sandy sediment to predictions based on the Biot theory of porous media. IEEE J. Oceanic Eng. 27, 413–428. https://doi.org/10.1109/JOE.2002.1040928

Williams, K.L., Jackson, D.R., Thorsos, E.I., Dajun Tang, Schock, S.G., 2002b. Comparison of sound speed and attenuation measured in a sandy sediment to predictions based on the Biot theory of porous media. IEEE J. Oceanic Eng. 27, 413–428. https://doi.org/10.1109/JOE.2002.1040928

Williams, P.J., 1995. Permafrost and climate change: geotechnical implications. Philosophical Transactions of the Royal Society of London. Series A: Mathematical, Physical and Engineering Sciences 352.

Wilson, P.S., Roy, R.A., Carey, W.M., 2003. An improved water-filled impedance tube. The Journal of the Acoustical Society of America 113, 3245–3252. https://doi.org/10.1121/1.1572140

Winkler, K., Nur, A., 1982. Seismic attenuation: Effects of pore fluids and frictional-sliding. Geophysics 47. https://doi.org/10.1190/1.1441276

Winkler, K., Nur, A., 1979. Pore fluids and seismic attenuation in rocks. Geophysical Research Letters 6, 1–4. https://doi.org/10.1029/GL006i001p00001

Winkler, K.W., 1985. Dispersion analysis of velocity and attenuation in Berea sandstone. Journal of Geophysical Research 90, 6793–6800. https://doi.org/10.1029/jb090ib08p06793

Winkler, K.W., Murphy III, W.F., 1995. Acoustic Velocity and Attenuation in Porous Rocks, in: Rock Physics & Phase Relations, AGU Reference Shelf. pp. 20–34. https://doi.org/10.1029/RF003p0020

Winters, W.J., Waite, W.F., Mason, D.H., Gilbert, L.Y., Pecher, I.A., 2007. Methane gas hydrate effect on sediment acoustic and strength properties. Journal of Petroleum Science and Engineering 56, 127–135. https://doi.org/10.1016/j.petrol.2006.02.003

Wróbel, G., Pawlak, S., 2007. A comparison study of the pulse-echo and through-transmission ultrasonics in glass/epoxy composites. Journal of Achievements in Materials and Manufacturing Engineering 22, 51–54.

Wyllie, M.R.J., A.R. Gregory, Gregory, A.R., Louis Wright Gardner, Gardner, L.W., 1956. Elastic Wave Velocities In Heterogeneous And Porous Media. Geophysics 21, 41–70. https://doi.org/10.1190/1.1438217

Xu, W., Lowell, R.P., Peltzer, E.T., 2001. Effect of seafloor temperature and pressure variations on methane flux from a gas hydrate layer: Comparison between current and late Paleocene climate conditions. J. Geophys. Res. 106, 26413–26423. https://doi.org/10.1029/2001JB000420

Xue, Y., Yue, L., Ding, R., Zhu, S., Liu, C., Li, Y., 2023. Influencing mechanisms of gas bubbles on propagation characteristics of leakage acoustic waves in gas-liquid two-phase flow. Ocean Engineering 273, 114027. https://doi.org/10.1016/j.oceaneng.2023.114027

Yang, D., Shen, Y., Liu, E., 2007. Wave propagation and the frequency domain Green's functions in viscoelastic Biot/squirt (BISQ) media. International Journal of Solids and Structures 44, 4784–4794. https://doi.org/10.1016/j.ijsolstr.2006.12.001

Yang, L., Jia, H., Han, L., Zhang, H., Tang, L., 2021. Hysteresis in the ultrasonic parameters of saturated sandstone during freezing and thawing and correlations with unfrozen water content. Journal of Rock Mechanics and Geotechnical Engineering 13, 1078–1092. https://doi.org/10.1016/j.jrmge.2021.06.006

Yin, Z., Rong Chong, Z., Kiang Tan, H., Linga, P., 2019. Effect of Multi-Stage Cooling on the Kinetic Behavior of Methane Hydrate Formation in Sandy Medium. Energy Procedia 158, 5374–5381. https://doi.org/10.1016/j.egypro.2019.01.627

You, Z., Li, Y., Yang, M., Wu, P., Liu, T., Li, J., Hu, W., Song, Y., 2024. Investigation of particle-scale mechanical behavior of hydrate-bearing sands using DEM: Focus on hydrate habits. Energy 289, 130088. https://doi.org/10.1016/j.energy.2023.130088

Yun, T.S., Francisca, F.M., Santamarina, J.C., Ruppel, C., 2005. Compressional and shear wave velocities in uncemented sediment containing gas hydrate. Geophys. Res. Lett. 32, L10609. https://doi.org/10.1029/2005GL022607

Yurikov, A., Lebedev, M., Pervukhina, M., 2018. Ultrasonic velocity measurements on thin rock samples: Experiment and numerical modeling. GEOPHYSICS 83, 47–56. https://doi.org/10.1190/geo2016-0685.1

Zhan, L., Liu, B., Zhang, Y., Lu, H., 2022. Rock Physics Modeling of Acoustic Properties in Gas Hydrate-Bearing Sediment. JMSE 10, 1076. https://doi.org/10.3390/jmse10081076

Zhang, P., Wu, Q., Mu, C., 2017. Influence of temperature on methane hydrate formation. Sci Rep 7, 7904. https://doi.org/10.1038/s41598-017-08430-y

Zhang, Q., Liu, X., He, T., Lu, H., 2022. Influence of Gas Hydrate on the Acoustic Properties of Sediment: A Comprehensive Review with a Focus on Experimental Measurements. Acta Geologica Sinica (Eng) 96, 713–726. https://doi.org/10.1111/1755-6724.14932

Zhang, Y., Gu, Y., Zhou, H., Yang, L., 2023. Extracting static elastic moduli of rock through elastic wave velocities. Acta Geophys. 72, 915–931. https://doi.org/10.1007/s11600-023-01139-9

Zhao, H., Gary, G., 1996. On the use of SHPB techniques to determine the dynamic behavior of materials in the range of small strains. International Journal of Solids and Structures 33, 3363–3375. https://doi.org/10.1016/0020-7683(95)00186-7

Zheng, J., Chong, Z.R., Qureshi, M.F., Linga, P., 2020. Carbon Dioxide Sequestration via Gas Hydrates: A Potential Pathway toward Decarbonization. Energy Fuels 34, 10529–10546. https://doi.org/10.1021/acs.energyfuels.0c02309

Zhu, T., Ajo-Franklin, J.B., Daley, T.M., 2017. Spatiotemporal changes of seismic attenuation caused by injected CO_2 at the Frio-II pilot site, Dayton, TX, USA. JGR Solid Earth 122, 7156–7171. https://doi.org/10.1002/2017JB014164

Zimmer, M., 2003. Seismic velocities in unconsolidated sands: measurements of pressure, sorting and compaction effects.

Zimmer, M., Prasad, M., Mavko, G., 2002. Pressure and porosity influences on VP−VS ratio in unconsolidated sands. The Leading Edge 21, 178–183. https://doi.org/10.1190/1.1452609

Zimmerman, R.W., King, M.S., 1986. The effect of the extent of freezing on seismic velocities in unconsolidated permafrost. GEOPHYSICS 51, 1285–1290. https://doi.org/10.1190/1.1442181